Dynamic of excitations of the Fractional quantum Hall effect : fractional charge and fractional Josephson frequency

Maëlle Kapfer

To cite this version:

Maëlle Kapfer. Dynamic of excitations of the Fractional quantum Hall effect : fractional charge and fractional Josephson frequency. Mesoscopic Systems and Quantum Hall Effect [cond-mat.mes-hall]. Université Paris Saclay (COmUE), 2018. English. NNT : 2018SACLS393 . tel-01978045

HAL Id: tel-01978045
https://theses.hal.science/tel-01978045v1

Submitted on 11 Jan 2019

université
PARIS-SACLAY

NNT : 2018SACLS393

Dynamics of excitations in the Fractional quantum Hall effect: fractional charge and fractional Josephson frequency

Thèse de doctorat de l'Université Paris-Saclay
préparée à Université Paris-Sud

Ecole doctorale n°564 Physique en Ile-De-France (EDPIF)
Spécialité de doctorat : Physique

Thèse présentée et soutenue à Gif-Sur-Yvette, le 26 octobre 2018, par

MAËLLE KAPFER

Composition du Jury :

Hélène Bouchiat	*LPS, CNRS Orsay*	Présidente de Jury
Clément Faugeras	*LNCMI, CNRS Grenoble*	Examinateur
Christian Glattli	*SPEC, CEA Saclay*	Directeur de thèse
Xavier Jehl	*INAC, CEA Grenoble*	Rapporteur
Preden Roulleau	*SPEC, CEA Saclay*	Co-directeur de thèse
Inès Safi	*LPS, CNRS Orsay*	Examinatrice
Maura Sassetti	*Physics Department, Genoa University*	Examinatrice
Xavier Waintal	*INAC, CEA Grenoble*	Rapporteur

Thèse de doctorat

Remerciements

On m' dit : "tu verras les remerciements c'est le plus dur à écrire". J'ai ri, je n'aurai pas dû. C'est donc parti pour un florilège de gratitude, de bons sentiments et autres choses positives parce que finalement c'est ce que je retire de ces trois années au SPEC.

Je souhaite évidemment en premier lieux remercier mon directeur de thèse Christian Glattli avec qui parler de physique et aussi passionnant que frustrant tant j'ai pu me rendre compte de l'immensité de mon ignorance et pour m'avoir fait profiter des conférences, en France et ailleurs. Je remercie aussi mon co-directeur de thèse, Preden dont l'expertise sur les mesures de bruit nous a bien profité.

Je tiens à remercier tous les membres du jury, particulièrement les Xavier (Jehl et Waintal) pour avoir accepté d'être les rapporteurs de cette thèse.

J'ai eu la chance d'arriver à un moment où toutes les planètes étaient alignées pour mener à bien les expériences. C'est le fruit des travaux précédents et j'ai notamment pu bénéficier de l'expertise de Matthieu qui m'a tout appris (surtout qu'il est possible d'être ami avec des gens dont les opinions sont opposées dans chaque domaine imaginable). J'espère avoir été à la hauteur avec Imen qui prend la relève et à qui je souhaite que tout se déroule aussi bien que dans mon cas.

Expérimentalement, rien n'aurait été possible sans le soutien de Patrice Jacques qui, en plus de jouer le rôle de mémoire de l'expérience, effectue un travail impeccable. Ca été un plaisir de partager la salle de manip'. Ce frigo nous en a fait voir de toutes les couleurs alors merci au groupe de Cryogénie : PP, Philippe et Matthieu pour le temps et l'énergie passés à comprendre l'origine du problème puis remettre la bête d'aplomb.

Un grand merci à tous les membres du groupe Nanoélectronique, particulièrement Patrice, François, Carlès et Fabien avec qui j'ai eu plaisir de parler de physique mais pas seulement et qui ont toujours été présents pour répondre à mes questions. Merci aussi à Claudine.

Merci aux membres du groupe Quantronique, notamment Pief, Hélène, Cristian, Marcello et Daniel, pour les conseils en fabrication et les diverses discussions, mais aussi à l'atelier, dont Dominique et Vincent. Merci aussi à la direction du SPEC et particulièrement Myriam pour son travail avec les thésards et son oreille attentive ainsi que le secrétariat, notamment Nathalie.

Un labo c'est aussi et surtout ses membres non permanents et j'ai pu profité d'une bonne fournée de thésards/post-doc notamment au sein du groupe et en premier lieu Ramiro pour sa gentillesse, pour avoir supporté les bizarreries du bureau et m'avoir rappelé les subtilités de la langue française, mais aussi Ambroise, Chloé, Jonas, Minky, Myunglae

Paul et Zubair, sans oublier les membres des autres groupes : Alizée, Camille, Fernanda et Leandro pour les séances de Yoga et enfin, les co-équipiers du foot du vendredi soir que j'ai lâchement abandonnés il y a quelques temps notamment Amal, Jean-Yves (qui n'était pas encore passé du côté permanent à mon arrivée) et Vincent. Pour m'avoir fait découvrir qu'à Massy on pouvait aussi boire des bières : Joël et Aurélie. Bon courage à Christopher pour la dernière année de thèse et la découverte que le temps passe bien trop vite.

Enfin je tiens à remercier toutes les personnes en dehors du labo qui ont participé de près ou de loin à ce que tout aille bien : Amélie, Anne-Chou, Laure, les montagnards Esther et Mathieu, les citadins Astrid et Kévin, les plus ou moins expatriées Leslie et Marion. Pour finir une énorme merci à ma famille pour tout : mes parents, Pierre et Coline, Mamie, Margaux et les cousins/ pièces rapportées !

Contents

List of Figures

List of Tables

Résumé en français

Ce travail s'inscrit dans le domaine de la physique mésoscopique où les échelles de longueurs considérées sont intermédiaires entre le monde macroscopique et l'échelle atomique. On s'intéresse notamment au cas où la longueur de cohérence de phase est plus grande que les dimensions de l'échantillon. Dans ce contexte, le régime de transport dit *balistique* présente un intérêt particulier car permettant de sonder le caractère ondulatoire des excitations lorsque la longueur d'onde de Fermi est plus petite que les dimensions caractéristiques de l'échantillon.

Grâce à leur faible densité de porteurs de charge résultant en une grande longueur d'onde de Fermi (typiquement de l'ordre de quelques dizaine de nanomètres), les semi-conducteurs permettent une réalisation expérimentale de conducteurs balistiques [44]. On s'intéresse ici aux gaz bi-dimensionnels formés à partir d'hétérostructures d'Asenure de Gallium. Les efforts faits en vue d'améliorer ces structures, notamment la mobilité, ont menés à l'observation d'un phénomène les plus remarquable de l'étude de la matière condensée : l'Effet Hall Quantique [104, 102]. Cet effet caractérisé par l'observation de plateaux de résistance Hall en fonction du champ magnétique pour des gaz bi-dimensionnels à faible température et soumis à un fort champ magnétique perpendiculaire. La position de ces plateaux, à des valeurs de h/ie^2 où i peut être entier (Effet Hall quantique entier EHQE) ou rationnel (Effet Hall quantique fractionnaire EHQF), et d'une grande importance en métrologie permettant la définition du standard de résistance électrique.

Lorsque le gaz bi-dimensionnel est dans le régime d'EHQF, le courant est transporté par des quasi-particules portant une charge fractionnaire [66]. Un moyen de mettre en évidence cette charge fractionnaire est de mesurer le bruit de grenaille résultant du partitionnement des quasi-particules à l'aide d'une lame semi-réfléchissante pour les électrons [91, 20].

Une autre propriété remarquable de ces quasi-particules est qu'elle ne présentent ni une statistique fermionique, ni bosonique mais intermédiaire appelée *anyonique* [2] qui n'est possible que pour les systèmes bi-dimensionnels [67]. Lorsque deux quasi-particules sont échangée de manière adiabatique, un terme de phase apparait entre les états initiaux et finaux :

$$|\Psi_1\Psi_2\rangle = e^{i\phi}\,|\Psi_2\Psi_1\rangle \tag{1}$$

Lorsque $\phi = 0$ ou π les particules obéissent respectivement à une statistique bosonique ou fermionique. Pour les anyons, ϕ peut prendre n'importe quelle valeur [112].

Pour le moment, les tests de cette statistiques basés sur des expériences d'interférométrie de Fabry-Pérot [114, 113] ou Mach-Zehnder [11, 12] avec des mesures DC ne se sont pas révélés convaincants. Réalisé des corrélations de charges fractionnaires de type Hong-Ou-Mandel (HOM) [47] devrait permettre de résoudre la statistiques [35]. Néanmoins pour cela il est nécessaire de pouvoir manipuler les quasi-particules de manière résolue en temps.

Le but de cette thèse est de vérifier la validité des processus dits "photo-assisté" dans le régime d'EHQF, permettant la manipulation des charges fractionnaires.

L'échantillon considéré est un Contact Ponctuel Quantique (QPC) qui consiste en deux systèmes bi-dimensionnels d'électrons au même facteur de remplissage de l'effet Hall quantique, séparés par un étroit conducteur uni-dimensionnel dont la transmission peut être contrôlée. Chaque système 2D est relié au reste du circuit par de grands réservoirs servant de bain thermique aux électrons. Le système est mis hors équilibre par l'application d'un potentiel V, qui peut être continu ou dépendant du temps, sur le réservoir (0) permettant d'injecter un courant noté I_0 dans le conducteur. Ce courant incident est ensuite partitionné en un courant réfléchi I_B et transmis I_t et mesuré respectivement via les réservoirs notés (4) et (1). Sauf mention du contraire, les mesures sont réalisée à la température de base T = 23 mK.

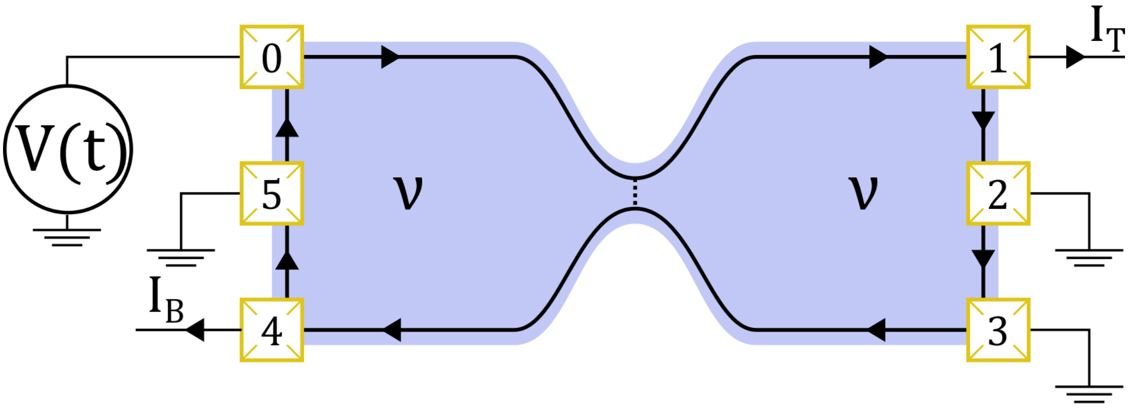

FIGURE 1 – Schéma de l'échantillon utilisé.

Détermination de la fréquence Josephson des charges fractionnaires

Ici est reportée l'étude de transport au travers d'un QPC en régime d'EHQF lorsque le conducteur est excité par une tension dépendante du temps. La tension appliquée est de la forme $V\left(t\right)=V_{ds}+V_{ac}sin\left(2\pi ft\right)$ avec f de l'ordre de la dizaine de GHz.

Le but est de vérifier la relation Josephson des charges fractionnaires [109] $f=\mathrm{f}_J$ avec

$$f_J=\frac{e^*V}{h} \tag{2}$$

L'état fractionnaire $\nu=2/5$

La plupart des mesures sont réalisées à un facteur de remplissage $\nu=2/5$, correspondant à un champ magnétique de 11,2 T. Lorsque l'on mesure la conductance au travers du QPC en fonction de la tension de grille à ce facteur de remplissage, apparaissent deux plateaux à 2/5 et 1/3 de e^2/h comme montré sur la figure 6.1. En partant du plateau 2/5, en changeant la tension de grille on change localement la densité de porteurs jusqu'à une valeur correspondant à 1/3 de e^2/h correspondant localement à un facteur de remplissage de 1/3. On différencie donc le facteur de remplissage du bulk noté ν_b toujours ici égal à 2/5 et celui du QPC noté ν_{QPC} pouvant être de 2/5 ou 1/3.

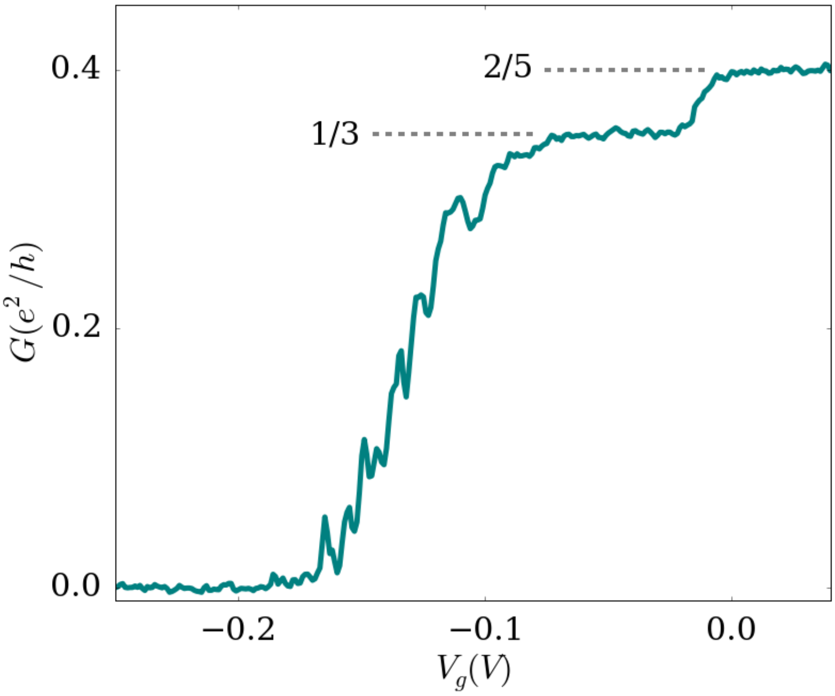

FIGURE 2 – **Coefficient de transmission aux travers du QPC à $\nu_b=2/5$.** Conductance en fonction de la tension de grille à B = 11.2 T. Deux plateaux apparaissent, un à 2/5 de e^2/h et le deuxième à 1/3 de e^2/h. La mesure est faite à la température de base ($\sim$ 30 mK) à une tension de bias $\mathrm{V}_{ds}=0$.

Vérification de la relation Josephson des charges fractionnaires

On s'intéresse dans un premier temps à l'état $\nu_{QPC} = 1/3$ où l'application d'un potentiel V_{ds} sur le contact (0) résulte en l'injection d'un courant I_0 :

$$I_0\left(V_{ds}\right) = \frac{1}{3}\frac{e^2}{h}V_{ds} \tag{3}$$

Toutes les mesures sont réalisées dans un régime dit de faible rétro-diffusion. Ce régime est défini lorsque le courant réfléchi est faible comparé au courant transmis : I_B « I_t. Dans ce cas, le bruit de grenaille DC mesuré est directement proportionnel à la charge fractionnaire [55] :

$$S_I^{dc}\left(V_{ds}, D, T\right) = 2e^* I_B\left(V_{ds}, D\right)\left(coth\left(\frac{e^*V_{ds}}{2k_BT}\right) - \frac{2k_BT}{e^*V_{ds}}\right) \tag{4}$$

Avec D = 1-R la transmission du QPC et T la température. La charge fractionnaire est alors donnée par la pente du bruit de grenaille DC en fonction du courant de rétro-diffusion I_B.

On se place pour la mesure à une tension de grille V_g = -0,09 V, correspondant à un coefficient de réflexion de R = 0,026 à zéro bias. Dans la suite, ce coefficient de réflexion va être considéré constant en fonction de V_{ds}. Cette approximation peut-être faite étant donné la caractéristique I-V :

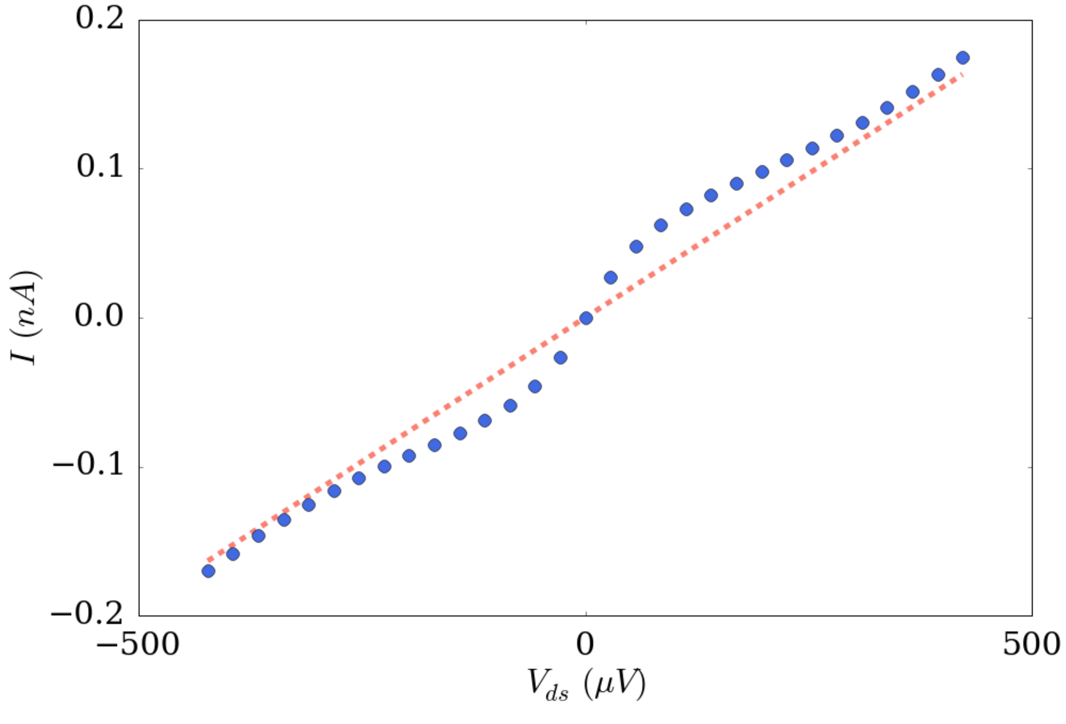

FIGURE 3 – **Caractéristique I-V à V_g = -0.09 V, ν_b = 2/5 et ν_{QPC} = 1/3.** Les points bleus représentent le courant mesuré, la ligne orange est le courant calculé pour un coefficient de réflexion constant de 0,026.

On mesure dans un premier temps le bruit de partitionnement lorsque le conducteur est excité avec une tension DC puis on superpose la tension dépendante du temps et le bruit de partitionnement est alors encore mesuré. Sur la figure suivante sont représentées ces deux mesures pour une fréquence de f = 10 GHz.

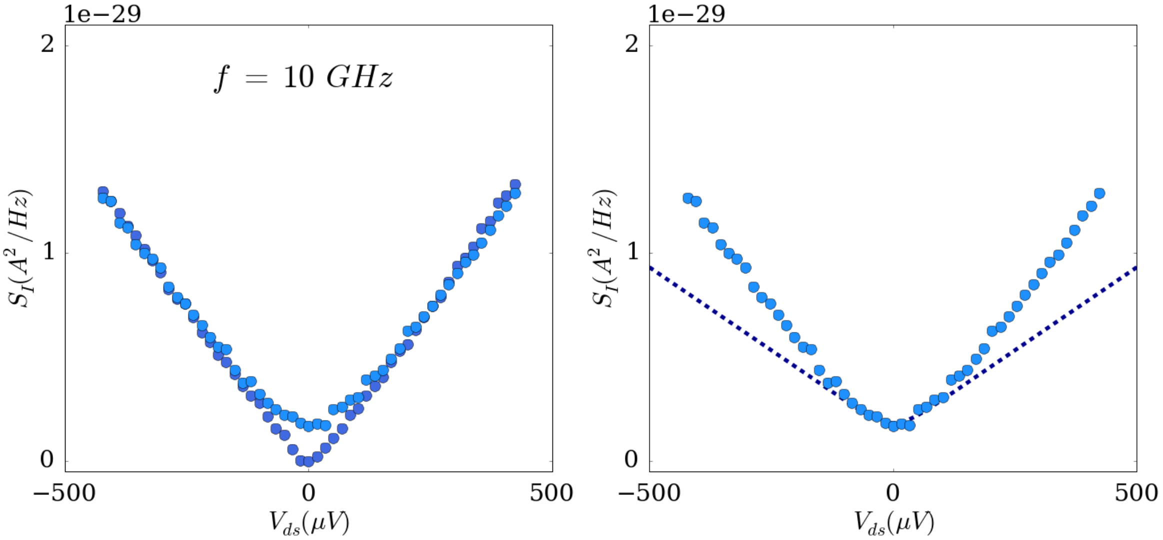

FIGURE 4 – **PASN à V$_g$ = -0.09 V, ν_b = 2/5 et ν_{QPC} = 1/3.**La figure de gauche correspond au bruit mesuré lorsque seul un bias DC est applique (bleu foncé) puis lorsque la tension dépendante du temps est superposée (bleu clair). Sur la figure de droite le bruit avec V(t) est simulée dans les faible bias par $|p_0|^2 S_I^{dc}(V_{ds})$.

Le bruit correspondant à des processus photo-assisté est [16, 19, 88] :

$$S_I^{ac}(f) = \sum_l |p_l|^2 S_I^{dc}\left(V_{ds} - \frac{lhf}{e^*}\right) \tag{5}$$

Afin de vérifier que le bruit mesuré avec l'application de V(t) correspond bien à des processus photo-assistés la contribution des quasi-particules qui n'ont ni émis, ni absorbé de photons est soustraite du bruit total. Pour se faire, le bruit mesuré avec V(t) est fité dans les faibles bias par la quantité $|p_0|^2 S_I^{dc}(V_{ds})$ où $|p_0|^2$ est un paramètre de fit et S_I^{dc} est le bruit DC mesuré.

Afin de vérifier la relation Josephson des charges fractionnaires, la fréquence d'excitation est changée et le même processus est répété.

Les points expérimentaux suivent les courbes théoriques avec f = f$_J$ pour des charges de e/3. De ces courbes, une tension seuil peut être extraite. Elle correspond à la tension à partir de laquelle le bruit en excès commence à augmenter. Pour des processus photo-assisté, la tension de seuil correspond exactement à hf/e*

Les points expérimentaux suivent la droite correspondant à f$_J$ = f avec e* = e/3 ce qui permet de valider l'observation de processus photo-assisté pour des charges e/3.

Grâce à la particularité de l'état 2/5 des charges fractionnaires différentes peuvent être sondées par simple changement de la tension de grille. En se mettant en faible rétrodiffusion de l'état 2/5, des charges e* = e/5 sont mises en évidence.

L'analyse précédent est réitérée à une tension de grille V$_g$ = -0,003 V correspondant à une réflexion moyenne de R = 0,06 et des fréquences f = 10 et 17 GHz.

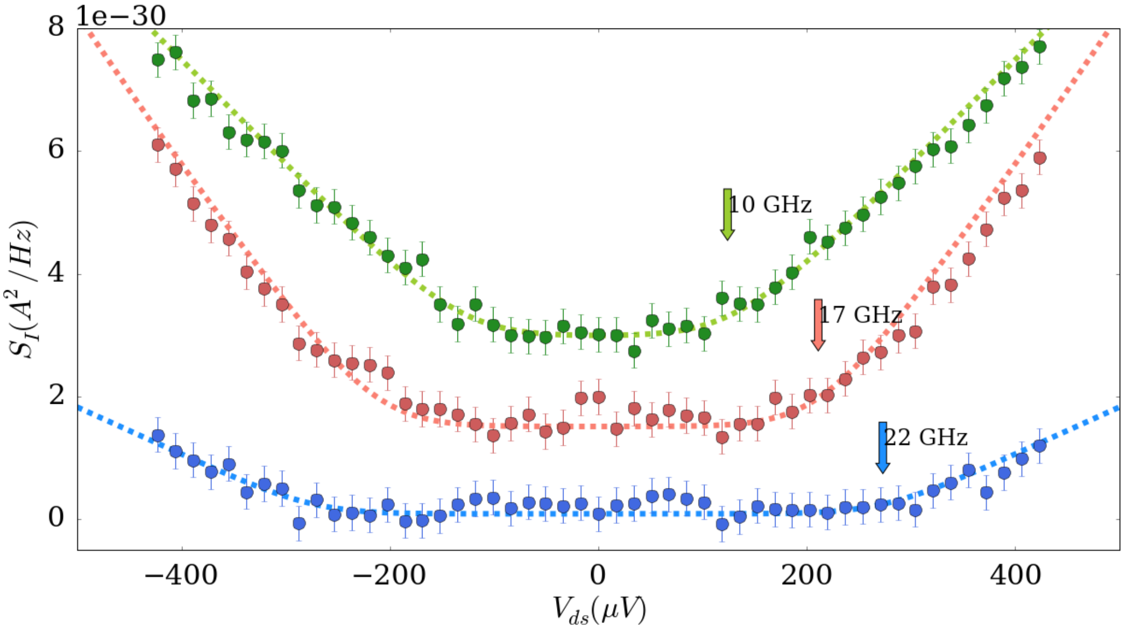

FIGURE 5 – **Bruit en excès à V$_g$ = -0.09 V pour $\nu_b = 2/5$ et $\nu_{QPC} = 1/3$.** Les lignes correpondent au bruit photo-assisté attendu pour $e^* = e/3$, $f_J = f$ et $\langle |p_0|^2 \rangle$ minimisant les variations du bruit en excès dans les faibles bias. Les points verts représentent la mesure à 10 GHz, les rouges à 17 GHz et les bleus à 22 GHz. Pour des questions de clarté, un offset est ajouté à chacune des courbes.

La relation Josephson est vérifiée pour une deuxième valeur de charge fractionnaire permettant. La vérification de cette relation permet de confirmer l'observation de processus photo-assistés pour les charges fractionnaires

Mesure de la charge fractionnaire à l'aide des corrélations croisées

Jusqu'à présent, les mesures montrées ont été réalisées en utilisant la technique dite de corrélation croisée. Le bruit est alors mesuré en utilisant les corrélations entre les fluctuations des courant réfléchis et transmis. Le système expérimental utilisé permet aussi de mesurer le bruit en utilisant la technique d'auto-corrélation correspondant aux corrélations de fluctuations de courant avec lui-même. Puisque seuls les évènements qui se produisent au QPC sont corrélés, la corrélations croisée ne portent que les informations propres au partitionnement alors que les auto-corrélations comprennent aussi le bruit dit thermique et les bruits parasites. Néanmoins ces bruits ne dépendent pas de la tension de bias V$_{ds}$ contrairement au partitionnement. L'évolution en fonction de V$_{ds}$ du bruit doit être identique qu'il soit mesuré en utilisant les auto-corrélations ou la corrélation croisée. Ce résultat se vérifie pour les mesures faites en régime EHQE.

Pourtant un résultat inattendu est apparu lors de la comparaison de ces quantités pour les mesures réalisés à $\nu = 2/5$ aussi bien pour un facteur de remplissage local de $1/3$

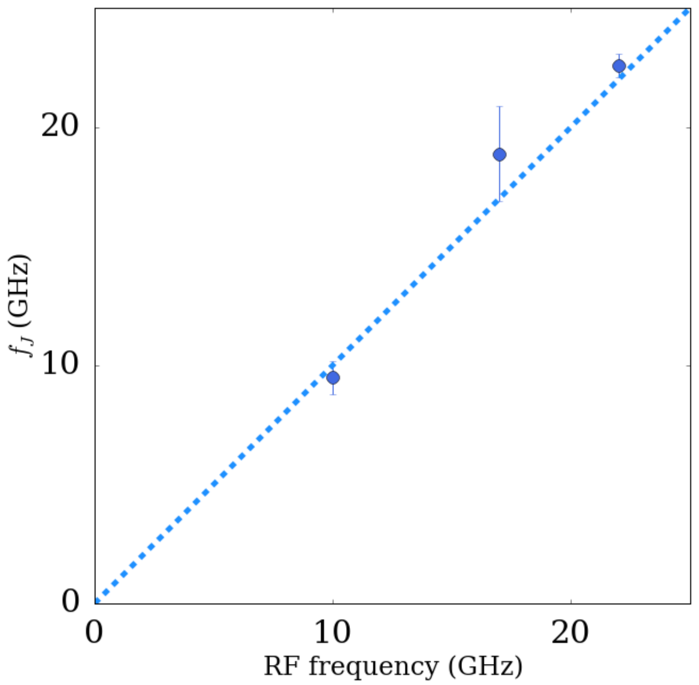

FIGURE 6 – **Fréquence Josephson des charges e/3 à $\nu_b = 2/5$ et $\nu_{QPC} = 1/3$.** Les points correspondent aux fréquence Josephson déduites des tensions seuils des bruits en excès. La ligne représente $f_J = f$ avec $e^* = e/3$.

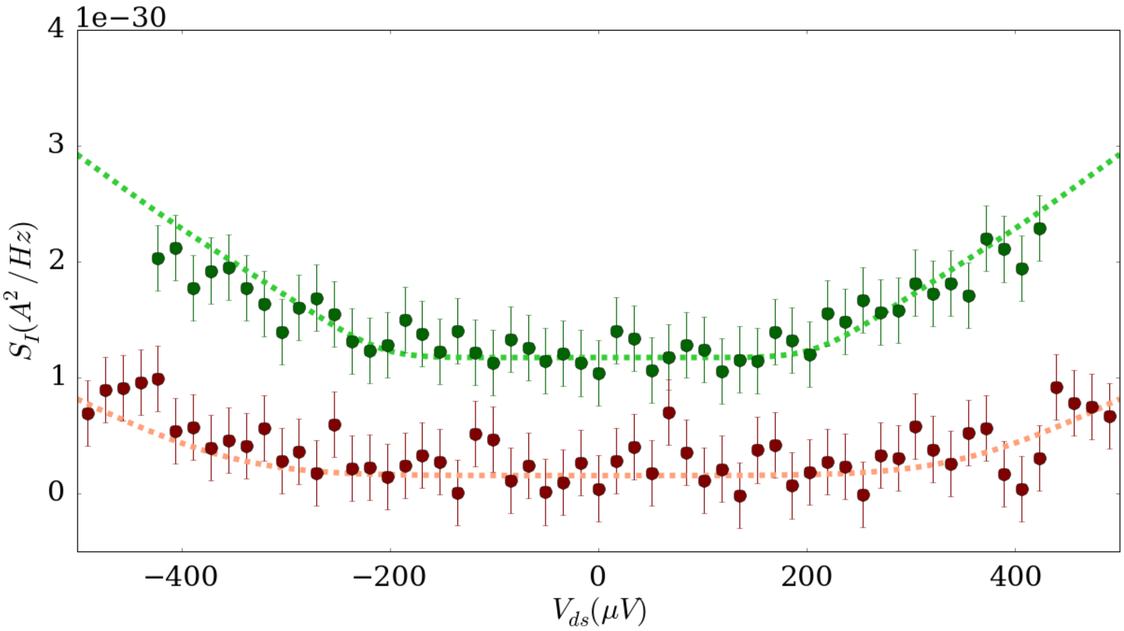

FIGURE 7 – **Bruit en excès à V_g = -0.003 V pour $\nu_b = \nu_{QPC} = 2/5$.** Les lignes correspondent au bruit photo-assisté pour $e^* = e/5$, $f_J = f$ et $\langle |p_0|^2 \rangle$ minimisant les variations du bruit en excès dans les faibles bias. Les points verts sont les mesures à 10 GHz et les rouges à 17 GHz. Pour des raisons de clarté un offset est ajouté.

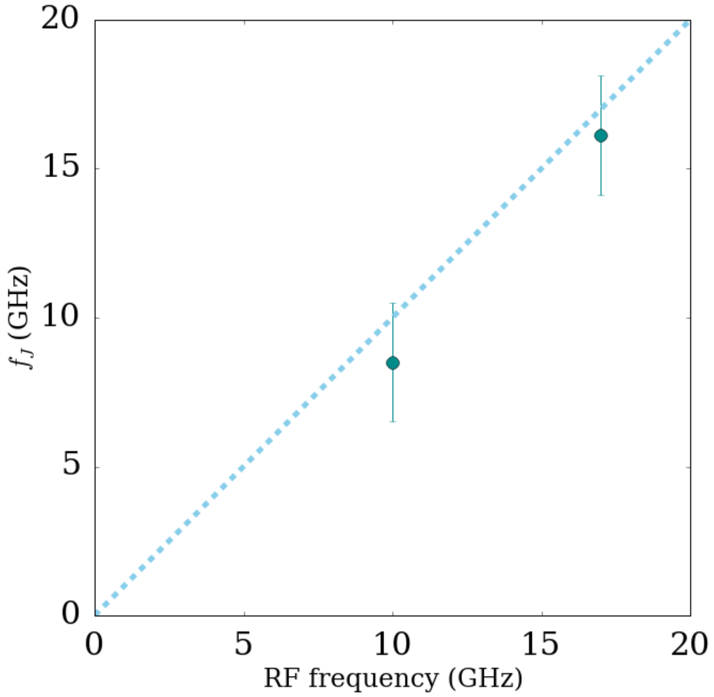

FIGURE 8 – **Fréquence Josephson des charges e/5 à $\nu_b = \nu_{QPC} = 2/5$.**Les points correspondent aux fréquence Josephson déduites des tensions seuils des bruits en excès. La ligne représente f$_J = f$ avec e$^* =$ e/5.

que de 2/5.

Alors que la valeur de charge fractionnaire (e/3 et e/5) est retrouvée pour les corrélations croisées, les auto-corrélations donnent des charges fractionnaires plus grandes qu'attendu. La même comparaison est effectuée pour les autres états fractionnaires développés $\nu = 2/3$ et 1/3.

Pour $\nu = 2/3$, la même différence est observée. Pour le 1/3 les mesures sont identiques à faible bias et s'éloignent à large bias. Néanmoins, la charges fractionnaire e/3 apparait à faible bias seulement et le bruit mesuré s'en éloigne ensuite.

Ces résultats sont similaires à ceux obtenus par un le groupe du Weizmann Institute où le bruit mesuré à l'aide des auto-corrélations donnait une charge fractionnaire supérieure à celle attendue [15, 4]. Une évolution de la charge fractionnaire en fonction de la température a été observée. On s'intéresse alors à l'évolution de cette différence en fonction de la température pour les états $\nu_b = 2/3$ et $\nu_{QPC} = 1/3$ avec $\nu_b = 2/5$. Une évolution de la charge fractionnaire mesurée par la méthode d'auto-corrélation est observée contrairement à la mesure utilisant la corrélation croisée. Les bruits mesurés avec les auto-corrélation s'effondrent lorsque la température augmente pour converger vers le bruit mesuré avec la corrélation croisée.

Cette comparaison entre bruit mesuré en corrélation croisée et auto-corrélation est aussi faite pour les mesures de bruit photo-assisté. La question est de savoir si la fréquence Josephson est celle des charges fractionnaires (mesurée à l'aide des corrélation croisées) ou

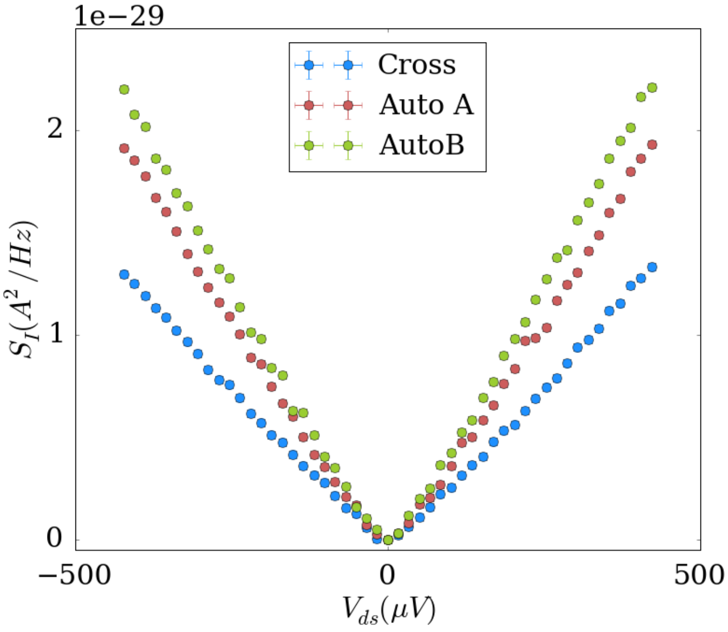

Figure 9 – **DCSN à $\nu_b = 2/5$ et $\nu_{QPC} = 1/3$ avec corrélations croisées et auto-corrélations.** Les points bleus représentent la mesure avec la corrélation croisée. En rouge le bruit et mesuré avec l'auto-corrélation des fluctuations du courant transmis, courant réfléchis en vert. Toutes les courbes sont fixées à 0 à $V_{ds} = 0$. La mesure est réalisée à température de base.

celle donnée par la pente des auto-corrélations. Une tension seuil est extraite du bruit en excès de manière similaire à ce qui a été réalisé pour les corrélations croisées. Cet tensions seuil correspond à des fréquences Josephson pour des charges fractionnaires de e/3 et e/5. Cette comparaison permet de vérifier encore une fois les effet photo-assisté des charges fractionnaires.

L'origine de la différence de mesures entre corrélation croisée et auto-corrélation reste néanmoins inconnue.

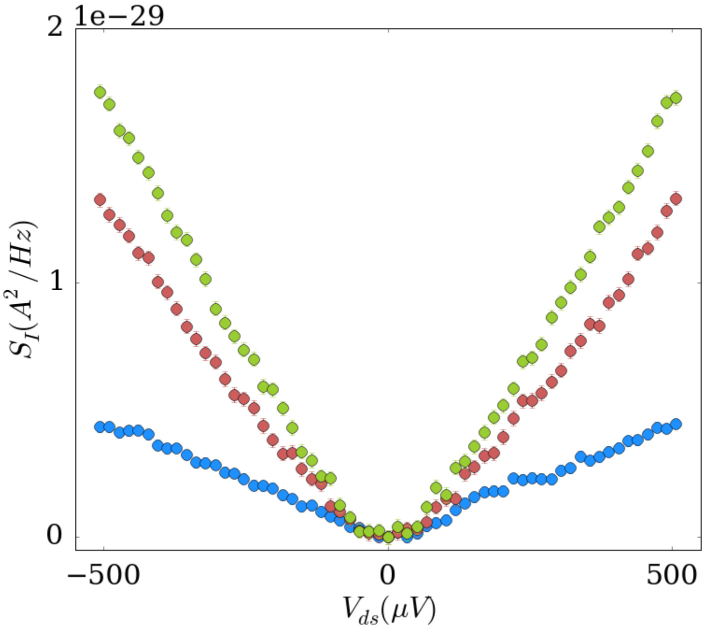

Figure 10 – **DCSN à $\nu_b = \nu_{QPC} = 2/5$ avec corrélations croisées et auto-corrélations.** Les points bleus représentent la mesure avec la corrélation croisée. En rouge le bruit et mesuré avec l'auto-corrélation des fluctuations du courant transmis, courant réfléchis en vert. Toutes les courbes sont fixées à 0 à V$_{ds}$ = 0. La mesure est réalisée à température de base.

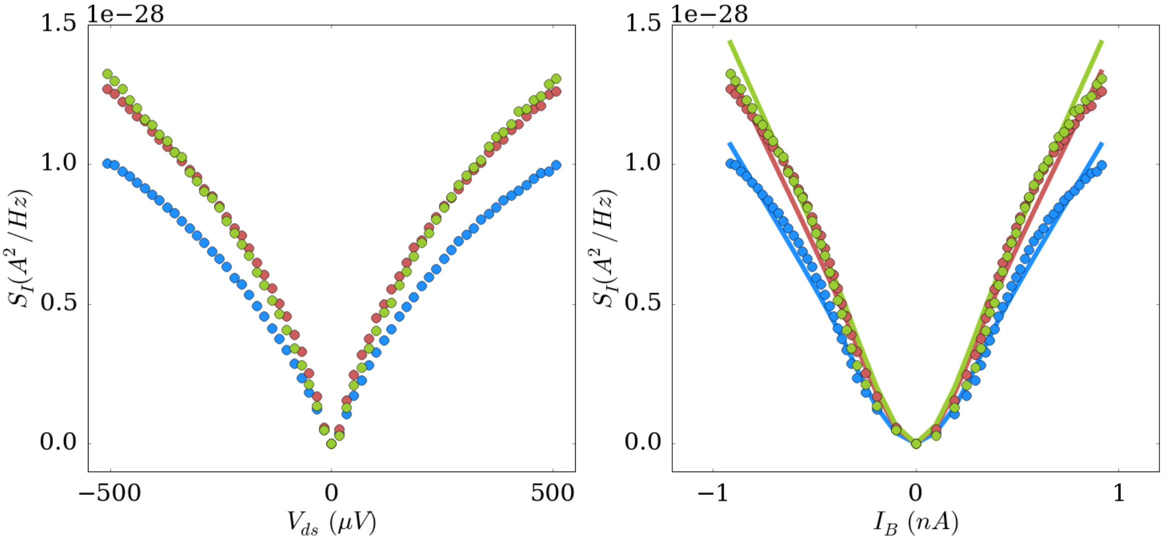

Figure 11 – **DCSN à $\nu_b = \nu_{QPC} = 2/3$ avec corrélations croisées et auto-corrélations.** A cause de la non-linéarité du courant, pour déterminer la charge le bruit est trac en fonction du courant rétro-diffusé.

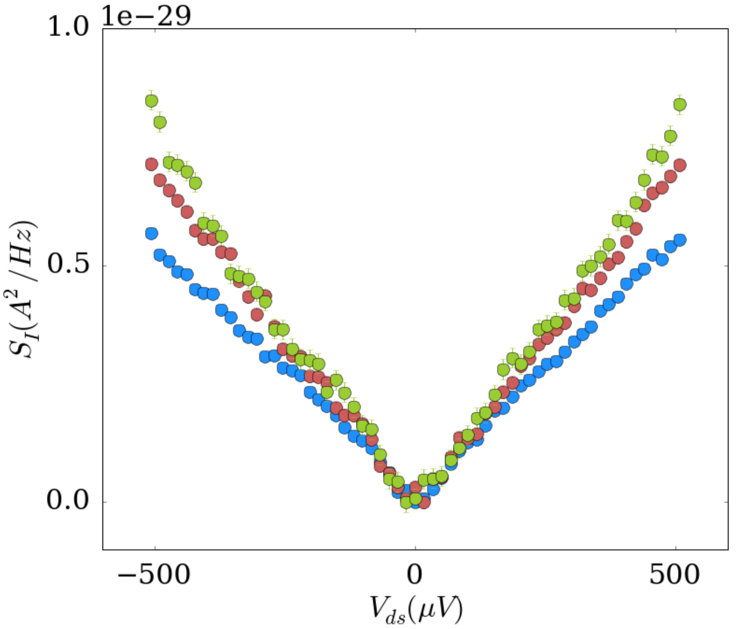

FIGURE 12 – **DCSN measurement at $\nu_b = 1/3$ avec corrélations croisées et auto-corrélations.**

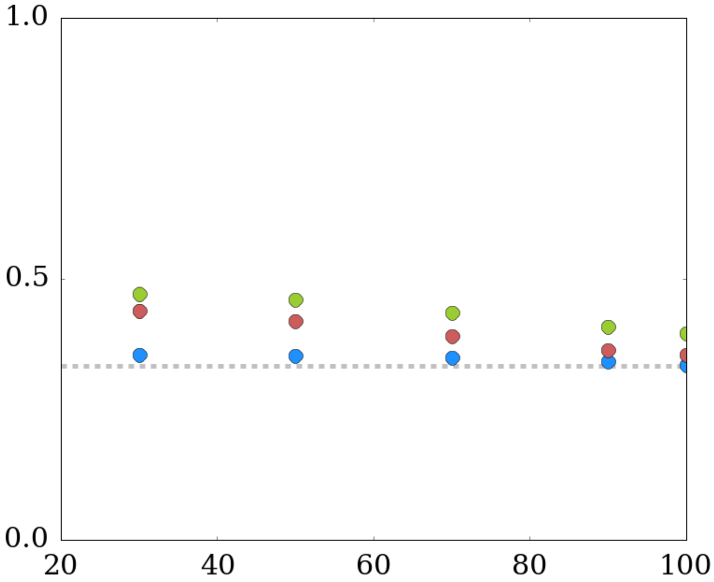

FIGURE 13 – **Evolution de la charge fractionnaire en fonction de la température à $\nu_b = \nu_{QPC} = 2/3$.** La ligne horizontale correspond à $e^* = e/3$.

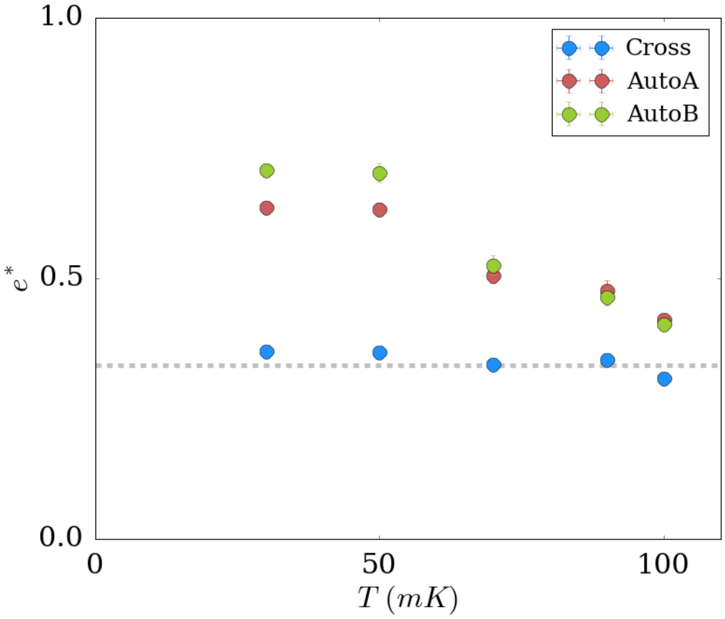

FIGURE 14 – **Evolution of the fractional charge as a function of the temperature at $\nu_b = 2/5$ and $\nu_{QPC} = 1/3$.** La ligne horizontale correspond à $e^* = e/3$.

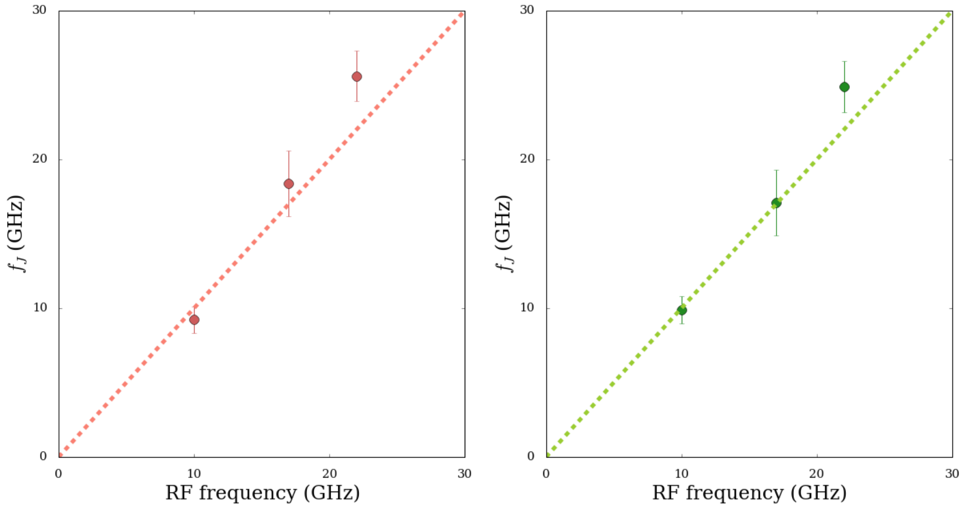

FIGURE 15 – **Relation Josephson à $\nu_b = 2/5$ et $\nu_{QPC} = 1/3$ pour les auto-corrélations.** Les deux figures représentent les fréquence Josephson trouvées à partir des auto-corrélations utilisant les fluctuations du courant transmis (gauche) et réflechis (droite). La ligne représente la droite $f_J = f$ où f_J est calculé pour une charge fractionnaire $e^* = e/3$.

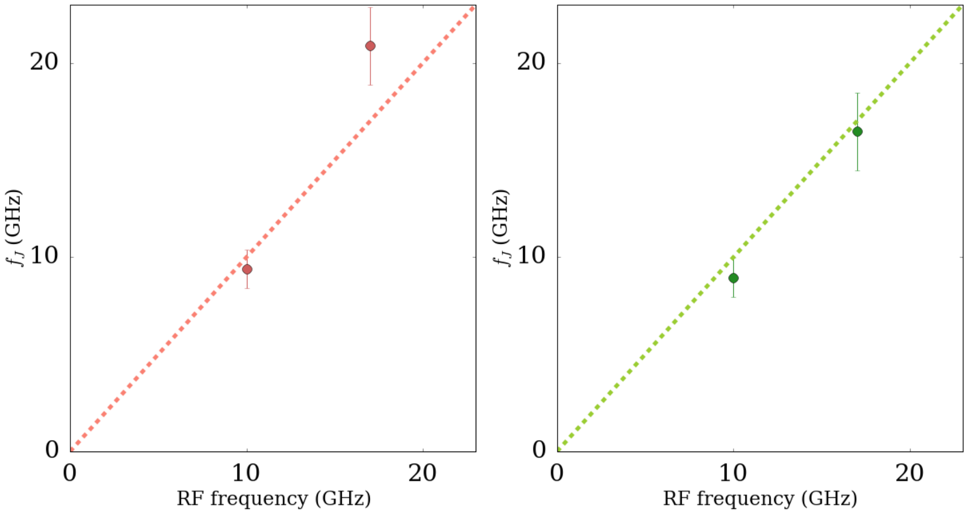

FIGURE 16 – **Relation Josephson à $\nu_b = \nu_{QPC} = 2/5$ pour les auto-corrélations.** Les deux figures représentent les fréquence Josephson trouvées à partir des auto-corrélations utilisant les fluctuations du courant transmis (gauche) et réflechis (droite). La ligne représente la droite $f_J = f$ où f_J est calculé pour une charge fractionnaire $e^* = e/5$.

Chapter 1

Introduction

This work is in the field of mesoscopic physics, which is a regime where length scales are intermediate between the macroscopic world and the atomic scale. Of all characteristics lengths considered : the Fermi wavelength λ_F, the mean-free path l_e which is the distance between two elastic scattering events and the phase breaking length l_ϕ, this is this last one that is of interest. Mesoscopic physics is defined when the phase breaking length is larger than the dimensions of the sample.

In this framework, a certain regime of transport called *ballistic* is interesting to study. It is defined when the transport of electron remains unchanged by interactions with phonons, impurities or other electrons [1]. If a narrow unidimensional conductor at low temperature of length L and width W is considered, the transport is ballistic when the mean free path is larger than both the characteristic dimensions of the conductor $l_e > L, W$. Moreover, the wave-like behaviour of excitations is probed when the Fermi wavelength λ_F is comparable to the dimensions of the sample.

The perfect candidates to study quantum ballistic transport are semi-conductors. Indeed they have a smaller density of carriers than metals, resulting in a larger Fermi wavelength, typically of the order of tenths of nanometres. Those dimensions can be reached while fabricating conductors using lithography techniques. Observations of ballistic transport in those structures is then possible [44]. The star of ballistic transport are the GaAs heterostructures as their fabrication is well controlled and high mobilities can be reached.

All the improvement made on 2D electron systems also led to the observation of one of the most remarkable phenomenon in condensed matter physics : the Quantum Hall Effect (QHE) [104, 102]. It occurs for two-dimensional systems at low temperature under a high perpendicular magnetic field. An exact quantization of the Hall resistance is observed at integer or fractional values of h/e^2 accompanied with a vanishing longitudinal resistance. The transport properties of particles in this regime is singular as it occurs along the edges of the sample. Moreover the transport is chiral and without backscattering.

For the Fractional QHE (FQHE), the number of electron is a fraction of the number of magnetic flux and the current is carried by quasi-particle that bear a fraction of the

---

[1] For complete reviews of quantum ballistic transport in narrow 1D conductor see [105]

electron charge [66]. The well-established fractional charge has first been experimentally observed by the mean of shot noise measurements [91, 20]. The shot noise results from the particle nature of excitations in quantum conductors. Indeed let us consider a quantum conductor with a scatterer. A current is injected in the conductor and the transmitted current behind the scatterer is measured. It is composed of a mean current and fluctuations arising from the probabilistic nature of transmission at the scatterer. The shot noise, as opposed to the current only, is sensitive to the nature of excitations involved in transport.

Another interesting propertie of those quasi-particles is that they are predicted to exhibit a fractional anyonic statistics [2]. Anyons, that are predicted to occur only in 2D systems [67], are intermediate between fermions and bosons. When adiabatically exchanging two particles, the initial and final states are linked by a phase factor :

$$|\Psi_1\Psi_2\rangle = e^{i\phi}\,|\Psi_2\Psi_1\rangle \tag{1.1}$$

When $\phi = 0$ or π the particles obey respectively a bosonic or fermionic statistics. For an anyonic statistics, ϕ can have any value [112].

For the moment the test of the fractional statistics have been made by the mean of Fabry-Pérot [114, 113] or Mach-Zehnder [11, 12] interferometers using DC measurements. Yet, no conclusive experimental evidence of the fractional statistics have been reported as the results obtained could not only be interpreted as signature of the fractional statistics [117]. Then another way to probe the fractional statistics would be to realize Hong-Ou-Mandel (HOM) [47] correlations of fractional charges [35]. HOM experiment for electron quantum optics consists in two separated sources of quasi-particles. One injects a charge in the conductor at a time t and the other at a time $t+\tau$ where τ can be varied. Those charges are injected towards the equivalent of a beam splitter for electrons : a quantum point contact (QPC). This requires to be able to generate a single fractionally charged quasi-particles. Recently it has been demonstrated that applying a Lorentzian pulse to a conductor leads to the injection of a minimal excitation [26]. Minimal means here that no additional electron-hole pairs are injected, but only electrons (or holes). The main motivation of this thesis is to validate photo-assisted processes in the FQHE which would enable the manipulation of a single fractionally charged anyon.

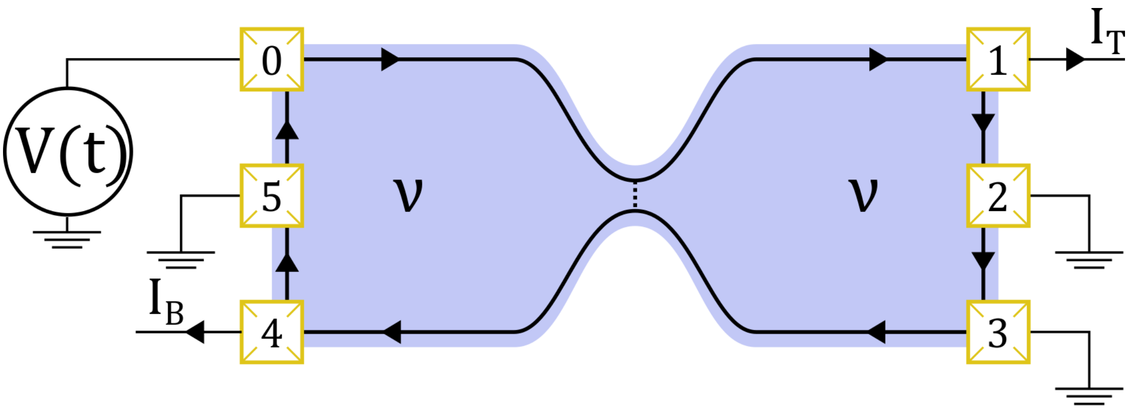

FIGURE 1.1 – Sketch of the sample considered.

In the following, we will study the transport of excitations of the FQHE in a conductor driven by both a DC and a time-dependent voltage. The conductor is composed of two identical 2D electron systems in the same QHE state or the same filling factor ν, separated by a narrow 1D conductor with a tunable transmission probability D. Each 2D electron system is connected to the circuit through large metallic contacts that also realize a thermal bath for particles. The system is put out of equilibrium by applying a voltage V, which can be a DC voltage or a time-dependent voltage, on the contact denoted (0), which injects a current I_0 in the conductor. This incoming current is partitioned at the 1D conductor and separated into transmitted I_t and backscattered I_B currents measured through contacts denoted (1) and (4) respectively.

Outline

This work is organized as follows. In a first chapter, the physics of 2D electron systems at low temperature and under a high perpendicular magnetic field is described. In the quantum picture, the energy spectrum of a real sample forms Landau levels. This energy spectrum as well as surprisingly disorder leads to the Quantum Hall Effect. For the FQHE, the description is full when considering interactions between the electrons. The unidimensional edge channels then form a chiral Luttinger Liquid (XLL). In a second chapter, the noise of a quantum conductor is introduced when the conductor is driven with a DC voltage and an AC voltage. The noise of a Luttinger liquid is presented and the formulas that will be compared to experimental data are introduced.

In a second part, the formation of a 2D electron gas (2DEG) in GaAs heterostructures is briefly presented as well as transport through a narrow constriction in the 2DEG realized by the mean of a Quantum Point Contact (QPC). The nanofabrication of the device used during this thesis is also presented. Then the experimental set-up to realize zero-frequency noise measurements at low temperature in the FQHE is introduced.

Finally, the experimental results are exposed. First are discussed shot noise measurements when the conductor is excited with a time-dependent voltage and the Josephson frequency of fractional charges is probed. Then a comparison of measurement using cross-correlation and auto-correlation techniques is done and we find that surprisingly for some filling factor an unexpected result is obtained.

Chapter 2

The Quantum Hall Effect

In 1980, the DC transport of an electron inversion layer of a Si-MOSFET at low temperature as a function of the magnetic field showed a Hall resistance quantized as $h/\nu e^2$ with ν an integer, while the transverse resistivity drops to zero [104]. Two years later the same measurements were done on a 2D electron gas (2DEG) in high mobility AlGaAs heterostructures. Plateaus of Hall resistance at fractional values of ν were observed, still accompanied by a vanishing transverse resistivity [102]. Those two observations, awarded by Nobel prizes in 1985 and 1998 for respectively the Integer Quantum Hall Effect and the Fractional Quantum Hall Effect, opened the door to a large field of condensed matter physics still of interest.

One of the main feature of the Quantum Hall effect is that the conductance quantization is universal and has a major role in metrology. It can be used to define the electrical resistance over a very large range of parameters and within a presicion of 10^{-9} [78]. This remarkable characteristic arises from the fact that the quantization does not depend on the materials or the geometry of the sample but only on two fundamental constants h and e. Moreover the observation of the QHE requires only a two-dimensional system and surprisingly disorder.

The Integer and Fractional QHE may seem similar but different pictures are required for their description. For both those QHE, a gap in the energy spectrum is opened, nevertheless the origin of this gap is different for the two effects. When the IQHE is easily and necessarily described using Landau levels and Fermi statistics, for the FQHE the Coulomb interaction between charged particles have to be considered. In both cases, transport properties are remarkable. The FQHE is of singular interest as the elementary 2D excitations carry a fractional charge and do not obey neither a fermionic nor a bosonic statistics.

In the following is shortly described the physics of 2D electrons in a perpendicular high magnetic field leading to the Integer and Fractional Quantum Hall Effects. The singular transport properties in those regimes are reviewed. Finally the Luttinger liquid behavior of edge states carrying fractional charge in the FQHE is considered.

2.1 Motion of 2D electrons in a perpendicular magnetic field

Here we first consider the classical motion of 2D electrons in a magnetic field. Let us consider spinless electrons confined in a xy plane. Interactions between electrons are neglected. A perpendicular magnetic field B is applied along the z-axis. Because of the Lorentz force, the motion of the electron of mass m is circular at the angular frequency ω, independent of the cyclotron radius r :

$$\omega = \frac{eB}{m} \tag{2.1}$$

If an electric field E is applied in the x-direction, the trajectory is a superposition of the cyclotron motion and a linear motion along the y-axis with a drift velocity $v_d = -E/B$. In that case, the Hall resistivity is $\rho_{xy} = B/en_s$ with n_s the electron density. As the current is orthogonal to the electric field, no dissipation is possible so the longitudinal resistivity is $\rho_{xx} = 0$.

2.2 The Integer quantum Hall effect

2.2.1 Landau levels

The well known quantum picture of the cyclotron motion is quickly presented here, considering a 2D system in a AlGaAs heterostructure. The Hamiltonian of 2D electrons in presence of a perpendicular magnetic field can be written using the kinetic momentum $\Pi = \mathbf{p} - e\mathbf{A}$ and the effective mass $m^* = 0.067m_e$ of the electrons in AsGa, with m_e the elementary electron mass.

$$H = \frac{1}{2m^*}\left(\mathbf{p} - e\mathbf{A}\right)^2 = \frac{1}{2m^*}\Pi^2 \tag{2.2}$$

The Hamiltonian can be reduced to that of an harmonic oscillator at cyclotron frequency ω. The energy spectrum is given by :

$$E_n = \hbar\omega\left(n + \frac{1}{2}\right) \tag{2.3}$$

The states with the same energy, or the same quantum number n are the n^{th} Landau levels (LL). Each Landau level is highly degenerated, as the arrangement of the center of the cyclotron orbits over the surface S of the 2DEG can be done in many different ways. Using $\phi_0 = h/e$, a flux quantum, the degeneracy is equal to the number of quantum flux in the surface :

$$N_\phi = n_\phi S = \frac{BS}{\phi_0} \tag{2.4}$$

To describe the system, the filling factor is defined as the number of electron per flux quantum.

$$\nu = \frac{n_s}{n_\phi} \tag{2.5}$$

When the filling factor is an integer, $\nu = p$, the p lowest LLs are completely filled with electrons and the $p+1$ LL are completely empty. Filling of the next LL *i.e.* adding an electron, corresponds to adding an energy $\hbar\omega$. The quantum fluid is called incompressible.

2.2.2 Edge states

In real samples, one needs to consider the confining potential at the edges *V(x)*. This potential modifies the energy spectrum in such a way :

$$E_n = \hbar\omega\left(n + \frac{1}{2}\right) + V(x) \tag{2.6}$$

The potential bends the LLs at the borders of the sample (see figure 2.1). The resulting confining electric field gives to the electrons a non zero drift velocity that move along the equipotential. Indeed the group velocity of the electrons can be written using the energy dependence as a function of the position in the n^{th} LL.

$$v_n(x) = -\frac{1}{eB}\frac{\partial E_n(x)}{\partial x} \tag{2.7}$$

The drift velocity is finite and has opposite sign on opposite edges. By contrast, the velocity of bulk electrons is zero, meaning that they do not contribute to the total current.

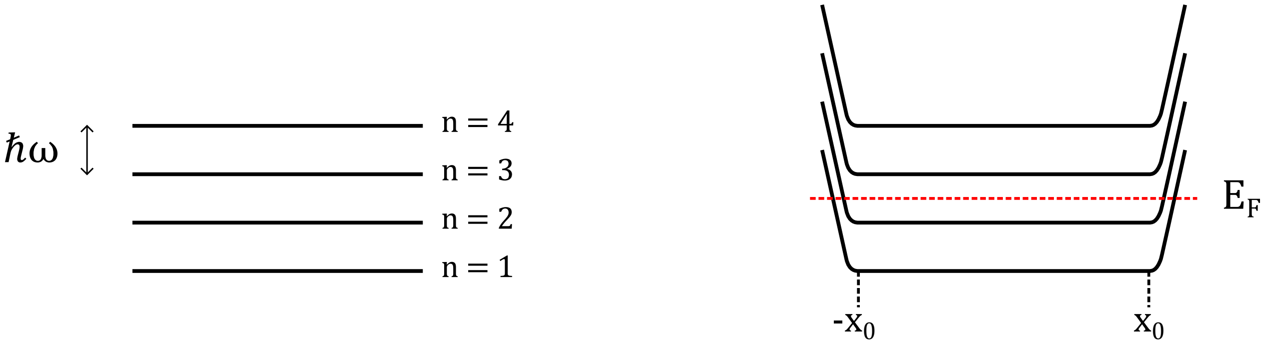

FIGURE 2.1 – **Landau levels.** Left figure shows the LL, separated by the energy $\hbar\omega$. Right figure shows LLs in a sample where they are bent due to the confining potential at the edges. This potential is equal to zero for position such as $|x| < x_0$ and increases at the borders of the sample. The Fermi energy is plotted in red, corresponding to a filling factor $\nu = 2$.

Hence the current is only carried by particles propagating along equipotential lines at the edges of the sample called *edge channels* [41, 98]. An edge channel is defined each time the Fermi energy crosses a LL so the number of edge channel is equal to the filling factor ν. Moreover, the propagation along the quasi-unidimensional edge channels is chiral : the excitations at opposite edge propagate in opposite direction. Inside one edge channel all carriers move in the same direction. Indeed even when scattered by an impurity, the electron is at most backscattered over a cyclotron radius [8]. Hence, the only way for an electron to be backscattered is by reaching the opposite edge, which is prevented by the spatial separation of the channels. In chapter 4 a way to achieve a controlled backscattering using a Quantum Point Contact is presented.

Nevertheless, the description of LL with a confining potential is not enough to explain the IQHE. Surprisingly disorder is the key ingredient.

2.2.3 The role of disorder

Disorder plays a major role for the observation of the QHE. Indeed, the Fermi energy is related to the density of state such as [17] :

$$\delta n_s \left(E_F\right) = N \left(E_F, B\right) \delta E_F \tag{2.8}$$

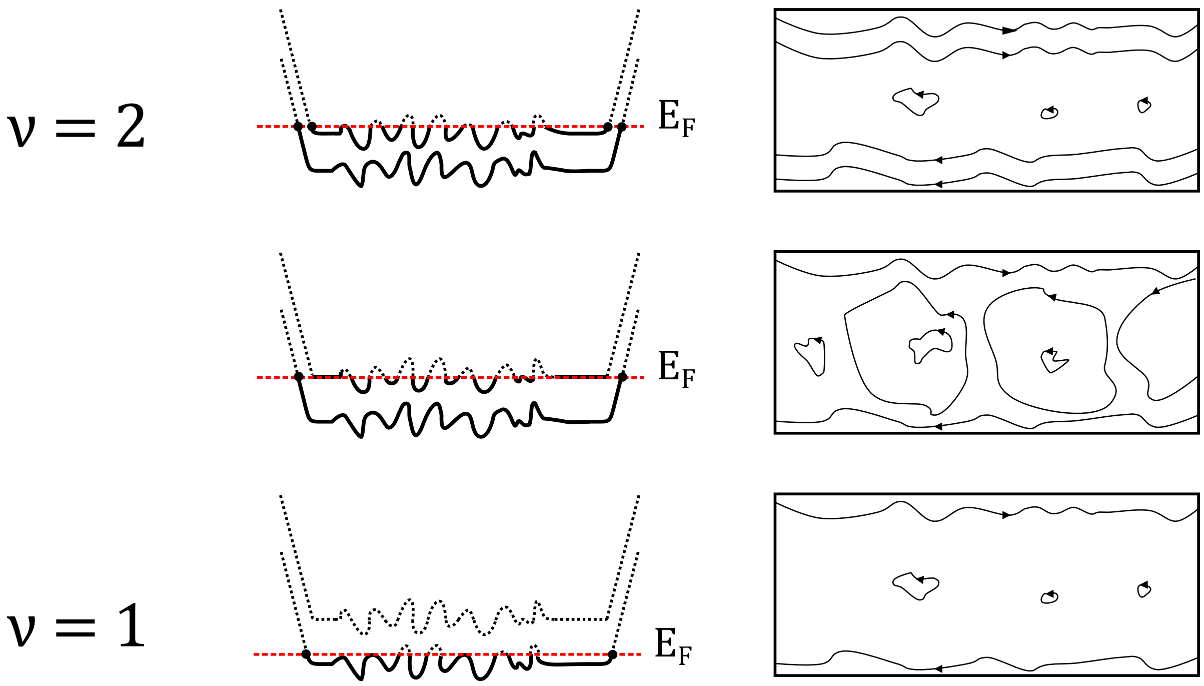

FIGURE 2.2 – **The role of disorder.** The full black lines are the occupied states, dotted lines are the empty states. The upper figure corresponds to the case of $\nu = 2$. The Fermi energy intersects two LLs at the edges and localized states developed in the bulk. When increasing the magnetic field the orbit of the localized states becomes larger and there is a non zero conductance through the bulk shown in the middle figure.

When few states are available, a change in the electron density results in a large change of the Fermi energy whereas when many states are available one needs to change a lot the electron density to change the Fermi energy.

Let us first consider the case of a bi-dimensional conductor under a high perpendicular magnetic field with no impurities. The density of states is peaked at the LL and decreases at the border of the conductor. The Fermi energy "jumps" from one LL to the other as there are only few states available between peaks. The only states occupied are those in the bulk, therefore, no edge states are developed and the Hall resistance evolves continuously with the magnetic field.

For a disordered conductor, the potential induced by the impurities has to be considered. Indeed, given the presence of impurities in the bulk of the conductor, a local minima or maxima of potential appears [81, 116]. Equipotential lines go around impurities in a closed loop.

Those impurities are responsible for the observation of plateaus of Hall resistance and zero longitudinal resistance. Indeed when the Fermi energy lies between LLs, because of the impurities there are states available in the bulk of the conductor and the Fermi energy can then lie between LL. While the excitation of the edge propagate, in the bulk electrons are localized at the impurities and do not contribute to a net current. This is represented in the upper and lower sketches of figure 2.2. The Hall resistance measured is then the same as long as localized states are spaced enough so they do not communicate. Between plateaus, when the Fermi energy lies in the middle of a LL, the orbit of the localized states is high enough so that electron can be transmitted through those states. The longitudinal resistance is not zero anymore.

2.2.4 Transport properties in the IQHE

Current When coupling a system that exhibits IQHE to large metallic reservoirs, one can study the transport properties in the quantum Hall regime. The reservoirs are at equilibrium with well defined temperature T and chemical potential μ. For reservoirs at different chemical potential such as $\Delta\mu = eV$ the current carried by one edge state is [65, 41] :

$$I = \frac{e}{h}\Delta\mu \tag{2.9}$$

The total current is the sum of all the contribution from each channel so for n edge channel it is nI. The two-terminal resistance is defined as :

$$R = \frac{1}{n}\frac{h}{e^2} \tag{2.10}$$

A Hall bar geometry can be used to measure both the Hall and longitudinal resistance. As the current flows along one edge channel without dissipation [8], the longitudinal resistance is zero while the two terminal resistance is equal to the Hall resistance.

When opposite channels are brought close enough, the scattering of electron at an impurity can induce backscattering *i.e* transfer of an electron from one edge to the other. The effect of backscattering in transport is well described using the Landauer-Buttiker-Martin formalism which is the object of the next chapter.

Edge channels When placed in a magnetic field such that the Hall resistance is on a plateau, the bulk electron density is a constant equals to an integer multiple of the density of magnetic flux. Hence the bulk is incompressible. Now, taking into account screening in electrostatics calculations in [14] it has been shown that the electron density varies smoothly from bulk density to zero at the edges. The confining potential bends the LLs as previously seen. Each time the Fermi level meets a LL, the electron density is not pined anymore to a fixed value and electrons can rearrange in order to screen the confining potential, forming a compressible state. Near the edges this smooth variation of the electron density leads to the formation of alternating compressible and incompressible strips.

2.3 The Fractional quantum Hall effect

The fractional quantum Hall effect is observed in high quality 2DEGs, which means samples presenting a large carrier mobility and for which the effect of the interactions between particles is large compared to disorder.

We consider the case where $\nu < 1$, when only the first Landau level is partially filled. The FQHE occurs when a LL is not completely filed, because of the high degeneracy of LLs there are a lot of possibilities to spread the electron wavefunction over a large number of states. Nevertheless, the Coulomb repulsive interactions partially lift the LL degeneracy and tends to order the electrons. For certain rational filling factor this interaction leads to a unique ground state : a correlated FQHE quantum fluid.

2.3.1 Laughlin's trial wavefunction

Let us consider the $\nu = 1/3$ FQH state whose physics have been elucidated by R. B. Laughlin. He proposed a trial wavefunction for fractional states at filling factor $\nu = 1/(2\text{p}+1)$ with p an integer [66, 81], writing the ground state of N quasiparticles at the position $z_j = x_j + iy_j$ and looking for the form of the wavefunction minimizing the energy. From the wavefunction of a single-particle state of a 2D electron moving in a plane with a perpendicular magnetic field in a symmetric gauge for the vector potential, he wrote the ground state of the FQHE as follows :

$$\Psi\left(z_1, \ldots, z_N\right) = \prod_{i<j}^{N} f\left(z_i - z_j\right) exp\left(-\frac{1}{4}\sum_{l}^{N}\left|z_l\right|^2\right) \tag{2.11}$$

Fortunately, there are many constraints to solve this problem resulting in a search of the minimum unnecessary. Indeed, to write the function f one needs to find the function that satisfies all the restrictions.

First, the probability for two particles to be at the same position z_i is zero because particles repel each others, then there is a component $f\left(z_i - z_j\right)$ that goes at zero when the argument is zero. The wavefunction was deduced from a the single-body state in a symmetrical gauge where f is a polynomial function. The function f is then written $f(z) = z^m$ with m an odd integer. Indeed, the wavefunction has to be antisymmetrical as electrons obey a Fermi-Dirac statistics. The wavefunction that answers all constraints is :

$$\Psi_m = \prod_{i<j}\left(z_i - z_j\right)^m exp\left(-\frac{1}{4}\sum_{l}\left|z_l\right|^2\right) \tag{2.12}$$

The number m is found to be equal to the inverse of the filling factor.

$$m = \frac{1}{\nu} \tag{2.13}$$

2.3.2 The fractional charge

The remarkable prediction made while trying to give a theoretical picture of the FQHE is that the elementary excitation would carry a fractional charge. To determine the charge of the excitation of the FQHE, the modulus square of the wavefunction is identified to the distribution probability of a plasma : repelling particles of charge m with background particles so as to keep the total charge neutral. An elementary excitation of the quantum fluid is done by adiabatically inserting a quantum flux in the fluid at a position denoted z_0, which corresponds to the creation of a quasi-hole. To do so, the wavefunction is multiplied by $\prod_i (z_i - z_0)$. This excitation is screened by the plasma to preserve the neutrality by engaging 1/m charges, corresponding to the charge of the quasi-hole.

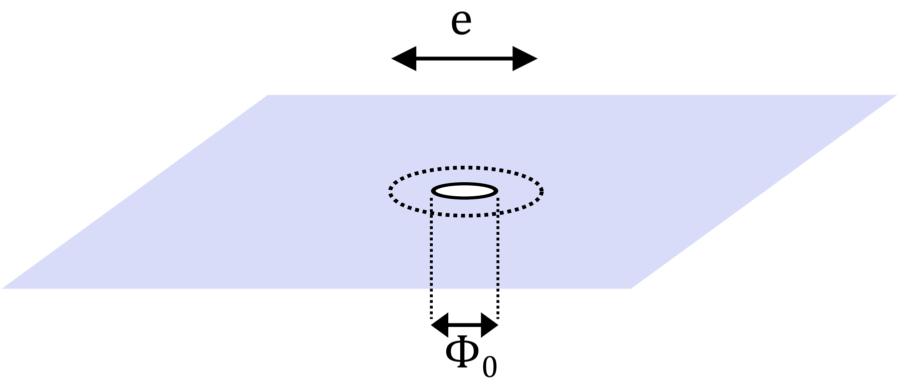

FIGURE 2.3 – **Fractional charge.** When adding a flux quantum a quasi-hole is created in the quantum fluid. As there are, for $\nu = 1/3$, three electrons per flux quantum, the charge of the quasi-hole is equal to e/3.

In other words, for example for the $\nu = 1/3$ state, there are three flux quanta occupying the same area as one electron (see figure 2.3). Hence one flux quantum occupies the equivalent of 1/3 of an electron. The charge of the quasi-hole is then of $e^* = -e/3$.

The fractional quantum hall liquid is also incompressible as adding or removing a quasi-particle costs a finite amount of energy corresponding to the fractional gap.

This theory predicts well filling factors in the first Landau level corresponding to $\nu = 1/(2p{+}1)$. Nevertheless other forms of fractional filling factors have been observed, hence the need for another pictures of those FQH states.

The fractional charges of the FQHE are believed to obey a statistics that is neither one of Fermions nor Bosons, but rather an intermediate called a fractional anyonic statistics [2].

2.3.3 The composite fermions theory

The composite fermions theory was developped by Jain in 1989 [48]. His work followed previous theoretical ones [40, 42] while attempting to explain the limited set of fractional filling factors experimentally observed[1].

---

[1] A review of fractional filling factor observed at that time is presented in [81].

Jain exposed the state of a 2D electron gas under a high perpendicular magnetic field as follows : to each electron are attached an even number $2p$ of flux quantum. Those composite particles, called composite fermions as the number of flux quantum is even [2], experience an effective magnetic field B_{eff} equals to zero when $\nu = 1/2$ [3]. The effective filling factor of composite fermions is $n = n_s\phi_0/B_{eff}$. From this, one can write the filling factor ν corresponding to the LL filling using the relation 2.5 :

$$\nu = \frac{n}{2np \pm 1} \tag{2.14}$$

When n is an integer, the FQHE at filling factor ν can be viewed as the IQHE of composite fermions at filling factor n. For example for $p = 1$, the fractional state $\nu = 1/3$ is the IQHE of CF at a filling factor $n = 1$ and the state $\nu = 2/5$ is the IQHE of CF at $n = 2$.

From this filling factor, the charge of the elementary excitation can be deduced [116]. Indeed, for the IQHE there are $1/n$ flux quantum per electron and the elementary excitation carry a charge e. For the FQHE there are $(2np+1)/n$ flux quantum per electron so by identifying this to the IQHE of CFs, the charge of a quasi-electron is written :

$$e^* = \frac{e}{2np + 1} \tag{2.15}$$

The filling factor $\nu = 1/2$ plays a central role in Jain's theory and the formation of a Fermi sea of CF [43] is used to explain some singular measurements at this filling factor. Indeed, the measurement of the longitudinal resistance shows Shubnikov-de-Haas oscillations that are symetrical around $B_{eff} = 0$ mimicking what is observed around B $= 0$ [97, 23]. Moreover, a convincing experimental observation of CFs was done by magnetic focusing measurement that rely on the deflection of electron trajectory under a magnetic field [38]. Current is injected through a constriction and the voltage is measured through another constriction at the right of the injection. One of the main result of this experiment was that for B$>B_{eff}$ periodic peaks of resistance were observed while for B$<B_{eff}$ no change in the resistance was measured. This result is similar to what is observed around zero magnetic field, supporting the interpretation of FQHE as a IQHE of CFs.

2.3.4 Edge channels of the FQHE as a chiral Luttinger liquid

Although the FQHE arises from interactions between electrons, a description of the transport in terms of edge channels is still valid for fractional filling factors. A first description has been given by Beenakker [3, 60] considering only thermodynamics arguments. At the edges of the 2D electron gas the density is reduced because of the confining potential (figure 2.1). If the confining potential presents a smooth variation along the x-axis, the increase of the density from the edge to the bulk presents steps each time $n_s = \nu_n n_\phi$ corresponding to one edge channel. For an ideally infinitely smooth potential all fractional

---

[2] A composite boson is formed if the number of flux attached is odd

[3] This effective magnetic field is written $B_{eff} = B \mp 2pn_s\phi_0$, with the sign given by the orientation of the attached flux quantum relatively to the applied magnetic field.

filling factor would be developed however in real samples only some filling factor (with the largest gap) are observed.

The current carried by the nth edge channel is

$$I_n = \Delta\nu_n \frac{e}{h} \Delta\mu \tag{2.16}$$

With $\Delta\nu_n$ the difference between two consecutive filling factor developed in the sample which is then fractional. From this approach only the two-terminal conductance can be derived.

Another model describing the edge channels in the FQHE was introduced by Wen [107, 108, 110, 109], from which more conclusion about transport properties can be drawn. In unidimensional quantum conductor when considering the interactions between electrons, a Fermi-liquid theory can no longer be used to describe the transport properties of the system. Instead, a Tomonaga-Luttinger liquid theory [101, 71] is used to describe the edge channels of the FQHE.

Because edge states of the FQHE are incompressible, the only possible excitations consist in a deformation at the boundary of the system (see figure 2.4) like the surface waves of an incompressible liquid. The equation of propagation of the deformation $h_{\pm}(X,t)$ along the boundary $\mathrm{Y} = \pm\mathrm{Y}_F$ is found using an analogy with a classical hydrodynamic approach with v_d the drift velocity of electrons at the Fermi energy [4].

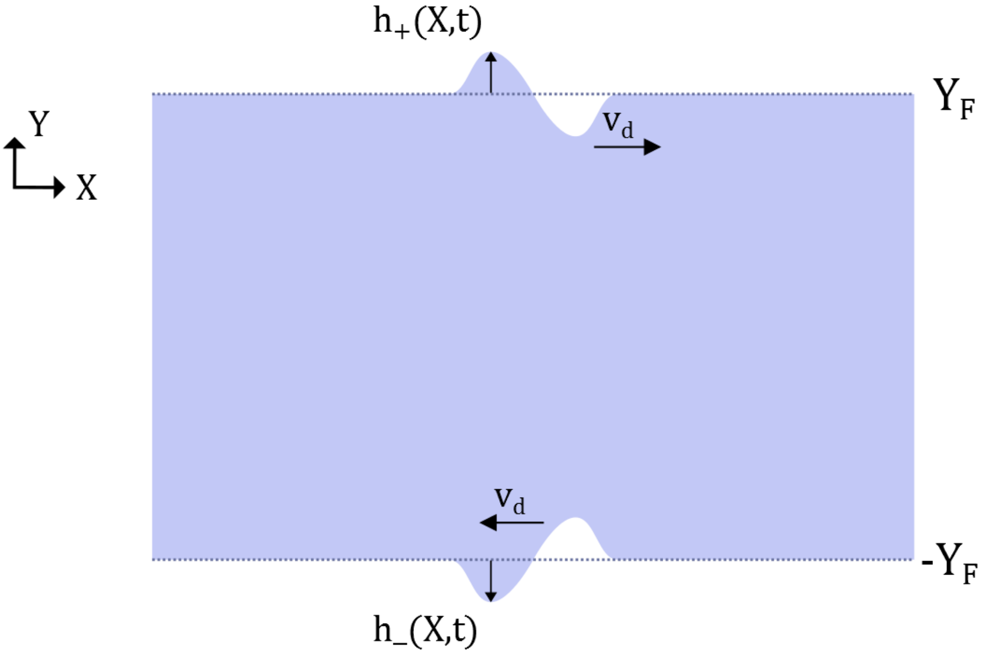

FIGURE 2.4 – **Chiral Luttinger Liquid.** The blue region is the incompressible FQH fluid at filling factor ν. Because of the incompressibility the only deformation of the liquid is a charge density wave propagating along the edge at the drift velocity v_d.

After introducing quantization in this classical approach, the description of edges in the FQHE is comparable to a chiral Luttinger liquid theory. For Luttinger liquids, when

---

[4] The confining potential is assumed to be symmetrical regarding the opposite edge so that the absolute value of the drift velocity is the same along each edge.

neglecting the spin of electron, the conductance is written

$$G = g\frac{e^2}{h} \tag{2.17}$$

In Luttinger liquid theory, the constant g is not universal, whereas in the framework of the FQHE, this constant does not depend on the sample geometry and is found strictly equal to the filling factor : $g = \nu$.

The tunneling conductance of particles between a metal and a Luttinger liquid has a power-law behavior as a function of temperature or bias voltage. The effects of temperature and bias on the conductance are comparable.

$$G(T) \sim T^{\gamma} \tag{2.18}$$

$$\frac{dI}{dV} \sim V^{\gamma} \tag{2.19}$$

with the constant γ

$$\gamma = \frac{1}{\nu} - 1 \tag{2.20}$$

A similar law is found for the tunneling between identical Luttinger liquids (FQH states at the same fractional filling factor) with a doubled exponent. Then, the main result of this Luttinger liquid description of the edge channels in the FQHE is that I-V characteristic is non linear as opposed to the case of the IQHE. This was experimentally observed for the first time at $\nu = 1/3$ for a sample using a “cleaved-edge overgrowth” geometry, which corresponds to tunneling between a metal and a 2DEG in a FQH state [13]. This geometry allows the study of electron tunneling through a sharp potential which is the model used in the theoretical framework exposed by Wen. The exponent found for the tunneling is however a bit smaller than the one predicted.

Later measurements were done on a Quantum Point Contact where tunneling between edge channels happen through scattering at an impurity. Experiements showed hints of a Luttinger liquid-like behavior of the tunneling conductance regarding the temperature [75] and the bias voltage [103]. However, the agreement with the theory seems only quantitative as the exponents are not equal to those predicted [34, 86]. Indeed, for tunneling between two FQH liquid at the same filling factor an exponent $\gamma = 2/\nu$-2 is predicted [54]. So for $\nu = 1/3$ one expects the zero bias tunneling conductance to evolve as T^4, while an evolution in T^2 was observed. One of the explanation given for this is that to reach the T^4 power law, one have to consider very low conductance, typically of the order of 0.1^4, requiring low temperature or low bias voltage while at higher excitation, higher order tunneling terms introduce terms with higher exponents.

2.3.5 Edge reconstruction

The picture in terms of single channel carrying fractional excitations in FQH states in the Laughlin sequence is well established. However for more complex filling factor or so called hole-conjugate states this simple picture do not apply. If an incompressible FQH state is written ν, its particle-hole conjugate state is also an incompressible FQH state at filling factor 1 - ν [32].

The first time the idea of counter propagating channels for fractional filling factors appeared when considering the state 2/3, which is the particle-hole conjugate of the 1/3 FQH state. MacDonald [72] predicted counter propagating modes of charge e/3. Indeed, according to its picture, the edge channel of quasi-particle of charge e^* of the 1/3 FQH state is changed in an edge channel of quasi-holes of charge $-e^*$ and an edge channel of charge e appears. The edge states consists then of two counter-propagating channels one carrying a fractional charge, the other an integer charge. However when studying the propagation of edge magneto-plasmons in the 2/3 FQH state, the results were that there are not hints of counter-propagating charged mode [1]. Moreover, if there were charged mode that counter propagate, then when an incoming excitation is scattered at an impurity it can be transferred to the counter-propagating channel and a quantized Hall resistance would not be expected.

Taking into account inter-edge scattering and the need for a universal Hall conductance, neutral modes were first predicted for the FQH state $\nu = 2/3$ [58] and generalized for fractional filling factor such that $\nu = \mathrm{n}/(\mathrm{np}+1)$ [57]. The transport is then supposed to happen through charged edge channels, accompanied by n - 1 neutral mode. The direction of propagation of those neutral modes is expected to be given by the sign of p : for p positive the neutral mode co-propagate and are counter-propagating for p negative [58].

Chapter 3

Noise in mesoscopic conductors

This chapter addresses the transport of electrons through phase-coherent ballistic conductors in the Quantum Hall effect. The device studied is composed of two reservoirs separated by a tunable potential barrier. The transport is described using mainly two quantities : the current and the noise, the noise corresponding to the fluctuations of the current. This quantity is especially interesting in the framework of the FQHE as it is sensitive to the charge of the carriers and has historically provided the most reliable fractional charge measurement [91, 20] compared to previous ones [37].

This chapter also addresses the current noise and the microwave photo-excitation of the anyonic quasiparticles of the FQHE. Combining these two aspects offers the possibility to find a way to manipulate and to probe these fractional excitations. An interesting aspect of microwave manipulation is the generation of levitons, minimal excitation corresponding to a defined charge with no more extra excitations.

The physics of photo-assisted process was first considered for a normal mesoscopic conductor. Then a similar physics with similar manifestation was found in interacting systems like superconducting-normal junctions, probing the charge of a Cooper pair, and finally for the FQHE regime. However as opposed to the other systems, no experimental study of photo-assisted processes in the FQHE have been reported yet.

In the following, is first described the noise and its origin as well as the formalism used to calculate the noise in non-interacting systems. Then the interactions with photons is probed by applying a periodic time-dependent voltage and studying their effect on the noise. Finally all this study is also done when considering the interactions between electrons leading to the expression of noises in the framework of the fractional quantum Hall effect which could later be compared to the experimental data.

3.1 Noise of a quantum conductor with no interactions

3.1.1 The scattering theory

We consider a unidimensional quantum conductor connected to reservoirs [1], here a 3D metal, wide enough to realize a good thermal bath for electrons. In the reservoir R_α the temperature T_α and chemical potential μ_α can be defined. The electrons are injected in the conductor by the reservoir through the lead α with the distribution function corresponding to a Fermi statistics.

$$f_\alpha(\epsilon) = \frac{1}{exp\left(\frac{\epsilon-\mu_\alpha}{k_B T_\alpha}\right)+1} \tag{3.1}$$

At equilibrium, temperature T_α and no bias applied between the leads, the distribution function is evaluated at the Fermi energy : $\mu_\alpha = E_F$. For out-of-equilibrium state, the increase of the chemical potential is taken into account such that $\mu_\alpha = E_F + eV_\alpha$, with eV_{ds} the difference between chemical potential of the leads.

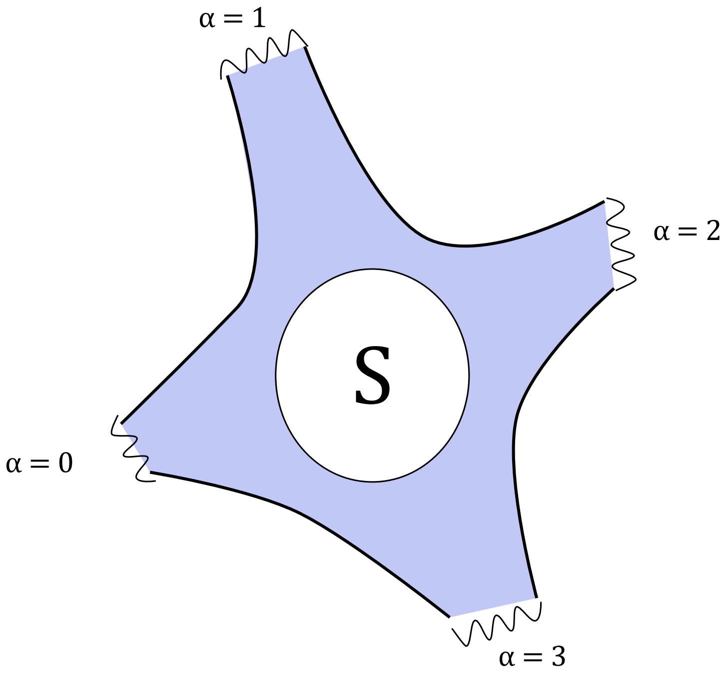

FIGURE 3.1 – **Multiterminal conductor.** The blue part is the 1D quantum conductor connected through leads to reservoir labeled $\alpha = 1 \to 3$. An impurity acting as a scatterer S is placed in the conductor to probe scattering properties.

The so called *scattering theory* aims at investigating transport properties by linking those to the known scattering properties determined by quantum mechanics. A scatterer is placed in the conductor so that an incoming particle has a probability D to be transmitted and R to be reflected at the potential barrier.

The transport through the conductor is described using the current fluctuations, or their power spectral density (also called noise). There are several sources of noise, part of those are not relevant for the physics of transport, for example the 1/f noise or noise

---

[1] called contacts when we will consider the real sample

coming from the measurement set-up. How the effect of those parasitic noises is reduced is exposed in chapter 5, while the following focuses on thermal and mostly shot noise.

3.1.2 Sources of noise

Thermal noise Also called Johnson-Nyquist noise, this noise is present as long as the temperature is not zero. It originates from the fluctuation around the energy μ_α of the occupation number of electrons in the lead α. Those current fluctuations are proportional to the temperature and are present even at equilibrium. It is responsible for a non-zero equilibrium current flowing through the conductor. The thermal noise is a white noise, meaning that it does not depend on the frequency, up to k_BT/h. The current fluctuations measured over the bandwidth $1/\delta f$ are written following a Johnson-Nyquist formula [50, 77].

$$\left\langle \delta i^2 \right\rangle = 4k_BTG\delta f \tag{3.2}$$

The quantity that is of interest is the power spectral density of current fluctuations or the current noise :

$$S_I = \frac{\langle \delta i^2 \rangle}{\delta f} = 4k_BTG \tag{3.3}$$

Shot noise As opposed to thermal noise, this noise is only observed when a conductor is out of equilibrium. It arises from the particle nature of electrons. It was first described by Schottky [94] for a classical case where particle of charge q are randomly injected in a vacuum tube by an electrode, generating fluctuations ΔI around the average value $\langle I \rangle$. The statistic of emission is Poissonian and the noise S_I is the mean number of electron injected $q \langle I \rangle$ during a time $\tau = 2/\Delta f$:

$$S_I = \frac{\langle \Delta I^2 \rangle}{\Delta f} = 2q \langle I \rangle \tag{3.4}$$

The solid-state equivalent of a vacuum tube is a tunnel junction which shows similar Poissonian noise. Let us now consider a quantum ballistic conductor with a scatterer connecting two reservoirs. When a voltage bias V_{ds} is applied on one reservoir of the conductor while the other is grounded, it generates a difference in chemical potentials $\Delta\mu = \mathrm{e}V_{ds}$. Due to Fermi statistics, a continuous and noiseless set of electrons separated by h/eV_{ds} is sent into the conductor (see figure 3.2), generating a current :

$$I_0 = e\frac{e}{h}V_{ds} \tag{3.5}$$

Those incoming electrons are scattered at the potential barrier and generate a transmitted current $\mathrm{I}_T = \mathrm{DI}_0$. As the incoming flow of electrons is noiseless, the only current noise arise from the quantum partitioning of electrons at the scatterer. This current noise is found to be a fraction F, called Fano factor, of the Schottky Poissonian noise :

$$S_I = 2e \langle I \rangle F \tag{3.6}$$

The noise is even reduced down to zero when there is no partitioning happening(D = 0 or 1), which is a straightforward consequence of the noiseless flow of electrons. The noise can also be reduced below the Poisson value because of interactions between electrons. This property is used for the measurement of the fractional charge as seen in the section 3.3 below.

In the case of a Quantum Point Contact with n incoming channels and D_n the probability for an incoming excitation in the n^{th} channel to be transmitted at the scatterer, the Fano factor is :

$$F = \frac{\sum_n D_n (1 - D_n)}{\sum_n D_n} \tag{3.7}$$

This relation was experimentally verified in Quantum Point Contacts through noise measurements [85, 62], where the Fano factor has been measured to be maximum at half transmission and zero when no partitioning happens.

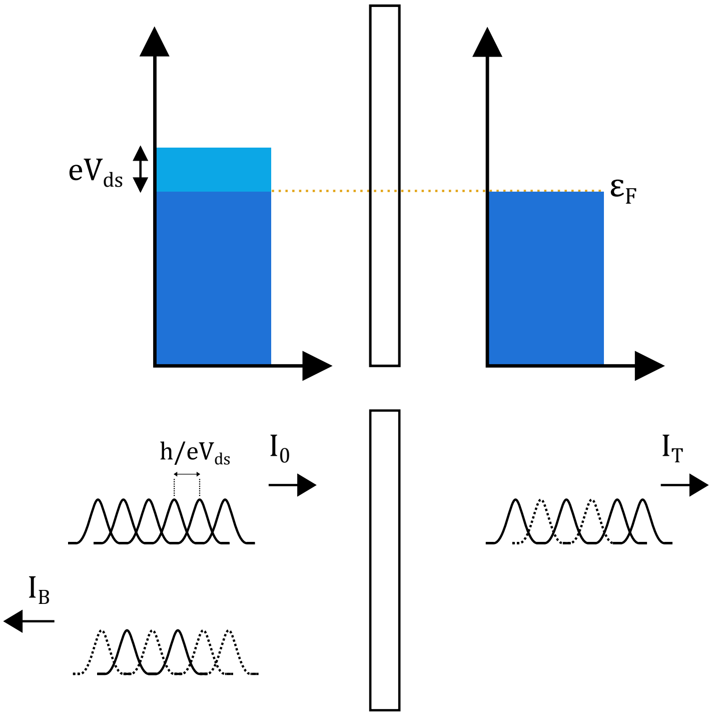

FIGURE 3.2 – **Injection of electrons in a conductor.** The reservoir of a quantum ballistic conductor is biased with a DC voltage injecting a current I_0 in the conductor. In the conductor an impurity scatter the incoming electrons generating I_B and I_T, respectively the backscattered and transmitted currents.

3.1.3 Average current and current fluctuations

The scattering theory for electron transport in quantum conductor is a powerful tool developed by Landauer, Buttiker and Martin [9, 10, 74, 6]. It allows to evaluate the averaged current through the conductor as well as the current fluctuations when considering elastic scattering. The details of calculation for the sample geometry used for the experiments presented in this manuscript are reported in Appendix A. Here are exposed the main results while considering the elastic scattering in a quantum conductor with several leads in which several electronic modes are flowing.

There are N_L leads connecting metallic reservoirs to the scatterer. In the lead α there are N_α electronic modes. In our case, as the conductor is in the QHE, the number of incoming mode is equal to the number of edge channels. The aim is to express the current fluctuations in the lead α

$$\Delta\hat{I}_\alpha(t) = \hat{I}_\alpha(t) - \left\langle \hat{I}_\alpha \right\rangle \tag{3.8}$$

and the symmetrized correlation function :

$$S_{\alpha\beta}(t-t') = \frac{1}{2}\left\langle \Delta\hat{I}_\alpha(t)\,\Delta\hat{I}_\beta(t') + \Delta\hat{I}_\beta(t')\,\Delta\hat{I}_\alpha(t) \right\rangle \tag{3.9}$$

For $\alpha \neq \beta$, the quantity is called *cross-correlation*, the *auto-correlation* are evaluated for $\alpha = \beta$. The quantity of interest is the power spectral density (PSD) of current fluctuations given by the Fourier transform of equation 3.9.

This quantity is expressed using creation and annihilation operators. The operator $\hat{a}^\dagger_{\alpha m}$ describes the creation of an incoming excitation in the lead α in the channel m while an outgoing excitation in the channel m of the lead α is created by the operator $\hat{b}^\dagger_{\alpha m}$. Those operators are related via the scattering matrix such as :

$$\hat{b}_{\alpha m} = \sum_{\beta n} s^{mn}_{\alpha\beta}\hat{a}_{\beta n} \tag{3.10}$$

The component $s^{mn}_{\alpha\beta}$ is the amplitude of probability for an excitation coming from the channel m of the lead α to be transmitted (or backscattered) in the channel n of the lead β. In the QHE, the scattering due to local impurity happens mostly among the same channel. Then the matrix element corresponding to the probability for an incoming excitation in channel m to be scattered in a different channel $n \neq m$ is equal to zero.

The Fourier transform of the current in the lead α is expressed using the operator $\hat{a}$:

$$\hat{I}_\alpha(\omega) = \frac{e}{h}\int dE \sum_{\beta\gamma} \hat{a}_\beta(E)\, A_{\beta\gamma}(\alpha, E, E+\hbar\omega)\, \hat{a}_\gamma(E+\hbar\omega) \tag{3.11}$$

With the matrix elements :

$$A_{\beta\gamma}(\alpha, E, E+\hbar\omega) = \mathbb{1}_\alpha \delta_{\alpha\beta}\delta_{\alpha\gamma} - s^\dagger_{\alpha\beta}(E)\, s_{\alpha\gamma}(E+\hbar\omega) \tag{3.12}$$

The Fourier transform of equation 3.9 gives the PSD of current fluctuations :

$$2\pi\delta(\omega+\omega')\, S_{\alpha\beta}(\omega) = \frac{1}{2}\left\langle \Delta\hat{I}_\alpha(\omega)\,\Delta\hat{I}_\beta(\omega') + \Delta\hat{I}_\beta(\omega')\,\Delta\hat{I}_\alpha(\omega) \right\rangle \tag{3.13}$$

We are interested in the zero-frequency shot noise $\omega = 0$ or when $\hbar\omega \ll k_B T$. In that case, the noise is white, hence does not depend on the frequency at which the noise is measured. After some calculations, a compact form of the PSD of current fluctuations is obtained :

$$S_{\alpha\beta} = \frac{e^2}{h}\sum_{\gamma\delta}\sum_{mn}\int dE\, A^{mn}_{\gamma\delta}(\alpha; E, E)\, A^{nm}_{\delta\gamma}(\beta; E, E)\left\{ f_\gamma(1-f_\delta) + f_\delta(1-f_\gamma) \right\} \tag{3.14}$$

Let us consider the geometry used for our sample where there are 6-contacts like schematically represented in figure 3.3. The current is injected through the contact denoted (0) and measured through the contacts (1) and (4) while the other contacts are grounded. All the work is performed in the framework of the QHE at filling factor ν, hence the number of electronic modes in the lead (0) is the number of edge channels ν. All contacts are supposed to be at the same temperature T.

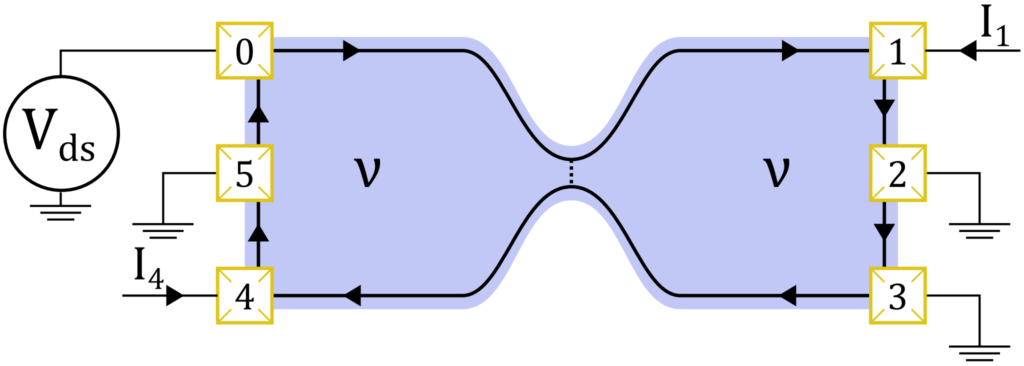

FIGURE 3.3 – **Schematic view of the sample.** The blue region represents the conductor in the IQHE at filling factor ν with the excitations propagating along edge channels (black lines). The edge channels are brought together by an external potential so that the tunneling probability from one edge to the other is not zero. The reservoirs are represented in yellow and denoted 0 → 6, with the reservoir (0) driven with a DC voltage while the transmitted and backscattered currents and their fluctuations are measured at contacts (1) and (4).

When a DC-voltage bias is applied on contact (0) and the potential barrier is tuned so that the transmission probability is D = 1-R, the cross-correlation power spectral density reads (see Appendix A for further calculation details) :

$$S_{I,14}\left(V_{ds}, D, T\right) = 4k_BT\frac{e^2}{h}RD\left(1 - \frac{eV_{ds}}{2k_BT}coth\left(\frac{eV_{ds}}{2k_BT}\right)\right) \tag{3.15}$$

The cross-correlation only measures fluctuations from the partitioned channel. Through this formula, the property of quantum shot noise being equal to zero when no partitioning happens (R = 0 or D = 0) is recovered. Moreover when no bias voltage is applied on contact (0), the cross-correlation is equal to zero.

When the temperature is zero, the cross-correlated shot noise is negative, meaning that it displays perfect anti-correlation :

$$S_{I,14}\left(V_{ds}, D, 0\right) = -2eV_{ds}\frac{e^2}{h}RD \tag{3.16}$$

Then the shot noise is still zero at zero bias voltage and evolves linearly with the bias voltage.

On figure 3.4 is plotted the expected absolute value of the cross-correlated shot noise evolution as a function of the bias voltage V_{ds} for a transmission D = 0.5 at zero temperature, T = 30 mK and 100 mK. The slope is exactly the same for all temperatures and

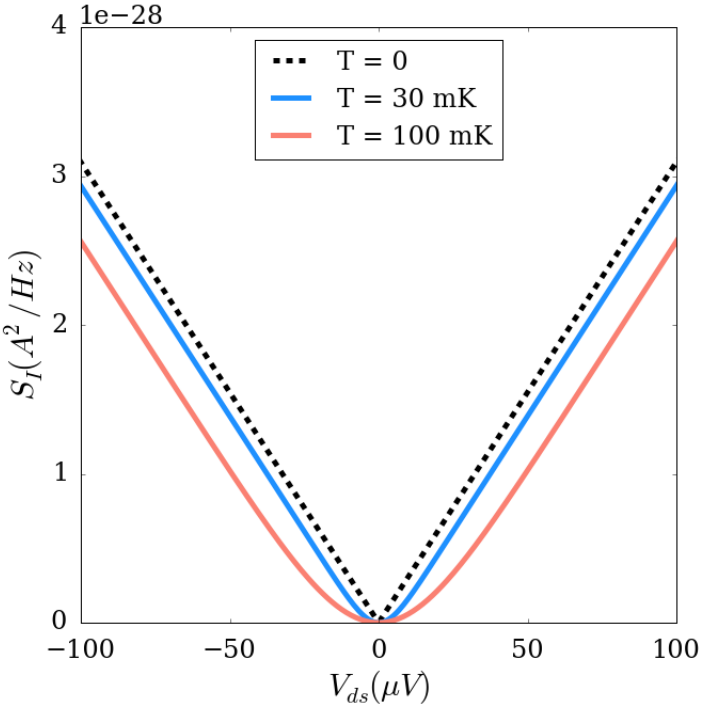

FIGURE 3.4 – **DC Shot noise in the IQHE.** The full lines are the opposite of the cross-correlated DCSN as calculated in equation 3.15 with D = 0.5 at T = 30 mK (blue) and T = 100 mK (red). The black dotted line curve is the opposite of the DCSN at T = 0.

the difference lies in bias voltages around zero due to the effect of the *coth* function whose argument depends on the temperature.

The auto-correlation functions bear the information about shot noise but also about the thermal noise generated in the contacts. Indeed, when no bias is applied, the Johnson-Nyquist noise is recovered in the auto-correlation and vanishes for the cross-correlation. It also depends on which channel is partitioned as one channel fully transmitted contribute with the Johnson-Nyquist noise to the total noise measured at the contact (1) using auto-correlation. For example let us write the noise at a filling factor ν with only the inner channel partitioned and all the other $\nu - 1$ channels fully transmitted :

$$S_{I,11}\left(V_{ds}, D, T, \nu\right) = 4k_BT\frac{e^2}{h}\left(\nu - 1 + R^2 + D^2 + RD\frac{eV_{ds}}{2k_BT}coth\left(\frac{eV_{ds}}{2k_BT}\right)\right) \tag{3.17}$$

The evolution as a function of the bias voltage V_{ds} is then the same as for the cross-correlated function. Nevertheless, there are some differences between the cross-correlated noise and the auto-correlated one. First of all, when no partitioning happens, the noise is not equal to zero.

$$S_{I,11}\left(V_{ds}, 0, T, \nu\right) = \nu \times 4k_BT\frac{e^2}{h} \tag{3.18}$$

A Johnson-Nyquist noise is recovered as the sample conductance is $\nu e^2/h$, meaning that all channels support a thermal noise of $4k_BTe^2/h$ and the total thermal noise is the sum over all channels in the conductor. When no bias voltage is applied on the conductor, the

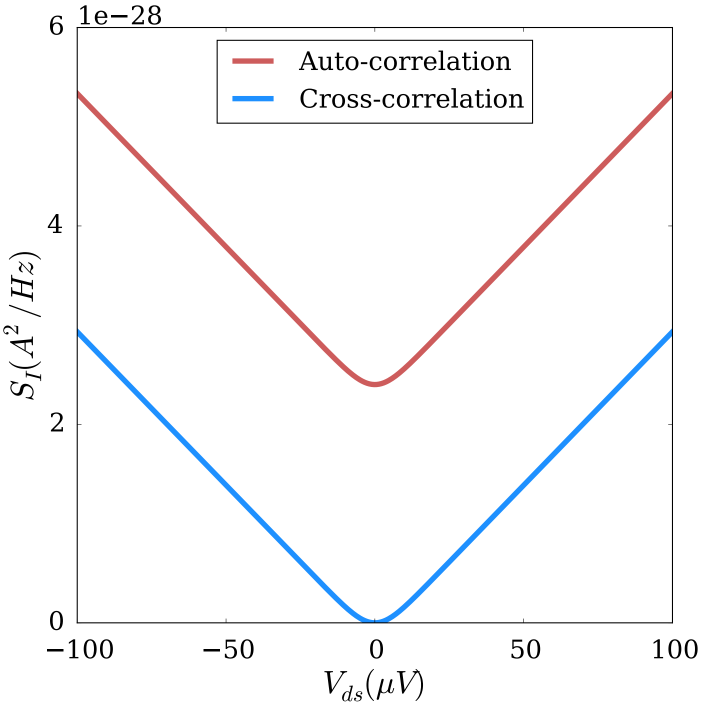

FIGURE 3.5 – **Comparison of DCSN using cross-correlation and auto-correlation.** The blue curve is the opposite of the cross-correlated DCSN as calculated in equation 3.15 at T = 30 mK and D = 0.5. The red curve is the auto-correlation at $\nu = 2$ with the inner channel partitioned with D = 0.5(equation 3.17) at 30 mK

auto-correlated shot noise is not zero but still contains the thermal noises of transmitted and partitioned channels.

Another difference is the sign before the part describing the evolution of the shot noise as a function of V_{ds}. Indeed, the auto-correlation is by definition a function describing correlated events whereas the cross-correlation describes anti-correlated events because of the fermionic statistics of electrons. On figure 3.5 are plotted the DCSN using cross-correlation and auto-correlation at 30 mK where the differences at $V_{ds} = 0$ can clearly be seen.

3.2 Effect of a time-dependent voltage

Up to now, the transport of electrons when the conductor is biased with a DC voltage has been considered. Applying a time-dependent voltage with a period T = 1/f, allows to probe how the carriers interact with external photons. For this section, the interactions between electrons is still neglected. The applied voltage is $V(t) = V_{ds} + V_{ac}(t)$ with $\langle V_{ac}(t)\rangle_T = 0$ and the current injected in the conductor is $I(t) = \nu\frac{e^2}{h}V(t)$ with ν the IQHE filling factor.

3.2.1 Floquet formalism

The Floquet scattering theory is used to solve problems where a system is driven with a periodic potential of arbitrary strength. It has been developed in the framework of mesoscopic conductors in [76] where the scatterer is periodically driven at frequency *f*. A Floquet scattering matrix is defined where the elements describe an incoming electron is the lead α at an energy E that is scattered in the lead β at an energy E + *lhf*. *l* is a natural integer describing the absorption of l photons (l>0) or the emission of l photons (l<0). In the experiments presented later, it is not the scatterer that is periodically driven but the reservoir, however a Floquet formalism can still be used.

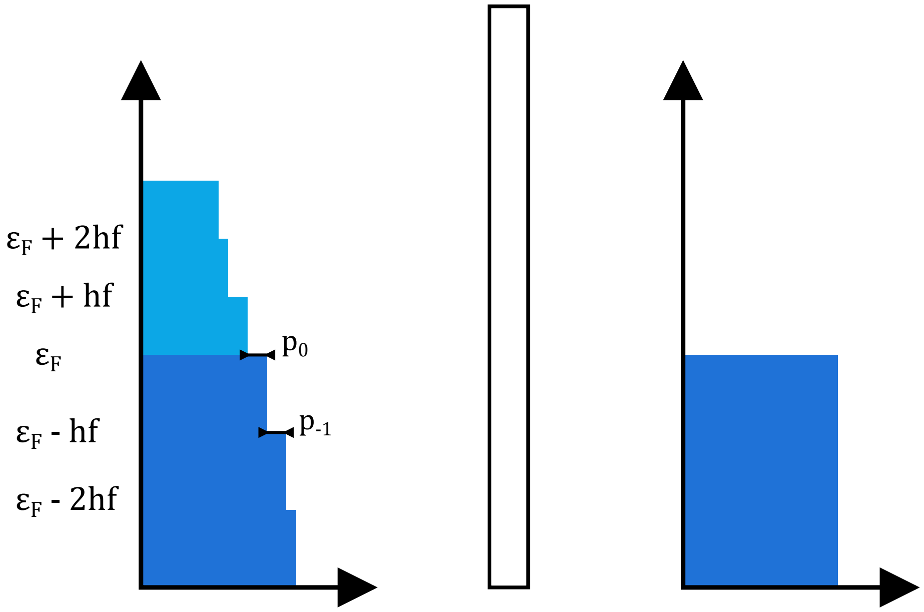

FIGURE 3.6 – **Distribution function of an irradiated reservoir.** A periodic time-dependent voltage at frequency f is applied on the left reservoir resulting in the injection of electron-hole pairs by absorption or emission of a photon at frequency *f*. The energy distribution function then takes a step-like structure of height hf and depth p_l corresponding to the probability to absorb or emit a photon.

A time-dependent voltage at frequency f is applied on the contact (0) of the conductor. The electrons of the excited contact gain an additional amplitude given by $e^{-i\phi(t)}$ with :

$$\phi\left(t\right)=\frac{e}{h}\int_{-\infty}^{t}V_{ac}\left(t'\right)dt' \tag{3.19}$$

As $\phi\left(t\right)$ is a periodic function of period T = $1/f$ it can be developed in a Fourier series :

$$e^{-i\phi(t)}=\sum_{l}p_l\left(\delta\epsilon\right)e^{-2i\pi\delta\epsilon t/h} \tag{3.20}$$

Meaning that the electrons at energy ϵ of the excited contact are scattered into states with energy ϵ + $\delta\epsilon$. The amplitude of probability corresponding to this shift in energy is given by $p_l\left(\delta\epsilon\right)$ and is called the *Floquet scattering amplitude.*

This discrete sum of phase term is interpreted as the emission (l<0) or the absorption (l>0) of a photon with a probability given by $P_l = |p_l|^2$. Then the energy shift experienced by the electron is equal to the energy quanta *lhf* [80].

The sum of all probabilities to absorb or emit l photons or not ($l = 0$) is equal to 1. Moreover the unitarity of the scattering matrix implies that :

$$\sum_{l=-\infty}^{+\infty} p_l^* p_{l'} = \delta_{ll'} \tag{3.21}$$

3.2.2 Photo-assisted shot noise

The current noise in quantum conductor irradiated with photons at frequency f has been derived in [68, 80, 25] using the scattering theory and the Floquet formalism previously described. Consequently, the definition of the noise remains the same as for a DC-driven conductor, thus obtained by calculating the average current and PSD of the correlation functions.

Taking into account the fact that an incoming state is in a superposition of several states whose occupation probability can be calculated by new annihilation/creation operators $\hat{a}$. Those new operators are expressed as the sum over the original annihilation and creation operators, now denoted $\hat{a}'$ which act on the unperturbed state of the reservoir at equilibrium.

$$\hat{a}_\alpha = \sum_l p_l \hat{a}'_\alpha \left(E - lhf\right) \tag{3.22}$$

The current in the lead α is written, using the newly defined operators $\hat{a}_\alpha$, as the difference between the number of excitations leaving and entering the contact :

$$I_\alpha\left(t\right) = \frac{e}{h} \int dE\, dE' \, \left(\hat{a}^\dagger_\alpha \left(E\right) \hat{a}_\alpha \left(E'\right) - \hat{b}^\dagger_\alpha \left(E\right) \hat{b}_\alpha \left(E'\right)\right) e^{i(E-E')t/\hbar} \tag{3.23}$$

Then, following the definitions given in section 3.1.3, the PSD of current correlations is calculated and the general form is written :

$$S_I^{ac}\left(V_{ds}, V_{ac}, f, D, T\right) = \sum_l P_l \left(\frac{eV_{ac}}{hf}\right) S_I^{dc}\left(eV_{ds} - lhf, D, T\right) \tag{3.24}$$

With S_I^{dc} the shot noise measured for $V_{ac} = 0$. The resulting noise can be viewed as the sum of measurements with bias voltage shifted by the value *lhf* weighted by the probability $|p_l|^2$ to have experienced this energy shift. Thus measuring the PASN gives a direct access to the energy distribution function of the excited reservoir.

In the case of a monochromatic sine wave applied on the conductor, p_l is the lth Bessel function [80]. For the experiments later presented a sine wave have been used, hence simulations will only be presented with $V\left(t\right) = V_{ds} + V_{ac}\, cos\left(2\pi f t\right)$.

Figure 3.7 shows the evolution of both DC and photo-assisted shot noise as a function of the bias voltage. A remarkable effect of the time-dependent voltage is that the noise is not any more zero at $V_{ds} = 0$. Moreover, the singularity at zero bias for the DCSN is

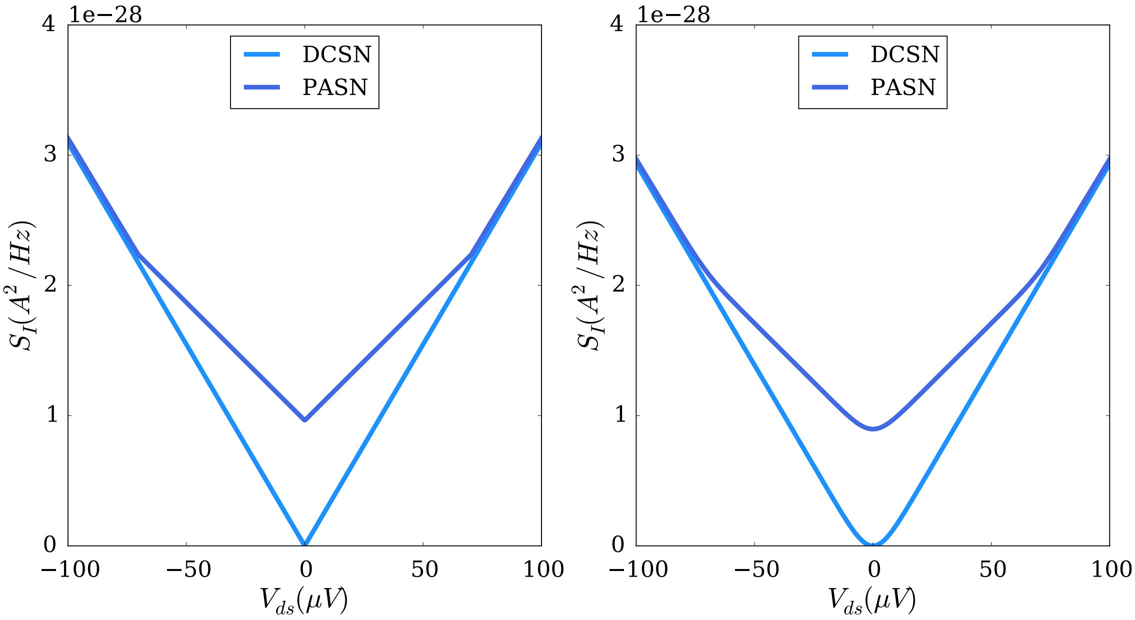

FIGURE 3.7 – **PASN in the IQHE.** The light blue line is the cross-correlated DCSN at D = 0.5. The dark blue line is the PASN at the same transmission for an AC-voltage at 17 GHz with an amplitude $V_{ac} = 70\ \mu V$. Left figure shows simulations with T = 0 while the right figure is done for a temperature of 30 mK.

recovered in the PASN at voltages such that $V_{ds} = hf/e$. The effect of the temperature is to round those singularities.

In order to highlight photo-assisted processes, it is convenient to write the excess noise which corresponds to the PASN from which the DC shot noise is removed.

$$\Delta S_I^{ac}\left(V_{ds}, V_{ac}, f\right) = S_I^{ac}\left(V_{ds}, V_{ac}, f\right) - S_I^{dc}\left(V_{ds}\right) \tag{3.25}$$

Defining the dimension-less quantities $\alpha = eV_{ac}/hf$ and $q = eV_{dc}/hf$, in the limit of zero temperature, the excess noise is written[2] :

$$\Delta S_I^{ac}\left(q, \alpha\right) = 2hf\frac{e^2}{h}RD\sum_l P_l\left(\alpha\right)\left(|q-l| - |q|\right) \tag{3.26}$$

The evolution as a function of the bias voltage V$_{ds}$ of the excess noise for the case of a sine pulse at frequency 17 GHz for both zero temperature and 30 mK is represented on figure 3.8.

Photo-assisted effects can also be seen when considering the evolution of the noise as a function of the RF amplitude at fixed bias voltage (generally $V_{ds} = 0$). The curve exhibits oscillations whose origin are the Bessel functions, the signature of photo-assisted processes (see figure 3.9).

---

[2] using $\sum_l P_l = 1$

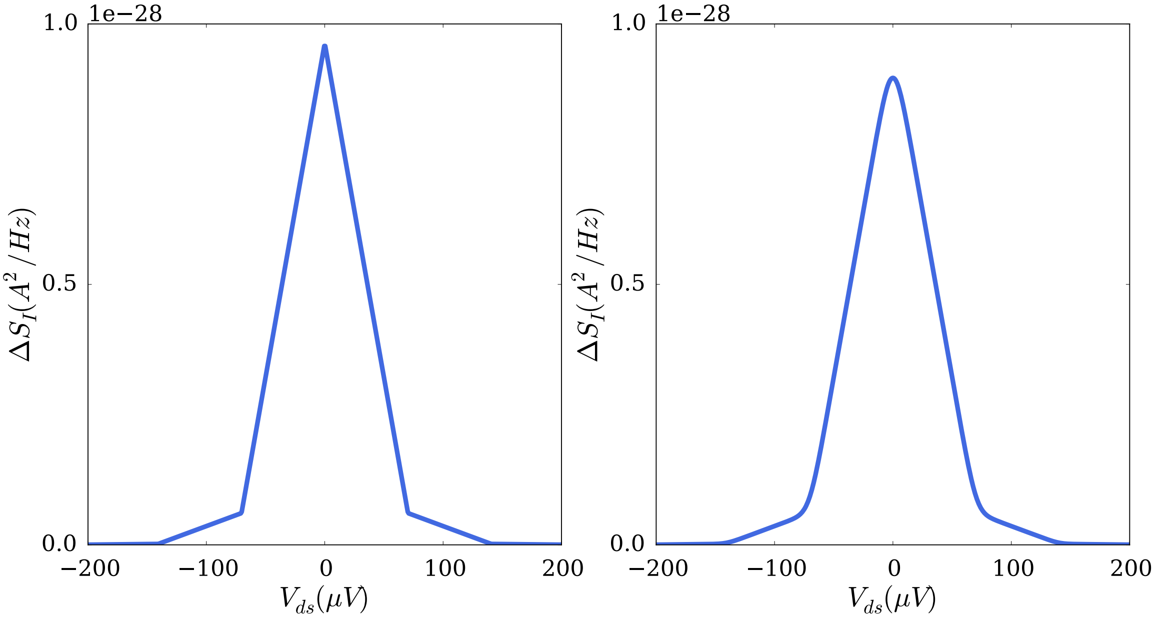

FIGURE 3.8 – **Excess PASN in the IQHE.** On the left figure the dotted curve is the excess PASN at D $= 0.5$, $f = 17$ GHz and zero temperature. The right figure corresponds to the case where T $= 30$ mK.

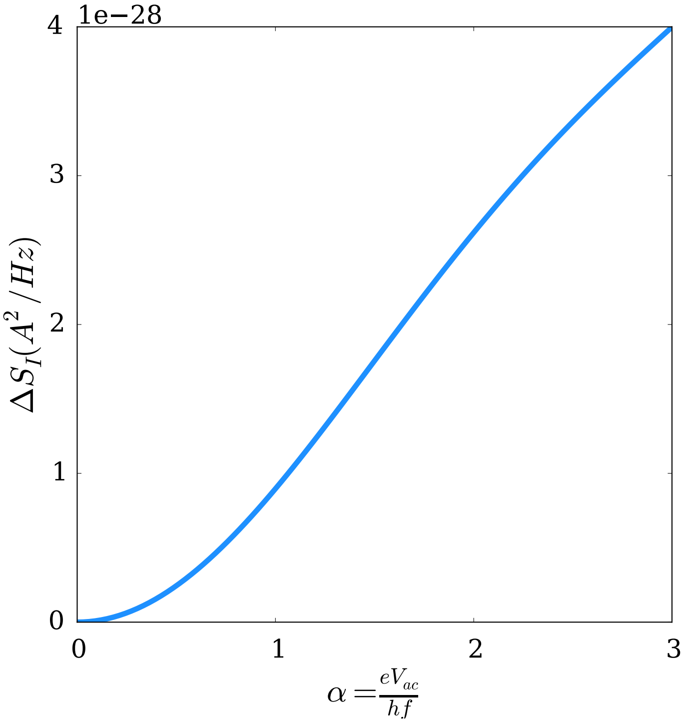

FIGURE 3.9 – **Evolution of the PASN as a function of the RF amplitude.** The noise is plotted as a function of the reduced variable $\alpha = eV_{ac}/hf$. The bias voltage is fixed at $V_{ds} = 0$, the transmission is D $= 0.5$. The RF amplitudes varies from 0 to 210 μV at 17 GHz.

3.2.3 Experimental observations of PASN

Even though theoretical work on photo-assisted shot noise started 30 years ago, experimental observation of PASN took longer as it requires to combine sub-Kelvin temperature with RF-voltages.

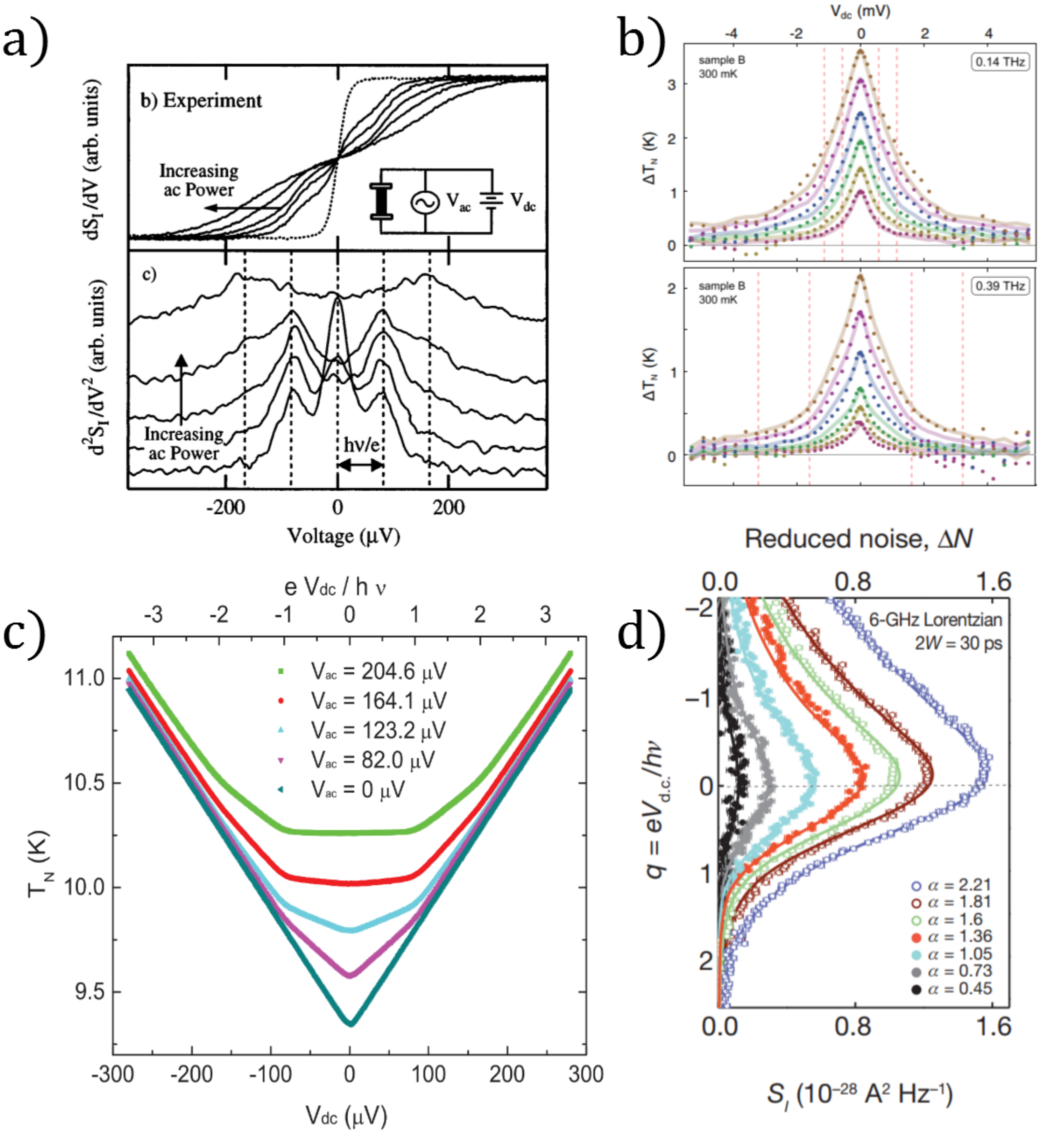

FIGURE 3.10 – **Experimental observations of PASN.** *a)* First and second derivative of the SN in a normal diffusive conductor from [93]. *b)*Excess noise in graphene from [79]. *c)* [31]. *d)* Excess noise of the QPC when irradiated with a Lorentzian pulse from [26].

The first experimental observation of Photo-assisted Shot Noise was realized in a normal diffusive conductor [93]. Well marked peaks were observed in the second derivative of the shot noise at bias voltages such as $V_{ds} = hf/e$ when the conductor is irradiated with photons at frequency f, in that case of a few tens of GHz well above k_BT/h.

Similar experiments have been performed in a diffusive normal metal-superconducting junction [61] where the second derivative of the noise exhibits peaks at the Josephson frequency of the Cooper pair [69], probing the charge of 2e. Observation of PASN in a graphene nanoribbon, which is a diffusive conductor, when irradiated with photons at THz frequency was reported in [79].

Later photo-assisted shot noise has been measured on ballistic conductor such as a Quantum Point Contact [83] where the conductance can be varied. Moreover the shot noise, directly measured, exhibited the expected singularities at $V_{ds} = hf/e$ when the conductor is irradiated with photons at frequency f.

The tunnel junction between normal metals once irradiated with RF voltages at GHz have also been shown to exhibit the hallmark of photo-assisted processes [31], both is the evolution of the noise as a function of the DC bias voltage and the RF amplitude.

Photo-assisted processes can also be used to generate on-demand single excitation [26]. This is done by applying a Lorentzian pulse shape on the conductor, here a QPC. Indeed, because of the asymmetry of the Lorentzian, no holes are injected in the conductor while only electrons are injected. Photo-assisted processes have also been validated in the non interacting IQHE [92].

3.3 Tunneling between edge states in the FQHE

All of the formalism developed above does not take into account interactions between electrons. It is well suited for QPC in the IQHE or without any magnetic field applied, however it cannot be used for the FQHE, although most features of PASN remain as described in a section below.

Derived from the Luttinger liquid theory, the Shot Noise of a conductor in the FQHE can be estimated in two separated limits called weak-backscattering and strong-backscattering. Here we only consider tunneling between edge states at the same filling factor ν in the Laughlin sequence.

3.3.1 Shot noise in chiral Luttinger liquids

What is the effect of interactions on the zero frequency shot noise ? The formalism developed by Buttiker to estimate the current and voltage fluctuations can no longer be applied. Instead, the out of equilibrium transport properties can be developed considering the fact that the edge channels of the FQHE realize, as previously described, a unidimensional chiral Luttinger liquid. From that the current and voltage fluctuations can be estimated for a FQH state at filling factor $\nu = 1/\mathrm{m}$. In [55] the current noise were estimated for two reservoirs at thermal equilibrium, driven out of equilibrium by a DC bias voltage V_{ds} inducing a difference of chemical potential eV_{ds}. The reservoir are separated by a tunable potential barrier. However, the expression for the noise is only found for restricted limits of quasi-particle tunneling presented in the following.

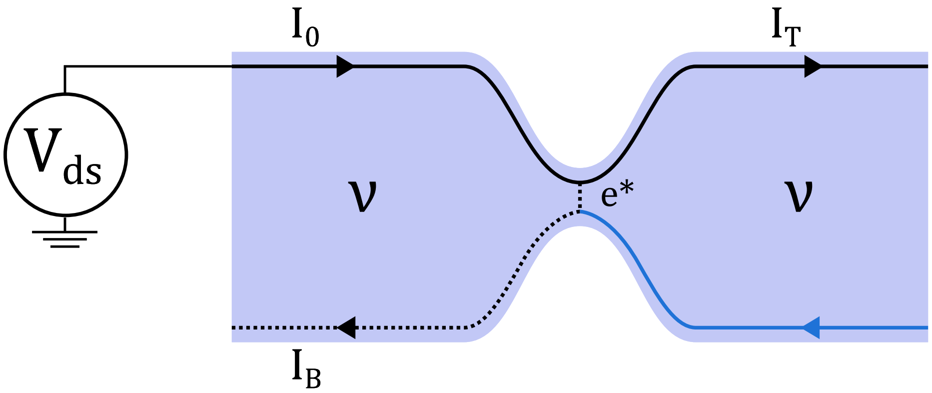

FIGURE 3.11 – **The Luttinger liquid in weak-backscattering regime.** A weak coupling between opposite edge state is considered. The black lines are trajectories followed by quasi-particles injected in the conductor while the blue line is the equilibrium current flowing in the conductor.

3.3.2 Weak-backscattering regime

The so called *weak backscattering regime* (WBS) is defined when the backscattered current is small compared to the transmitted current I$_B \ll$ I$_T$. It means that almost all particles are transmitted at the potential barrier and the transfer of a quasi-particle from one edge to the other are rare and uncorrelated events. In that case, the fractional fluid is only lightly disturbed by the impurity potential and fractional charges are expected to be transferred from one edge to the other counter-propagating mode. It has been showed that the current fluctuations are proportional to the elementary charge of the current carriers, as the transfer of quasi-particles obey a Poissonian law. With e^* the fractional charge and I_B the backscattered current. The PSD of current fluctuation at zero temperature reads [55, 28] :

$$S_I = 2e^*|I_B| \tag{3.27}$$

At finite temperature, the cross-correlated shot noise takes a form similar to equation 3.15, introducing the fractional charge e* [3] :

$$S_I^{dc}\left(V_{ds}, D, T\right) = 2e^* I_B\left(V_{ds}, D\right)\left(coth\left(\frac{e^*V_{ds}}{2k_BT}\right) - \frac{2k_BT}{e^*V_{ds}}\right) \tag{3.28}$$

This equation is comparable to the non-interacting case where the charge of the electron has been replaced by the fractional charge. A very convenient aspect of this result is the presence of a zero temperature singularity at zero bias voltage.

3.3.3 Strong backscattering regime

On the other hand, when the transmitted current is small compared to the backscattered current, I$_T \ll$ I$_B$, there is a strong coupling between edge states. FQH fluid from

---

[3] No absolute value of the current is needed at finite temperature as it is rectified by the sign of V$_{ds}$.

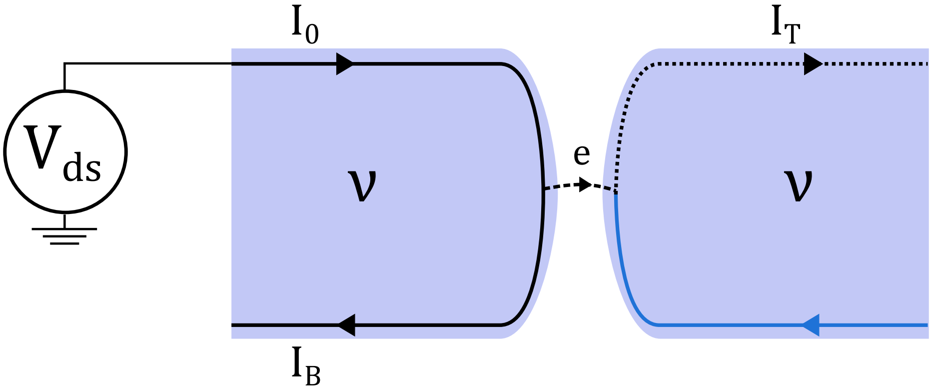

FIGURE 3.12 – **The Luttinger liquid in strong-backscattering regime.** This time a strong coupling between edge states is considered meaning that only electrons are expected to tunnel through the potential barrier.

left and right sides of the impurity are separated from one another because of the high potential induced by the impurity and interactions are lost. In that case, only electron are expected to tunnel through the potential barrier and the Poissonian shot noise is then expected to be proportional to the charge of the electron. The noise is written using the transmitted current I_T :

$$S_I = 2e|I_T| \tag{3.29}$$

This regime is called *strong backscattering* (SBS).

3.3.4 A brief history of the fractional charge

Shot noise has been used to probe the charge of carriers. For example the charge of a Cooper pair was measured using the shot noiseof a diffusive normal - superconducting junction which was found twice as large as the one observed for just a normal diffusive conductor [49].

As for the fractional charge, the attemps to measure it in the FQH regime by the mean of the shot noise have started 20 years ago. Using cross-correlation functions [91] as well as auto-correlation functions [20] in the weak backscattering regime of transfer of charge, the elementary charge of the $\nu = 1/3$ FQH state was measured. As shown in figure 3.13 the current noise is proportional to the backscattered current with a factor e/3.

At $\nu = 2/5$ the charge of the quasiparticle was measured to be e/5 [84] and the charge of quasi particle in the state $\nu = 5/2$ has been measured such that $\mathrm{e}^* = \mathrm{e}/4$ [22].

With the improvement of cryogenic technics, those measurements were later performed at lower temperatures (T $\approx$ 10 mK) and an evolution of the fractional charge as a function of the temperature [15, 4] or the transmission [39] was observed (see figure 3.14)[4]. The charges at filling factor $\nu = 2/3$ and 2/5 were found to be doubled at low temperature when measured using auto-correlation. For the 2/3 FQH state this measurement were interpreted as the observation of counter-propagating neutral modes [5] predicted by the

---

[4] We can note that those measurements were performed using auto-correlation which will have its importance later.

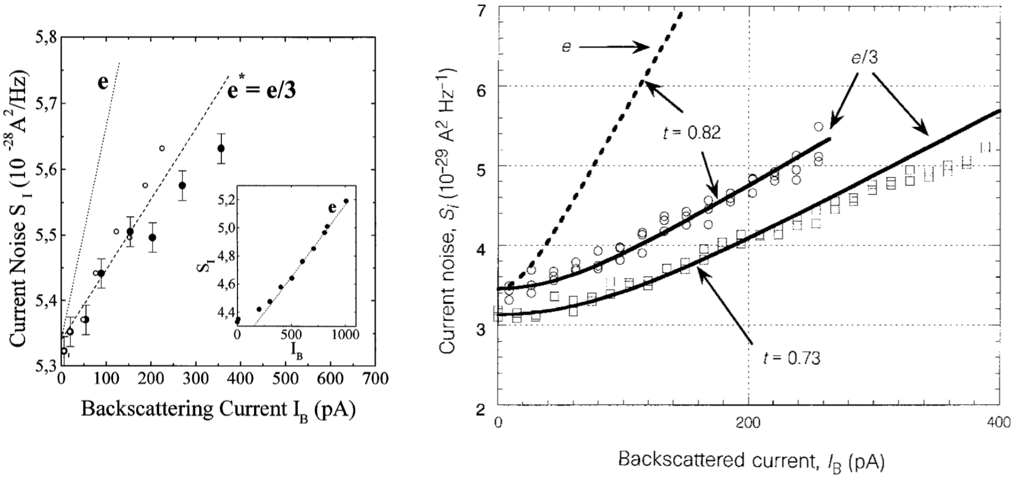

FIGURE 3.13 – **First fractional charge measurements using DCSN.** Both figures represent the evolution of the current shot noise as a function of the backscattered current. Left figure from [91] and right figure from [20].

edge reconstruction of this state. For the $\nu = 2/5$ state neutral modes have also been considered to explain the unexpected doubling of the fractional charge [29, 30] expect here neutral modes are expected to propagate with the same chirality as the charge mode.

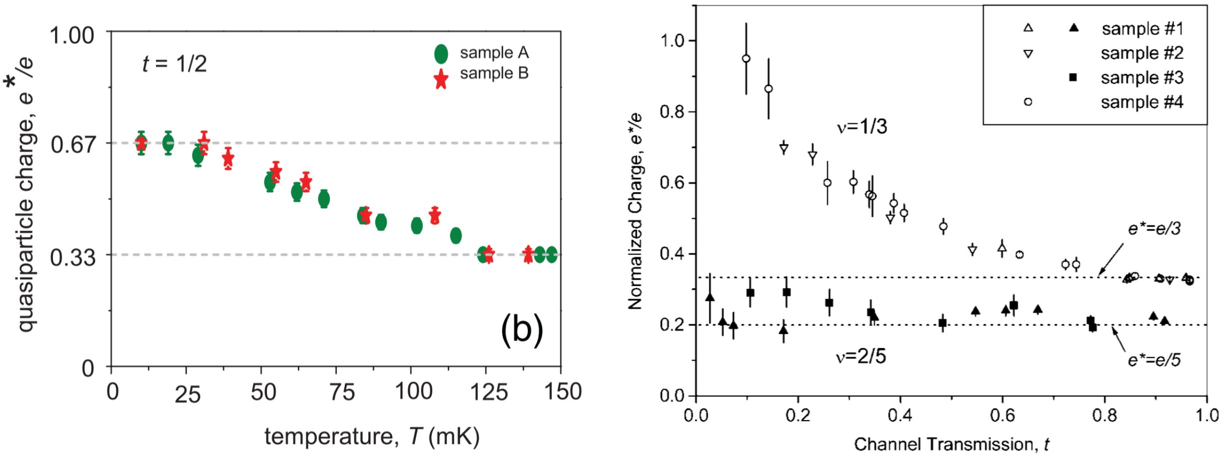

FIGURE 3.14 – **Evolution of the fractional charge as a function of the temperature or transmission.** Left figure is from [4] showing the evolution of the measured fractional charge at $\nu = 2/3$ as a function of the temperature. Right figure, from [39] shows the evolution of the measured charge at $\nu = 2/5$ and $1/3$ as a function of the transmission.

The DCSN was also measured in the SBS regime where a Poissonian transfer of charge e was observed (at $\nu = 1/3$) as expected [34]. Surprisingly, for very low temperature ($T < 25$ mK) the noise measured was more than twice of the Poisson value which remain unexplained. Moreover what happens at the transition between the WBS and SBS regimes remains unknown.

3.4 PASN in the FQHE

As for DCSN, interactions in the FQHE are expected to modify the noise when applying a time-dependent voltage at frequency f. As seen before, in the non-interacting case, a singularity in the PASN is present at $\mathrm{eV} = \mathrm{h}f$ where f can be identified as the Josephson frequency of normal systems. Similarly for the normal-superconducting junction, the singularity is observed at the Josephson frequency of a Cooper pair [61]. A straightforward question would then be : what happens at the Josephson frequency of fractional charges $f_J = \mathrm{e}^*\mathrm{V}/\mathrm{h}$?

In the following the formalism developed to obtain a PASN formula is presented. A way to highlight photo-assisted processes is exposed that leads to the measurement of the Josephson frequency of fractional charges.

3.4.1 Photo-assisted processes in the FQHE

Here is exposed a simplified reasoning on the states of an excited reservoir with a time-dependent voltage using the Floquet formalism developed above. It is applied to edge channels along which quasi-particles of charge e* are propagating. Several calculations using chiral LL properties thus considering the interactions between particles have been done in [19, 16, 88] and the same result is obtained in this calculation.

Let us consider two reservoirs at chemical potential μ_0 and μ_1. The reservoirs are supposed to be weakly coupled, meaning that there is a weak transfer of particles of charge e* from one edge state to the other. Their ground states are written $|\mu_0>$ and $|\mu_1>$. The system is put out of equilibrium by applying a DC bias voltage V_{ds} on the contact (0). As the charge experiencing this voltage drop are the fractional charge e*, it leads to a difference in chemical potential of the two reservoirs of $\Delta\mu \;=\; e^*V_{ds}$.

The quantum mechanical expected value of an observable $\tilde{O}$ is :

$$\mathbf{O}^{DC} =< \mu_0|\otimes < \mu_1|\tilde{O}|\mu_1 > \otimes|\mu_0 > \tag{3.30}$$

Where the observable describes the DC transport properties of the system, such as current or noise.

If now, a time-dependent voltage $V_{ac}\left(t\right)$ is also applied on the reservoir (0), as seen in section 3.2.1, the ground state of the excited quasi-particles acquires an extra phase :

$$\phi\left(t\right) = \frac{e^*}{\hbar}\int_{-\infty}^{t} dt'\, V_{ac}\, cos\left(2\pi f t'\right) = \frac{e^*}{h} V_{ac}\, sin\left(2\pi f t\right) \tag{3.31}$$

The Floquet amplitudes are still defined as the Fourier transform of the phase term :

$$p_l = \frac{1}{2\pi}\int_{t}^{t+T} dt'\, exp\left(2i\pi l f t'\right) e^{i\phi(t')} \tag{3.32}$$

All the carriers of the reservoir on which the time-dependent voltage is applied see their energy shifted by the value lhf with a probability amplitude of p_l. As for the non-interacting case, the incoming state is then in a superposition of states with the extra phase $e^{2i\pi l f t}$.

Let us now write the expected value of the observable $\tilde{O}$ similarly to equation 3.30 :

$$\mathbf{O} = \left(\sum_{l'} p_{l'} e^{2i\pi l' ft} < \mu_0|\right) \otimes < \mu_1|\tilde{O}|\mu_1 > \otimes \left(\sum_{l} e^{-2i\pi lft}|\mu_0 >\right) \tag{3.33}$$

We are interested in the time average value of the observable

$$\bar{\mathbf{O}} = \sum_{l} |p_l|^2 \left(e^{2i\pi lft} < \mu_0|\right) \otimes < \mu_1|\tilde{O}|\mu_1 > \otimes \left(e^{-2i\pi flt}|\mu_0 >\right) \tag{3.34}$$

As all the particles of the excited reservoir have their energy shifted with the value *lhf*, this writes :

$$\bar{\mathbf{O}} = \sum_{l} |p_l|^2 < \mu_0 + lhf| \otimes < \mu_1|\tilde{O}|\mu_1 > \otimes|\mu_0 + lhf > \tag{3.35}$$

This corresponds to the time averaged expected value of the DC case for $\Delta\mu = e^* V_{ds} + lhf$ (see equation 3.30)

$$\bar{\mathbf{O}} = \sum_{l} |p_l|^2 O^{DC} \left(e^* V_{ds} + lhf\right) \tag{3.36}$$

This equality applies to any transport properties. Those of interest in the framework of this manuscript are the current and the current shot noise. This expression has recently been generalized to strongly correlated systems in [89]

First introduced in [109] for the current and in [18, 19] for the noise of a conductor in the FQHE excited with a periodic drive at frequency *f* was expected to exhibit singularities near integer values of the *Josephson frequency* $\mathrm{f}_J = \mathrm{f}$ defined as :

$$f_J = \frac{e^* V}{h} \tag{3.37}$$

The Josephson frequency was originally written for superconductors [51] tunnel coupled. When a difference of chemical potential is induced across the tunnel barrier, the current oscillate at a frequency equal to the Josephson frequency of a Cooper pair. A striking manifestation of the Josephson frequency appears while measuring the current of a superconducting junction excited with a time-dependent voltage at frequency *f*. In that case, the I-V characteristics exhibit singularities in the form of jumps, so called the Shapiro steps [95] each time the voltage is equal to an integer value of hf/2e.

For a normal metal irradiated at a frequency $f = \mathrm{f}_J$, the zero-frequency shot noise is expected to exhibit singularities at the Josephson frequency. The PASN is written using equation 3.36 in terms of f_J :

$$\begin{aligned} S_I^{ac}(f) &= \sum_{l} |p_l|^2 S_I^{dc} \left(V_{ds} - \frac{lhf}{e^*}\right) \\ &= \sum_{l} |p_l|^2 S_I^{dc} \left(f_J - lf\right) \end{aligned} \tag{3.38}$$

The zero-bias singularity is then expected to be recovered at $\mathrm{f}_J = l\mathrm{f}$.

As for the current, a similar result was obtained in [90], where the expression found for the current induced by tunnelling of charge e* between two reservoirs driven by a time-dependent voltage at frequency *f* is :

$$I^{ac}\left(V_{ds}\right) = \sum_{l} |p_l|^2 I^{dc} \left(V_{ds} + \frac{lhf}{e^*}\right) \tag{3.39}$$

Where $|p_l|^2$ is the probability to absorb or emit a photon at frequency f. The result found in equation 3.36 is consistent with those previously found. Once again if a zero bias singularity exists in the DC measurement, it is expected to be recovered at the Josephson frequency of the fractional charge.

3.4.2 PASN as a function of the DC bias voltage in the FQHE

Let us now look at the evolution of the photo-assisted shot noise previously found as a function of the bias voltage. We focus on the noise because from the equation, a strong singularity at zero bias is evident and then replicas are expected in the PASN at $V_{ds} = lhf/e^*$. In the CLL theory, the current is expected to exhibit a strong zero-bias singularity. However experimentally this singularity has not been clearly seen as exponents have been found lower than predicted. Moreover the effect of the temperature is to flatten the singularities as seen in section 3.2.2. Hence shifted singularity in the current are not expected to be experimentally observed.

In the following, the differential conductance will be considered to be weakly non-linear, allowing to define a mean value denoted D or R = 1-D. This approximation is useful as is first allows to plot all noises as a function of the DC bias voltage but it is also recovered experimentally in the weak backscattering regime.

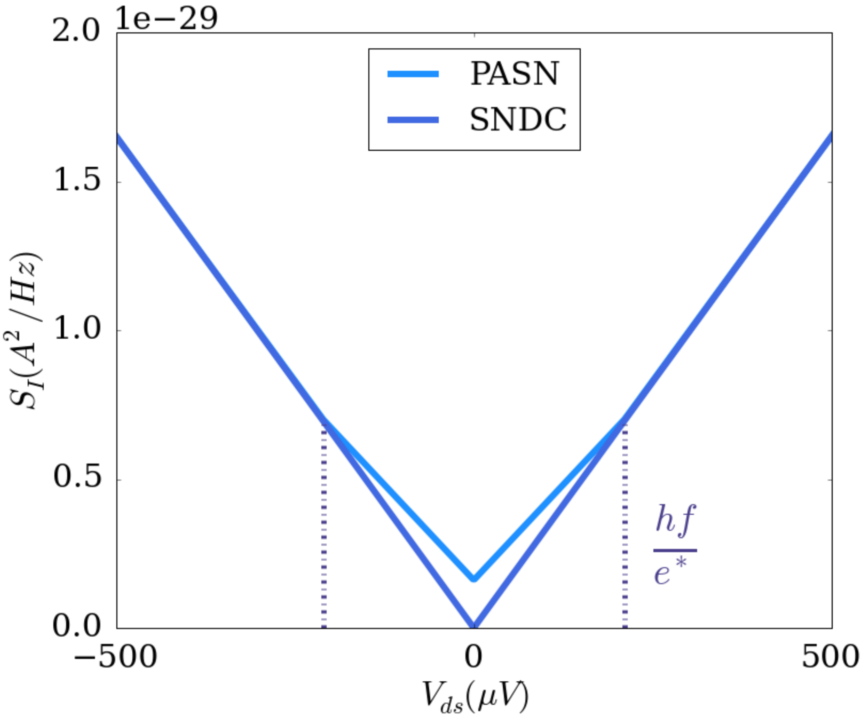

FIGURE 3.15 – **PASN in the FQHE at $\nu = 1/3$.** The dark blue line is the DCSN at $\nu = 1/3$ and zero temperature for a reflection coefficient of 0.1. The light blue line is the PASN for $f = 17$ GHz and an amplitude $V_{ac} = 150$ μV. Those simulations are done considering a non-interacting formula for the DCSN.

On figure 3.15 is represented the evolution of both DCSN and PASN in the WBS of the $\nu = 1/3$ FQH state at T = 0, considering a non-interacting formula for the DCSN. The conductor is irradiated with a sine wave at 17 GHz and of an amplitude of 150 μV and the PASN is calculated using the formula 3.38.The singularity of the DCSN at $V_{ds} = 0$ is recovered in the PASN at the fractional Josephson frequency. The difference with the IQHE is that as the fractional charge are expected to be transferred between edges, energy are shifted with a value taking into account the fractional charge e^*.

Our simulations show that by just looking at the raw PASN measurement or the excess noise, it could be hard to discriminate those from a classical adiabatic averaging of the DCSN with a time-dependent voltage (see figure 3.16). The classical averaging would present a wide parabolic variation in the low bias voltage and no shifted singularities. However because the measurements are performed in the FQHE, the signals that are to be measured are small and the difference between pure photo-assisted processes and a classical average is difficult even using the equation defined in equation 3.26. Thus another way to highlight the singularities has to be found.

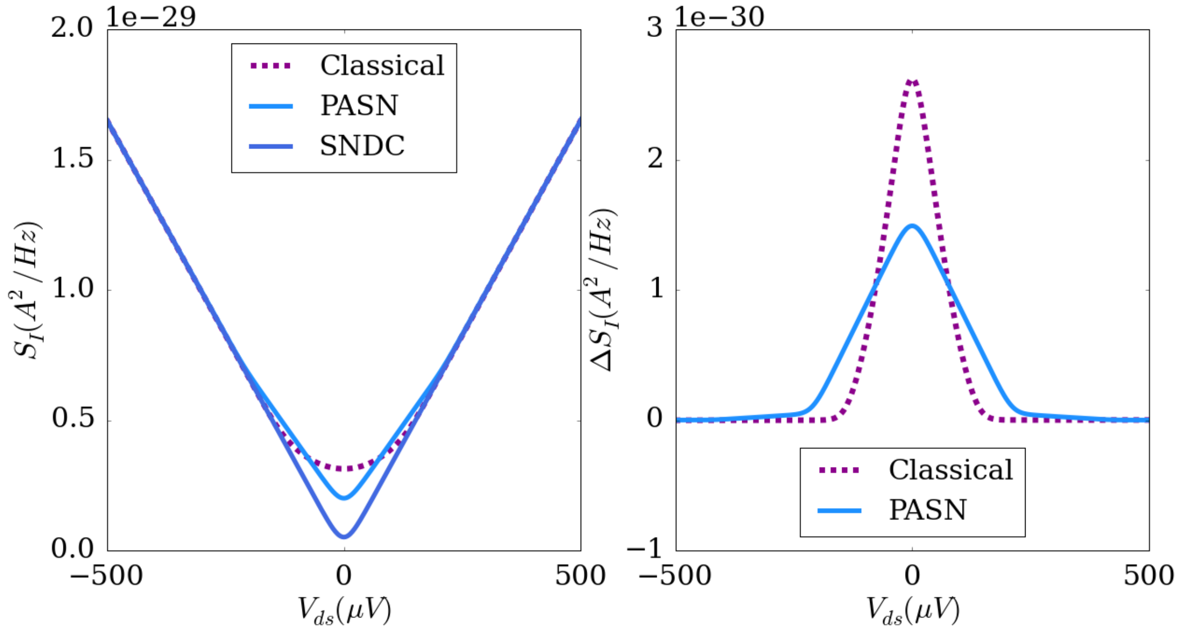

FIGURE 3.16 – **PASN in the FQHE and comparison with a classical mean.** The dark blue line is the DCSN at $\nu = 1/3$ and 30 mK for a reflection coefficient of 0.1. The light blue line is the PASN for $f = 17$ GHz and $\alpha = 0.6$ while the dotted line is the classical mean in the same conditions. The figure on the right shows the excess noise.

3.4.3 The Josephson frequency of a QH fluid

In order to highlight photo-assisted processes, the *excess noise* is written such that the contribution of particles that have not experienced photo-assisted processes is removed from the PASN :

$$\Delta S_I^{ac}\left(V_{ds}, V_{ac}, f, D, T\right) = S_I^{ac}\left(V_{ds}, V_{ac}, f, D, T\right) - \left|p_0\left(\frac{e^* V_{ac}}{hf}\right)\right|^2 S_I^{dc}\left(V_{ds}\right) \tag{3.40}$$

This corresponds to removing from the measured PASN the independently measured DCSN weighted by the probability $|p_0|^2$ to not have emitted or absorbed photons at frequency f. The contributions l = -1,0,1 are plotted on figure 3.17. Because of the Bessel functions, the contributions of +1 and -1 are symmetric regarding $V_{ds} = 0$ and the sum of those contributions is constant over a voltage bias range equals to $2hf/e^*$. Then removing the contribution of quasi-particles that have not seen photo-assisted processes leads to a flat variation over this voltage bias range, as represented on figure 3.17. A threshold voltage equals to ± hf/e^* is introduced. It corresponds to the voltage above which (or below for negative V$_{ds}$) the excess noise rises due to the partitioning of photo-created excitations and is then the hallmark of a singularity in the noise. Looking at the evolution of the threshold voltage with the excitation frequency f is then a good tool to probe photo-assisted processes in the FQHE. The position of the singularity is also a new way to measure the fractional charge of the quasi-particle.

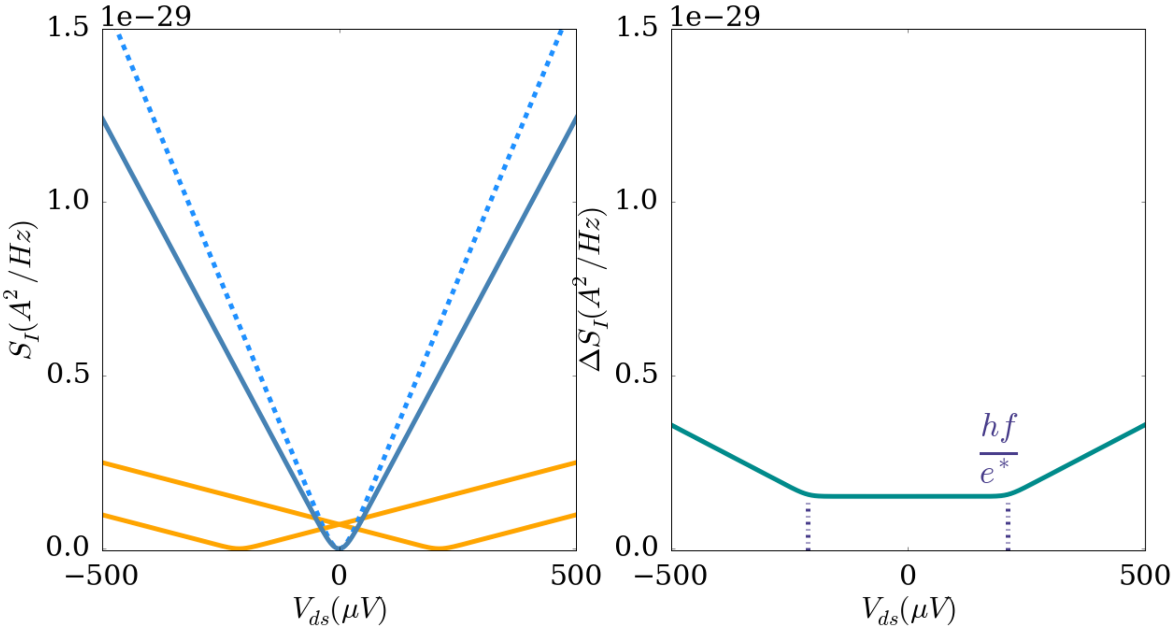

FIGURE 3.17 – **PASN in the FQHE at $\nu = 1/3$.** On the left figure, the dotted line is the DCSN at 30 mK, for a reflection coefficient of 0.1. The green full line is the contribution $l = 0$ of the PASN and the orange full lines are the contributions $l = \pm 1$. The time-dependent voltage has an amplitude of 150 μV and is at 17 GHz. The right figure is the excess noise as described in equation 3.40.

Moreover, finding a flat variation of the excess noise in the low range of $|V_{ds}|$ provides a determination of the amplitude probability $|p_0|$. As the sum of all amplitude probabilities has to be equal to 1, it also provides a determination of the following orders. Indeed, the highest reduced amplitude $\alpha = \mathrm{e}^* \mathrm{V}_{ac}/(\mathrm{h}f)$ that we are to use is for $f = 10$ GHz, $\mathrm{e}^* = \mathrm{e}/3$ and an AC amplitude $\mathrm{V}_{ac} = 190\ \mu$V. In that case, α is 1.5 and we have :

$$|p_0(\alpha)|^2 + |p_1(\alpha)|^2 + |p_{-1}(\alpha)|^2 = |p_0(\alpha)|^2 + 2|p_1(\alpha)|^2 \approx 0.88 \tag{3.41}$$

This means that almost all the information about photo-assisted processes can be understood by only considering the orders $l = 0$ and 1. This reduced amplitude corresponds to the "worst" case. For most of the measurements that will be presented (α<1.5) the second order can be neglected without loosing any information.

Finally, this technique is a good tool to discriminate photo-assisted processes from a classical mean. Indeed, with a classical averaging of the DCSN, a flat variation for $|V_{ds}| < hf/e^*$ is not to be expected. Instead, as represented in figure 3.18 the "adiabatic" excess noise presents a sinusoidal shape around zero bias voltage.

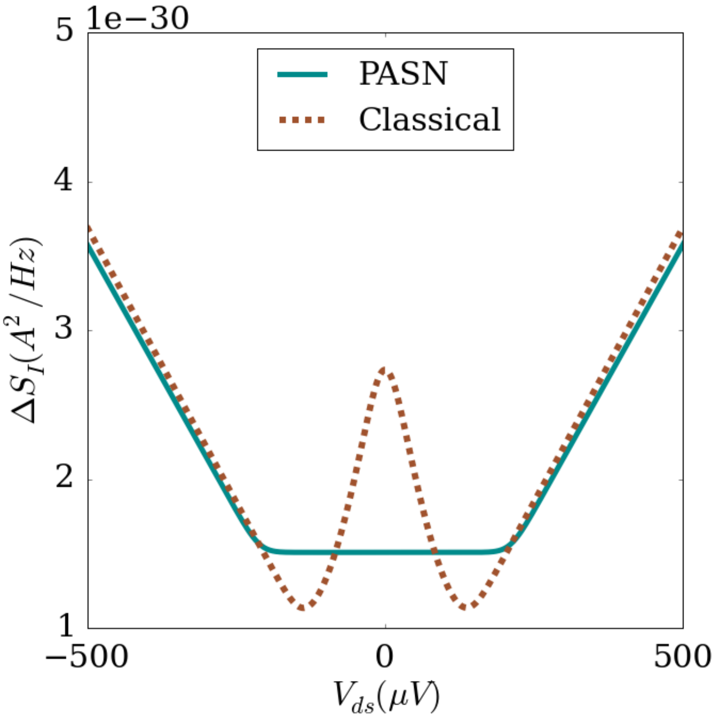

FIGURE 3.18 – **PASN in the FQHE at $\nu = 1/3$ and comparison with a classical mean.** The excess PASN is plotted for $f = 17$ GHz, $\mathrm{V}_{ac} = 150\ \mu$V, $\mathrm{e}^* = \mathrm{e}/3$, for a reflection coefficient of 0.1 and at 30 mK. The dotted line is the excess noise considering a classical mean of the sine pulse.

Chapter 4

Experimental realization of quantum transport in the QHE

Ever since the first realization of a 2DEG at the interface of Gallium Arsenide heterostructures, those have largely been used to study quantum transport. Indeed, thanks to lithography techniques, samples with dimensions lower than the elastic and inelastic mean free paths can be designed allowing the study of ballistic transport. Moreover, as opposed to metal, the Fermi wavelength in such structures is large enough to be compared to the device dimension, so a quantum description of the system is needed. Once placed at low temperature and in a high perpendicular magnetic field, this device can be used to investigate the Quantum Hall regime.

By introducing a smooth potential barrier in the structure, the quantization of the conductance as a function of this potential is observed, revealing that a limited number of discrete modes propagate. The conduction of the sample can be described using Landauer-Buttiker formalism. With a magnetic field applied, the backscattering along one edge channel is forbidden but the conductance quantization is still observed.

In this chapter the physics leading to the formation of 2D a electron system at the interface of two semiconductors is briefly described. Then is presented the experimental realization of a quantum coherent unidimensional ballistic conductor : the Quantum Point Contact. The transport in such devices is briefly reviewed, without and with a strong perpendicular magnetic field. Finally the nanofabrication is presented. More details about the fabrication can be found in appendix B.

4.1 The 2D electron gas

We present the formation of a 2DEG at the interface of two semiconductors and its interest in the framework of mesoscopic physics.

The first realization of a 2D system was done at the interface of a metal and a semiconductor, giving birth to MOSFET technology. Later the interface between two semiconductors presenting different energy gap have been studied [99]. In this framework, the GaAs-$Al_xGa_{1-x}As$ [1] heterostructure has largely been used. GaAs and AlGaAs have similar lattice constants, resulting in few defects at the interface. Moreover, this structure is MBE grown, hence the thickness of all layers is well controlled, particularly the doping layer of Si in AlGaAs.

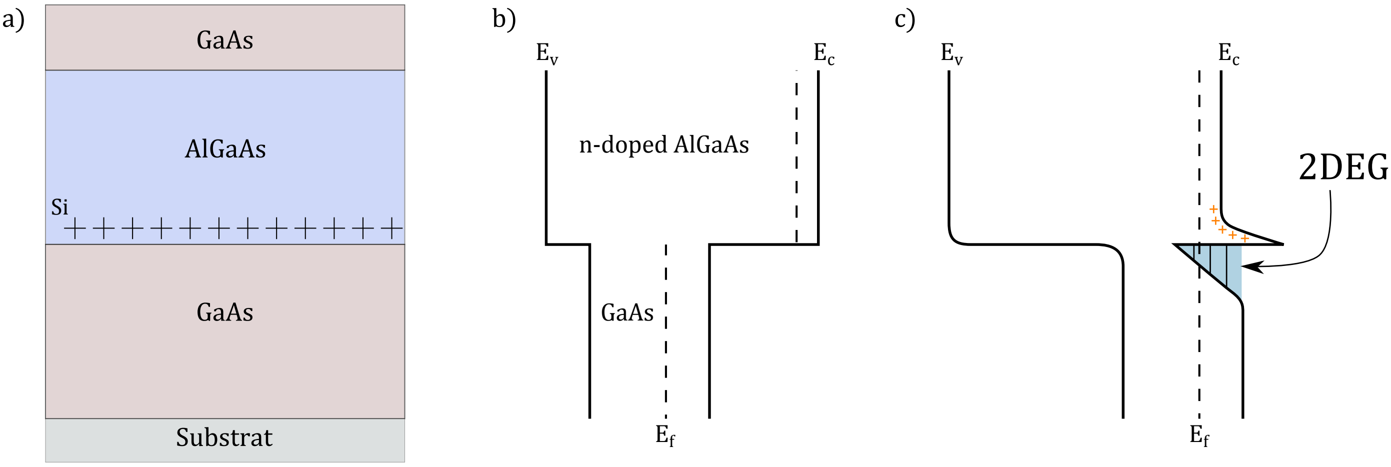

FIGURE 4.1 – **Formation of the 2DEG.** a) Heterostructure scheme. Si donors are in the AlGaAs layer allowing the formation of the 2DEG. b) Band structure at the n-AlGaAs/i-GaAs interface before charge equilibration. The dotted line represents the Fermi Energy in each structure, it is more important in AlGaAs than in GaAs. Solid lines are valence and conduction bands. c) Band structure after charge equilibration. The 2DEG, colored in blue, is formed at the interface of AlGaAs and GaAs while positively charged donors, in orange, accumulate at the AlGaAs side. The well is about 300 meV high [70].

AlGaAs has a wider gap and a higher Fermi energy than GaAs. The Si layer in AlGaAs introduces free electrons in the material. The electrons from the n-doped AlGaAs flows towards the minimum of energy, corresponding to the GaAs, leaving behind positively ionized Si donors. Bands are bent because of the electric field induced by the accumulation of negative charges on one side and positive charges on the other side. The electrons are confined in a triangular potential well at the interface of the semiconductors and the wave vector is quantized in the direction perpendicular to the interface. The spatial separation between charge carriers (here electrons) and the impurities (Si donors) gives rise to mobilities larger than 10^6 cm.V^{-1}.s. For the sample used here, an undoped AlGaAs

---

[1] x refers to the proportion of Al that replace Ga atoms in the GaAs crystal. Here, x=0.3.

layer of 40 nm is placed between GaAs and n-AlGaAs in order to increase the distance between the donors and charge carriers to obtain higher mobilities[46]. In the well, energy levels are distant of several tens of meV [96], meaning that at the working temperature ($<$100 mK), only the first level is occupied.

Finally this system realizes a coherent quantum conductor. Indeed in our case, the electron-phonon interaction is limited because of low temperatures. There are no magnetic impurities in the sample that would reverse the electronic spin, inducing a loss of coherence. Hence, the dominant mechanism for an electron to loose its phase coherence is the electron-electron inelastic interaction. The time between two collisions of 2D electrons can be estimated using [115] :

$$\frac{1}{\tau_{e-e}} = \frac{E_F}{4\pi\hbar}\left(\frac{k_BT}{E_F}\right) ln\left(\frac{E_F}{k_BT}\right) \tag{4.1}$$

For our sample, the electron-electron inelastic collision length is about $l_{e-e} = 10\ \mu m$ at 100 mK.

In the FQHE, the transport is 1D and chiral and such expression is not useful. The notion of quasiparticle with a finite lifetime τ_{e-e} has to be replaced by the bosonic excitation in a chiral Luttinger liquid description. The value of the coherence length in the FQHE has never yet been measured, but is has however been done for electrons in AsGa in the regime of IQHE. The coherence length has been measured at 20 mK to be of the order of tens of μm [87].

4.2 The QPC as a realization of a quantum ballistic conductor

Now that a 2DEG is obtained, let us focus on the study of ballistic transport, which is done by the mean of a quasi unidimensional conductor : a Quantum Point Contact (QPC). Metallic gates are placed on top of the heterostructure previously described, as first realized in [100, 118]. The shape of the 2DEG below is changed by the smooth potential induced by the gates and this potential can be varied by applying a negative voltage on the gates. When the size of the constriction in the 2DEG is comparable to the Fermi wavelength, $\lambda_F \approx 75$ nm a quantum description of the electronic transport through this narrow and short conductor is needed. The 2DEG far from the constriction and the ohmic contacts are reservoirs for the electrons.

In the following, the transport through the QPC without and with magnetic field is briefly described.

4.2.1 The conductance quantization

A QPC is seen as a ballistic 1D conductor connected to two reflectionless electron reservoirs denoted (L) and (R). Those reservoirs are electrons baths at temperature T and at chemical potential μ_L and μ_R. A potential V applied on one reservoir, let's say

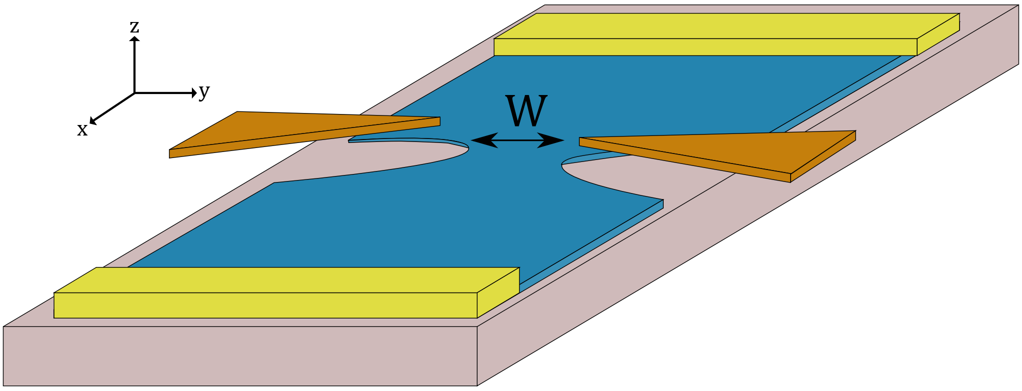

FIGURE 4.2 – **Scheme of a QPC.** In blue is the 2DEG with the constriction induced by the gate voltage. W is the width of the constriction that can be changed with the gate voltage. The gates are in orange and the ohmic contacts in yellow. Ohmic contacts and the 2DEG far from the constriction are the electron reservoirs. The substrate is in grey.

(L), while the other is grounded results in a difference of chemical potential : $\mu_L - \mu_R = \text{eV}$. The current flows between the two reservoirs with a conductance $G = I/V$. Because of the confinement of the electrons in the y-direction by the split-gates, the movement in that direction is quantized, leading to the formation of subbands. There are $\text{int}(2W/\lambda_F)$ electronic mode in the conductor, with W the width of the constriction and each electronic mode carry a conductance of $2e^2/h$.

The potential induced by the gates acts like an impurity and an incoming mode m has a certain probability T_m to be transmitted. The two-terminal conductance of the device is expressed using Landauer's formula [63, 64], assuming that T_m is not energy dependent :

$$G = \frac{2e^2}{h} \sum_m T_m \tag{4.2}$$

By applying a negative gate voltage, the width of the constriction is decreased which allows to change the transmission of each channel of conduction one by one.

Experimentally, the conductance is quantized and plateaus at integer values of $2e^2/h$ are observed [106, 111].

4.2.2 The QPC in high magnetic field

For a 2DEG in a high perpendicular magnetic field, as seen in section 2.2.2, energy levels are quantized in Landau levels. When the Fermi energy lies between two Landau levels, the transport of electrons is forbidden in the bulk [36, 73] and only occurs in chiral unidimensional channels that follow equipotential along the edges of the sample [65, 41].

A QPC is then used to induce backscattering as it brings opposite channels closer and so that the transfer of electron from one edge to the other is possible. The scattering of edge channels at the QPC is described using Landauer-Büttiker formalism as the edge states realize a unidimensional ballistic conductors and the scattering at the QPC is done through elastic processes.

At integer filling factor ν, when changing the gate voltage, the electron density is changed at the QPC until reaching a local filling factor of $\nu - 1$... Then the transmission of each channels, which carry a current e^2/h, can be tuned by the gate voltage

For the FQHE, an equivalent of the multiterminal Landauer formula is derived in [3] where the current in reservoir α at chemical potential μ_α and filling factor ν_α is calculated considering a transmission or reflection[2] probability $T_{\alpha\beta}$ from reservoir β at chemical potential μ_β, each of these channels carrying a fraction $\nu_p - \nu_{p-1}$ of current[3] e^2/h where p varies from 1 to the total number of edge channels and ν_p is a fraction.

$$I_\alpha = \frac{e}{h}\mu_\alpha \nu_\alpha - \frac{e}{h}\sum_\beta T_{\alpha\beta}\mu_\beta \tag{4.3}$$

Starting at bulk filling factor ν_p, when varying the gate voltage, the electron density at the QPC is changed until reaching a local filling factor of ν_{p-1}.

4.3 QPC nanofabrication

Here is reported the nanofabrication of the sample. The 2DEG used was grown by I. Farrer and D. A. Ritchie at the Cavendish Laboratory of Cambridge. The density is 1.11 10^{11} cm^{-2} and the mobility is 3 10^6 V^{-1}.cm^2.s^{-1}. The lithography was performed at SPEC following a design by M. Santin. The sample characteristics such as the nanofabrication details can be found in Appendix B.

4.3.1 Mesa etching

In order to minimize leakage between the gates and the 2DEG, the surface of the conducting gas under the gates is reduced by chemical etching. Electrons of the etched area move towards to surface where they are deeply localized and are no longer available to provide a 2DEG at the interface. The remaining unetched region defines the mesa, which size is 200 μm x 200 μm (figure 4.3). The resistance of the mesa is 130 Ω for the sample used.

4.3.2 Ohmic contacts

A metallic alloy is used to connect the 2DEG to the external circuit. At the interface of a metal and a semiconductor, a Skottky barrier is formed and is insulating at low temperature. To reduce this barrier height, the metal is directly connected to the 2DEG, buried 90 nm under the surface of the sample. To do so, an Au-Ge alloy is used. Indeed, this alloy forms an eutectic mixture whose melting temperature at air pressure is less than 400° C. Ni is used as a wetting layer to help the alloy to diffuse towards the 2DEG [7].

---

[2] for $\beta = \alpha$

[3] This fraction is the only difference between the generalized multiterminal Landauer formula in the IQHE and the FQHE.

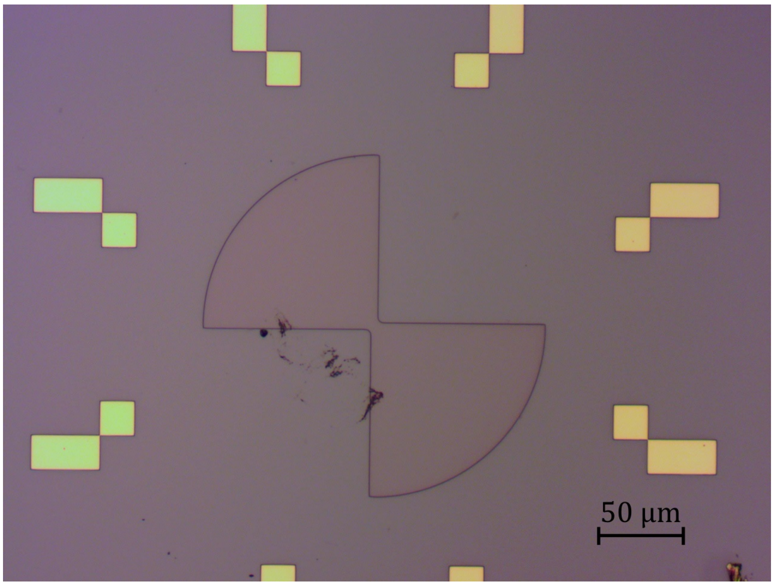

Figure 4.3 – **Mesa etching.**

The ohmic contacts have a meander shape (figure 4.4) as the contact resistance depends on the orientation angle between the contact and the cristallographic axis [53]. At 4 K, a contact resistance of 100 Ω is obtained.

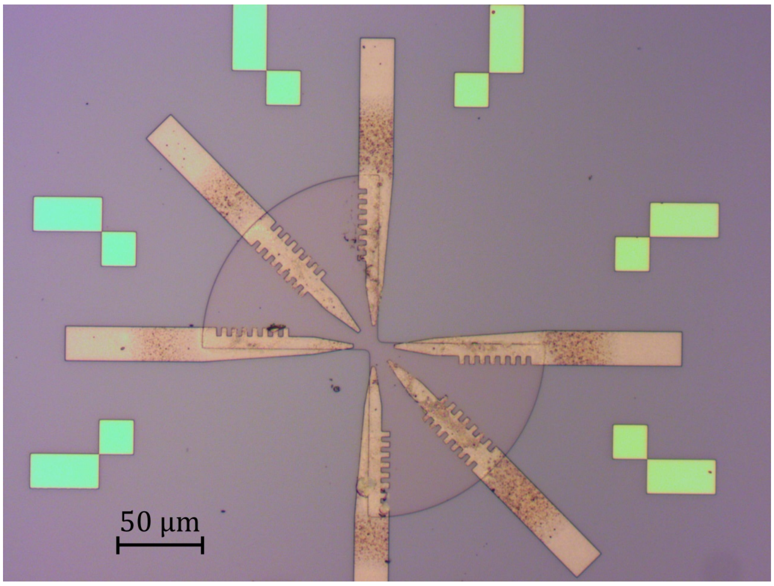

Figure 4.4 – **Ohmic contacts.**

Contacts are essential for the observation of the QHE. Indeed, in the case of a non ideal contact, electrons injected at the potential μ_L will populate the edge state with different chemical potential [8, 56]. The equilibration between edge states occur only after a length equals to the inelastic scattering length.

4.3.3 Gates deposition

The constriction is done by depositing gates on top of the 2DEG. For the sample used it is 300 nm wide and 300 nm long (see figure 4.5).

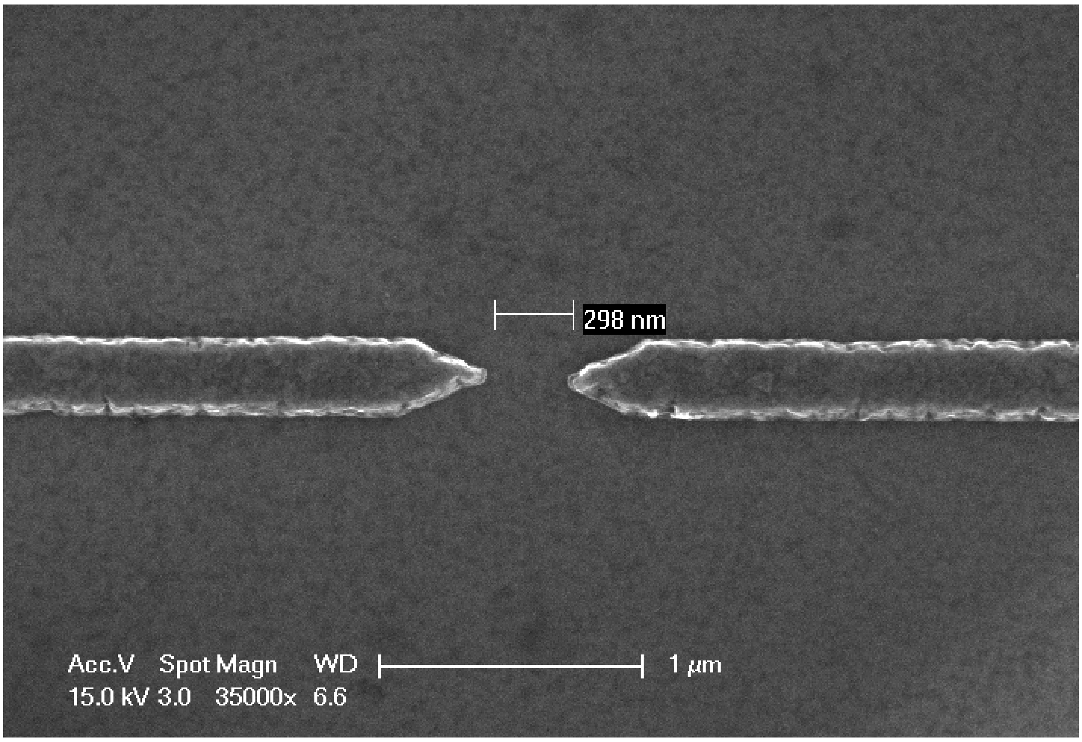

Figure 4.5 – **SEM image of the gates.**

A SEM image of the finished sample is shown in figure 4.6 as a close-up in the center of the mesa showing the placement of the gates.

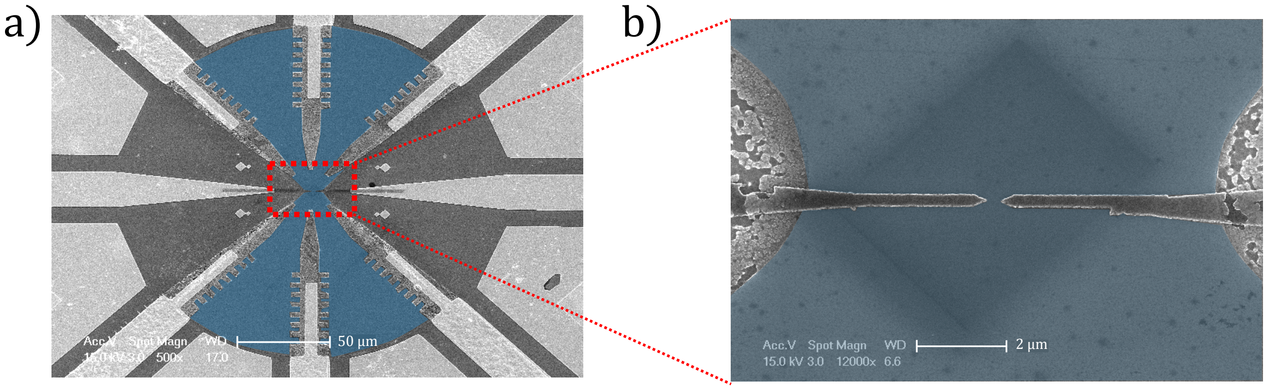

Figure 4.6 – **SEM image of the finished sample.** a) Image realized by electron microscope of the sample. The 2DEG is artificially colored in blue. The large bright circuit are golden leads connecting the ohmic contact in grey to the external circuit. The black lines are the gates. A zoom (figure b)) is realized at the center of the mesa where the gates are placed.

Chapter 5

Experimental set-up

Noise measurements in the FQHE are combined with DC and RF voltages. To observe PASN in the FQHE, a sensitivity of the order of 10^{-31} A^2/Hz has to be reached in a time of the order of some minutes.

Measurements are realized in a Cryoconcept® Helium free dilution refrigerator equipped with a 14.5 T Cryomagnetics® coil. As schematically shown in figure 5.1, low-loss coaxial cables bring both RF and DC voltages from room temperature to a PCB. A small AC excitation with frequency below 1 kHz is also sent to the PCB for conductance measurements. Coplanar waveguides designed by CST microwave studio etched on the PCB bring the RF at contact (0) of the sample (see [24]). DC voltage is delivered by a voltage source Yokogawa 7651 and RF voltage by an Agilent N5183A MXG Analogic signal generator.

Transmitted and backscattered current and their fluctuations are converted into voltages via the Hall relation at contacts (1) and (4) respectively, see figure 5.6, and sent to RLC resonators with resonant frequency f_0=2.5 MHz. Those voltages and voltage fluctuations are first amplified by a home made cryogenic amplifier at 3.6 K. A splitter separates low-frequency signal from high-frequency signal.

The high frequency signal is amplified at room temperature by low noise commercial amplifiers NF SA-421F5 and pass through a Chebyshev filter to finally be sent to a digital acquisition card ADLink 9826 so that a PC computed the cross-correlation and auto-correlation spectrum. The low frequency signal is amplified at room temperature by commercial amplifiers LI-75A and sent to a lockin amplifier.

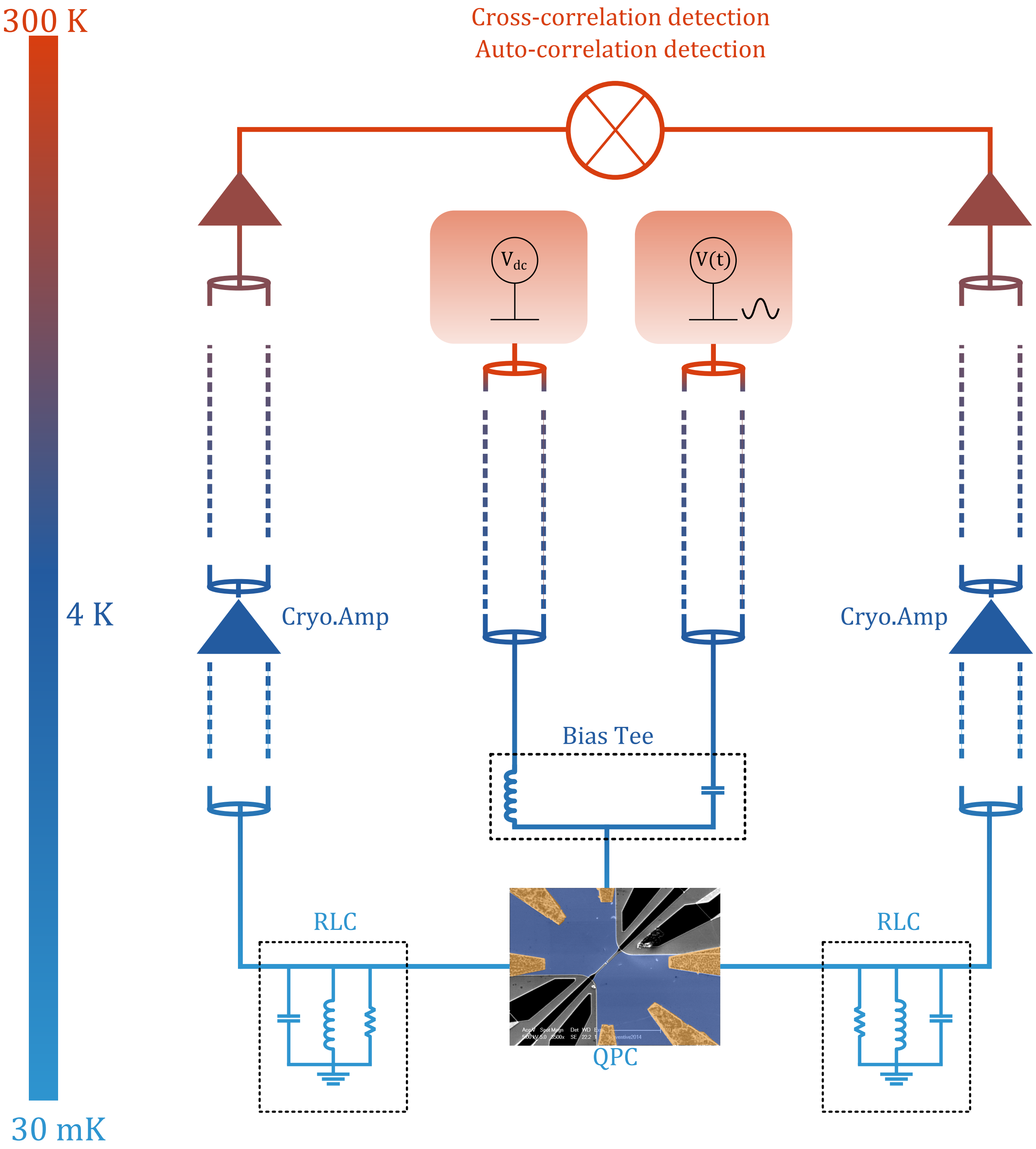

Figure 5.1 – **Overview of the experimental noise measurement set-up**. A DC voltage and RF source placed at 300 K sent a signal V(t) to the sample. DC and AC voltages are mixed through a bias-tee at 20 mK then send on one contact of the sample. Backscattered and transmitted current as well as their fluctuations are converted into voltages through a RLC resonator then amplified at 3.6 K by a home-made cryogenic amplifier. Those fluctuations are sent to an acquisition card and a PC realizes the FFT of signals.

Circuit board	Temperature
Sample	23 mK
RLC	23 mK
Cryo-amplifier	3.6 K
Splitter	300 K
LI-75A	300 K
NF SA-421F5	300 K

TABLE 5.1 – Temperature of different circuit boards

5.1 Injection lines

Here we present the design and the realization of the electrical lines used to apply a DC or low frequency excitation to the sample. This is followed by a description of the microwave lines used for PASN experiments. The wirering has been made so as to reduce the environmental noise and noise coming from the experimental set-up. Another fundamental feature is to limit the heating power brought by the coaxial cables as it goes from room temperature to the sample at 20 mK. Heat can be brought either by phonons, electrons or photons. At low temperature, excitation of phonon modes is negligible. Radiation coming from the propagation of photons has to be considered for RF lines.

5.1.1 DC lines

Both the bias voltage V_{ds} and the gate voltage V_g are delivered by DC-voltage sources Yokogawa 7651. Voltages are brought to the sample by LakeShore coaxial cables stainless steel. Those wires have a resistance of 23.6 Ω/m and a capacitance of 173.9 pF/m. There is 2 m of DC wires, the cut-off frequency can be estimated $f = 1/2\pi RC$, where C is the total capacitance of the wires and R the resistance seen at the end of the wires so the sample resistance. f is found to be less than 40 kHz. This is a suitable cut-off frequency as only DC or low-frequency voltages are to be sent through those wires.

The outer conductor is made of braided stainless, the inner conductor is stainless steel while the dielectric is Teflon. The wires are anchored at each stages of the cryostat through SMA connectors and filtered at each stages of the cryostat by low-loss low-pass filters (DC to 80 MHz), thermalizing the outer conductor at the stage temperature. For temperature below 4 K, the thermal conductivity of Teflon decreases as T^2. Hence wire have to be long enough to ensure a good thermalization of the inner conductor. Moreover the inner conductor does not directly go to the sample holder as it first passes through a bias-tee (see 5.1.2) thermalized on the 20 mK stage. The heating power brought by the wires can be estimated using the Wiedemann-Franz law :

$$\dot{Q} = \int_{T_{min}}^{T_{max}} \frac{\pi^2}{3} \left(\frac{k_B}{e}\right)^2 \frac{T}{R_{wire}} \, \mathrm{d}T \tag{5.1}$$

For the coldest region of the cryostat, between the 100 mK and 20 mK stages, the heating power is equal to 10 pW for a 50 cm long wire. This value is much lower than the cooling power of the mixing chamber stage which is of 2 μW ensuring that there is no overheating due to the wires.

The thermal power spectral density of an impedance R at temperature T is written [50, 77] :

$$S_V(\nu) = \frac{4Rh\nu}{exp(\frac{h\nu}{k_B T}) - 1}$$

At low-frequency, $h\nu \ll k_B T$, this relation simplifies as $S_V(\nu) = 4k_B TR$ recovering the Jonhson-Nyquist white noise. Voltage fluctuations are recovered by summing those contribution over a certain bandwidth.

One can estimate the voltages fluctuations brought from room temperature through the DC wire Δ V < 1 μV which corresponds to a noise temperature of less than 12 mK.

5.1.2 RF lines

RF voltage is provided by an Agilent N5183A MXG Analogic signal generator. RF lines are home-made coaxial cables. The inner and outer conductors are silver-plated stainless steel and the dielectric if Teflon, except for 5 cm after the 100 mK stage where the outer conductor is copper while the inner conductor is superconducting, made of Niobium-Titanium. Attenuators of 20 dBm are placed on the 4 K, 800 mK and 100 mK stages. For thermal radiations attenuators are considered as 50 Ω impedances black body sources.

To estimate the heating of the sample by the 300 K photons the thermal noise has to be calculated. This is done by summing all the thermal contributions of all components of impedance R_k at temperature T_k modulated by the attenuation denoted A_k over the frequency range :

$$\Delta V^2 = \sum_k \int_{\Delta\nu} \frac{4R_k h\nu}{exp(\frac{h\nu}{k_B T_k}) - 1} A_k \tag{5.2}$$

This calculation was made for the wires used here in [24] [1]. We find that the voltage fluctuations are equal to $\Delta V \approx 0.4$ μV or less than 4 mK.

5.2 Measurement lines

In this section are presented the component used to efficiently detect the small current fluctuations produced by the partitioning at the QPC. First a RLC resonator circuit is

---

[1] The only difference is that the 10 dB attenuators on the mixing chamber stage has been removed in order to apply larger AC voltages.

used to convert current fluctuations into voltages at low frequency (~ MHz) and then those signals are amplified at low temperature.

5.2.1 Resonator

Component	Value
R_1	20 kΩ
C_1	22 nF
C_2	9.4 nF
L	22 μH

Table 5.2 – Passive component value

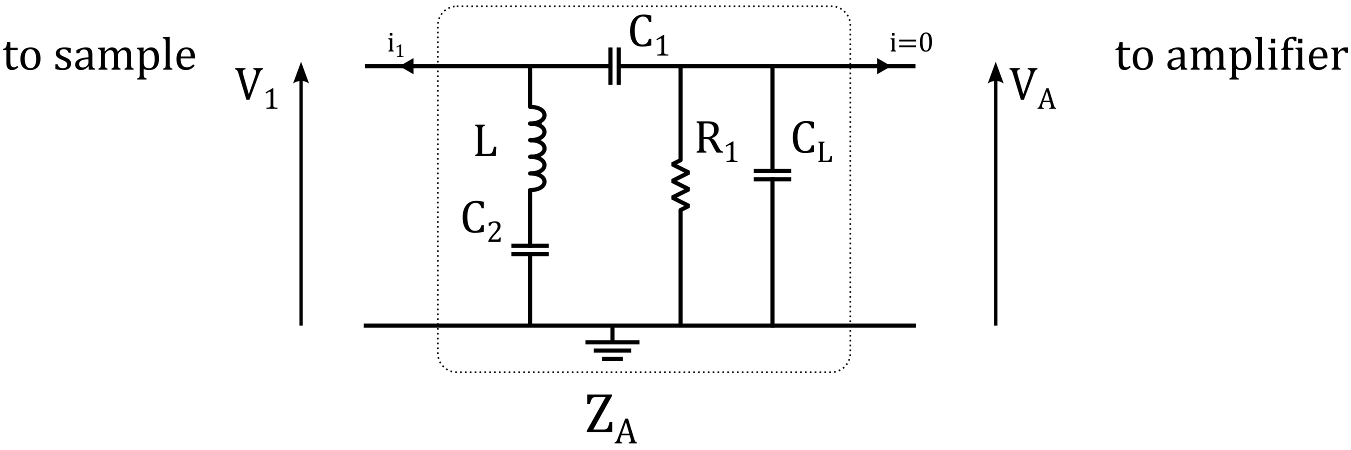

Figure 5.2 – **Schematic view of the resonator.** C_L is the wire capacitance.

Resonators of impedance Z_A and Z_B are used to convert backscattered and transmitted current through the sample into voltages V_A and V_B.
Passive components are chosen so that they maintain a constant value from room temperature to 20 mK and are stable under high magnetic field. For resistance we use thin film CMS 0805 whose value measured at 4 K varied of less than 5%. Capacitors are also CMS 0805. The inductance is a Coilcraft ceramic chip inductor with no magnetic core. This inductor has a non zero inner resistance r_C. It was measured to be of 9.5 Ω at 300 K and zero magnetic field. This resistance is expected to be lower at low temperature, nevertheless the skin depth effect increases its value at few MHz.

The sensitivity reached up to now was of 1 10^{-29} A^2/Hz. As seen in section theory, signals we are to measure are small compared to previous experiments [24, 52, 92]. Hence the resonator was changed in order to increase the voltage measured across R_1. To do so we increased the value of this resistor, setting it to $R_1 = 20\ k\Omega$. The values of the other components are reported in table 5.2.

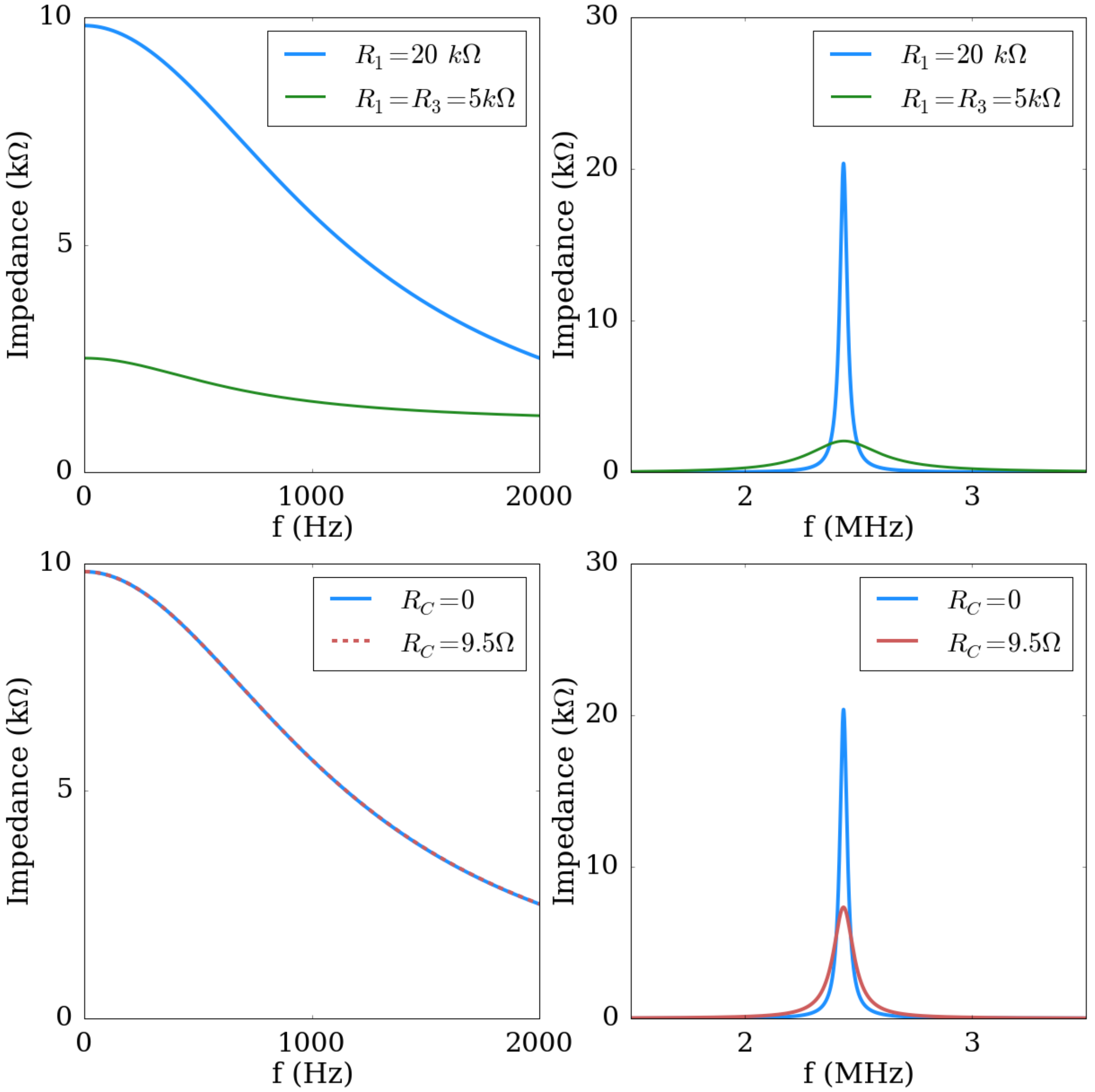

FIGURE 5.3 – **Resonance shape of RLC circuit with inductance resistance.** *Top left* RLC impedance as a function of the frequency for low frequency. The green line is a simulation using the old RLC board, the blue one is for the new circuit board shown in figure 5.2. *Top right* resonance at 2.5 MHz. *Bottom left* comparison of the impedance at low frequency taking into account r_C for the new RLC circuit. *Bottom right* Comparison of the effect of the inner resistance at resonance frequency. The effective impedance to convert current coming from the sample into voltage is lowered by this impedance. For the simulation we used C_L=200 pF

At low frequency, for differential conductance measurement, we measure the voltage along R_1 shunted by the capacitor C_2. Capacitor C_1 enhance the voltage measured at low frequency. The inner resistance of the inductance does not affect the low-frequency measurement (see figure 5.3).

For high-frequency measurements, namely noise measurements, R_1, L and C_l, the wire capacitor, form a parallel RLC circuit with resonant frequency :

$$f_0 = \sqrt{\frac{1}{(2\pi)^2 L C_L}} \tag{5.3}$$

Here the resistance r_C plays a damageable role as it decreases the total impedance used to convert current into voltage (see figure 5.3).

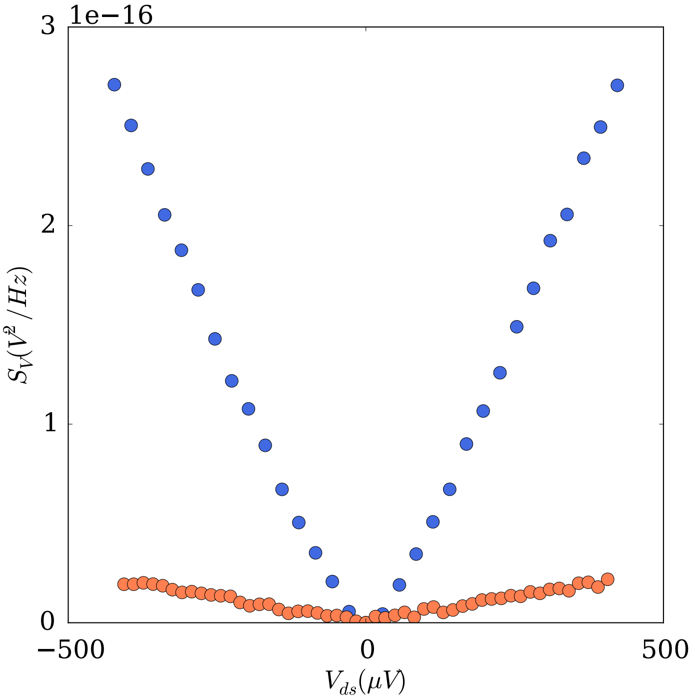

FIGURE 5.4 – **Voltage noise measured through different impedances.** The voltage noise is obtained after the conversion of the current shot noise of the sample by the resonator and increases with bias voltage V_{ds}. The orange dotted curve is measured through two 5 $k\Omega$ resistors in parallel while the blue one in measure with only 20 $k\Omega$ and the Hall resistance R_H. Both measurements are done at $\nu = 2/5$ for a QPC transmission of 0.9 at 30 mK.

Figure 5.4 shows a comparison of voltage noise measurement in comparable conditions one with the old resonator (orange curve), the other with figure 5.2 resonator (blue curve). An increase of the measured signal can clearly be seen.

5.2.2 Cryogenic amplifiers

The home made cryogenic amplifiers, developed during Thibaut Jullien's thesis [52], are based on commercial HEMT and the relation between the gate voltage and the drain voltage. For a HEMT two main quantities are important : the transconductance g_m and the conductance g_D.

$$g_m = \frac{\partial I_{ds}}{\partial V_g} \tag{5.4}$$

$$g_d = \frac{\partial I_{ds}}{\partial V_{ds}} \tag{5.5}$$

The gain is defined as $G = \partial V_D / \partial V_g$, so as a small variation of gate voltage results in a large variation of drain voltage. For a transistor alone, $G = g_m/g_d$. Here the differential conductance cannot be directly measured.

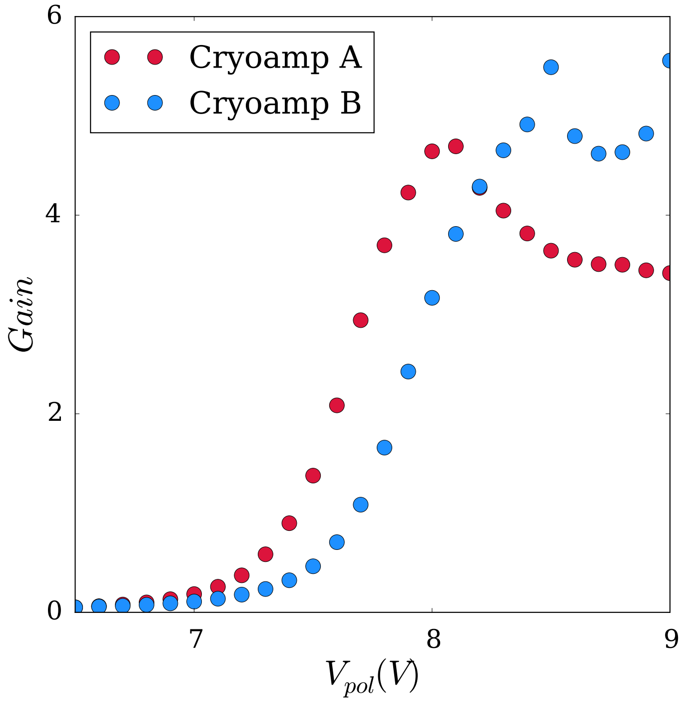

FIGURE 5.5 – **Evolution of the amplifier gain as a function the polarization voltage.** Noise is measured at zero bias and for a QPC fully openend. A polarization voltage of 7.9 V is used for cryo-amplifier A and for cryo-amplifier B the polarization voltage is set at 8.4 V. A Johnson-Nyquist thermal noise calibration (see Annexe C.2) is used to determine the gain of the cryo-amplifiers at polarization voltage chosen. The gain for the other polarization voltages are deduced from this calibration.

In order to choose the operating point, the gain of the amplifiers is measured as a function on the polarization voltage, imposed through a polarization resistance R_p, reported in figure 5.5. This voltage was set to maximize the gain of the amplifiers and maintain a good stability over time, which is why the polarization voltage giving the highest gain is not chosen, but a slightly lower value of V_{pol}.

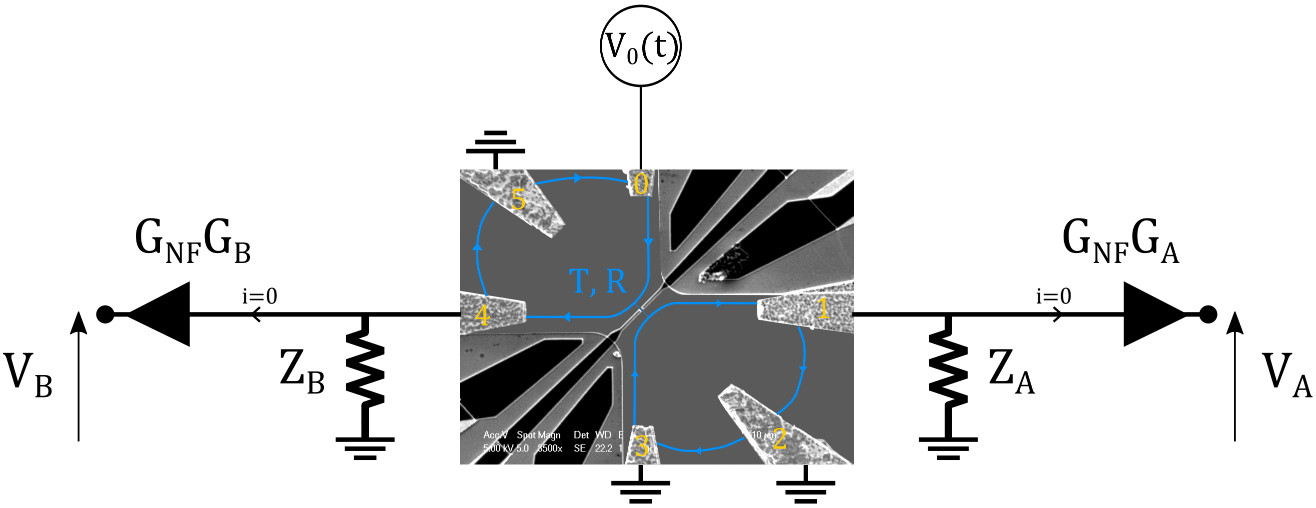

FIGURE 5.6 – **Details of the conductance measurement.** A small AC excitation $V_0(t)$ at frequency f=680 Hz is send on one contact of the QPC. Z_A and Z_B are the equivalent impedances of the resonators at low frequency. G_A and G_B are the gain of the cryogenic amplifiers while G_{NF} is the gain of the amplifiers at room temperature. V_A and V_B are the voltages measured by the lockin amplifiers.

5.3 Conductance measurements

5.3.1 Principle

We perform a low-frequency measurement of the conductance through two lockin amplifiers Signal recovery 7265. A small AC excitation at 680 Hz is sent along with the DC voltage on contact (0) which injects electron towards the QPC. Transmitted and backscattered current are converted into voltage through the RLC resonators, amplified at 3.6 K by homemade cryogenic amplifiers followed by commercial LI-75A low noise preamplifiers (gain $\sim$ 100) at room temperature. The detail of this measurement is schematically represented on figure 5.6. Such a measurement will give the transmission and reflection values with only one unknown value : the cryogenic amplifier gain at low frequency.
Indeed, using Buttiker's formalism in the IQHE at filling factor ν [10] :

$$< I_\alpha >= \frac{e}{h}(\nu\mu_\alpha - \sum_\beta T_{\alpha\beta}\mu_\beta) \tag{5.6}$$

For the sample :

$$< I_0 >= \frac{e}{h}(\nu\mu_0 - \mu_5) \tag{5.7}$$

$$< I_1 >= \frac{e}{h}(\nu\mu_1 - T\mu_0 - R\mu_3) \tag{5.8}$$

$$< I_4 >= \frac{e}{h}(\nu\mu_4 - R\mu_0 - T\mu_3) \tag{5.9}$$

After some calculations, one can easily find that :

$$V_A = \frac{G_A G_{NF}}{1 + R_H/Z_A(f)} \frac{T}{\nu} V_0 \tag{5.10}$$

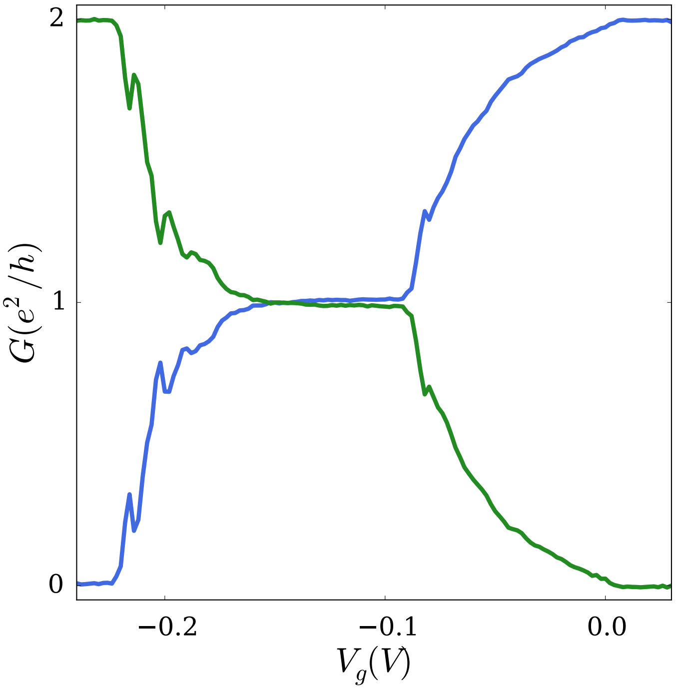

FIGURE 5.7 – **Reflection and transmission coefficients as a function of the gate voltage at ν=2.** A signal at frequency f=680 Hz of amplitude V_0^{ac}=15 μV is sent. The blue curve is the transmission coefficient T, the green curve is the reflection coefficient R. Formulas 5.11 and 5.10 are used and $G_{A/B}$ is determined by aligning Hall plateaus. We find G_A=7.9 and G_B=8.7.

$$V_B = \frac{G_B G_{NF}}{1 + R_H/Z_B(f)} \frac{R}{\nu} V_0 \tag{5.11}$$

The gain of the cryogenic amplifiers is found by aligning Hall plateaus. Figure 5.7 shows the transmission and reflection for ν=2.

5.3.2 Hall resistance

A good way to characterize the 2DEG is to realize a measurement of Hall resistance R_H as a function of the magnetic field. Indeed, the position of the plateaus give access to the electronic density n_s of the 2DEG.

The measurement is done while increasing the magnetic field for a QPC fully closed, ensuring that the transmission coefficient is equal to the filling factor and at $V_{ds} = 0\ V$. From the measured voltage after total amplification V_B, the Hall resistance is found :

$$R_H = Z_B(f) \left(G_B G_{NF} \frac{V_0}{V_B} - 1 \right) \tag{5.12}$$

Where G_B is the gain of the cryo-amplifiers on line B and $G_{NF} \approx 100$ is the gain of the LI-75A amplifiers at room temperature.

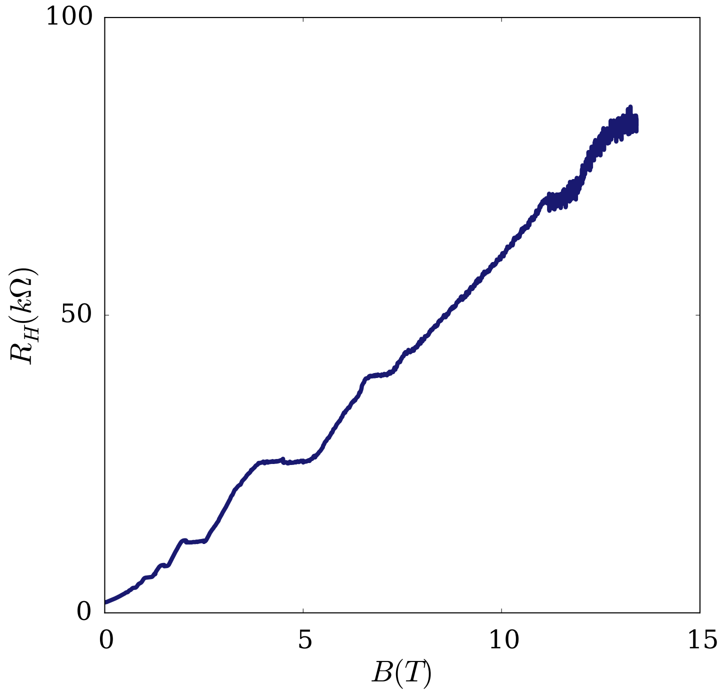

FIGURE 5.8 – **Hall resistance as a function of the magnetic field.** A signal at frequency f=680 Hz of amplitude V_0^{ac}=30 μV is sent. The bias is set at zero while the QPC is fully closed

5.4 Measuring the Shot Noise

5.4.1 Data acquisition and treatment

The high frequency voltages V_A and V_B are sent to an ADLink PCI 9826 digitizer. This digitizer records signals over a bandwidth from 0 to 10 MHz at a rate of 20 GS.s^{-1} and stores data in a buffer of 262 000 points. Half of this buffer is used to store data while calculations are computed using the other half of size N_S=131 000 points. Fourier transform of voltages $\tilde{V}_A$ and $\tilde{V}_B$ is calculated using N_S points thanks to a C++ program. Finally the PSD is computed simultaneously for auto-correlation $|\tilde{V}_A\tilde{V}_A^*|$, $|\tilde{V}_B\tilde{V}_B^*|$ and real and imaginary part of the cross-correlation $|\tilde{V}_A\tilde{V}_B^*|$. The PSD is calculated only over a limited number of points fixing the measurement bandwidth and averaged during a time τ.

A final, absolute calibration is made using Johnson-Nyquist thermal noise (see Appendix C).

5.4.2 Power spectral density

Figure 5.9 displays a cross-correlated PSD V_AxV_B^*.

The power spectral density is fitted with :

$$P(f, V_{ds}) = \frac{A(V_{ds})}{1 + (f^2 - f_0^2)^2/(f\Delta_r)^2} \tag{5.13}$$

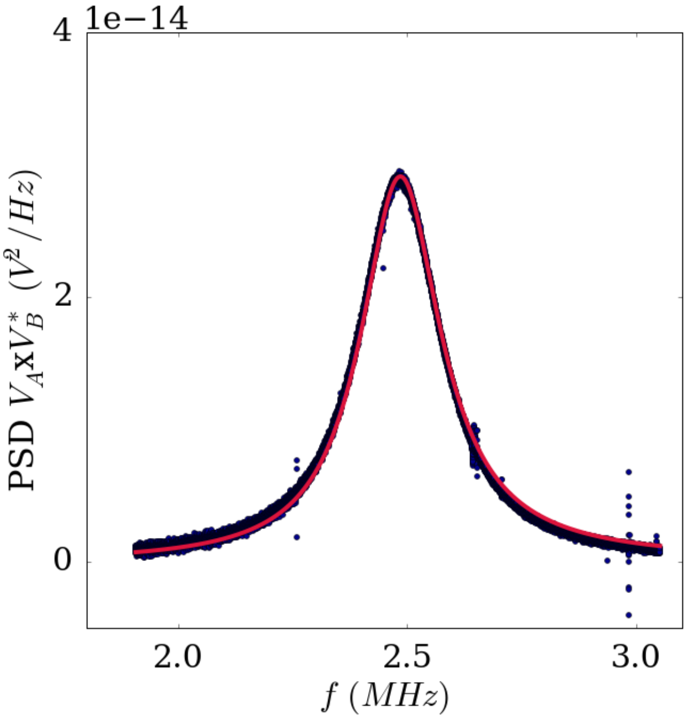

FIGURE 5.9 – **Cross-correlated power spectral density.** The PDS is realized at ν=3 for $V_{ds} = 100\mu V$ at D=0.9, averaging during 40 mn (blue dots). The equilibrium spectrum ($V_{ds} = 0$) is removed. The red curve is a fit using formula 5.13. We find $f_0 = 2.48\ MHz$, $A(V_{ds}) = 2.91\ 10^{-14}\ V^2/Hz$ and $\Delta_r = 213\ kHz$.

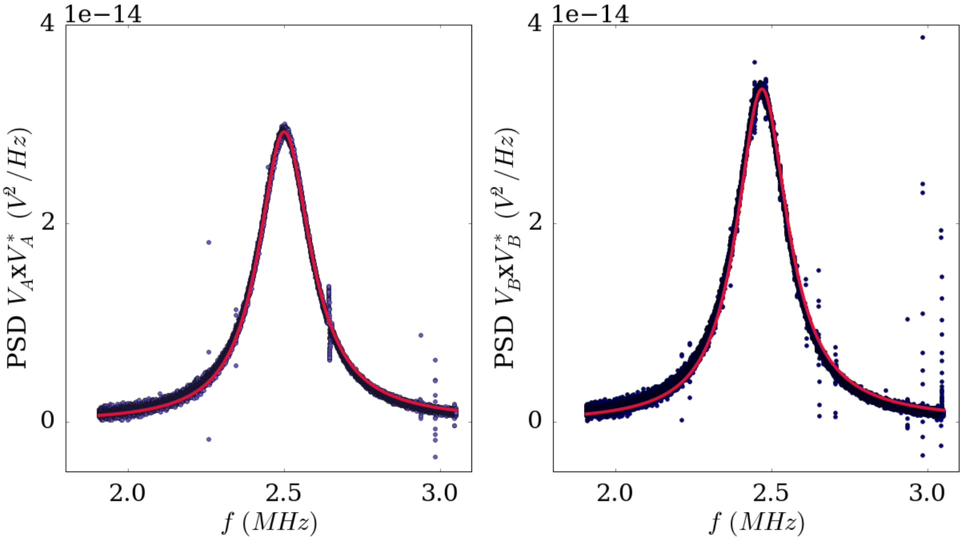

FIGURE 5.10 – **Auto-correlated power spectral densities.** PSD for Shot Noise measurement at ν=3 for $V_{ds} = 100\mu V$ and D=0.9, averaged during 40 mn. Left figure corresponds to the auto-correlated PSD for measurement line A, left figure for measurement line B. Once again the equilibrium spectrum is removed. We find $f_0^A = 2.5\ MHz$ and $\Delta_r^A = 204\ kHz$. For line B : $f_0^B = 2.47\ MHz$, $\Delta_r^B = 199\ kHz$

Which corresponds to a white noise filtered by a RLC resonator at resonant frequency

f_0 (see equation 5.3) and half power bandwidth Δ_r as proposed in [21]. Those values are expected to be the same for different bias voltage and gate voltage, which is experimentally verified. From f_0 we find C_l = 187 pF.

We can also extract information from auto-correlation power spectral densities (figure 5.10). Resonant frequency are found slightly different on A and B lines because of the difference in the capacitor lines (184 pF for line A and 189 pF for line B). Nevertheless, this difference is low enough so that the imaginary part of the cross-correlated spectrum is zero and only the real part of the cross-correlated PSD will be considered.

5.5 System performances

5.5.1 Integration time

Figure 5.11 shows a measurement of voltage noise using auto-correlation as a function of time realized during one hour. Blue dots corresponds to an integration time of τ=6 s and orange dots to an integration time of τ=120 s.

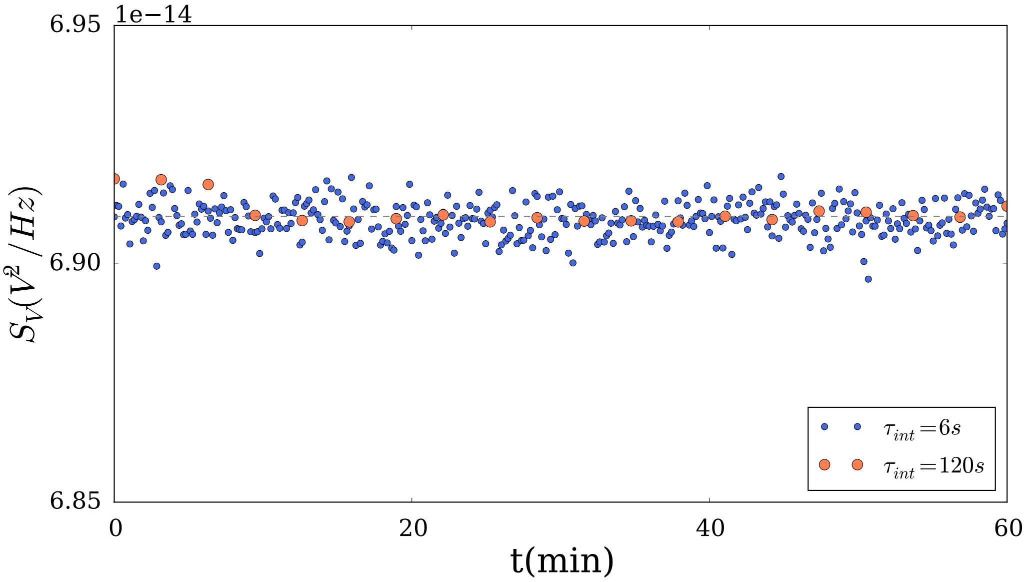

FIGURE 5.11 – **Voltage noise as a function of time for different integration times.** The QPC was completely pinched off at $\nu = 3$ with $V_{ds} = 0\ V$. Noise using auto-correlation is measured as a function of time for different integration times. Blue dots correspond to τ_{int}=6 s while orange dots to τ_{int}=120 s. For the orange dotted curve, a jump in the background noise can clearly be seen at 10 mn of measurement.

We noticed jumps of the noise level for the orange dotted curve (at t≈10 mn). Those jumps are believed to happen because of a bi-stability of the HEMTs gain. It typically happens once a day. To minimize such effect, the integration time τ was decreased while the total number of curve realized N_{av} was increased, keeping the measurement time $\tau.N_{av}$ constant. As a result, if a jump happens during the measurement, the effect will be reduced by the high number of averages. Moreover, the accuracy obtained for the long integration time and the short integration time is the same over the same measurement time. Note that cross-correlation are less sensitive to gain jumps as the large HEMT background noise is suppressed in the cross-correlation information (see section 5.13).

5.5.2 Noise accuracy

The input noise of the amplifiers is at 2 MHz of 220 pV/$\sqrt{Hz}$. At ν=2/5, we expect to measure noise through a total impedance of $\approx$ 15 kΩ, however because of r_c the inner resistance of the inductance the total impedance is reduced at 4 kΩ. Hence the expected current noise is 3 10^{-27} A^2/Hz. We average during 6 s over an effective bandwidth of 210 kHz. We can reach an accuracy of 2.7 10^{-30} A^2/Hz, 10 times lower than for the previous set-up. We typically measure over the night ($\approx$ 9 hours) for the electromagnetic environment is more stable. Taking 50 points for a shot noise measurement we can average over $N_{av} = 100$. Hence, a sensitivity of $\sigma/\sqrt{N_{av}} = 2.7\ 10^{-31}$ A^2/Hz can be reached.

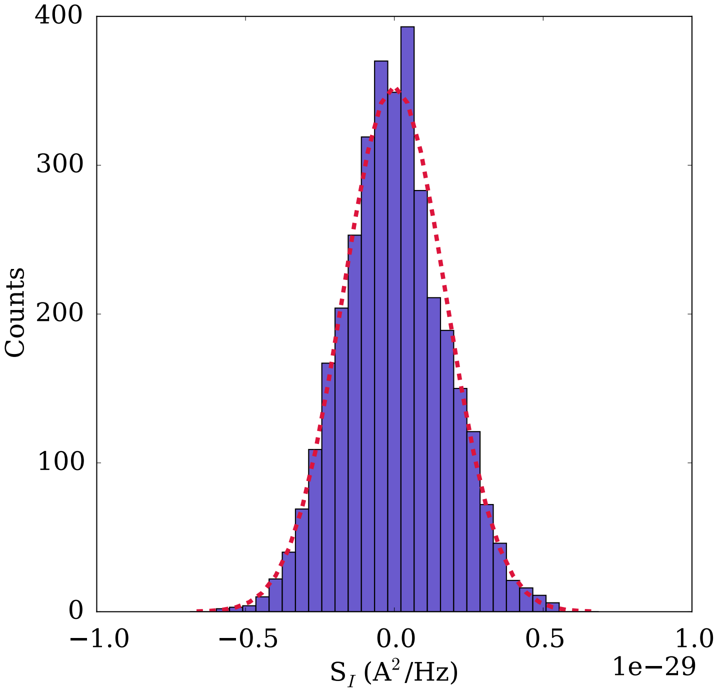

FIGURE 5.12 – **Probability distribution of data.** Blue rectangles are the histogram of a noise measurement, averaged over 31 points during 111 times 15 s each. The red line is a normal distribution calculated using the standard deviation found for the measurement.

For PASN experiment, measurements are done using the ON-OFF procedure. This takes twice as much time and the σ is multiplied by $\sqrt{2}$. So a good PASN measurement is done in one day with an accuracy of 3.8 10^{-31} A^2/Hz.

Figure 5.12 is the measurement histogram. It corresponds to a Shot Noise measurement as a function of bias voltage with 31 points in bias. Each point is averaged τ=15 s because the conductance is simultaneously measured, and the measurement is repeated N_{av}=111 times. The sensitivity reached is of σ=1.63 10^{-31} A^2/Hz. The red line corresponds to a normal distribution with standard deviation found for the measurement.

5.6 Cross-correlation versus Autocorrelation

This set-up allows to measure simultaneously auto-correlated and cross-correlated PSD of current fluctuations. The cross-correlation technique exposed in [33] has the advantage to remove from the measured signal all uncorrelated noises, for example, the thermal noise or noise coming from the amplifiers. Nevertheless, the partition noise is expected to be the same using auto- or cross-correlation. An extra thermal noise term from the reservoir is included in the auto-correlation but absent in the cross-correlation as reservoirs are not correlated in the QHE (see Annexe C).

As the incoming current on contact (0) is noiseless, for the shot noise only we have :

$$< \delta i_B^2 >=< \delta i_T^2 >= - < \delta i_B \delta i_T > \tag{5.14}$$

Where δi_T are the fluctuations of the transmitted current, measured through contact (1) and δi_B the fluctuations of the backscattered current measured through contact (4).

An example of shot noise measurement while exciting contact (0) with a DC voltage at filling factor $\nu = 3$ is shown in figure 5.13. The thermal contribution is seen for auto-correlation measurement as an offset while the shot noise is the only noise component that evolves with the bias voltage. Once the thermal offset is subtracted from the measurement, the evolution as a function of V_{ds} are the same whatever the method used.

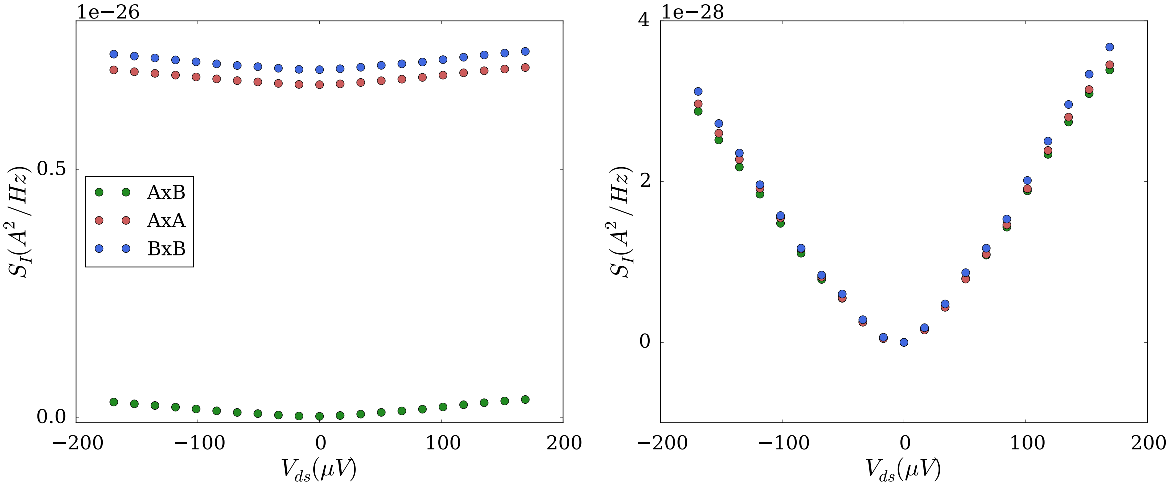

FIGURE 5.13 – **Comparison of DCSN using auto- and cross-correlated PSD.** The measurement is done at filling factor $\nu = 3$ for a transmission of D = 0.9. *Left :* "raw" current noise measurements. In green is the measurement using cross-correlation while blue and red are the measurement using auto-correlation. Those are not 0 for $V_{ds} = 0$ because of the thermal noise of the cryo-amplifiers and resonators whereas the cross-correlation goes to 0. *Right :* Measurement with the value for $V_{ds} = 0$ subtracted. The evolution as a function of the bias voltage is the same for all the measurements.

Chapter 6

PASN measurement and determination of fractional Josephson frequency

In this chapter is reported the first study of the effect of a time-dependent voltage on fractional charge in the Quantum Hall effect. Indeed, even though photo-assisted processes have already been observed for strongly correlated systems, namely a normal metal - supraconductor junction, on can wonder if those processes are still valid in the FQHE.

The Josephson frequency of fractional charge is a good tool to realize such study as it is expected to scale with the fractional charge e* but also with the excitation frequency *f*.

This chapter is organized as follows : first the state $\nu_b = 2/5$, which allows to probe two different fractional charges by only changing the gate voltage, is presented. Then, the data analysis method is presented on an example where charges e/3 are probed and the fractional Josephson frequency associated is extracted. More measurement and the comparison with the theoretical expectation is exposed. Finally, the origin of an offset in the PASN measurement is discussed.

6.1 The Jain state 2/5

Let us first described the Jain state $\nu = 2/5$ at which most of the measurements have been done. This state is observed at around 11 T for our sample as seen on figure 5.8. While measuring the conductance through the QPC, two plateaus were observed (see figure 6.1).

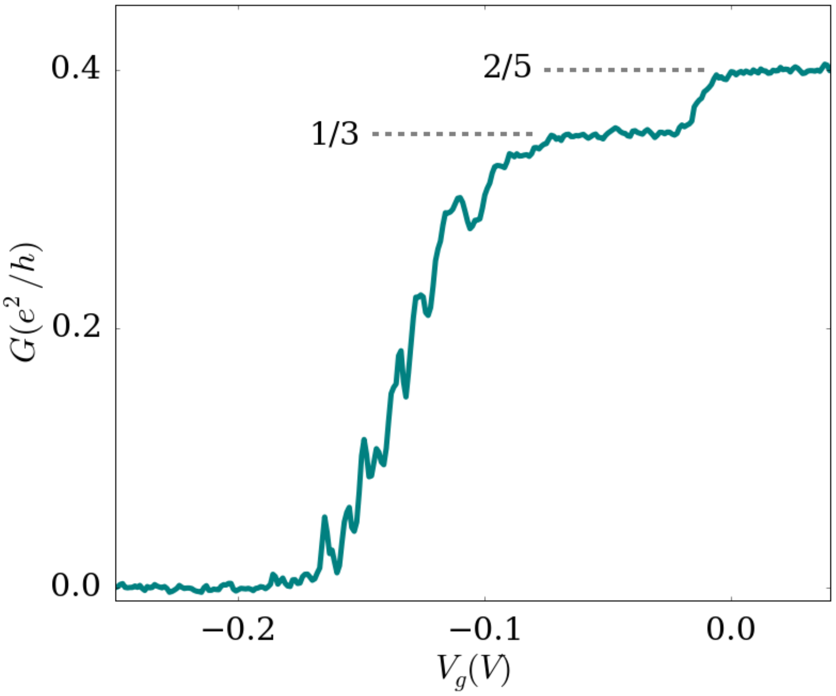

FIGURE 6.1 – **Transmission coefficient through the QPC at $\nu_b = 2/5$.** Conductance of the sample as a function of the gate voltage at B = 11.2 T. Two plateaus appear, one at 2/5 of e^2/h and the other at 1/3 of e^2/h. The measurement is performed at base temperature (~ 30 mK) for a bias voltage $V_{ds} = 0$.

A first plateau is at 2/5 of e^2/h and the second at 1/3 of e^2/h. Indeed, by changing the gate voltage, the electron density is locally changed until a local fractional state at filling factor 1/3 is obtained. The bulk filling factor is denoted ν_b (here always equal to 2/5) while the filling factor at the QPC is ν_{QPC} (2/5 or 1/3).

The picture in terms of edge channels for this state is represented on figure 6.2. We consider two co-propagating edge channels. For $V_g \in$ [-0.05,0.03] V the inner channel is partitioned while the outer channel is fully transmitted. For $V_g <$ -0.05 V, the inner channel is fully reflected while the outer channel is partitioned. Hence transmission and reflection coefficient, varying between 0 and and 1, for each channel can be defined. The conductance for each channel is written :

$$\begin{aligned} g_{1/3} &= \frac{1}{3}\frac{e^2}{h} \\ g_{2/5} &= \left(\frac{2}{5} - \frac{1}{3}\right)\frac{e^2}{h} \end{aligned} \tag{6.1}$$

Weak backscattering and strong backscattering limits for both channels can be defined. In the WBS regime of the 2/5 state charges of $e^* = e/5$ were measured [84] while in the WBS regime of the 1/3 state the fractional charge measured was $e^* = e/3$.

Performing measurements at this filling factor allows to probe the effect of the fractional charge on the Josephson frequency of the quasi-particle simply by changing the gate voltage which is more convenient than changing the magnetic field. In the following all the measurement are performed in the WBS regime of transmission for the considered channel.

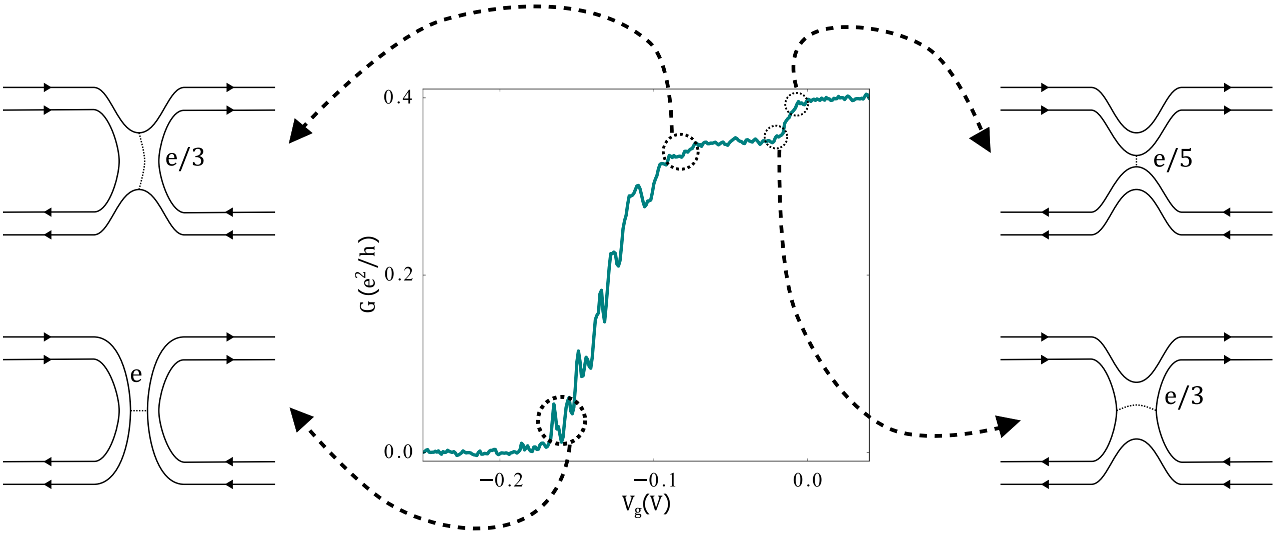

FIGURE 6.2 – **Edge states and fractional charge at $\nu = 2/5$.** Quasi-particle propagate along two co-propagating edge channels. Weak and strong backscattering regimes are defined and associated with a schematic picture of partitioning and the expected fractional charge probed in this limit.

6.2 PASN in the FQHE

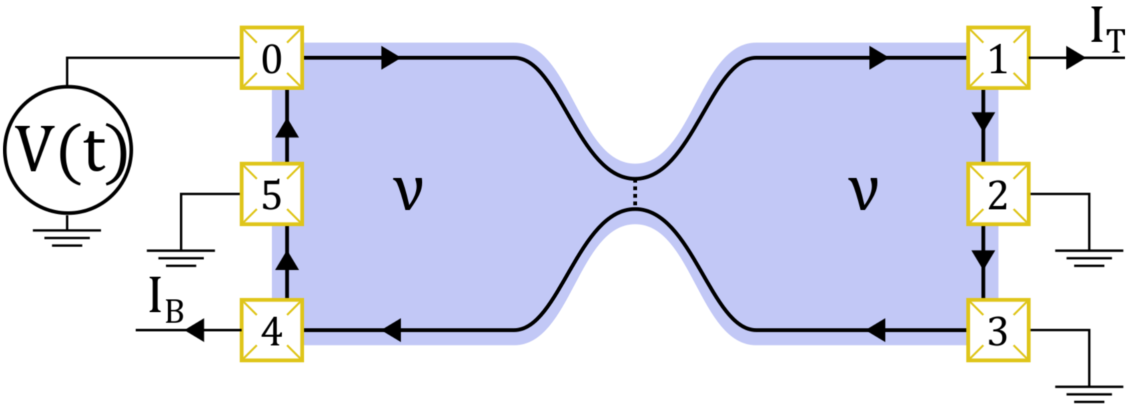

FIGURE 6.3 – **QPC excited with a time-dependent voltage.** The current is injected through contact (0) and measured through contacts (1) and (4).

Even though the FQHE is a strongly correlated system, photo-assisted processes are predicted as for non interacting system (see section 3.4). We report the observation of photo-assisted processes through the measurement of the Josephson frequency f_J of fractional charges when the conductor is irradiated at different frequency *f*. In the following are reported the results for different filling factor allowing to probe the effect of the fractional charge on f_J.

6.2.1 PASN measurements at 2/5

Here are presented the PASN measurements for a bulk filling factor $\nu_b = 2/5$. First, at $\nu_b = 2/5$ and $\nu_{QPC} = 2/5$, measurements are performed at a gate voltage of V$_g$ = - 0.09 V.

A DC bias voltage is applied on contact (0), leading to the injection of a current I$_0$ in the outer edge channel of the conductor :

$$I_0\left(V_{ds}\right) = \frac{1}{3}\frac{e^2}{h}V_{ds} \tag{6.2}$$

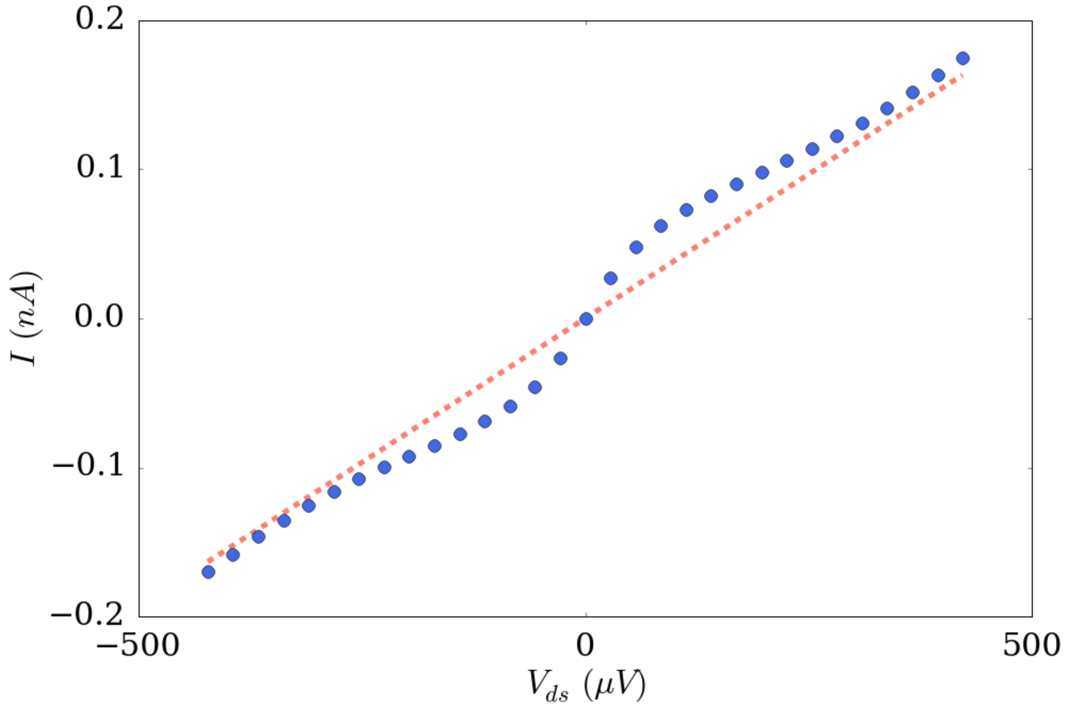

FIGURE 6.4 – **I-V characteristics at V$_g$ = -0.09 V, ν_b = 2/5 and ν_{QPC} = 1/3.** The blue points are the current calculated from the measured reflection coefficient. The orange line is the current calculated with a constant R = 0.026.

This incoming current on the outer channel is divided at the QPC in a backscattered I$_B$ = RI$_0$ and transmitted I$_T$ = I$_0$ - I$_B$ current while the inner channel remains unpartitioned. Because the edge channels in the FQHE form a Luttinger liquid, one expect the reflection coefficient to be energy-dependent. However in the very WBS regime, the evolution of R as a function of V$_{ds}$ is neglected and the backscattered current is :

$$I_B\left(V_{ds}\right)=\frac{1}{3}R\frac{e^2}{h}V_{ds} \tag{6.3}$$

With R the mean value of the reflection coefficient, here R = 0.026, corresponding to a WBS regime.

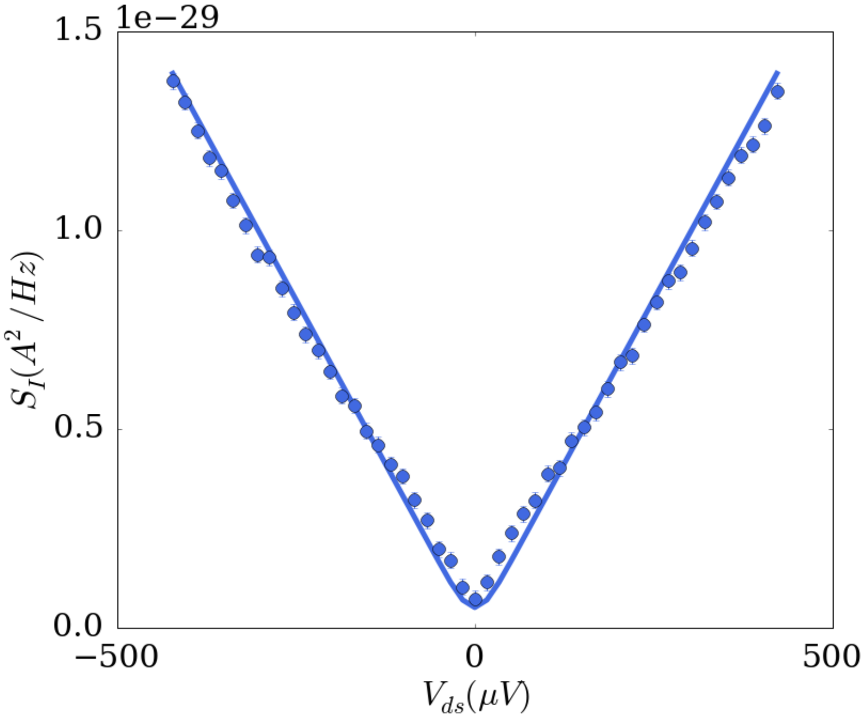

FIGURE 6.5 – **DCSN at V$_g$ = -0.09 V, ν_b = 2/5 and ν_{QPC} = 1/3.** DCSN at 11.2 T, in the WBS regime of the 1/3 FQH state. The full line is the shot noise at 30 mK with a reflection R = 0.026 and a fractional charge e* = e/3.

To justify this approximation, the comparison between the equation 6.3 and the backscattered current calculated while taking into account the energy dependence of R is done on figure 6.4. Apart from a deviation at low bias voltages the two curves are comparable. For simplicity the noise will then be shown as a function of the bias voltage V$_{ds}$ and compared with formula using the mean value R of the reflection coefficient.

Because measurements are performed in a very WBS regime, the DCSN is given by :

$$S_I^{dc}\left(V_{ds},T\right)=2e^*I_B\left(V_{ds}\right)\left(coth\left(\frac{e^*V_{ds}}{2k_BT}\right)-\frac{2k_BT}{e^*V_{ds}}\right) \tag{6.4}$$

On figure 6.5 is represented the experimental result for DCSN as a function of the bias voltage and compared with the expected shot noise of equation 6.4 with e* = e/3, using the mean reflection R defined above and the base temperature T = 30 mK, meaning that there are no fitting parameters. The experimental points are well described by the theory where the reflection is approximated constant over V$_{ds}$.

Then the time dependent voltage $V_{ac}\,cos\left(2\pi ft\right)$ is superimposed to the DC bias voltage in order to probe the Josephson frequency.

At fixed fractional charge (or V$_g$) one can vary the frequency f and the nominal RF power, corresponding to the amplitude V$_{ac}$. First, the frequency f is kept constant and the measurement is performed as a function of V$_{ds}$ at different fixed V$_{ac}$ amplitudes. For clarity, the shot noise measurements at different V$_{ac}$ are averaged (for the same V$_g$ and f).

We first present the shot noise measurements at $f = 10$ GHz, on the left figure 6.6 in light blue (the dark blue dots is the DCSN measurement). Does this measurement corresponds to a photo-assisted shot noise ?

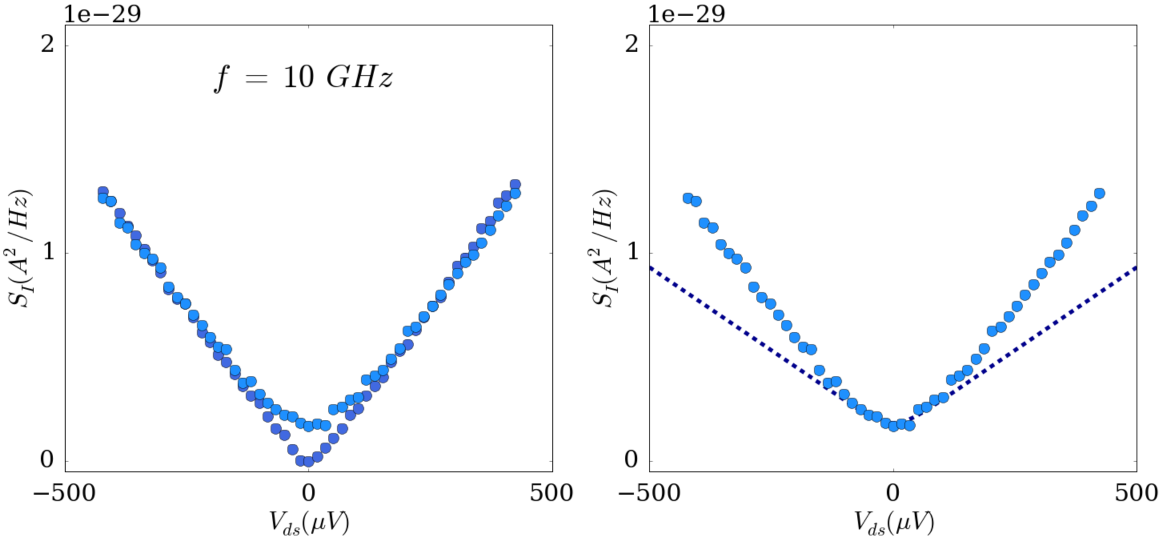

FIGURE 6.6 – **PASN at V$_g$ = -0.09 V, $\nu_b = 2/5$ and $\nu_{QPC} = 1/3$.** PASN at 11.2 T, in the WBS regime of the 1/3 FQH state. On the left figure are represented both the DCSN (dark blue) and PASN (light blue) at $f = 10$ GHz. On the left figure is the same PASN and the dotted line is the fit in the low bias voltage using the expression $|p_0|^2 S_I^{dc}(V_{ds})$.

As explained in section 3.4.3, the photo-assisted processes are highlighted by considering the excess noise defined as $\Delta S_I(V_{ds}) = S_I^{ac}(V_{ds}) - |p_0|^2 S_I^{dc}(V_{ds})$. It is expected to show a flat variation in the low bias voltage range.

As the actual AC amplitude is unknown because of the inner attenuation of the wires, the shot noise evolution as a function of V$_{ds}$ when V(t) is applied is fitted by $|p_0|^2 S_I^{dc}(V_{ds})$ in the low bias voltages, which is illustrated on right figure 6.6. The $S_I^{dc}(V_{ds})$ used is the actual independently measured DCSN and $|p_0|^2$ is a fitting parameter providing the RF amplitude as $|p_0|^2 = J_0(\alpha)^2$ with $\alpha = e^* V_{ac}/hf$. The fit in the low bias voltage range is plotted in dotted line on figure 6.6. Here as measurement at different fixed V$_{ac}$ are averaged, an average value $\langle |p_0|^2 \rangle$ is found. Moreover, as processes that involve more than 1 photon are neglected, the average value $\langle |p_0|^2 \rangle$ also provides the 1 photon processes as $\langle |p_1|^2 \rangle = (1 - \langle |p_0|^2 \rangle)/2$.

The next step for the data analysis is to remove from the shot noise measured with V(t) applied, the measured DCSN weighted by the amplitude probability $\langle |p_0|^2 \rangle$ previously found with the fit, providing the experimental excess noise.

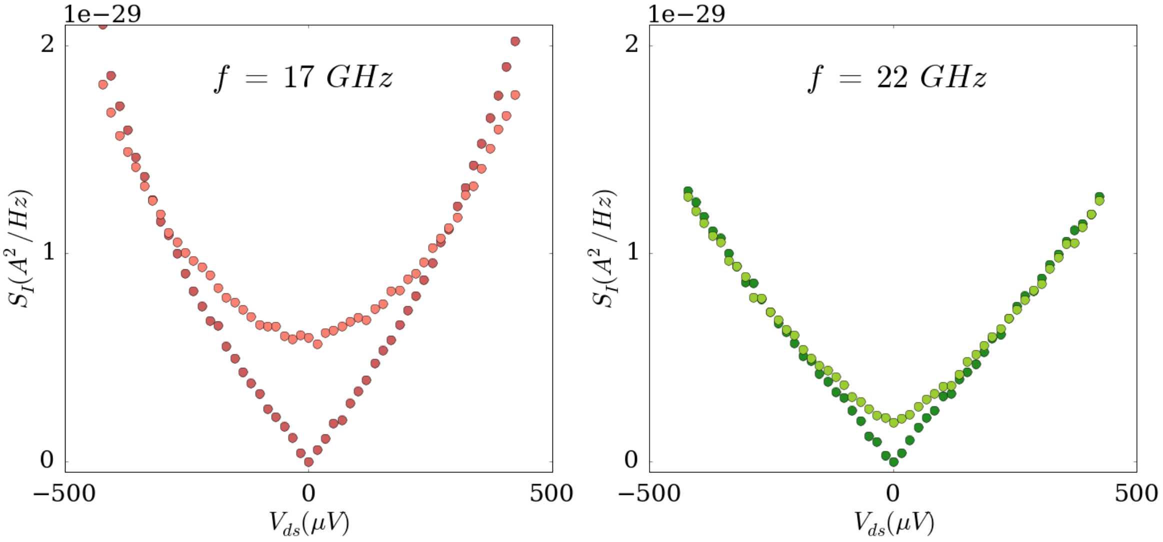

FIGURE 6.7 – **PASN at V_g = -0.09 V for ν_b = 2/5 and ν_{QPC} = 1/3.** The line is the expected excess PASN with $e^* = e/3$, $f_J = f$ and $\langle|p_0|^2\rangle$ minimizing the variation of the excess noise in the low bias voltage range. The red dots at 17 GHz and the blue ones at 22 GHz. The data are offseted for clarity

This measured excess noise is then to be compared with the PASN formula with $f_J = e^*V_{ds}/h$, with here $e^* = e/3$ and the frequency f at which the contact (0) is irradiated :

$$\Delta S_I^{ac}(f_J) = \left\langle|p_1|^2\right\rangle S_I^{dc}(f_J - f) + \left\langle|p_1|^2\right\rangle S_I^{dc}(f_J + f) \tag{6.5}$$

The amplitude probabilities are those determined from the fit at low bias voltage.

The excess noise is represented on figure 6.8 for the frequency f = 10 GHz. A good agreement between the experimental data and the expected excess PASN is found. First of all, we manage to observe a flat variation in the excess noise. Second and more remarkably, the threshold voltage beyond which the excess noise increases V_J is comparable to hf/e^*, within thermal rounding effect of k_BT/e^*, strongly supporting photo-assisted processes. To validate those processes one can in a first place change the exciting frequency f.

Then, similar measurements are realized for a frequency f = 17 GHz then f = 22 GHz and once again the different measurements at fixed V_{ac} for the same frequency are averaged.

Repeating the same steps as previously, a fit in the low bias range of the shot noise measured with V(t) applied is first realized. This fit provides the averaged amplitude probabilities $\langle|p_0|^2\rangle$ and $\langle|p_1|^2\rangle$.

The excess noise for f = 17 and 22 GHz is represented on figure 6.8. Once again a flat variation is found in the excess noise and the experimental data are well represented by the theoretical formula for photo-assisted processes with $e^* = e/3$ and photons at frequency f.

On can note that the DCSN measured during the 17 GHz set of measurement is slightly different from the others and that its evolution as a function of V_{ds} is not as linear as for

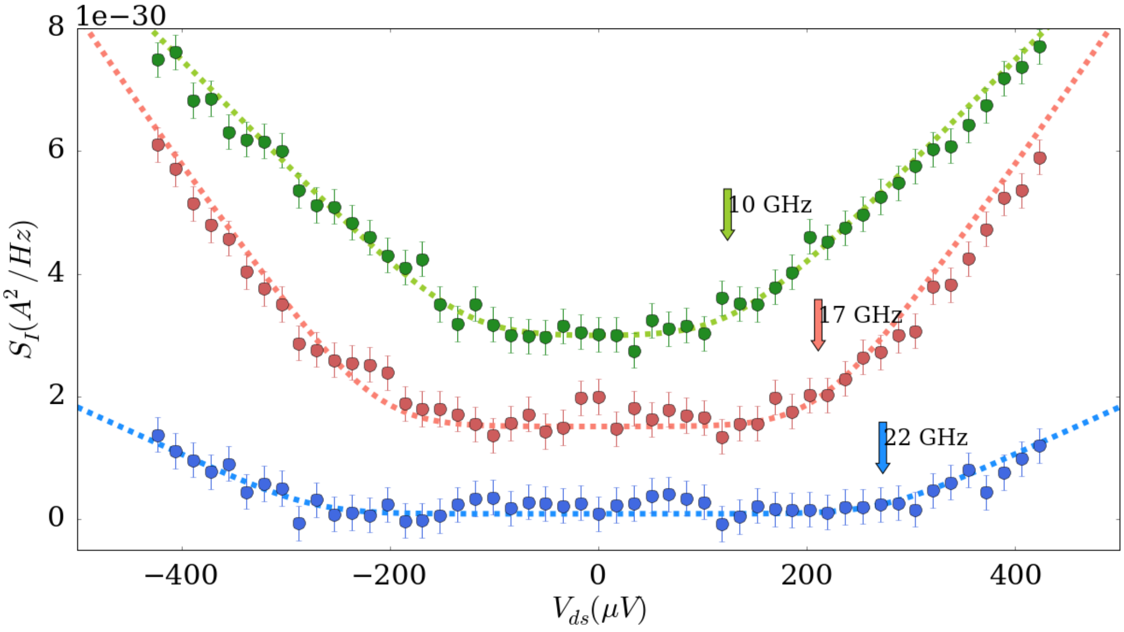

FIGURE 6.8 – **Excess PASN at V$_g$ = -0.09 V for $\nu_b = 2/5$ and $\nu_{QPC} = 1/3$.** The line is the expected excess PASN with e* = e/3, f$_J$ = f and $\langle|p_0|^2\rangle$ minimizing the variation of the excess noise in the low bias voltage range. The green dots are the measurements at 10 GHz and the red ones at 17 GHz and the blue ones at 22 GHz. The data are offseted for clarity

the 10 and 22 GHz measurements.

To probe the Josephson frequency, a linear fit of excess noise at large bias voltage is performed. This gives the threshold voltage which is converted into a Josephson frequency and compared to f on figure 6.9. For photo-assisted processes one expect this Josephson frequency to be strictly equal to the exciting frequency f.

The evolution of the threshold voltage with f strongly support the validity of equation 3.38.

Finally, coming back to the shot noise measurement when the conductor is excited with V(t) at frequency f, the data are compared to the theoretical PASN using the value of $\langle|p_l|^2\rangle$ with l = 0,1. It remarkably well represents the shot noise measurement which is represented in figure 6.10 for the three frequencies f tested.

To probe the measurement of the Josephson frequency one can now change the fractional charge. This is done by changing the gate voltage and switching to regions of backscattering where charges e* = e/5 are transferred.

Similar measurements are performed in the WBS regime of the 2/5 state at a gate voltage of V$_g$ = - 0.003 V. Now, the outer channel is fully transmitted while the inner channel is partitioned. The backscattered current determined using the measured reflection coefficient is compared with a constant R = 0.06.

On figure 6.11 are represented DCSN the measurements as a function of the bias voltage V$_{ds}$ and we can see that,once again, using a mean reflection coefficient can well

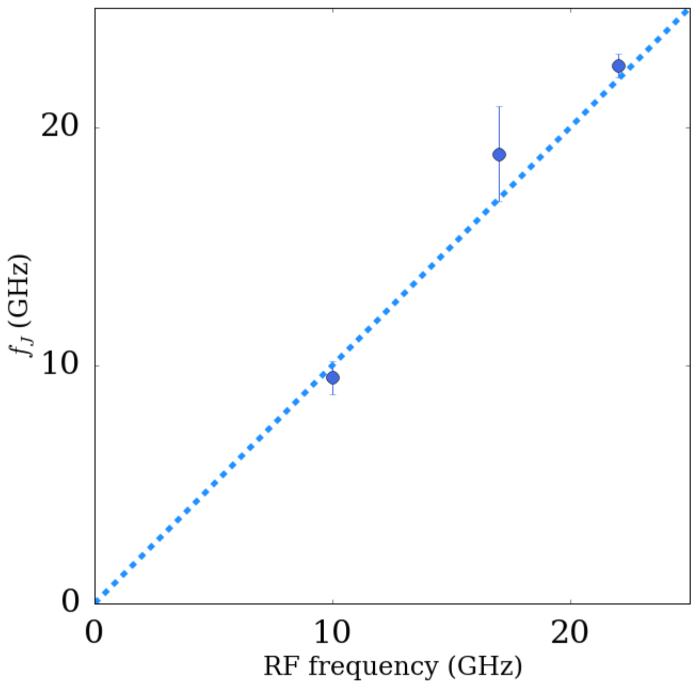

FIGURE 6.9 – **Josephson frequency of e/3 charges at $\nu_b = 2/5$ and $\nu_{QPC} = 1/3$.** The experimental point is extracted from the excess noise measurement by realizing a linear fit of the excess noise in the high voltage range leading to a determination of the threshold voltage. The line is plotted with the equation $f_J = f$ using $e^* = e/3$.

represented the data except for a small deviation at low bias voltage, as expected. However as this deviation is small, all measurements will be represented as a function of V_{ds}.

The time-dependent voltage is superimposed to the DC bias and the shot noise is measured as a function of V_{ds}. At fixed excitation frequency f, all measurements at different amplitude V_{ac} are averaged.

Then the fit of shot noise measurements at low bias provides a determination of $\langle|p_0|^2\rangle$ as well as the averaged amplitude probability for the 1 photon processes $\langle|p_1|^2\rangle$. Then the excitation frequency f is changed in order to probe the evolution of the threshold voltage with f. The excess noise at different f as well as the comparison with the theoretical excess noise is shown on figure 6.12.

A linear regression of the excess noise is the large bias voltage is done to probe the threshold voltage converted into Josephson frequency $f_J = e^* V_J/h$ and compared with the linear curve $f_J = f$ with $e^* = e/5$ (see figure 6.13). The evolution of measurement observed for different frequency f and fractional charge confirms that it is the Josephson frequency of the fractional charge that is measured.

Finally the shot noise measured with V(t) applied on the conductor is compared to the PASN formula with $e^* = e/5$ and the amplitude probabilities determined above.

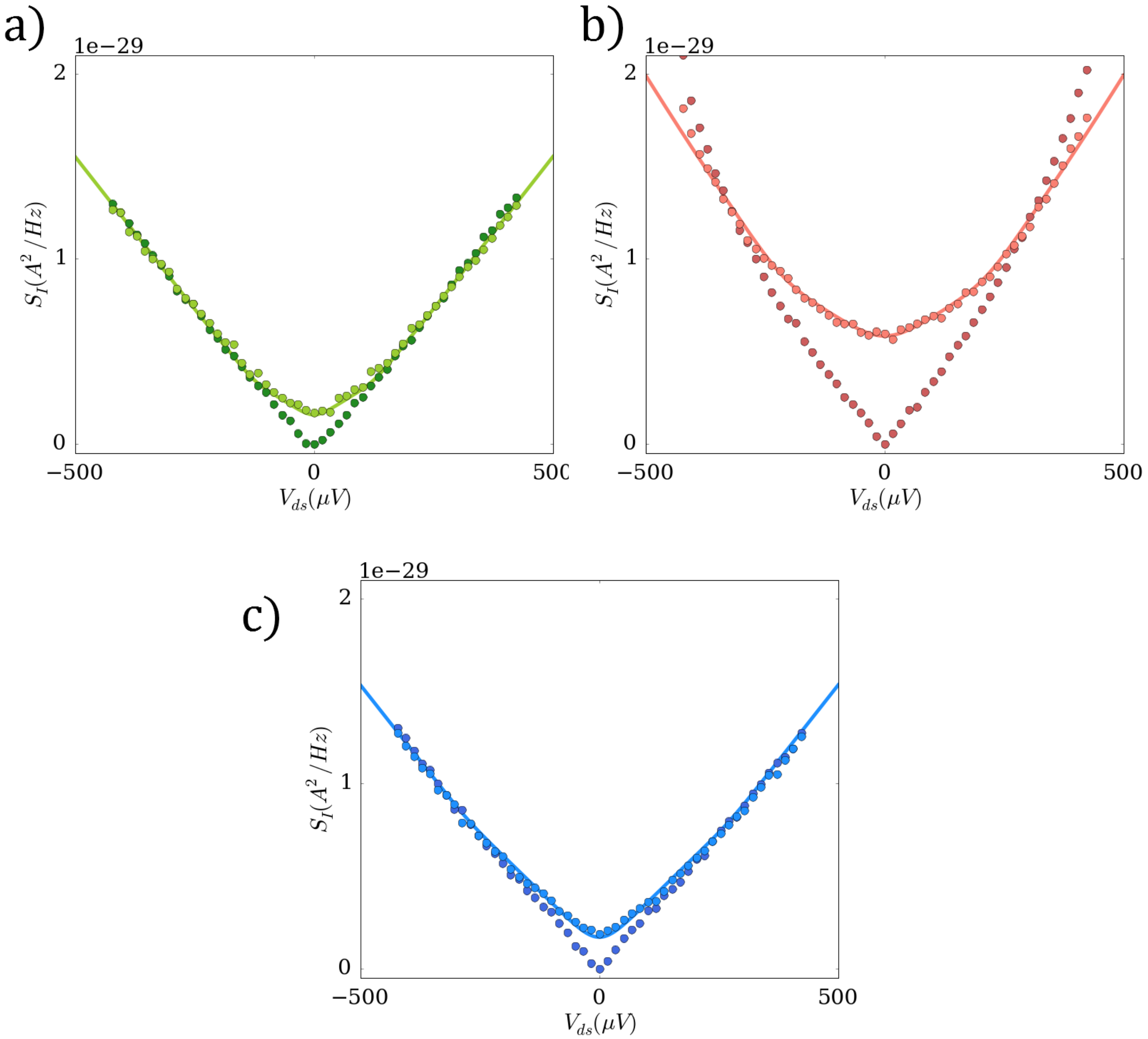

FIGURE 6.10 – **Shot noise measurement at V$_g$ = -0.09 V and theoretical PASN curve.** Shot noise realized when the conductor is excited with V(t) at 11.2 T, in the WBS regime of the 1/3 FQH state. The full line is the theoretical PASN with e* = e/3 and the averaged amplitude probability determined with a fit in the low bias voltage range of the PASN. *a)* f = 10 GHz *b)* f = 17 GHz *c)* f = 22 GHz.

6.2.2 Heating from RF

In all the theoretical curves above for photo-assisted processes, heating from the injection of RF has been taken into account. Indeed, removing the DCSN weighted by the amplitude probability $|p_0|^2$ does not fully cancel the variation of the excess noise in the low bias voltages. Small variations, different from a classical adiabatic averaging are observed in the form of a small bump around zero bias voltage (see figure 6.15). To fix this, the DCSN measured is not removed from the PASN but instead a theoretical curve with the temperature, denoted T$_{RF}$, as a parameter is subtracted. This gives an estimation of the heating due to the injection of RF.

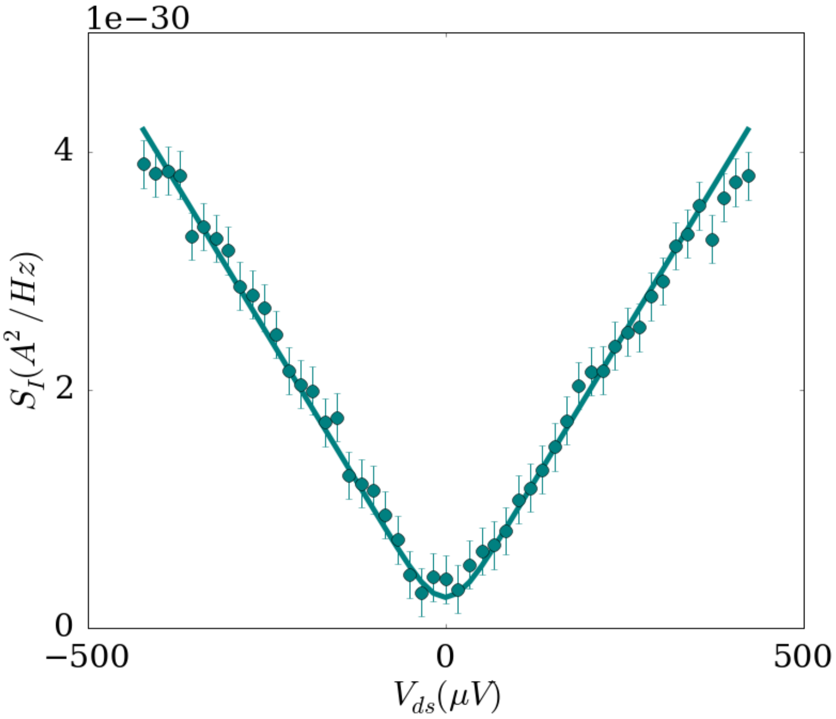

FIGURE 6.11 – **DCSN at V_g = -0.003 V for $\nu_b = \nu_{QPC}$ = 2/5.** The dots are the experimental datas at 11.2 T. The full line is the shot noise at 30 mK with a mean reflection R = 0.06 and a fractional charge $e^* = e/5$.

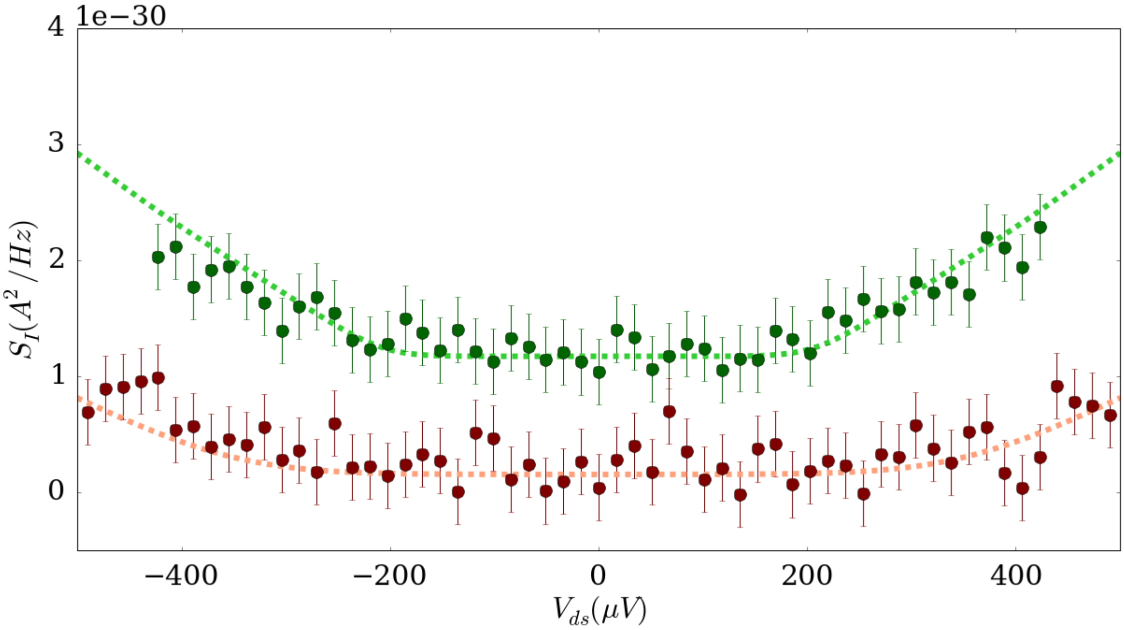

FIGURE 6.12 – **Excess PASN at V_g = -0.003 V for $\nu_b = \nu_{QPC}$ = 2/5.** The line is the expected excess PASN with $e^* = e/5$, $f_J = f$ and $\langle|p_0|^2\rangle$ minimizing the variation of the excess noise in the low bias voltage range. The green dots are the measurements at 10 GHz and the red ones at 17 GHz. The data are offseted for clarity

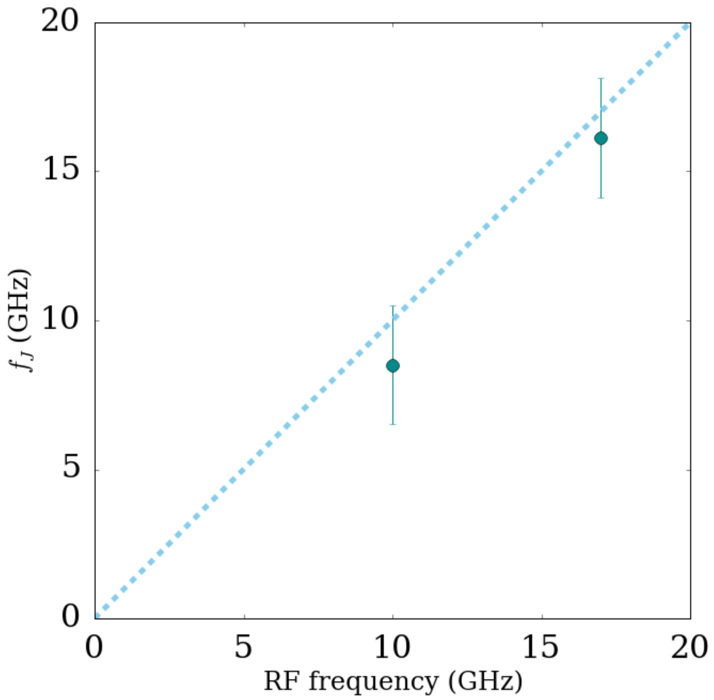

FIGURE 6.13 – **Josephson frequency of e/5 charges at $\nu = 2/5$.** The experimental point is extracted from the excess noise measurement by realizing a linear fit of the excess noise in the high voltage range leading to a determination of the threshold voltage. The line is plotted with the equation $f_J = f$ using $e^* = e/5$.

The excess noise is then written, taking the different temperatures into account :

$$\Delta S_I\left(V_{ds}\right) = S_I^{ac}\left(V_{ds}\right) - |p_0|^2 S_I^{dc}\left(V_{ds}, T_{RF}\right) \tag{6.6}$$

6.2.3 PASN at bulk filling factor 1/3

The density and mobility of the 2DEG used allow to probe other fractional filling factor such that the Laughlin state $\nu = 1/3$ at ~ 13 T. As previously, measurements are performed in the WBS regime. The reflection coefficient is kept almost constant as a function of the bias voltage V_{ds}. We measure the shot noise when contact (0) is only excited with a DC bias voltage (figure 6.17), which is well represented by the equation 6.4 using $e^* = e/3$ only in the low voltage bias range.

The time-dependent voltage at frequency $f = 22$ GHz is superimposed and the measurement is repeated at several AC amplitude and the average value is displayed here for clarity (figure 6.17).

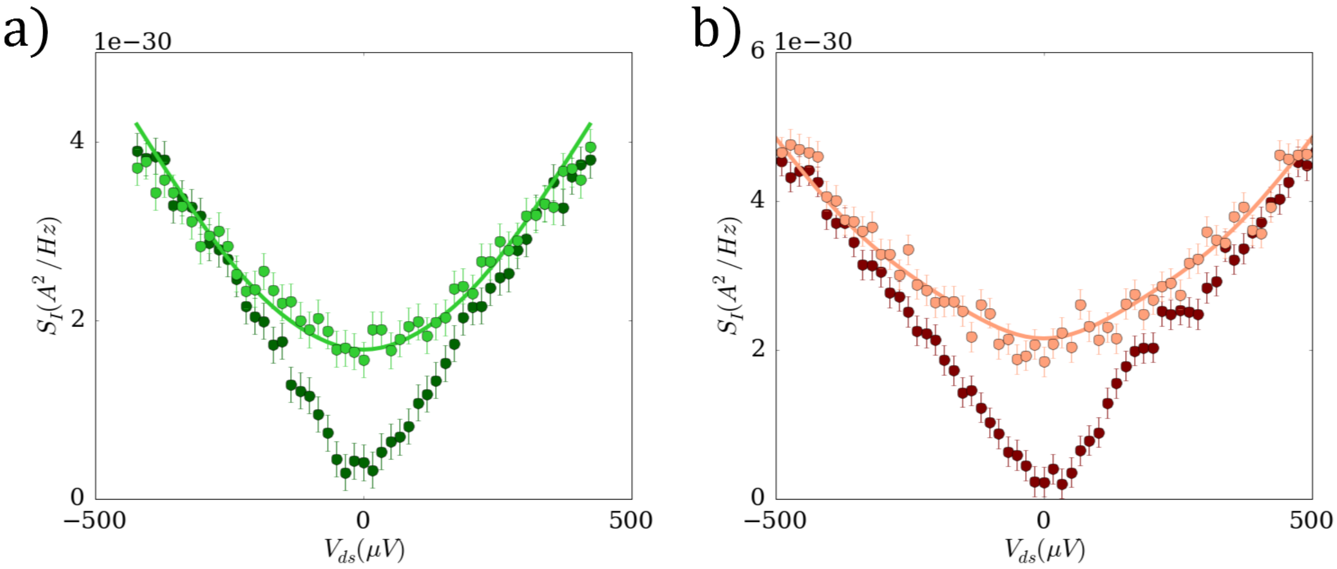

FIGURE 6.14 – **PASN at V_g = -0.003 V and theoretical curve.** PASN at 11.2 T, in the WBS regime of the 2/5 FQH state. The full line is the theoretical PASN with $e^* = e/5$ and the averaged amplitude probability determined with a fit in the low bias voltage range of the PASN. *a)* Measurement at $f = 10$ GHz. The dark dots are the DCSN simultaneously measured and the light green dots are the shot noise measurement when the time-dependent voltage is applied *b)* Measurement at $f = 17$ GHz.

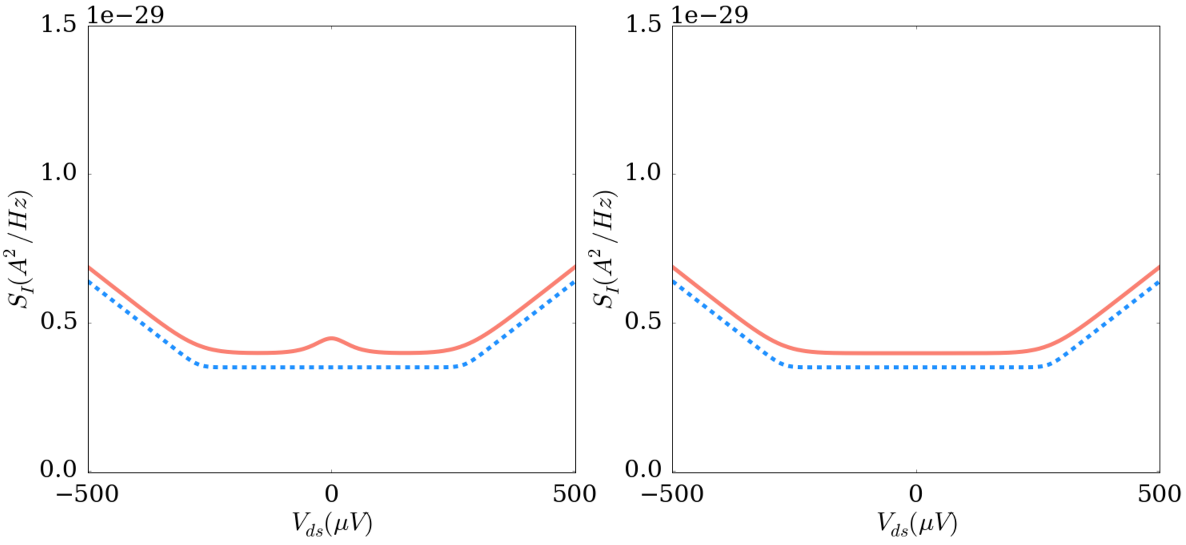

FIGURE 6.15 – **Excess PASN for different DCSN temperature.** The noises are plotted with $e^* = e/3$, $f = 22$ GHz and $V_{ac} = 270$ μV. On the left figure the blue dotted line is the excess noise without heating from the RF and the red full line is the excess noise when the DCSN removed from the PASN does not take into account heating. On the right figure, the heating has been taken into account and the excess noise is cancelled in the low bias range.

The averaged amplitude probability $\langle|p_0|^2\rangle$ is determined from a fit in the low bias voltage. It is then injected in the PASN formula using $e^* = e/3$ and compared to the

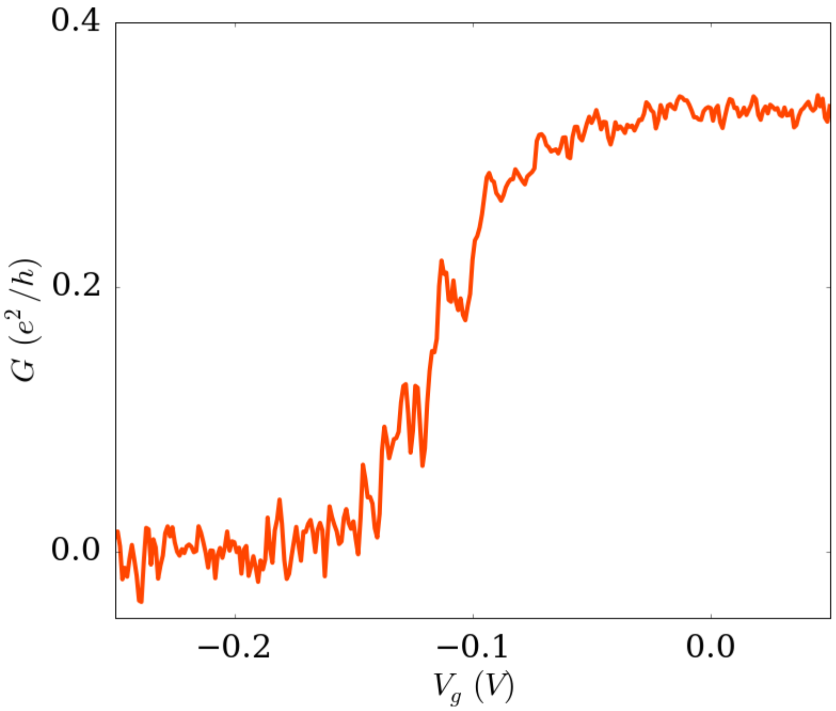

FIGURE 6.16 – **Transmission coefficient through the QPC at $\nu_b = 1/3$.** Conductance of the sample as a function of the gate voltage at B = 13 T. The measurement is performed at base temperature (∼ 30 mK) for a bias voltage V$_{ds}$ = 0.

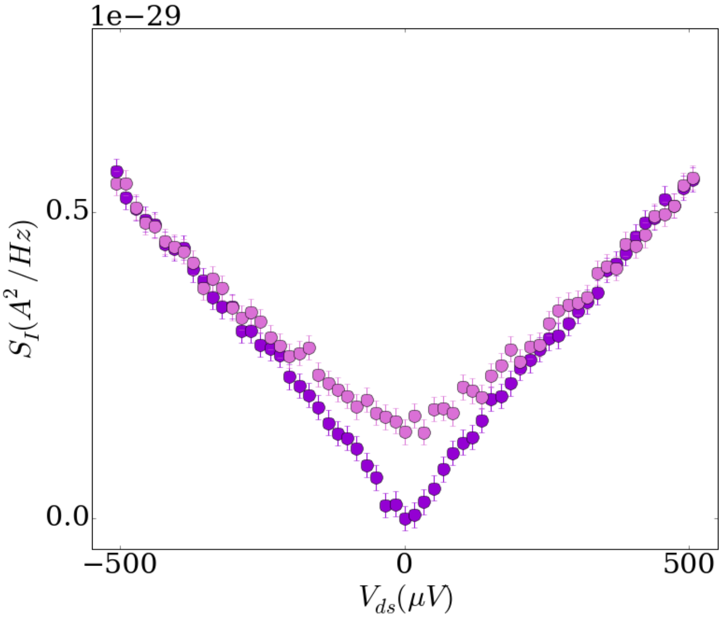

FIGURE 6.17 – **PASN at $\nu_b = 1/3$.** The violet points are the measurements when the QPC is excited with a DC bias voltage. The light violet ones are those when a time-dependent voltage at $f = 22$ GHz is superimposed to the DC voltage.

measured PASN from which the DCSN weighted by $\langle |p_0|^2 \rangle$ has been removed. A very

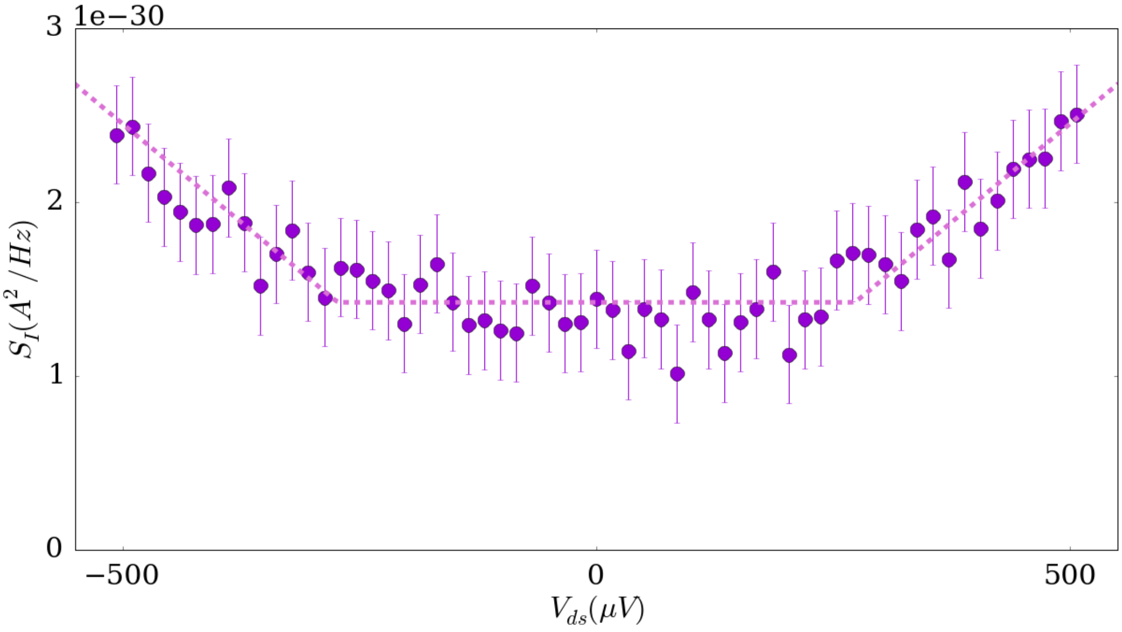

FIGURE 6.18 – **Excess PASN at $\nu_b = 1/3$.** The dots are the PASN measurements to which the DCSN weighted by $\langle |p_0|^2 \rangle$ found by a fit of the PASN in the low bias voltage range. The line is a comparison with the theory.

good agreement between the theoretical formula and the measurement is found.

6.3 Offset in PASN measurements

In the previous analysis, all data are offseted for clarity as to probe PA effects one only needs to study the evolution as a function of the bias voltage V$_{ds}$. However, unexpected behavior of the shot noise measured when the conductor is irradiated at frequency f has been observed for the bulk filling factor $\nu = 2/5$. Indeed, the noise measured when applying V(t) is clearly offseted compared to the noise measured with only V$_{ds}$, which is not contained in the theoretical formula. An example is shown on figure 6.19, corresponding to an important amplitude of excitation in order to highlight the phenomenon. This phenomenon is not observed at bulk filling factor $\nu = 1/3$.

The exact origin of this offset is unknown but do not appear to impede photo-assisted processes. Moreover, an heuristic law for the evolution of the offset as a function of the attenuation at fixed frequency f and fixed gate voltage can be estimated (see appendix F).

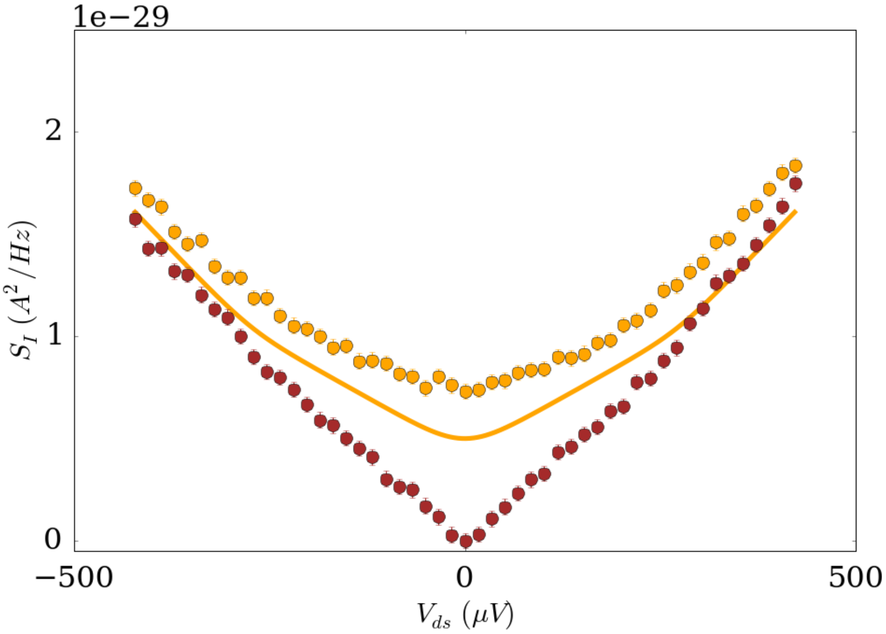

FIGURE 6.19 – **Evolution of the offset for PASN measurements at $\nu_b = 2/5$ and $\nu_{QPC} = 1/3$.** The red dots is the measured DCSN while the orange dots are the measured noise when irradiating the sample with a time-dependent voltage at $f = 22$ GHz with an amplitude V$_{ac} = 290$ μV. The full line is the expected PASN. The offset is defined as the difference between the noises is the high bias voltage range.

6.4 PASN as a function of the RF power

Similarly to what has been done in QPC when studying non-interacting regime, measurements as a function of the AC amplitude at fixed bias V$_{ds}$ and fixed frequency f is done.

In figure 6.20 are shown the measurements at $\nu_b = 2/5$ and $\nu_{QPC} = 1/3$ as a function of V$_{RF}$. This voltage is the one provided by the source which does not take into account the attenuation and it is directly proportional to the effective amplitude V$_{ac}$ seen by the sample. The proportionality factor only depends on the frequency f of excitation. The evolution of the PASN is not as expected (see figure 3.9), indeed, a quadratic behavior at low V$_{ac}$ or here, low V$_{RF}$ is expected. Instead the measurements starts linearly before becoming sub-linear [1]. One may wonder if this unexpected evolution is caused by the offset ? To answer that question, the offset as deduced using the equation F.1 is subtracted from the data using the A and x_0 parameters reported on table F.1. The result is shown on figure 6.21. We can clearly see that the only effect of this subtraction is to lower the amplitude of the noise but the general shape remains the same.

It is then interesting to do the same measurement at $\nu_b = 1/3$ where no offset in the PASN measurement have been observed. The PASN at V$_{ds} = 0$ and as a function of V$_{RF}$ is displayed on figure 6.22. However once again, the behavior of the noise is not as expected. This observed behavior shows that $|p_l\left(V_{ac}\right)|^2$ is not given by $J_l\left(e^* V_{ac}/hf\right)^2$.

---

[1] Which is also different from a linear evolution given by a classical averaging.

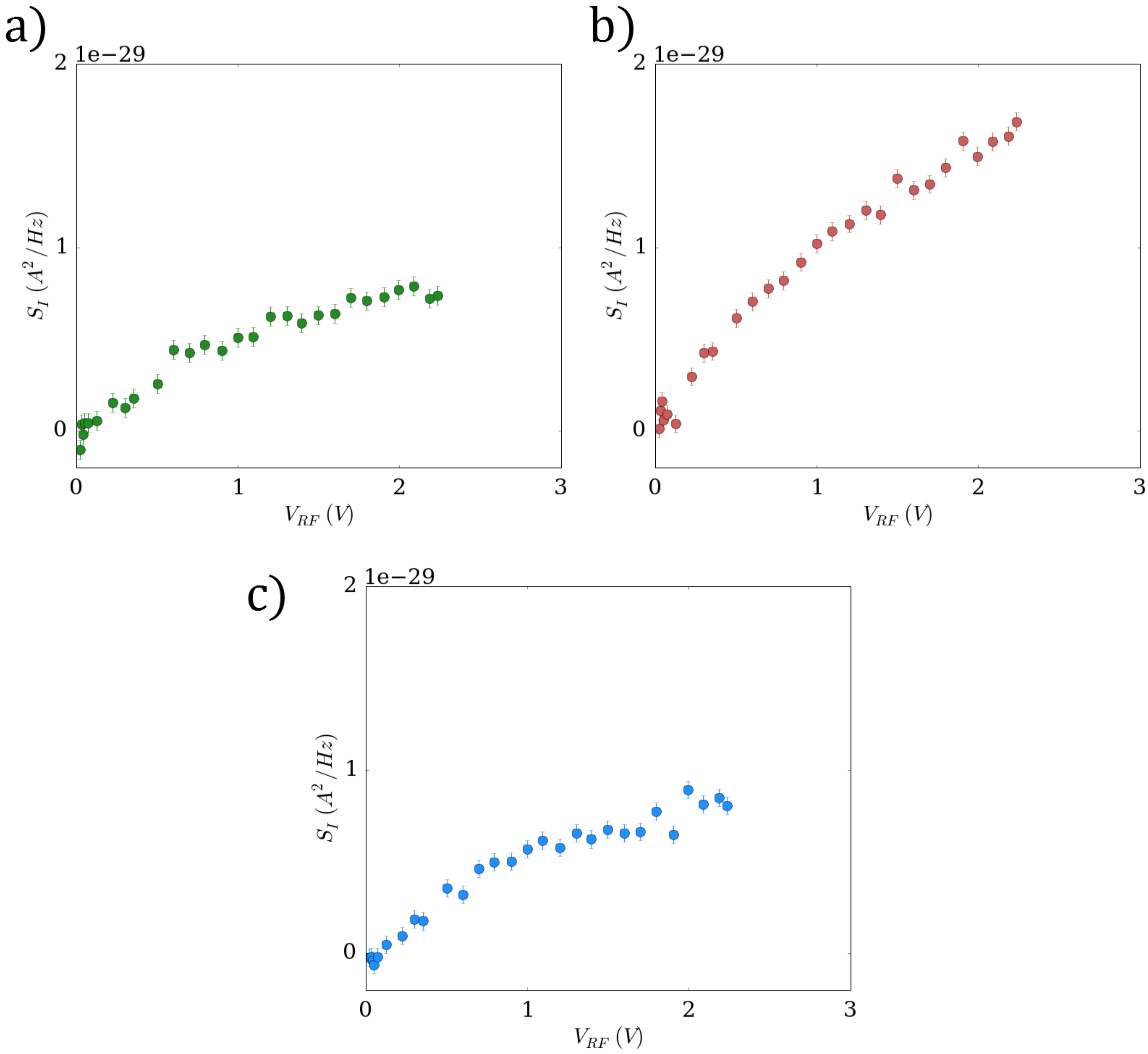

FIGURE 6.20 – **PASN as a function of V$_{ac}$ and V$_{ds}$ $= 0$ at $\nu_b = 2/5$ and $\nu_{QPC} = 1/3$.** The measurements are performed at 11.2 T and V$_g$ = -0.09 V. The color code is the same as for all other measurements : *a)* 10 GHz *b)* 17 GHz *c)* 22 GHz. All data are set at 0 for V$_{RF}$ = 0.

This expression assumes a uniform V$_{ac}$ in the leads while dynamical screening may occur, according to the non-linear Luttinger liquid response.

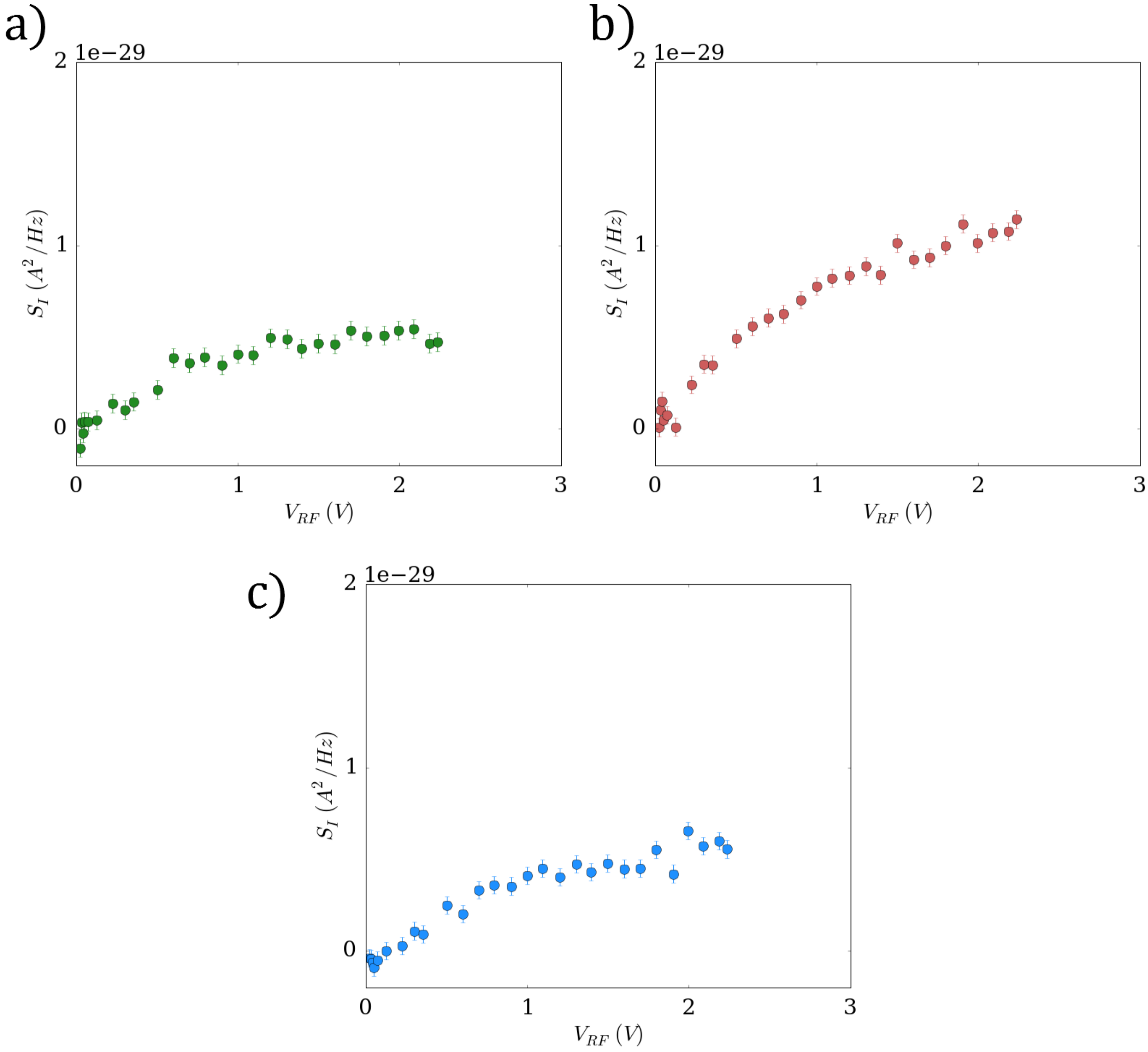

FIGURE 6.21 – **Subtraction of the offset for PASN as a function of V$_{ac}$ at $\nu_b = 2/5$ and $\nu_{QPC} = 1/3$.** *a)* 10 GHz *b)* 17 GHz *c)* 22 GHz.

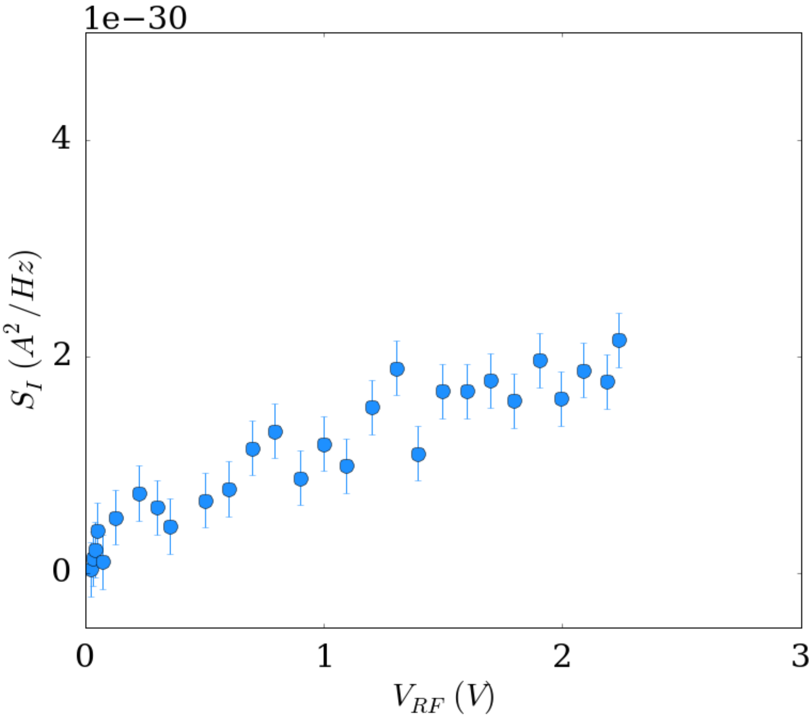

FIGURE 6.22 – **PASN as a function of V_{ac} and $V_{ds} = 0$ at $\nu_b = \nu_{QPC} = 1/3$.** The measurement is performed at V_g = -0.003 V and f = 22 GHz.

Chapter 7

Reliable fractional charge measurements using cross-correlation

This chapter focus on the comparison of Shot noise measurement using the two techniques presented previously : the auto-correlation and the cross-correlation. So far, only cross-correlated shot noise measurements have been presented. Two main reasons lead to this choice. The first one is that the cross-correlated shot noise only contains information about the correlated fluctuations of the transmitted and backscattered current hence about the partitioning occurring at the QPC. Moreover, the signal over noise ratio is expected to be better using cross-correlation and as current fluctuations measured are very small we look for the best accuracy. Giving that the evolution as a function of the bias voltage is expected to be the same using auto- and cross-correlated shot noise, this second technique was favored. However for certain FQH states an unexpected difference was observed.

In this chapter we first report the DCSN measurement in the FQHE at different fractional filling factors using auto- and cross-correlated shot noise. Then the evolution of the measurement as a function of the temperature and the transmission are reported. Then the PASN measurements using auto-correlations are presented and compared to the results presented in the previous chapter.

7.1 DCSN in the FQH regime

This section focuses on measurement when only a DC bias voltage is applied on the contact (0) of the sample.

7.1.1 Comparison Auto/Cross

Bulk filling factor 2/5 First are presented the results for $\nu_b = 2/5$. Figure 7.1 shows the shot noise measurement at a QPC filling factor of 1/3 in the WBS regime or V$_g$ = -0.09 V at 30 mK. Only a DC voltage V$_{ds}$ is applied on contact (0) of the QPC. The cross-correlation shot noise as a function of V$_{ds}$ is represented in blue. The auto-correlation denoted "A" in red corresponds to the fluctuations of the transmitted current while the one denoted "B" in green corresponds to the current fluctuations of the backscattered current.

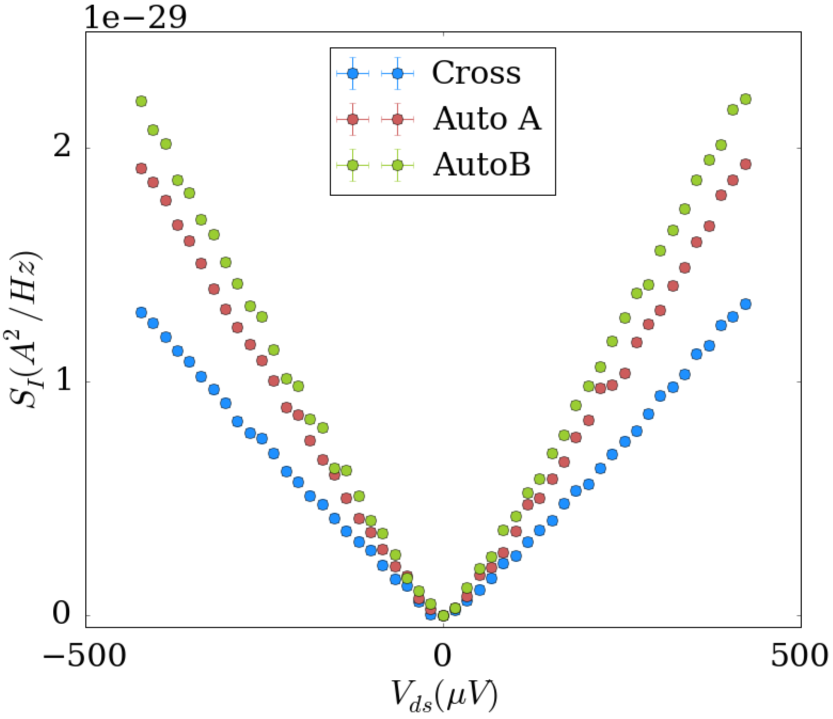

FIGURE 7.1 – **DCSN measurement in the WBS regime at $\nu_b = 2/5$ and $\nu_{QPC} = 1/3$ using auto and cross-correlation.** The blue dots represent the measurement using cross-correation while auto-correlations are in red (using fluctuations of the transmitted current) and green (using fluctuations of the backscattered current). All data are set to 0 at V$_{ds}$ = 0. The measurement is performed at 30 mK

Here, a striking and surprising result appears : the evolution of the shot noise as a function of the bias voltage is not the same if it is calculated using auto- or cross-correlation technique. The auto-correlations, which both have a comparable evolution, have an amplitude almost twice as large as the cross-correlation !

Three effective fractional charges can then be extracted using the equation 3.28. From the cross-correlated noise the effective charge is found to be $e^* = e/3$. Using the auto-correlations effective charges of the order of 2e/3 are found.

The same measurement is realized at $\nu_{QPC} = 2/5$ in the WBS regime or V_g = -0.003 V and at a temperature of 30 mK (see figure 7.2). Once again a large difference between auto- and cross-correlation is observed, even higher as there is here a factor 3 between auto- and cross (note that the color code is the same as the previous figure and will remain identical all along this section).

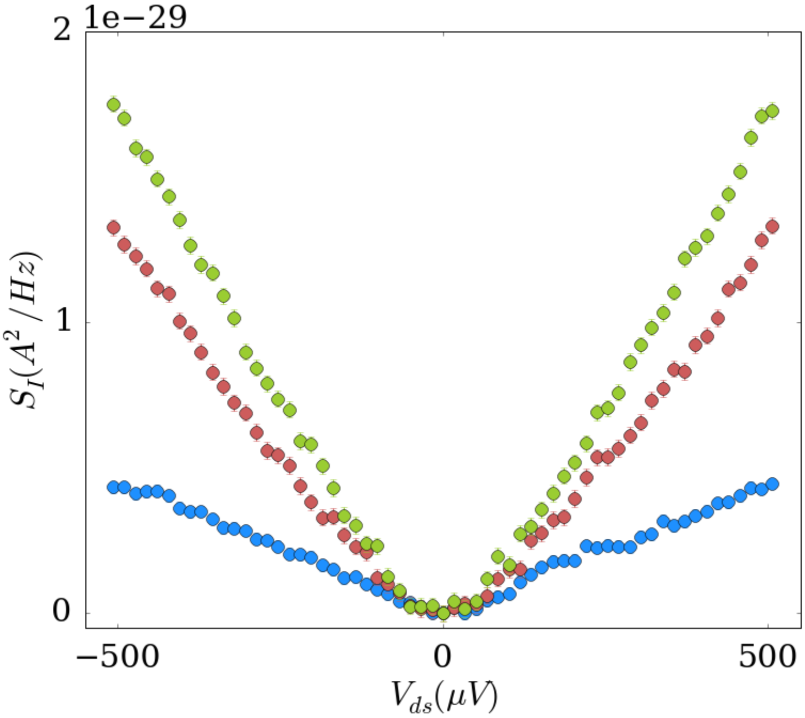

FIGURE 7.2 – **DCSN measurement in the WBS regime at $\nu_b = \nu_{QPC} = 2/5$ using auto and cross-correlation.** The blue dots represent the measurement using cross-correlation while auto-correlations are in red (using fluctuations of the transmitted current) and green (using fluctuations of the backscattered current). All data are set to 0 at $V_{ds} = 0$. The measurement is performed at 30 mK

Bulk filling factor 2/3 The same comparison is done at bulk filling factor of 2/3 in the WBS regime. Once again a difference in the evolutions as a function of V_{ds} is observed for cross- and auto-correlated shot noise (see figure 7.3) at 30 mK. From this measurement, the result presented in [4] is recovered, where the DCSN at $\nu = 2/3$ was measured using the auto-correlated shot noise in the WBS regime and effective charges of 2e/3 was found at very low temperature (T≈10 mK). The effect of the non-linear I-V characteristic[1] is seen here as indeed, the shot noise measured is not linear as a function of the bias voltage. In order to extract the effective charges, the noises are represented as a function of the

---

[1] See Appendix E for the I-V characteristic at $\nu = 2/3$.

backscattered current. At low temperature the effective charge deduced is of ≈ 0.5e using auto-correlations while for the cross-correlation an effective charge of 0.35e is found.

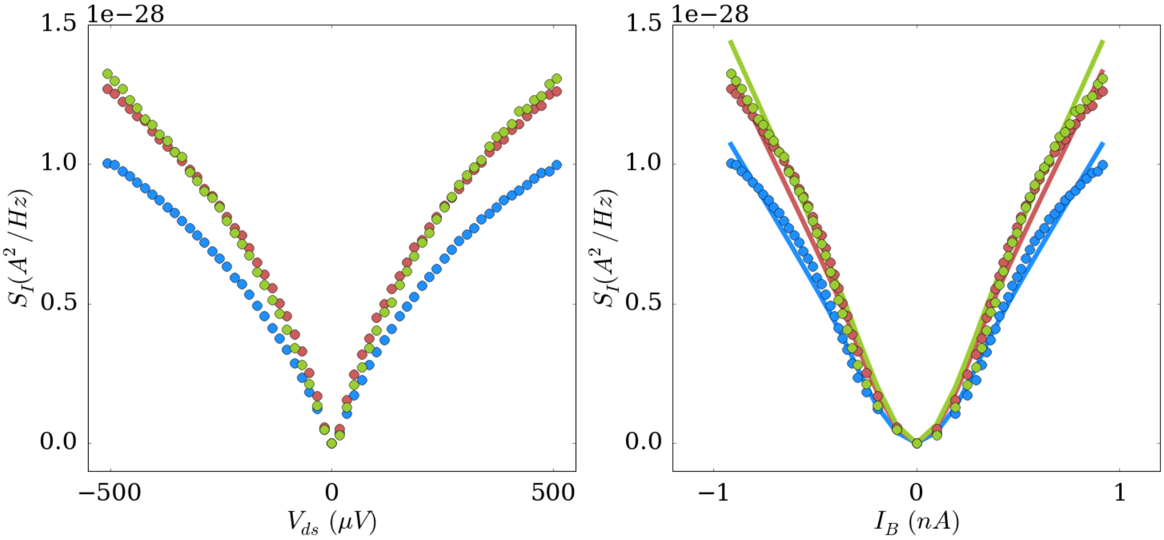

FIGURE 7.3 – **DCSN measurement at $\nu_b = \nu_{QPC} = 2/3$ using auto and cross-correlation.** The blue dots represent the measurement using cross-correlation while auto-correlations are in red (using fluctuations of the transmitted current) and green (using fluctuations of the backscattered current). All data are set to 0 at $V_{ds} = 0$. The measurement is performed at 30 mK. *Left* : DCSN as a function of the bias voltage. *Right* : DCSN as a function of the backscattered current.

Bulk filling factor 1/3 The filling factors 2/5 and 2/3 are in the Jain sequence and can host several edge channels, counter-propagating charged or neutral modes . . . The Laughlin state $\nu = 1/3$ is expected to host a single edge channel along which excitations propagate with a fractional charge $e^* = e/3$.

The comparison of auto- and cross-correlated shot noise is shown on figure 7.4 and we can see that the evolution as a function of V_{ds} is comparable for all the DCSN, similarly to what is found in the IQHE.

From those comparisons we can conclude that this difference in the evolution of the shot noise as a function of V_{ds} is not an experimental artefact but a physical result linked to the intricate physics of edge channels of some fractional quantum Hall states.

7.1.2 Evolution as a function of the temperature

The results obtained in terms of fractional charge, namely a fractional charge twice as large as expected at low temperature using auto-correlation, recall the previous measurements performed at the Weizmann institute [4, 15]. In those experiments an evolution of this fractional charge with the temperature was reported. Then we performed the DCSN measurement for $\nu = 2/5$ and $\nu = 1/3$ at higher temperature.

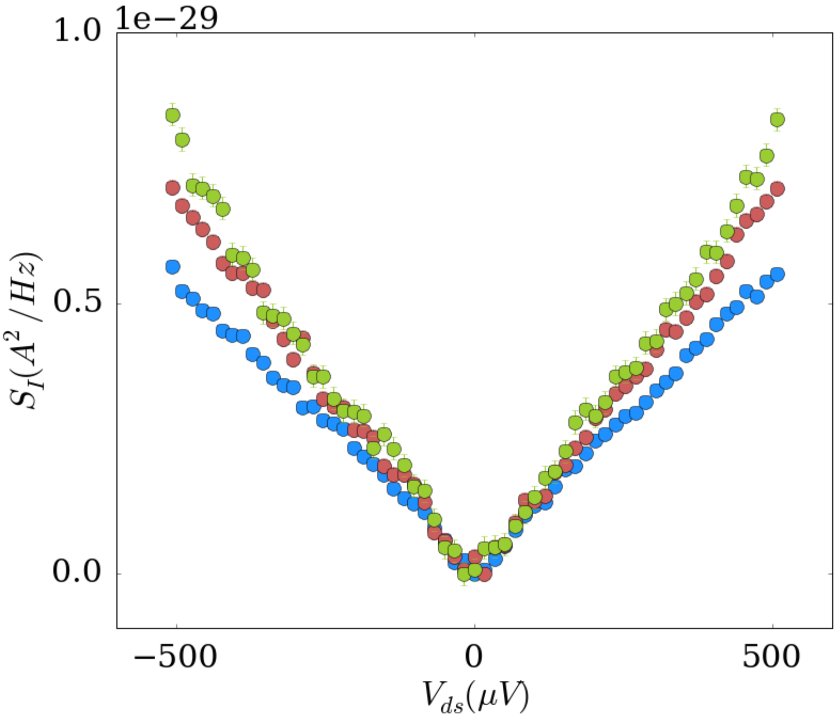

FIGURE 7.4 – **DCSN measurement at $\nu_b = 1/3$ using auto and cross-correlation.** The blue dots represent the measurement using cross-correlation while auto-correlations are in red (using fluctuations of the transmitted current) and green (using fluctuations of the backscattered current). All data are set to 0 at V$_{ds}$ = 0. The measurement is performed at 30 mK

Bulk filling factor 2/5 The DC shot noise measurement at V$_g$ = -0.09 V was repeated at 50, 70, 90 and 100 mK. The evolution of the auto- and cross-correlated shot noise are shown on figures 7.5 and 7.6. We can see the auto-correlated shot noise collapse on the cross-correlated shot noise while this one do not seem to evolve except for the thermal rounding around V$_{ds}$ = 0.

To confirm this observation, the curves are fitted using equation 3.28 with the fractional charge e* being a fitting parameter. In appendix E is reported the evolution of the backscattered current as a function of V$_{ds}$ with the temperature. There is a small change in the value of the mean reflection coefficient R that is taken into account in the data analysis.

The results are summarized on figure 7.7 where the evolution of the fitting parameter e* in units of the electron charge e as a function of the temperature is represented. The blue dots are the fractional charges found using the cross-correlation while the green and red dots are the fractional charges found using the fluctuations of respectively the backscattered and transmitted currents. The vertical doted line corresponds to e/3. While the fractional charge associated with the cross-correlation remains constant around 1/3 of the electron charge, the ones associated with the auto-correlation evolve with the temperature. At the lower temperature it is almost 2e/3 and drops towards e/3 for T ∼ 90 mK. At

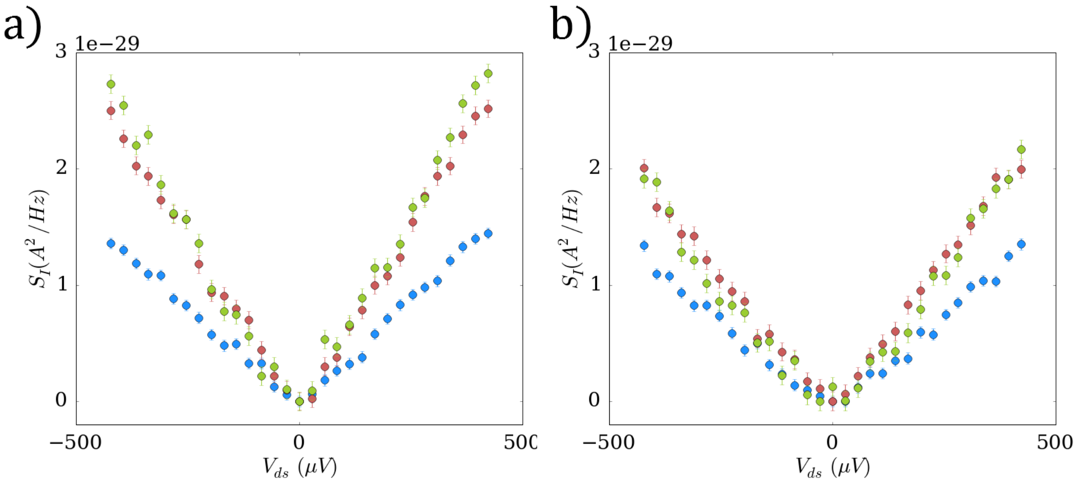

FIGURE 7.5 – **DCSN measurement at $\nu_b = 2/5$ and $\nu_{QPC} = 1/3$ using auto and cross-correlation.** All DCSN measurements are performed at V$_g$ = -0.09 V and datas are set to 0 at V$_{ds}$ = 0. The blue dots are the DCSN using the cross-correlation of current fluctuations, the red the auto-correlation of fluctuations transmitted currents and the green, the auto-correlation o fluctuations of backscattered current. *a)*Measurement at 50 mK. *b)*Measurement at 70 mK.

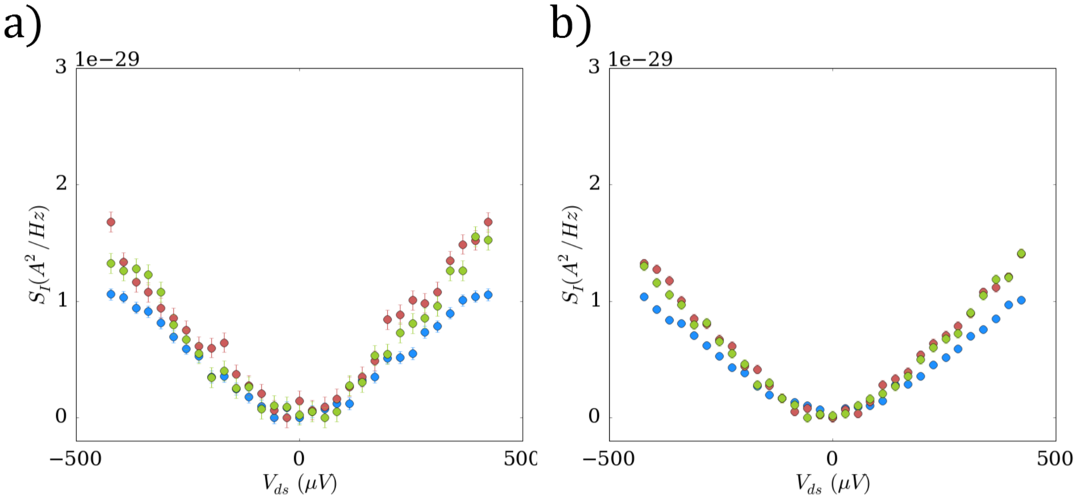

FIGURE 7.6 – **DCSN measurement at $\nu_b = 2/5$ and $\nu_{QPC} = 1/3$ using auto and cross-correlation.** All DCSN measurements are performed at V$_g$ = -0.09 V and data are set to 0 at V$_{ds}$ = 0. The blue dots are the DCSN using the cross-correlation of current fluctuations, the red the auto-correlation of fluctuations transmitted currents and the green, the auto-correlation o fluctuations of backscattered current. *a)*Measurement at 70 mK. *b)*Measurement at 100 mK.

low temperature we notice that the auto-correlation A is larger than the auto-correlation B. This hierarchy is exchanged at higher temperature.

Bulk filling factor 2/3 The same analysis was performed for the FQH state $\nu = 2/3$ and similar results were obtained. The comparison of the noises is reported on figure 7.8

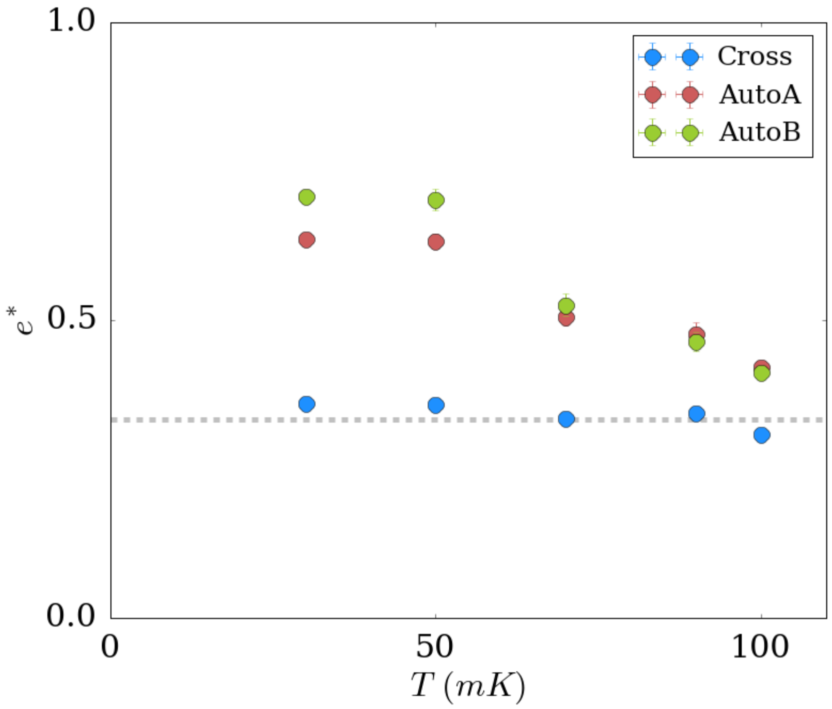

FIGURE 7.7 – **Evolution of the fractional charge as a function of the temperature at $\nu_b = 2/5$ and $\nu_{QPC} = 1/3$.** The horizontal doted line represents the value e* = e/3.

for 50 and 70 mK and on figure 7.9 for 90 and 100 mK. This time the fractional charge is extracted from equation 3.28 by taking into account the non linearity of the current. The backscattered current and its evolution with the temperature is reported in Appendix E.

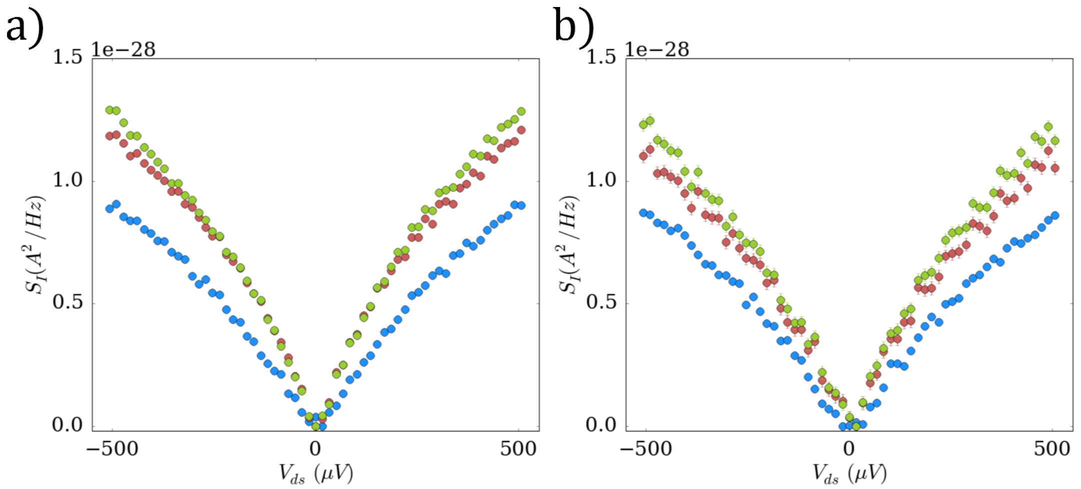

FIGURE 7.8 – **DCSN measurement at $\nu_b = \nu_{QPC} = 2/3$ using auto and cross-correlation.** All DCSN measurements are performed at V$_g$ = -0.165 V and datas are set to 0 at V$_{ds}$ = 0. The blue dots are the DCSN using the cross-correlation of current fluctuations, the red the auto-correlation of fluctuations transmitted currents and the green, the auto-correlation o fluctuations of backscattered current. *a)*Measurement at 50 mK. *b)*Measurement at 70 mK.

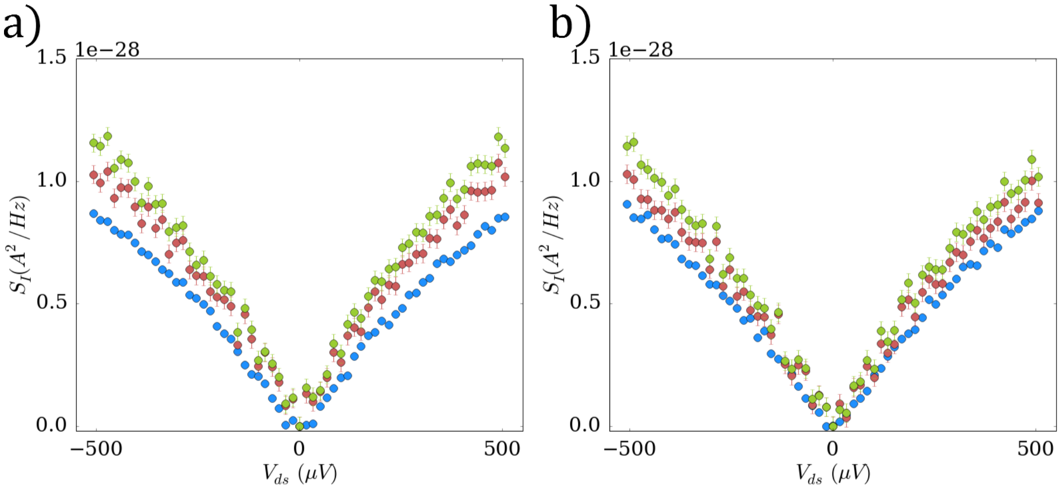

FIGURE 7.9 – **DCSN measurement at $\nu_b = \nu_{QPC} = 2/3$ using auto and cross-correlation.** All DCSN measurements are performed at V$_g$ = -0.165 V and data are set to 0 at V$_{ds}$ = 0. The blue dots are the DCSN using the cross-correlation of current fluctuations, the red the auto-correlation of fluctuations transmitted currents and the green, the auto-correlation o fluctuations of backscattered current. *a)*Measurement at 90 mK. *b)*Measurement at 100 mK.

On figure 7.10 is represented the evolution of the fractional found using auto- and cross-correlation as a function of the temperature. Similarly to the previous case, the fractional charge using cross-correlation shows almost no evolution with the temperature as opposed to the auto-correlations.

Finally we can note that at bulk filling factor 1/3, the DCSN using auto-correlation (and cross-correlation) was not found to evolve with the temperature (except for the thermal rounding).

7.1.3 Measure on plateaus

Another comparison that can be done is to look at the noise on plateaus, where no partitioning is expected, hence no shot noise. On figure 7.11 are represented those measurements in the FQH state $\nu = 2/5$. Looking back to the edge channel picture of the 2/5 state, three regions where no partitioning is expected can be identified. On the first plateau at 2/5 of e^2/h all channels are fully transmitted, then on the plateau at 1/3 of e^2/h, one channel is fully transmitted while the other is fully reflected. Finally all channels are reflected when the QPC is closed.

Is that picture confirmed by DC shot noise measurements ? At V$_g$ = -0.24 V, the QPC is closed and the DCSN measured using both auto- and cross-correlation is found to show no variation as a function of V$_{ds}$. At V$_g$ = 0.03 V, all channels are transmitted. No variation of the DCSN using cross-correlation is observed, as expected, however the auto-correlated shot noise presents an evolution as a function of the bias voltage. Finally, at V$_g$ = -0.03 V once again the auto-correlated DCSN is found the evolve with V$_{ds}$, with an amplitude comparable to the measurement for an open QPC. The cross-correlated

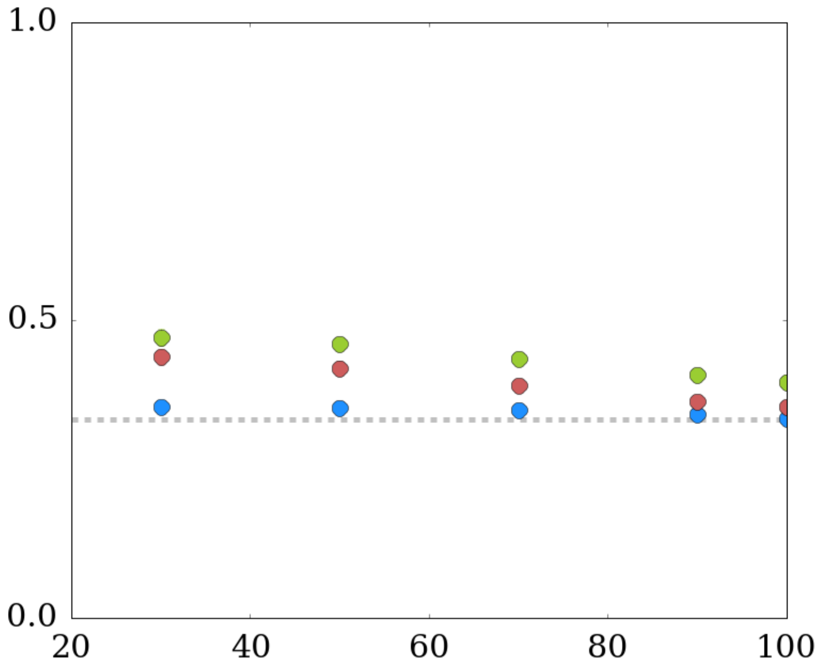

FIGURE 7.10 – **Evolution of the fractional charge as a function of the temperature at $\nu_b = \nu_{QPC} = 2/3$.** The horizontal doted line represents the value $e^* = e/3$.

DCSN is also found to evolve with V_{ds}, however the transmission is not found to be constant over a large range of DC bias, meaning that the channel is partitioned over a certain bias, explaining the small evolution of the cross-correlated shot noise. From those measurement we think that the two channel picture can be validated even though a small noise is measured using cross-correlation on the 1/3 plateau. But this picture does not explain the evolution of the auto-correlated shot noise on both plateau, especially for a QPC fully opened where no partitioning happen.

A comparison with the measure on the plateau at bulk filling factor 1/3 is done where the auto- and cross-correlated shot noise are measured for a QPC fully closed and opened. There when there is no partitioning, no evolution for all measurement types is observed (see figure 7.12).

7.2 Comparison of PASN measurement

The comparison can be done while applying a time-dependent voltage on the contact (0) of the sample. The question raised is where will the Josephson frequency appear (if it is the appear at all) in the auto-correlation measurements ? Will it scale with the effective charge found using the auto-correlation, the cross-correlation or another value ?

The analysis done is identical to the one presented in chapter 6 and the averaged PASN measurements at bulk filling factor of 2/5 are presented. The excess noise is compared to the expected excess PASN. The excess noise at f = 10,17 and 22 GHz is presented of

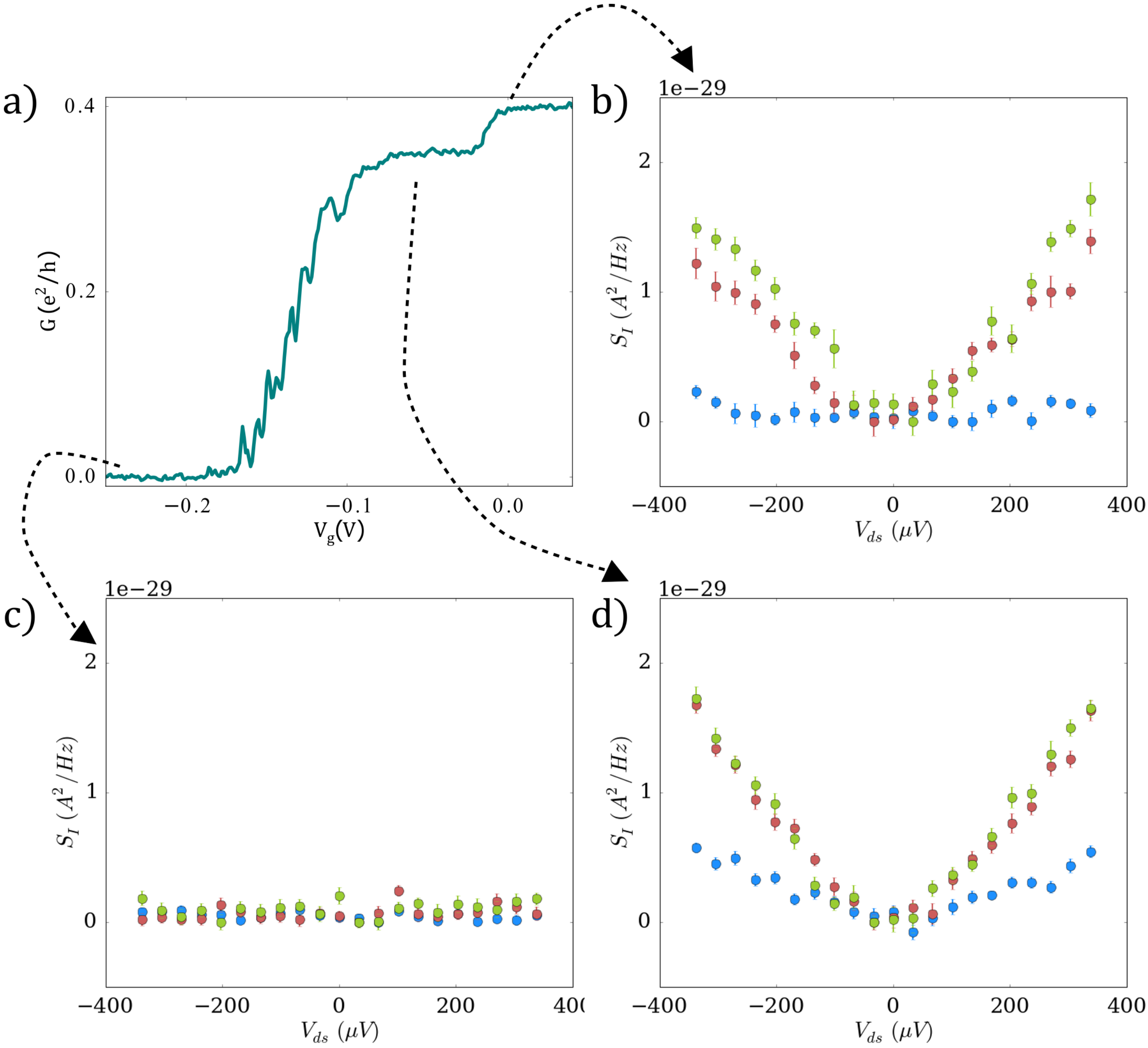

FIGURE 7.11 – **Noise on the plateaux at $\nu_b = 2/5$.** *a)* Transmission as a function of the gate voltage at $\nu = 2/5$ and 30 mK. *b)* DCSN at $V_g = 0.03$ V on the 2/5 plateau. *c)* DCSN at $V_g = -0.24$ V, for a QPC fully closed *d)* DCSN at $V_g = -0.03$ V on the 1/3 plateau. All data are set to 0 at $V_{ds} = 0$.

figure 7.13 for the auto-correlation A and figure 7.14 for the auto-correlation B.

From those excess noises, two Josephson frequencies are measured, corresponding to the two auto-correlations. Figure 7.15 shows the evolution of f_J as a function of f. The measurements are compared with the expected evolution $f_J = f$ with $f_J = e^*V/h$ for $e^* = e/3$. The data are in a very good agreement with the theory using $f_J = f$ with $e^* = e/3$.

The similar analysis is done for the measurement at $\nu_b = \nu_{QPC} = 2/5$ or $V_g = -0.003$ V. On figure 7.16 is reported the evolution of the Josephson frequency as a function of the excitation frequency. Once again those are compare with $f_J = f$ where f_J is calculated

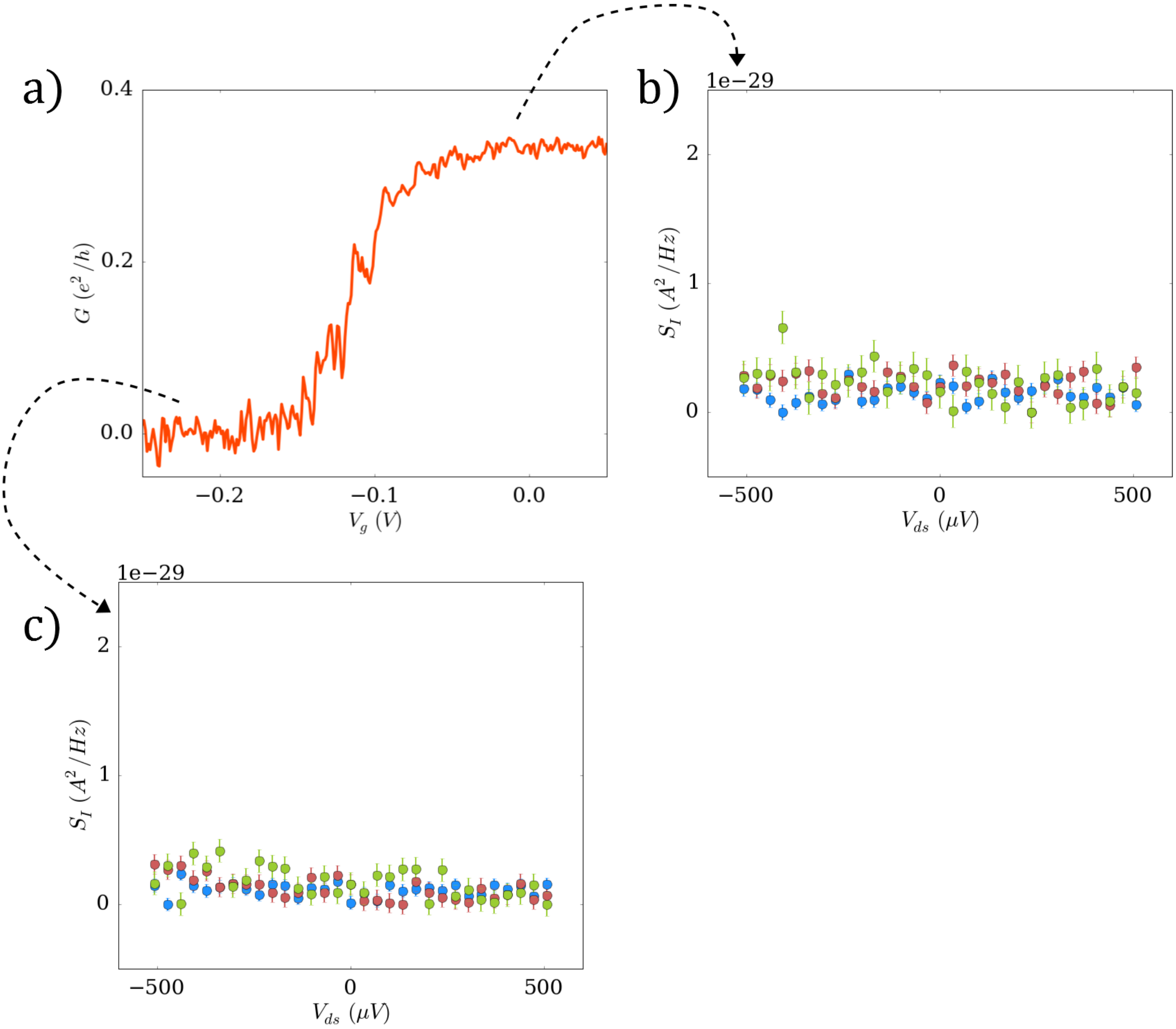

FIGURE 7.12 – **Noise on the plateaus at $\nu_b = 1/3$.** *a)* Transmission as a function of the gate voltage at $\nu = 1/3$ and 30 mK. *b)* DCSN at V$_g$ = 0.03 V on the 1/3 plateau. *c)* DCSN at V$_g$ = -0.24 V, for a QPC fully closed. All data are set to 0 at V$_{ds}$ = 0.

using e* = e/5 and there the Josephson frequency is found to scale with *f*.

Surprisingly, even though the amplitudes of shot noise measured using cross- and auto-correlation are very different for the measurement presented above, the amplitude probabilities $|p_l|^2$, deduced from a fit a low bias voltage range of the shot noise with V(t) applied, are comparable and equal for most measurements. This amplitude probability depends on the reduced amplitude $\alpha = e^* V_{ac}/hf$ which depends on the fractional charge.

On top of the comparable reduced amplitude α, a striking result from this comparison is that the Josephson frequency does not scale with the effective charge measured using DC shot noise in auto-correlation but with the actual fractional charge ! For measurements in the WBS regime of the 2/5 state, the effective charge found using auto-correlation is about 3e/5 while the fractional charge is found to be of e* = e/5. It is obvious that

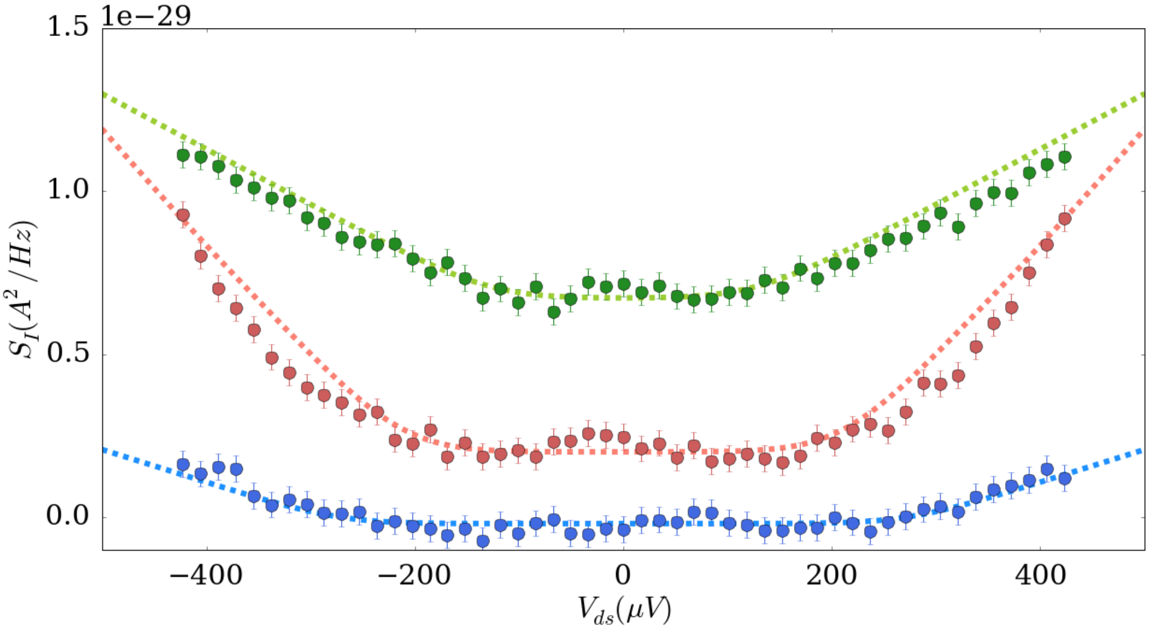

FIGURE 7.13 – **PASN at $\nu_b = 2/5$ and $\nu_{QPC} = 1/3$ using auto-correlation A.** The measurement is realized a 11.2 T, V_g = -0.09 V and for a base temperature of 30 mK. The dots are the measured excess PASN and the line a comparison with the theory using $e^* = e/3$. The green curve is for f = 10 GHz, 17 GHz for the red curve and 22 GHz for the blue curve.

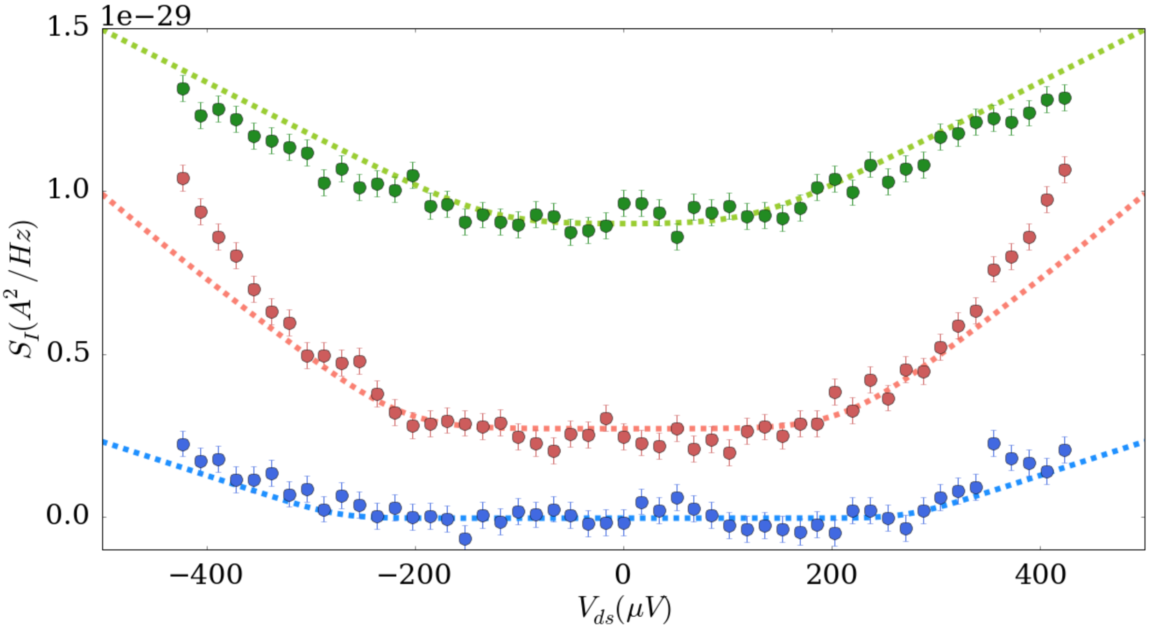

FIGURE 7.14 – **PASN at $\nu_b = 2/5$ and $\nu_{QPC} = 1/3$ using auto-correlation B.**

the threshold voltage, the voltage beyond which the excess noise increases, is not to be compared with charges 3e/5 and measurements are in a good agreement with charges e/5.

One could argue that heating from the RF has to be taken into account. Indeed, from the analysis done in the previous section, the effective charge found using auto-

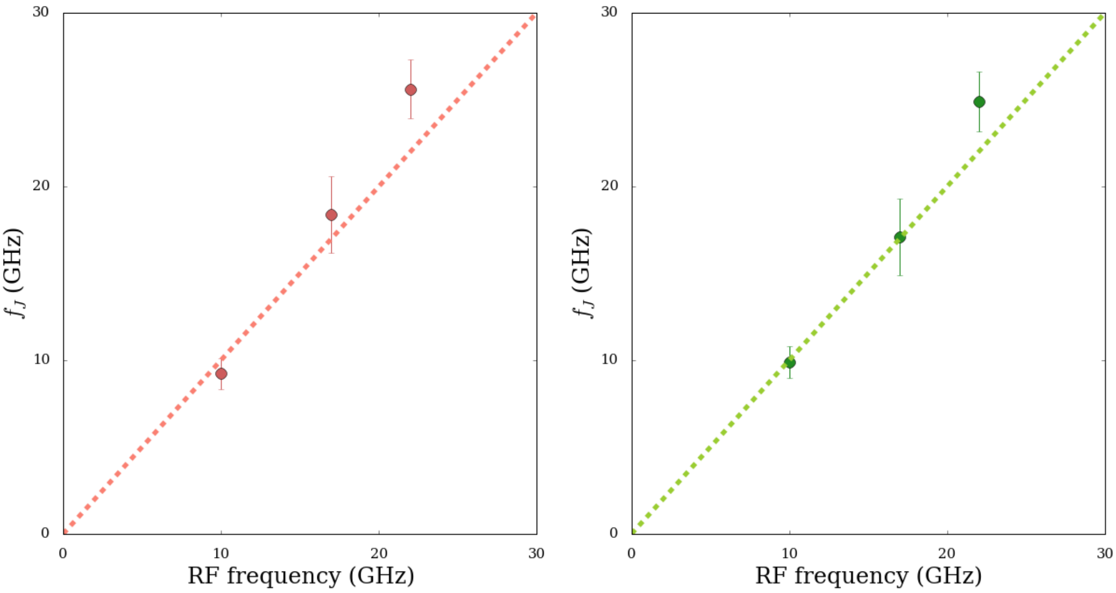

FIGURE 7.15 – **Josephson relation at $\nu_b = 2/5$ and $\nu_{QPC} = 1/3$ using auto-correlations.** The left figure is for the auto-correlation A and the right one for the auto-correlation B. The line displays $f_J = f$ where f_J is calculated using the fractional charge $e^* = e/3$.

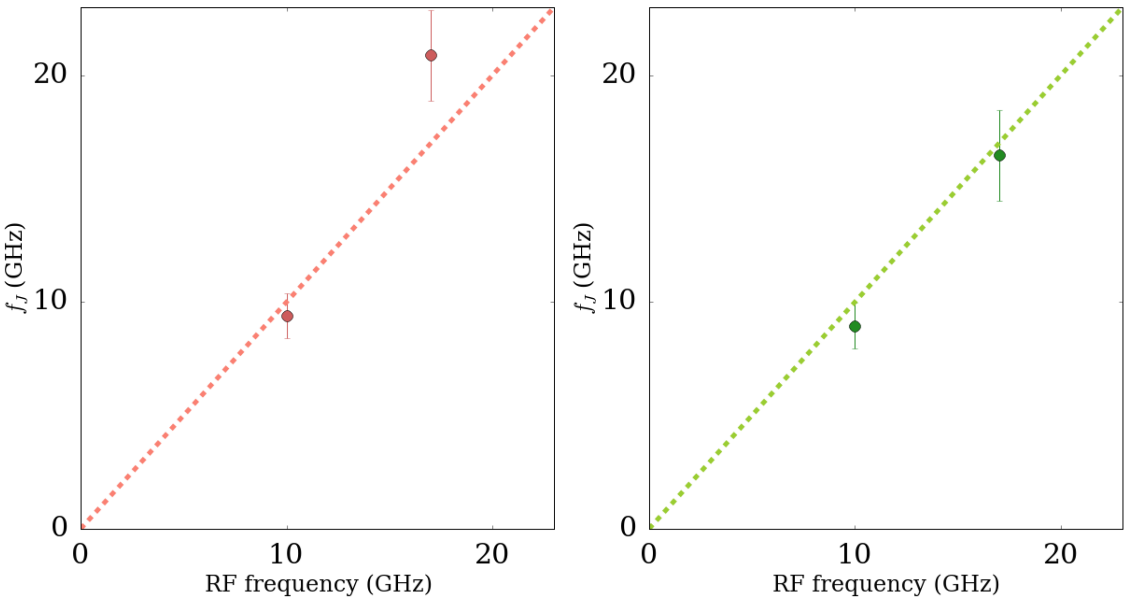

FIGURE 7.16 – **Josephson relation at $\nu_b = \nu_{QPC} = 2/5$ using auto-correlations.** The left figure is for the auto-correlation A and the right one for the auto-correlation B. The line displays $f_J = f$ where f_J is calculated using the fractional charge $e^* = e/5$.

correlation was evolving with the temperature. Here, for PASN measurement in the WBS of the 1/3 state, the temperature is equal to 60 mK when RF are applied. From figure

	$\alpha = e^*V_{ac}/hf$					
	$V_g = -0.09$ V			$V_g = -0.003$ V		
f (GHz)	Cross	Auto A	Auto B	Cross	Auto A	Auto B
10	1.15	0.91	0.85	1.38	1.05	1.07
17	1.3	1.21	1.22	1.14	1.17	1.33
22	0.73	0.76	0.8			

Table 7.1 – Comparison of fitting parameters using cross- and auto-correlation for PASN measurement.

7.7, the effective charge measured using auto-correlation can be estimated at e/2 at this temperature compared to the value of 0.55e at 30 mK. Once again, the threshold voltage does not scale with this value but with the fractional charge e/3.

This comparison confirms that photo-assisted processes are experienced by the fractional charges and that the long predicted fractional Josephson frequency reflects this fractional charge. The PASN can then be used to reliably determine the fractional charge.

7.3 Possible physical interpretation

For the FQH state $\nu = 2/5$, co-propagating neutral modes, having the same chirality as the charged modes, have been suggested. Can this explain the measurement at this filling factor ? Let us simply model neutral modes by an evolution of the temperature as a function of the bias voltage at the excited contact. This evolution would have an impact on the auto-correlations. Indeed, the Johnson-Nyquist noise measured by the auto-correlation would not just be an offset anymore but a term evolving with V_{ds} as :

$$S_I = 4k_B\nu\frac{e^2}{h}T\left(V_{ds}\right) \tag{7.1}$$

However it would not change the cross-correlation. Then the evolution of cross- and auto-correlated shot noise as a function of V_{ds} should be different.

This could also explain why when the QPC is fully opened an evolution of the noise as a function of V_{ds} in auto-correlations is observed, even when no partitioning occur. However, considering that picture, there is no reason for the transmitted and reflected auto-correlated shot noise to present the same evolution as a function of V_{ds}. Finally, an evolution of the auto-correlated shot noise should also be observed when the QPC is fully closed, which is not the case.

Another explanation that was considered was the backscattering of particles through the bulk. At finite temperature, in a variable range hopping picture, the probability for a particle on a localized state in the bulk to tunnel to another localized state is not equal to zero. The evolution of longitudinal resistance with the temperature is written [27] :

$$\sigma_{xx} = \sigma_0 \; exp \left(\frac{T_0}{T} \right)^{1/2} \tag{7.2}$$

Then we can imagine that the excitations injected at the contact (0) on the upper edge channel can be backscattered to the lower edge channel through the bulk and not the QPC. This would lead to a noisy incoming current and to noises measured using auto-correlations of backscattered and transmitted current to be equal and higher than the expected noise measured with just one QPC and should evolve with the ratio T/T_0. Indeed, if the hopping length $L_h \sim \xi \; T_0/T$ with ξ the localization length, is larger than the sample width W for small T, then electron partitioning would result in shot noise. This would also explain the evolution with the temperature in the auto-correlations as for large temperature, $L_h <$ W.

This could be modeled as two QPCs in series and following the results obtained in [45] a difference in the cross-correlated and auto-correlated shot noise is observed. However this would also lead to an evolution of the cross-correlated shot noise with the temperature which is not observed in our experiments.

Chapter 8

Conclusion & prospects

Conclusion

In this manuscript are presented results on the dynamics of excitations in the fractional quantum Hall effect. We measured the photo-assisted shot noise of a quantum point contact in the FQHE. To do so the sample was irradiated at low temperature with a sine wave at GHz frequency and the small current fluctuations induced by the partitioning were measured.

This allow us to measure the fractional Josephson frequency associated with charges e/5 and e/3 providing a new way to measure the fractional charge and to validate our understanding of photo-assisted processes in the FQHE. Finally, thanks to this set-up that allow to measure simultaneously the auto- and cross-correlated shot noise, the cross-correlation was confirmed to be a reliable fractional charge measurement.

However some open questions remains. Even though it seems like is does not affect photo-assisted processes the origin of the rising noise offset with the RF power in PASN measurements is still unknown. It should also allow to sort the evolution of the PASN measurement as a function of the AC amplitude. Another question is the difference between auto and cross-correlated DC shot noise. The exact origin of this difference is not known and calls for a complete experimental study as well as theoretical study. Repeating on a sample where the bulk properties can also be probed with the edge properties should bring more information and help to discriminate hypothesis as for the origin of this difference.

Further measurements have to be made to realize a full study of DCSN in the FQHE regime. For example no study of the dependence of the fractional charge at $\nu_b = \nu_{QPC} = 2/5$ has been made.

An interesting study for the FQH state $\nu = 2/3$ would be to reverse the magnetic field which will reverse the chirality of propagation. In that case, if we look at the sample sketch in figure 6.3, the charged modes are expected to flow directly towards contact (5) which is grounded, while counter-propagating neutral modes would go towards the QPC [4, 5]. Then no shot noise in cross-correlation is expected whereas an evolution as a function of the bias voltage is to be observed using auto-correlation functions.

Perspectives

Now that a step towards the understanding of photo-assisted processes in the FQHE has been made, the next step would be the realization of a source of single fractionally charged quasi-particle to probe the anyonic statistics. The idea is then to apply a Lorentzian pulse to the sample in order to inject a single fractionally charged particle in the conductor, as for the leviton in the non-interacting case. Nevertheless, as opposed to what was first described in [59] a fractionally charged Lorentzian pulse would not lead to a minimal excitation in the FQHE. Indeed, it has recently been theorically demonstrated that only a Lorentzian pulse with an *integral* charge would translate into a minimum of noise, *i.e.* no extra particle-hole pairs injected [82, 88].

Then in order to realize (HOM) correlation of fractionally charged quasi-particle three QPCs would be necessary as suggested in [35]. Two QPCs are used to generate the leviton-like fractional charge with a delay τ while a third one plays the role of beam-splitter and fluctuations of the backscattered and transmitted current can be measured.

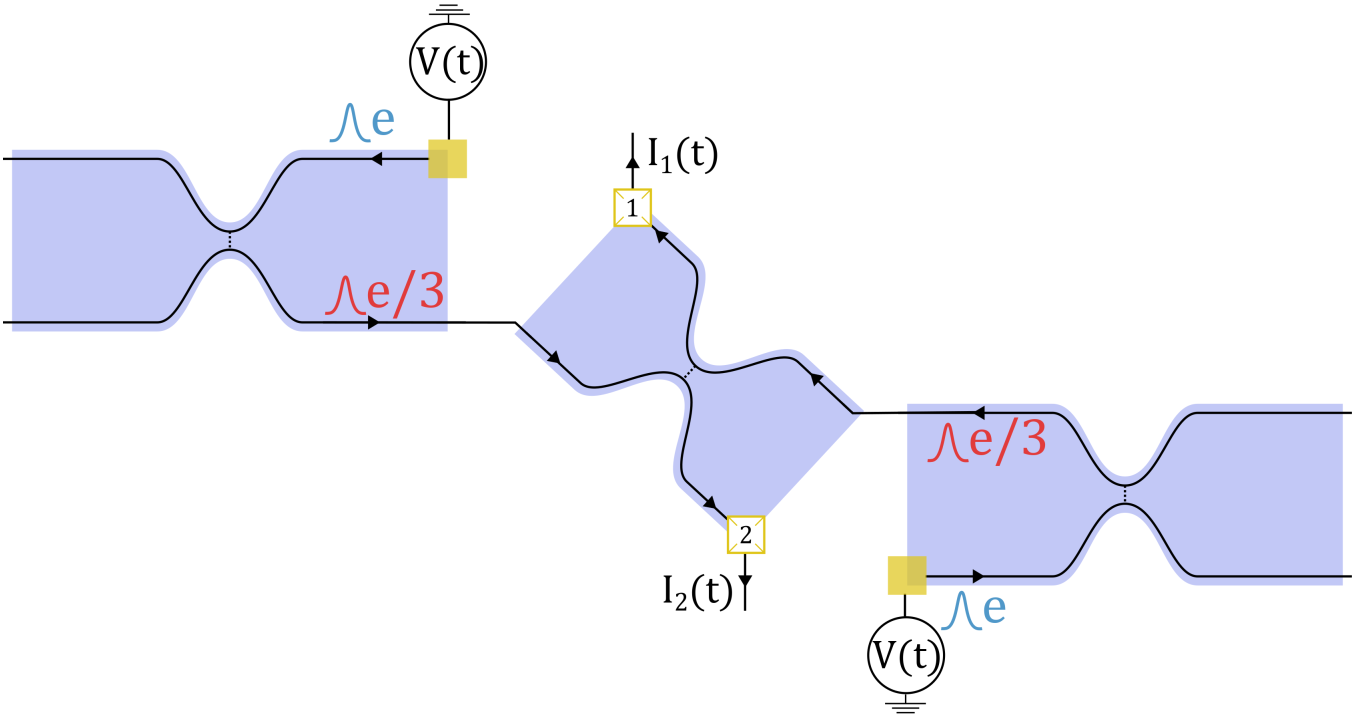

Figure 8.1 – **HOM in the FQHE.** A Lorentzian pulse of integer charge is applied on a QPC in the FQHE in the regime of weak backscattering where charges e/3 are measured. On a second QPC, in the FQHE, in the WBS regime of transmission, a Lorentzian pulse of integer charge is applying with a delay τ. The two leviton-like fractional charges are sent to a third QPC playing the role of a beam-splitter.

Appendices

Appendix A

Scattering theory

A.1 Scattering matrix

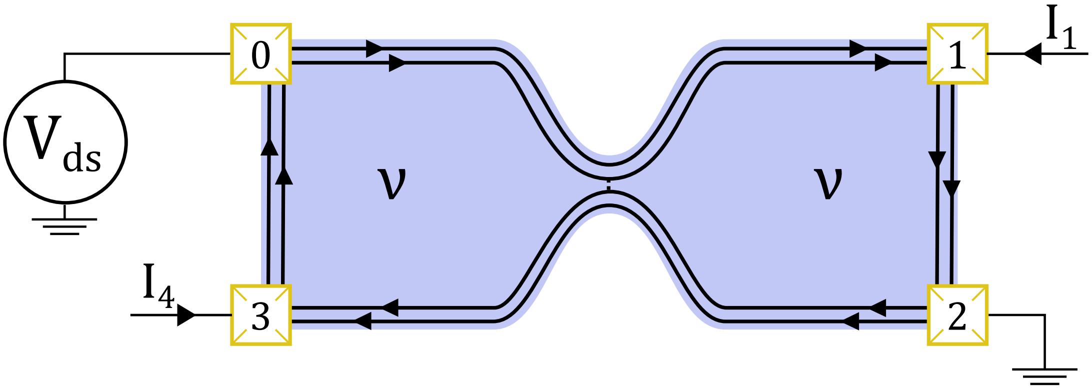

Figure A.1 – **Schematic view of the sample.**

We consider a 4-terminal mesoscopic quantum conductor in the QHE at filling factor $\nu = 2$. Even though in our experiment there are 6 contacts the results are identical. The scattering matrix of such a conductor, defined in section 3.1.3 using equation 3.10, is written below. The elements are labeled $s^{nm}_{\alpha\beta}$, m and n run over the channels $[\![0,1]\!]$ where 0 stands for the inner channel and 1 for the outer channel, and α and β run over the contacts $[\![0,3]\!]$. It corresponds to the amplitude of probability for a particle coming from the contact α on channel n to be scattered in the channel m of the contact β.

$$\begin{pmatrix} 0 & 0 & 0 & 0 & 0 & 0 & s_{03}^{00} & 0 \\ 0 & 0 & 0 & 0 & 0 & 0 & 0 & s_{03}^{11} \\ s_{10}^{00} & 0 & 0 & 0 & s_{12}^{00} & 0 & 0 & 0 \\ 0 & s_{10}^{11} & 0 & 0 & 0 & s_{12}^{11} & 0 & 0 \\ 0 & 0 & s_{21}^{00} & 0 & 0 & 0 & 0 & 0 \\ 0 & 0 & 0 & s_{21}^{11} & 0 & 0 & 0 & 0 \\ s_{30}^{00} & 0 & 0 & 0 & s_{32}^{00} & 0 & 0 & 0 \\ 0 & s_{30}^{11} & 0 & 0 & 0 & s_{32}^{11} & 0 & 0 \end{pmatrix}$$

We suppose that there is no inter-channel scattering, hence all scattering elements from the channel n to the channel m is zero when $n \neq m$.

A.2 Zero-frequency noise

The zero frequency noise is :

$$S_{\alpha\beta} = \frac{e^2}{2\pi\hbar} \sum_{\gamma\delta} \sum_{mn} \int dE A_{\gamma\delta}^{mn}(\alpha, E, E) A_{\delta\gamma}^{nm}(\beta, E, E)(f_\gamma(1 - f_\delta) + f_\delta(1 - f_\gamma)) \tag{A.1}$$

With of the matrix elements at contact α defined as :

$$A_{\beta\gamma}^{mn}(\alpha, E, E) = \delta_{mn}\delta_{\alpha\beta}\delta_{\alpha\gamma} - \sum_k s_{\alpha\beta,mk}^{\dagger} s_{\alpha\gamma,kn} \tag{A.2}$$

A.2.1 Inner channel partitioned

We consider the conductor represented in figure A.1 at $\nu = 2$ when the outer channel is fully transmitted and the inner channel is partitioned. The scattering matrix is expressed using the tunneling probabilities.

$$\begin{cases} s_{03}^{00} = s_{03}^{11} = s_{10}^{11} = s_{21}^{00} = s_{21}^{11} = -s_{32}^{11} = 1 \\ s_{12}^{00} = s_{30}^{11} = 0 \\ s_{10}^{00} = s_{32}^{00} = d \\ s_{12}^{00} = -s_{30}^{00} = r \end{cases}$$

So that $d^*d = D$ and $r^*r = R$.

We calculate the element of matrix A at contacts (1) and (3) :

$$\begin{cases} A_{00}^{00}(1) = -D & A_{00}^{00}(3) = -R \\ A_{11}^{11}(1) = 1 & A_{33}^{11}(3) = 1 \\ A_{11}^{00}(1) = 1 & A_{33}^{00}(3) = 1 \\ A_{00}^{11}(1) = -1 & A_{22}^{11}(3) = -1 \\ A_{22}^{00}(1) = -R & A_{22}^{00}(3) = -D \\ A_{02}^{00}(1) = -d^*r & A_{02}^{00}(3) = d^*r \\ A_{20}^{00}(1) = -r^*d & A_{20}^{00}(3) = r^*d \end{cases}$$

All the components that are not expressed here are equal to zero.

The Cross-correlation is expressed using all the elements above with $\alpha = 1$ and $\beta = 3$

$$\begin{aligned} S_{13} &= \frac{e^2}{2\pi\hbar}\int dE\, 2RD\left\{f_0(1-f_0) + f_2(1-f_2) - [f_0(1-f_2) + f_2(1-f_0)]\right\} \\ &= -2RD\frac{e^2}{2\pi\hbar}\int dE\ (f_0 - f_2)^2 \end{aligned} \tag{A.3}$$

Let us now write the auto-correlation functions :

$$S_{11} = \frac{e^2}{2\pi\hbar}\int dE\, 2\left\{\left(D^2+1\right)f_0\left(1-f_0\right) + 2f_1\left(1-f_1\right) + R^2 f_2\left(1-f_2\right) + RD\left[f_2\left(1-f_0\right) + f_0\left(1-f_2\right)\right]\right\} \tag{A.4}$$

$$S_{33} = \frac{e^2}{2\pi\hbar}\int dE\, 2\left\{\left(D^2+1\right)f_2\left(1-f_2\right) + 2f_3\left(1-f_3\right) + R^2 f_0\left(1-f_0\right) + RD\left[f_2\left(1-f_0\right) + f_0\left(1-f_2\right)\right]\right\} \tag{A.5}$$

Giving that $R^2 + RD = R$ the auto-correlations can be expressed using the opposite of the cross-correlation

$$S_{11} = 2\frac{e^2}{2\pi\hbar}\int dE\ \left\{(D+1)\,f_0\left(1-f_0\right) + 2f_1\left(1-f_1\right) + Rf_2\left(1-f_2\right) + RD\left(f_0-f_2\right)^2\right\} \tag{A.6}$$

$$S_{33} = 2\frac{e^2}{2\pi\hbar}\int dE\ \left\{(D+1)\,f_2\left(1-f_2\right) + 2f_3\left(1-f_3\right) + Rf_0\left(1-f_0\right) + RD\left(f_0-f_2\right)^2\right\} \tag{A.7}$$

An integrated form of the cross-correlation in the case where all contacts are at the same temperature T and the contact 0 is biased with a voltage V_{ds} such that $f_0(\epsilon) = f(\epsilon + eV_{ds})$ and $f_1(\epsilon) = f_2(\epsilon) = f_3(\epsilon)$ can be found using the fact that :

$$\int dE\, f\left(\epsilon\right)\left[1 - f\left(\epsilon + \Delta\right)\right] = \frac{\Delta}{exp\left(\beta\Delta\right) - 1} \xrightarrow[\Delta\to 0]{} \frac{1}{\beta} \tag{A.8}$$

with $\beta = 1/k_BT$. Then the cross-correlation is :

$$S_{13} = 4k_BT\frac{e^2}{h}RD\left(1 - \frac{eV_{ds}}{2k_BT}coth(\frac{eV_{ds}}{2k_BT})\right) \tag{A.9}$$

The auto-correlations contain the cross-correlation to which Johnson-Nyquist noises are added.

A.2.2 Outer channel partitioned

Now the inner channel is fully reflected while the outer channel is partitioned. The scattering matrix is :

$$\begin{cases} s_{03}^{00} = s_{03}^{11} = s_{12}^{00} = s_{21}^{00} = s_{21}^{11} = -s_{30}^{00} = 1 \\ s_{10}^{00} = s_{32}^{00} = 0 \\ s_{10}^{11} = s_{32}^{11} = d \\ s_{12}^{11} = -s_{30}^{11} = r \end{cases}$$

The non-zero elements of the matrix A evaluated for contacts (1) and (3) are :

$$\begin{cases} A_{00}^{11}(1) = -D & A_{00}^{11}(3) = -R \\ A_{11}^{11}(1) = 1 & A_{33}^{11}(3) = 1 \\ A_{11}^{00}(1) = 1 & A_{33}^{00}(3) = 1 \\ A_{22}^{11}(1) = -R & A_{22}^{11}(3) = -D \\ A_{22}^{00}(1) = -1 & A_{00}^{00}(3) = -1 \\ A_{02}^{11}(1) = -d^*r & A_{02}^{11}(3) = r^*d \\ A_{20}^{11}(1) = -r^*d & A_{20}^{11}(6) = d^*r \end{cases}$$

The cross-correlation remains the same as before as it only takes into account the partitioned mode, whereas the auto-correlation are different :

$$S_{11} = 2\frac{e^2}{2\pi\hbar}\int dE\ \left\{Df_0(1-f_0) + (R+1)\,f_2(1-f_2) + 2f_1(1-f_1) + RD\,(f_0-f_2)^2\right\} \tag{A.10}$$

$$S_{33} = 2\frac{e^2}{2\pi\hbar}\int dE\ \left\{(R+1)\,f_0(1-f_0) + Df_2(1-f_2) + 2f_3(1-f_3) + RD\,(f_0-f_2)^2\right\} \tag{A.11}$$

Appendix B

Sample characteristics

B.1 Characteristics of the 2DEG

The sample electronic density is $n_s = 1.11\ 10^{11}\mathrm{cm}^{-2}$ and the mobility is $\mu = 3\ 10^6\ \mathrm{V}^{-1}.\mathrm{cm}^2.\mathrm{s}^{-1}$.

Fermi Energy	$E_F = \frac{\hbar^2 k_F^2}{2m^*}$	$4meV$
Fermi wave vector	$k_F = \sqrt{2\pi n_s}$	$8,3.10^7 m$
Fermi velocity	$v_F = \frac{\hbar^{k}_{F}}{2m^*}$	$143km.s^{-1}$
Fermi wavelength	$\lambda_F = \sqrt{\frac{2\pi}{n_s}}$	$75nm$
Mean free path	$l_{el} = \frac{h\mu_s\sqrt{n_s}}{\sqrt{2\pi e}}$	$16\mu m$
Collision time	$\tau_{el} = \frac{l_{el}}{v_F}$	$112ps$
Fermi temperature	$T_F = \frac{E_F}{k_B}$	$45K$
Resistance per square	$R_\Box = \frac{1}{en_s\mu_s}$	18Ω

TABLE B.1 – Sample characteristics

m* is the effective mass of an electron in GaAs, $m^* = 0.067m_e$ where m$_e$ is the mass of the electron.

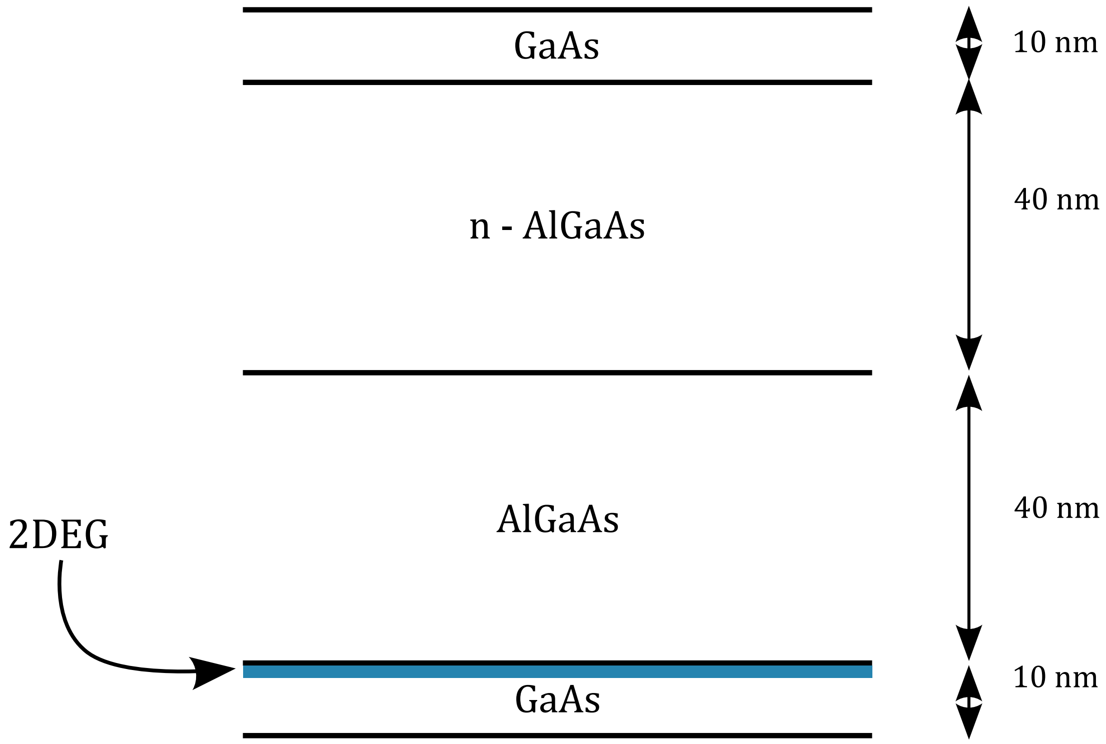

Figure B.1 – **Schematic view of the 2DEG.** The 2DEG is formed at the interface bewteen GaAs and AlGaAs, represented in blue. A first GaAs layer is used in order to avoid oxidation of the AlGaAs layer. AlGaAs is doped with Si donors allowing the formation of the 2DEG and a non doped AlGaAs layer is inserted to enhance the 2DEG mobility, increasing the spatial separation between donors and charge carriers.

Here is schematically reported the heterostructure leading to the formation of the 2DEG used. A first layer of 40 nm thick of undoped AlGaAs is MEB grown on a AsGa wafer. Then another 40 nm thick layer of n-doped AlGaAs is placed on top and finally the cap layer of GaAs is grown. The 2DEG is formed at the interface of GaAs and AlGaAs, 90 nm below the surface.

B.2 Nanofabrication details

Here are reported the different steps of fabrication of the sample. Beginning from a wafer as described in figure B.1, a 2 mm x 2 mm size portion is cleaved. All steps are done using electron lithography.

Markers

The first step is to place markers on the sample, as shown in figure B.4, to ensure good alignment. A PMMA6 positive resist is spin-coated on the raw sample and the lithography is performed. The development is done using a solution 1 : 3 of MIBK,IPA for 1 mn 30 s, then stopped by putting the sample for 1 mn in IPA. The markers are made by deposing a 100 nm high layer of Gold with a 5 nm high Titanium layer below as a sticking layer. We use Gold as there is a high contrast between Au and AsGa for both optical microscope and SEM. The lift-off is performed in hot Acetone for 10 mn.

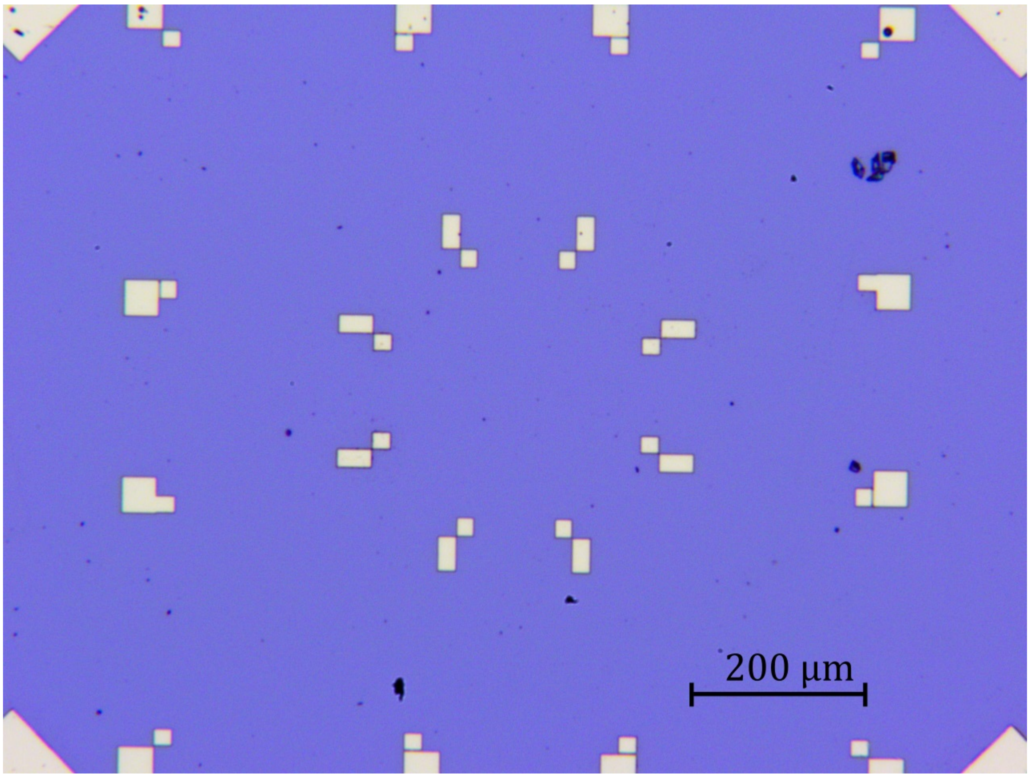

FIGURE B.2 – **Optical microscope image of the markers.**

Mesa etching

Then the Mesa etching is performed. A negative MaN resist is used, development and lift-off are the same as for the previous step. The sample is, after insulation, chemically etched, using a H_3PO_4 solution for 4 minutes. About 90 nm of the sample is etched apart from the mesa (see figure 4.3).

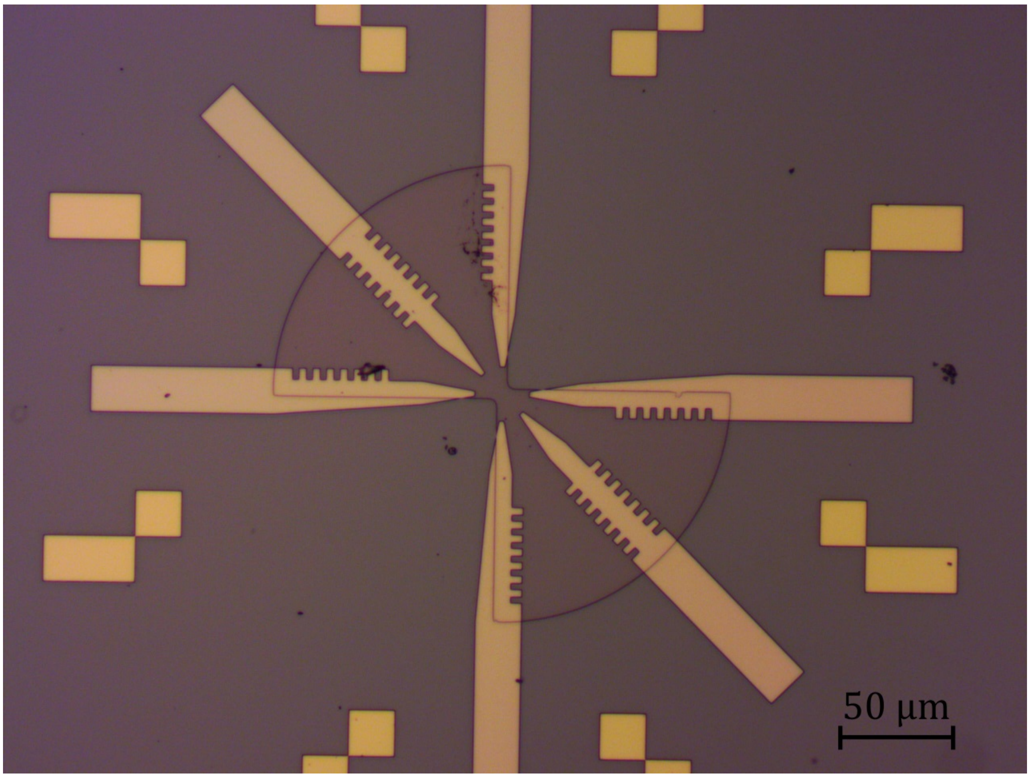

FIGURE B.3 – **Optical microscope image of the ohmic contacts before annealing.**

Ohmic contacts

The following step is the Ohmic contact deposition. The lithography steps are the same as for the markers. Using a recipe from C2N, the contacts are done by deposing 4 nm of Ni / 60 nm of Ge / 120 nm of Au / 25 nm of Ge / 20 nm of Au. The sample is annealed at 470 $^\circ$ C for 4 minutes in a H_2/N_2 atmosphere for the alloy can penetrate the AlGaAs heterostructure and realize a perfect electrical contact with the 2DEG.

The second to last step is the deposition of large golden leads to connect the ohmic contacts and the later gates to the PCB. This step is similar to the marker deposition apart from the design.

Gates deposition

Finally, the gates are done by evaporating 200 nm of Al on top of the mesa after an electron lithography following the same steps as for markers. The gates are separated by 300 nm (see figure 4.5).

The sample is later connected to the PCB by Al wires.

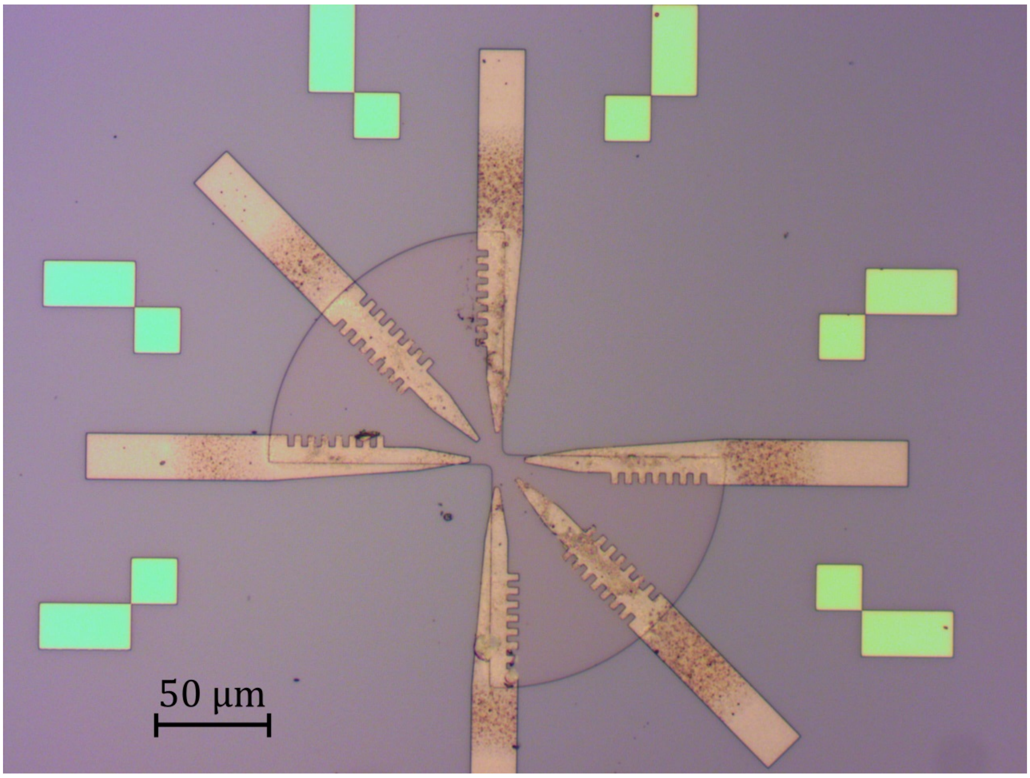

Figure B.4 – **Optical microscope image of the ohmic contacts after annealing.**

Appendix C

From voltage to current noise

C.1 What coefficient

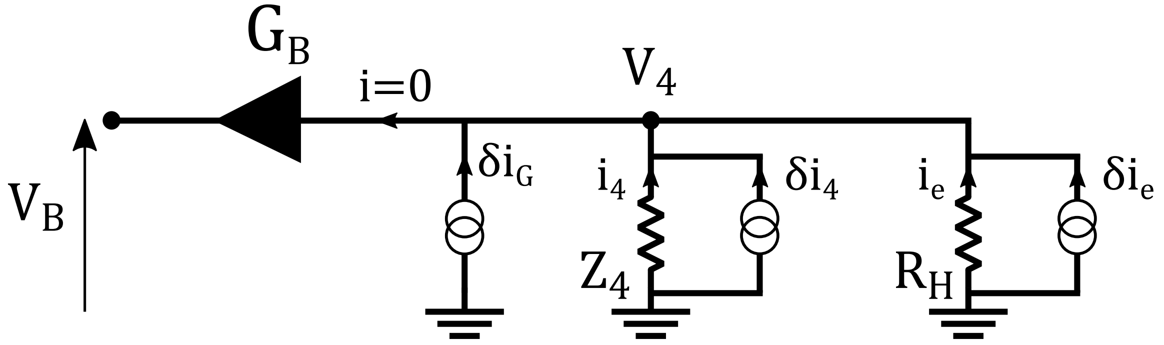

FIGURE C.1 – **Principle of current noise measurement.** The sample with resistance R_H current fluctuations δi_e corresponding to the shot noise. Z_4 is the resonator impedance at measurement frequency and G_B is the gain of the cryo-amplifiers. Each of those add a thermal contribution to the noise. The measurement is the same for line A.

Because the measurements are performed in the QHE, the particles propagate along the edge channels. Then, there are no correlation between current fluctuations coming from the different resonators or cryo-amplifiers.

One can write that :

$$\delta i_G^B = i_4 + \delta i_4 + i_e + \delta i_e \tag{C.1}$$

Giving :

$$V_B = -G_B Z_4 i_4 \tag{C.2}$$

The measured voltage at output B is :

$$V_B = G_B Z_B \{\delta i_G^B + \delta i_4 + \delta i_e\} \tag{C.3}$$

where Z_B is the total impedance of the resonator in parallel with the Hall resistance. Similar result is obtained for line A by replacing B ← A and 4 ← 1. The relevant quantity is the power spectral density of current fluctuation at zero frequency :

$$S_I(\omega = 0) = \frac{\widetilde{\delta i}^2}{\delta f} \tag{C.4}$$

The measured quantities are, for auto-correlation :

$$S_{V_A} = |V_A|^2 = G_A^2 |Z_A|^2 \{ \left|\delta i_G^B\right|^2 + |\delta i_4|^2 + |\delta i_e|^2 \} \tag{C.5}$$

$$S_{V_B} = |V_B|^2 = G_B^2 |Z_B|^2 \{ \left|\delta i_G^A\right|^2 + |\delta i_1|^2 + |\delta i_e|^2 \} \tag{C.6}$$

For cross-correlation, as there are no correlations between the measurement lines A and B, the expression of the voltage noise is :

$$S_{V_A V_B} = |V_A V_B^*| = G_A G_B Z_A Z_B |\delta i_e|^2 \tag{C.7}$$

C.2 Calibration using the Johnson-Nyquist thermal noise

An absolute calibration of the cryo-amplifiers is done using Johnson-Nyquist thermal noise. To do so, PSD at filling factor ν, all channels fully reflected and for several mixing chamber temperatures T is done. Hence the shot noise is zero and the remaining noise measured is the thermal noise of the cryo-amplifiers and the resonators. As the cryo-amplifiers are thermalized at the 4 K stages their thermal contribution is not changed by the increase of the mixing chamber temperature. To suppress their contribution, the PSD at base temperature T_{base} is removed from all measurement and the expected excess noise is the thermal noise of the resonators at temperature T-T_{base}.

First, the value of T_{base} is found by summing the excess voltage noise over the measurement bandwidth Δf = [2.1,2.8] MHz. From this measurement, a temperature of the electrons in the resonators of 30 mK is found (see Figure C.2).

Then the shape of the resonance is used to determine the unknown parameters which are :

- the cryo-amplifiers gain $G_{A/B}$ given by the amplitude of the PSD ;
- the total line capacitors $C_l^{A/B}$ given by the resonance frequency ;
- the inner resistance of the inductor $r_C^{A/B}$ given by the bandwidth of the resonance.

As seen in section 5.1.1, the voltage noise from an impedance Z at temperature T is $4k_BT\mathbf{Re}(Z)$. Then the excess noise will be, following equation C.1

$$\Delta S_V(f) = S_V(f)|_T - S_V(f)|_{T_{base}} = G^2 4k_B(T - T_{base})\mathbf{Re}(Z(f)) \tag{C.8}$$

The line capacitance and the inductor inner resistance are found equal to those found using the method in section 5.4.2.

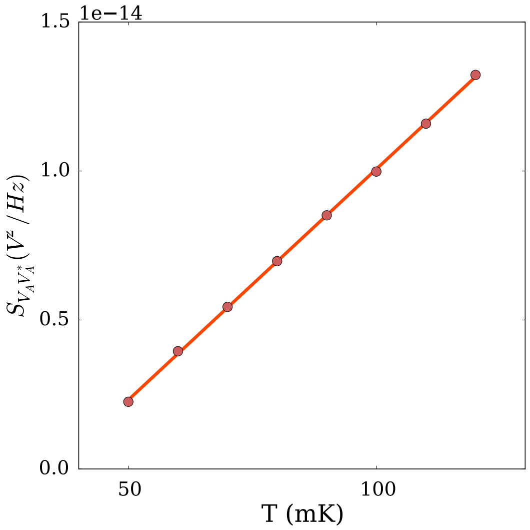

FIGURE C.2 – **Voltage noise as a function of the temperature.** Red dots are the measurement, done at ν=2 for V_{ds}=0 and all channels fully reflected. The PSD at base temperature is removed from PSD at higher temperatures and the excess PSD is integrated over a bandwidth Δf. The line is a linear fit giving the temperature of the electrons in the resonators.

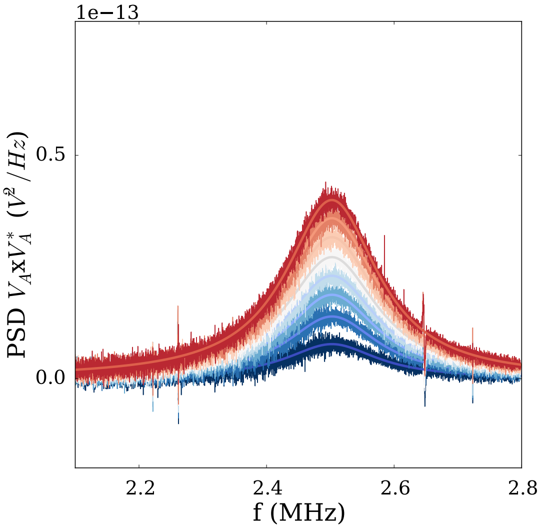

FIGURE C.3 – **Excess voltage noise as a function of the temperature.** The measurement is done at ν=2 for V_{ds}=0 and all channels fully reflected. The blue curve corresponds to the lowest temperature (50 mK) and the red curve to the higher temperature (120 mK). The PSD at base temperature is removed. Solid lines are fits using equation C.8

Appendix D

Data for PASN measurements

Here are reported the datas for photo-assisted shot noise measurements. While in the main text of this manuscript displays the averaged PASN at fixed frequency f and fixed gate voltage V$_g$, here are presented the datas at each different time dependent voltage amplitude V$_{ac}$.

D.1 The 2/5 state

As shown in section 6.1, from a bulk filling factor $\nu_b = 2/5$, two local filling factors can be probed at the QPC : $\nu_{QPC} = 2/5$ and 1/3.

D.1.1 Local filling factor 2/5

The nominal power in dBm written does not take into account the inner attenuation of the wires which changes with the frequency. The excess noise is found the same way as in the main text and compared with the theory with the appropriate e* and the amplitude probability $|p_0|^2$ found using a fit of the PASN datas. We then compare the PASN with the theory using all those parameters. Are presented here the measurements at fixed V$_{ac}$, those are generally averaged over a night and the DCSN measured at the same time as the PASN remains the same. However between 2 measurements (few days apart) slight changes in the DCSN have been observed. This phenomenon is not frequent but has a significant effect on the data analysis as seen on figure D.7. This deviation of the DCSN measurement at $\nu_{QPC} = 1/3$ is also observed for all measurements performed at $f = 17$ GHz.

D.1.2 Local filling factor 1/3

Here it seems like the excess noise is not well represented by the theory. This a consequence of the non-linearity of the DCSN measurement performed at the same time as the PASN measurement (see figure D.8).

D.2 The 1/3 state

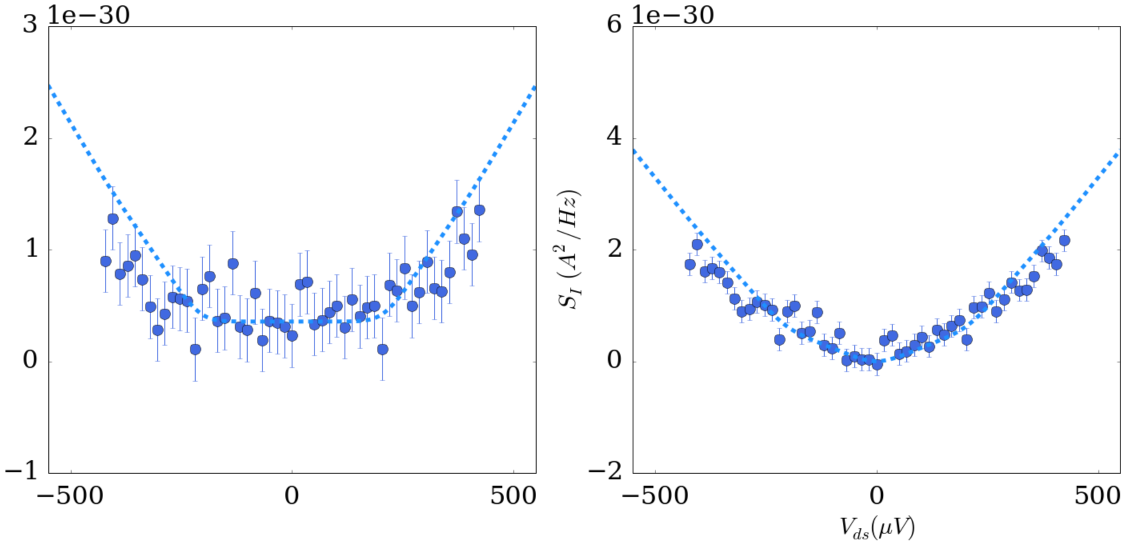

FIGURE D.1 – **PASN at V$_g$ = -0.003 V, 10 GHz and 50 dBm.** The left figure is the excess PASN at 13 T, in the WBS regime of the 2/5 FQH state. The full line is the theoretical PASN with e* = e/5 and the amplitude probability determined by a fit in the low bias voltage range of the PASN measurement. The right figure if the measured PASN compared with the theoretical curve with fit parameters previously found. The extracted value of $|p_0|^2$ corresponds to a value α = 1.31 of V$_{ac}$ = 270 μV.

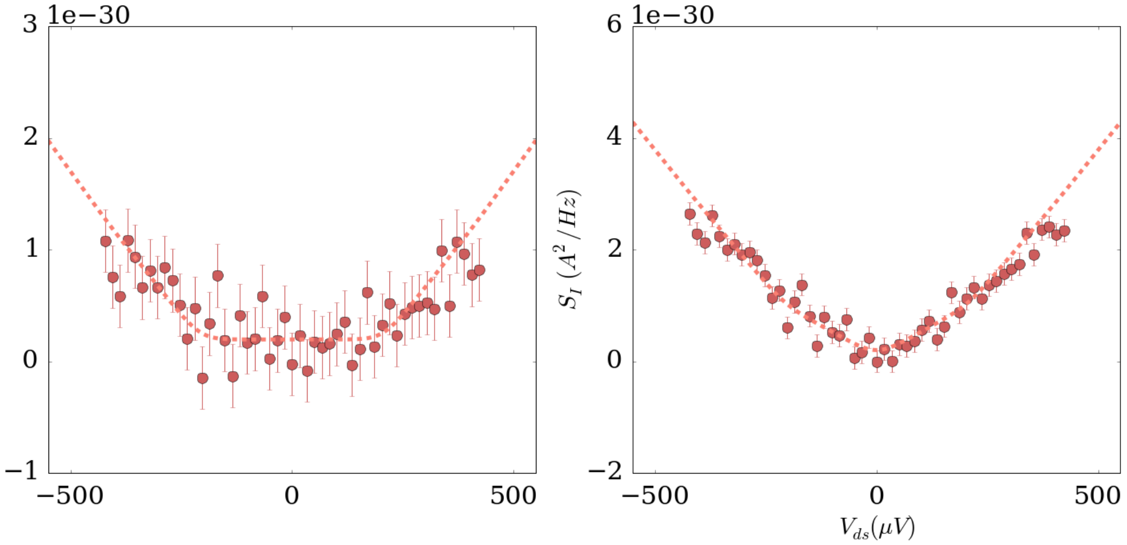

FIGURE D.2 – **PASN at V$_g$ = -0.003 V, 10 GHz and 55 dBm.** The extracted value of $|p_0|^2$ corresponds to a value α = 1.21 of V$_{ac}$ = 250 μV.

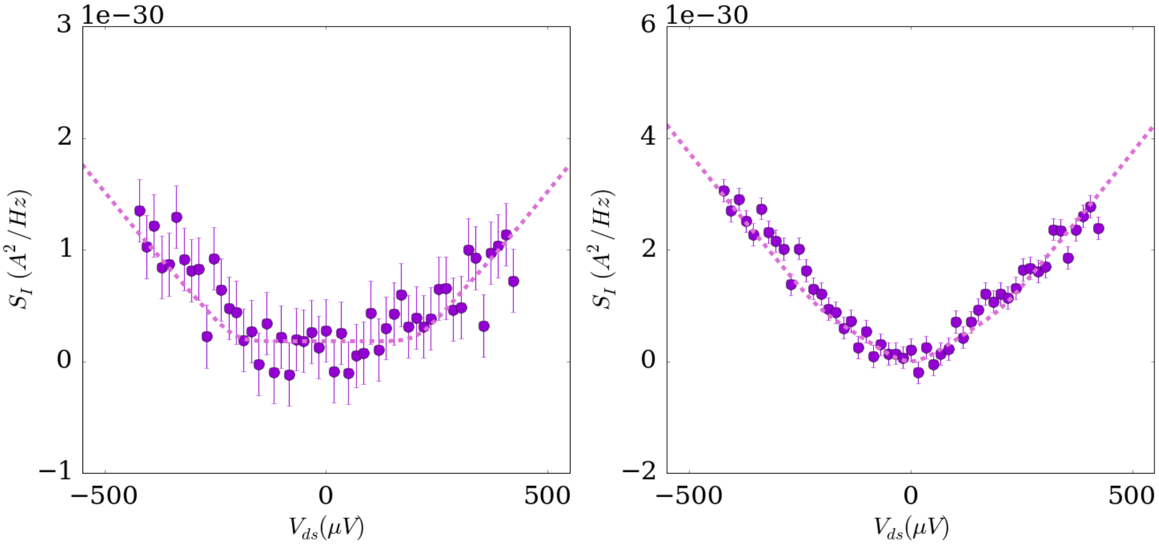

FIGURE D.3 – **PASN at $\mathbf{V_g}$ = -0.003 V, 10 GHz and 58 dBm.** The extracted value of $|p_0|^2$ corresponds to a value $\alpha = 1.1$ of $V_{ac} = 227\ \mu$V.

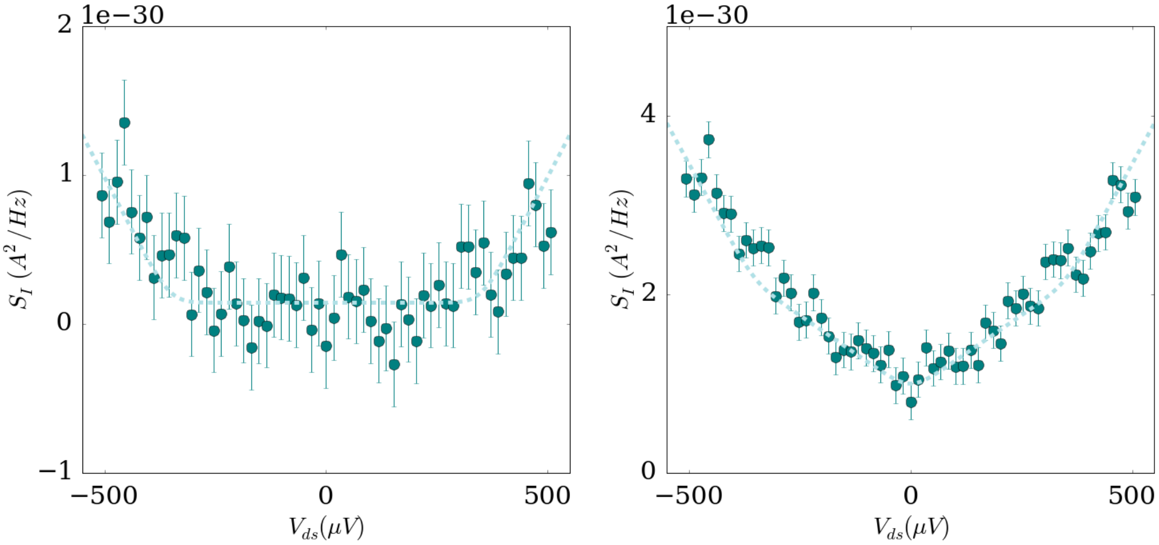

FIGURE D.4 – **PASN at $\mathbf{V_g}$ = -0.003 V, 17 GHz and 55 dBm.** The extracted value of $|p_0|^2$ corresponds to a value $\alpha = 1.36$ of $V_{ac} = 478\ \mu$V.

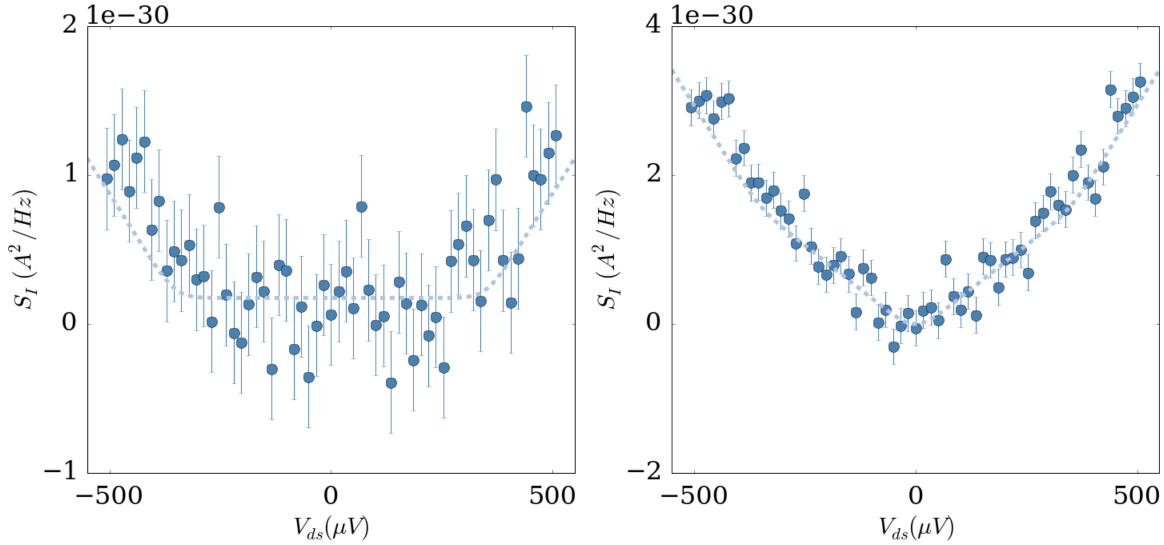

FIGURE D.5 – **PASN at V_g = -0.003 V, 17 GHz and 58 dBm.** The extracted value of $|p_0|^2$ corresponds to a value $\alpha = 1.16$ of $V_{ac} = 408\ \mu$V.

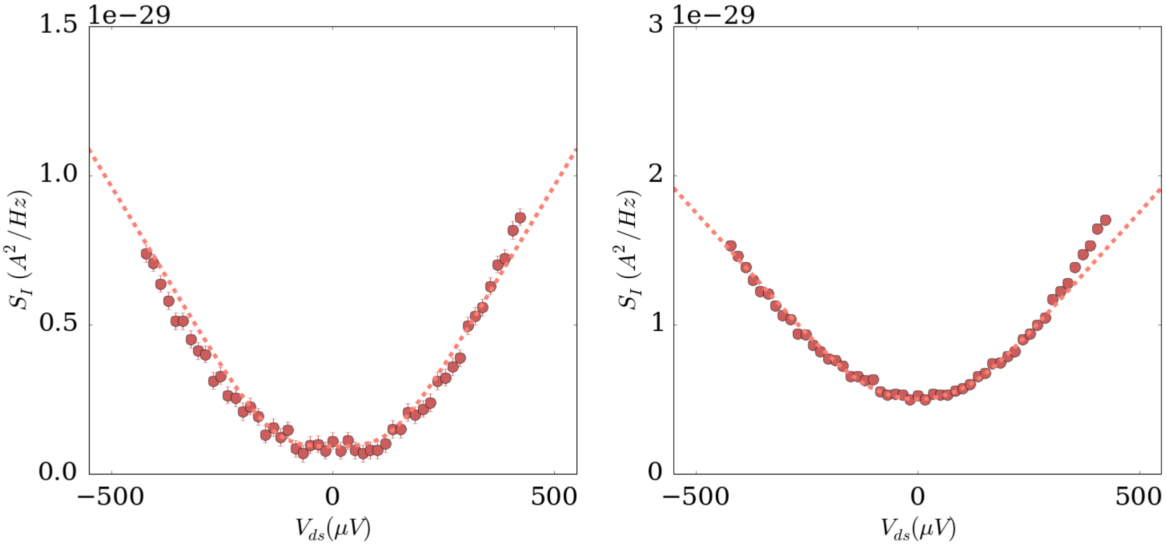

FIGURE D.6 – **PASN at V_g = -0.09 V, 10 GHz and 53 dBm.** The left figure is the excess PASN at 11.2 T, in the WBS regime of the 1/3 FQH state. The full line is the theoretical PASN with $e^* = e/3$ and the amplitude probability determined by a fit in the low bias voltage range of the PASN measurement. The right figure if the measured PASN compared with the theoretical curve with fit parameters previously found. The extracted value of $|p_0|^2$ corresponds to a value $\alpha = 1.52$ or $V_{ac} = 189\ \mu$V.

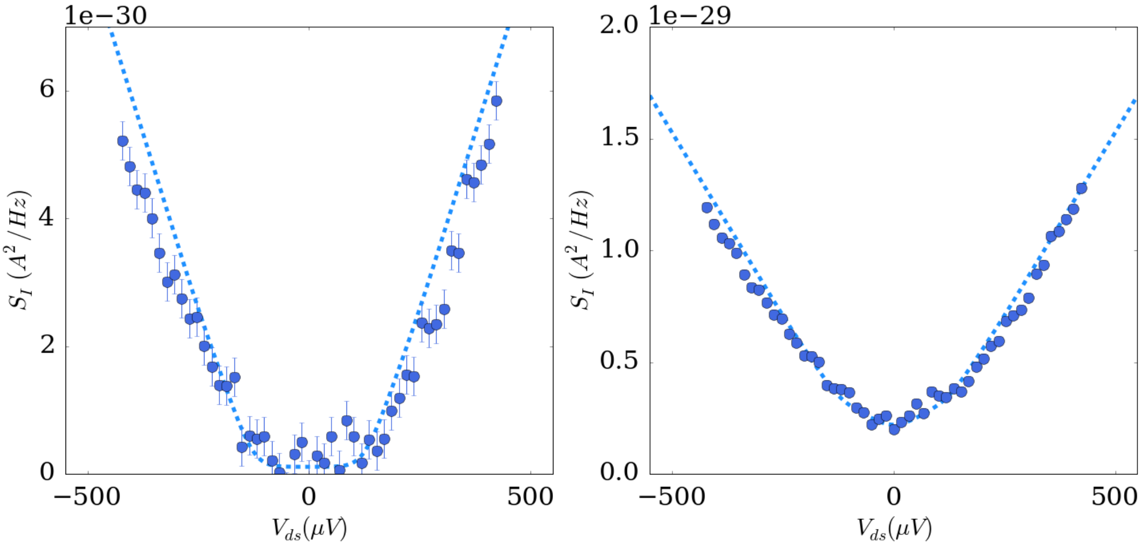

FIGURE D.7 – **PASN at V$_g$ = -0.09 V, 10 GHz and 55 dBm.** The extracted value of $|p_0|^2$ corresponds to a value $\alpha = 1.23$ or V$_{ac}$ = 153 μV.

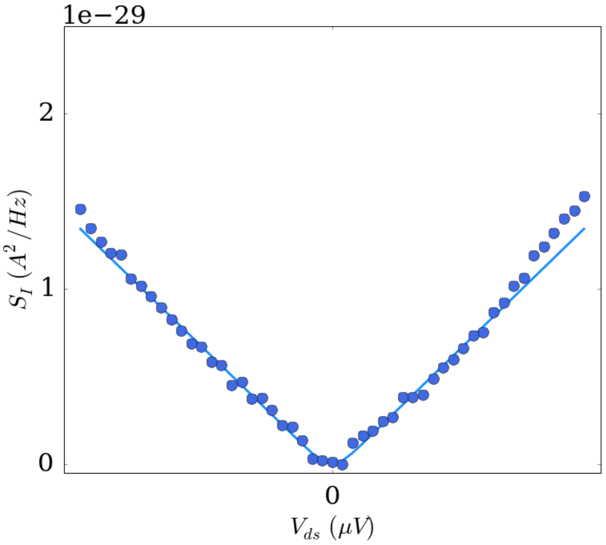

FIGURE D.8 – **DCSN at ν_b = 2/5, ν_{QPC} = 1/3 during the PASN measurement at 10 GHz and 58 dBm.** A deviation from the theoretical shot noise with a constant reflection is observed at high bias voltage.

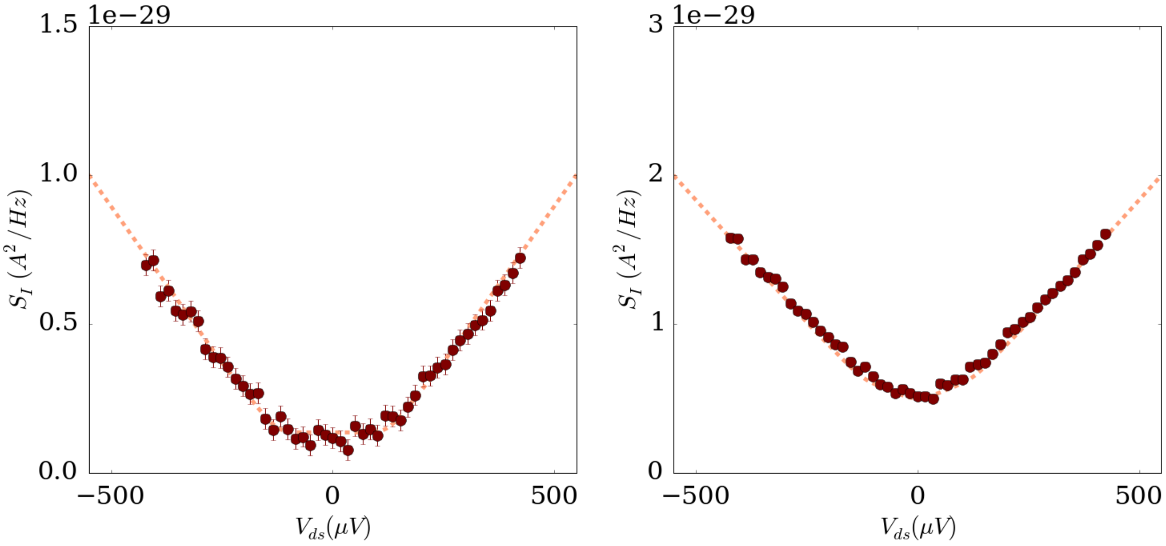

FIGURE D.9 – **PASN at V_g = -0.09 V, 10 GHz and 65 dBm.** The extracted value of $|p_0|^2$ corresponds to a value $\alpha = 0.86$ or $V_{ac} = 107\ \mu$V.

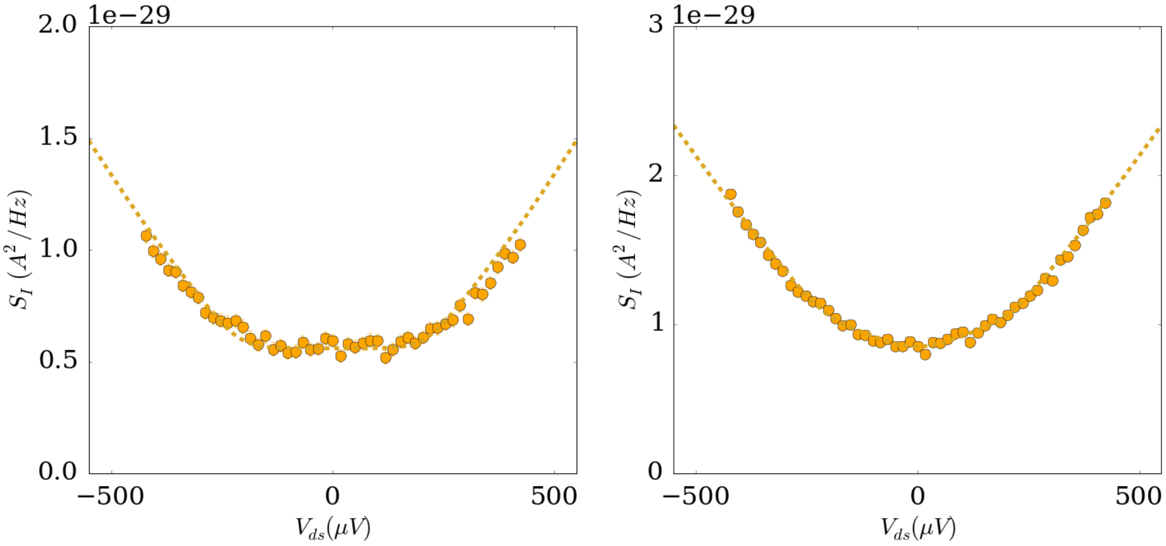

FIGURE D.10 – **PASN at V_g = -0.09 V, 17 GHz and 55 dBm.** The extracted value of $|p_0|^2$ corresponds to a value $\alpha = 1.4$ or $V_{ac} = 295\ \mu$V.

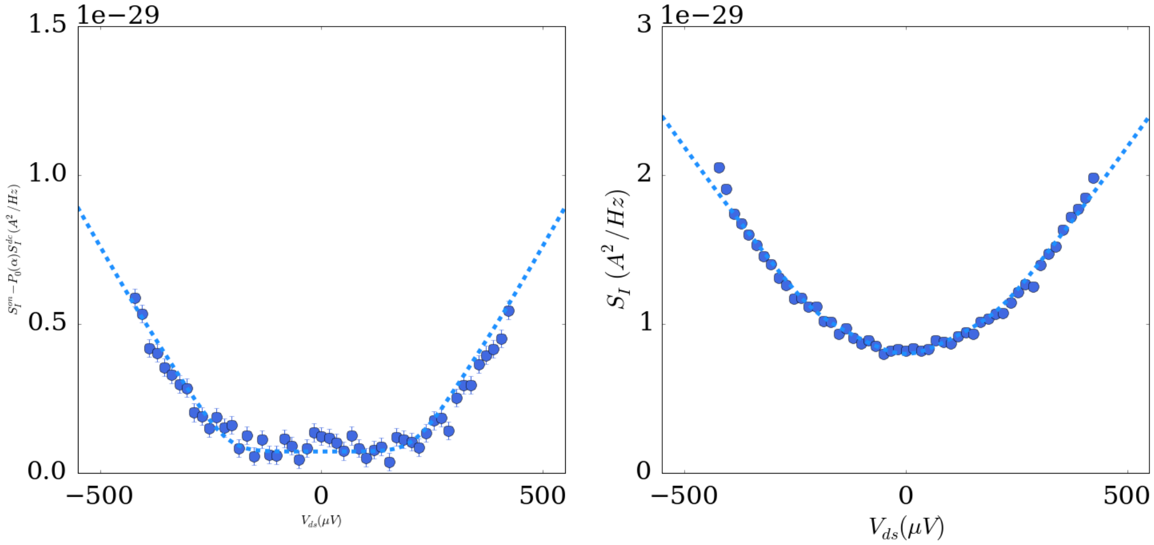

FIGURE D.11 – **PASN at V_g = -0.09 V, 17 GHz and 58 dBm.** The extracted value of $|p_0|^2$ corresponds to a value $\alpha = 1.33$ or $V_{ac} = 280\ \mu V$.

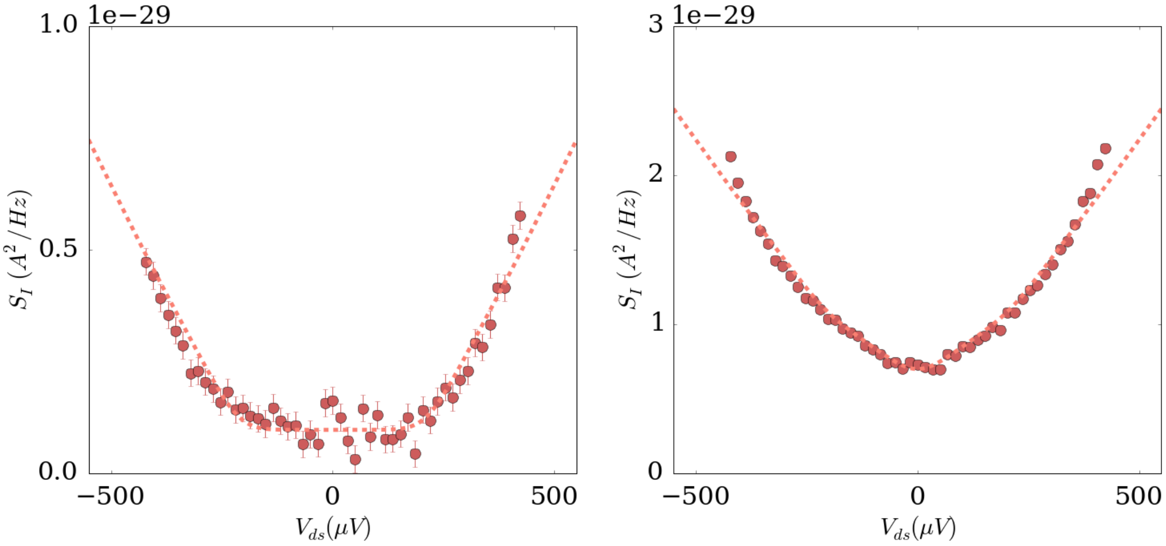

FIGURE D.12 – **PASN at V_g = -0.09 V, 17 GHz and 63 dBm.** The extracted value of $|p_0|^2$ corresponds to a value $\alpha = 1.11$ or $V_{ac} = 234\ \mu V$.

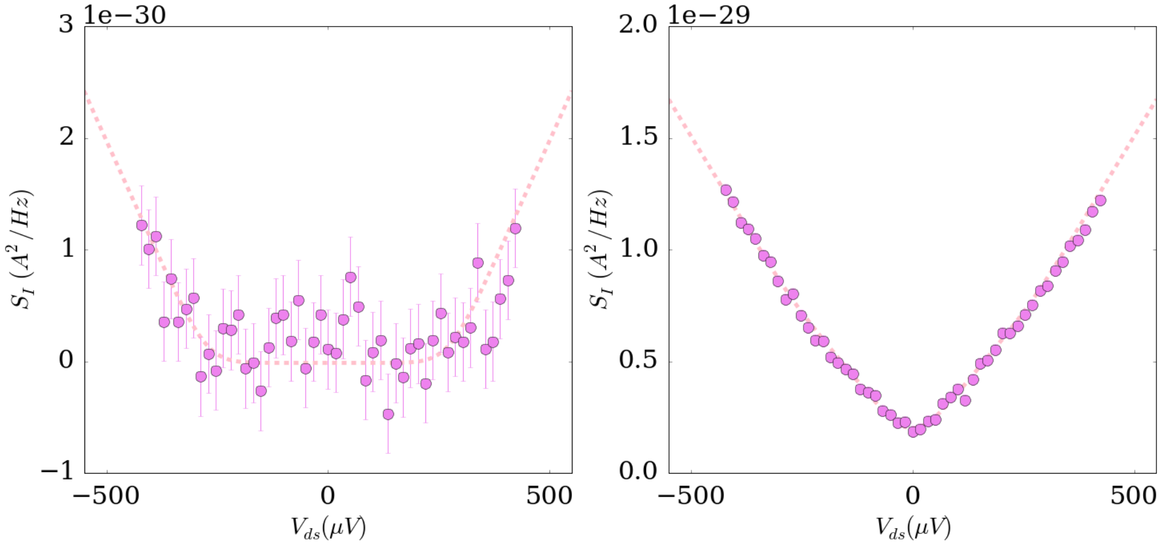

FIGURE D.13 – **PASN at V$_g$ = -0.09 V, 22 GHz and 61 dBm.** The extracted value of $|p_0|^2$ corresponds to a value $\alpha = 0.79$ or V$_{ac}$ = 216 μV.

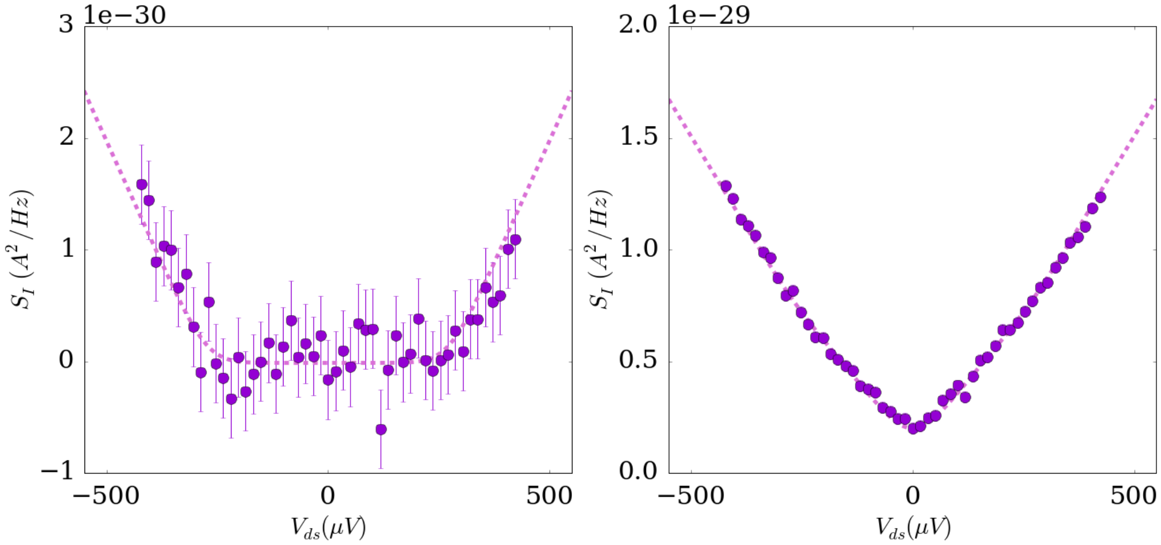

FIGURE D.14 – **PASN at V$_g$ = -0.09 V, 22 GHz and 63 dBm.** The extracted value of $|p_0|^2$ corresponds to a value $\alpha = 0.77$ or V$_{ac}$ = 210 μV.

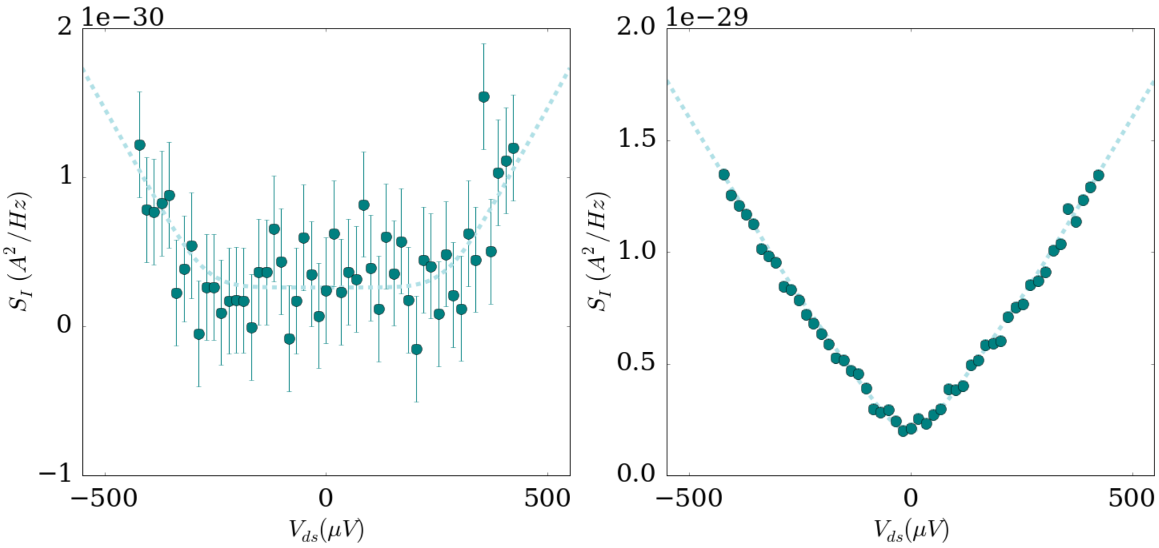

FIGURE D.15 – **PASN at V_g = -0.09 V, 22 GHz and 67 dBm.** The extracted value of $|p_0|^2$ corresponds to a value $\alpha = 0.59$ or $V_{ac} = 161$ μV.

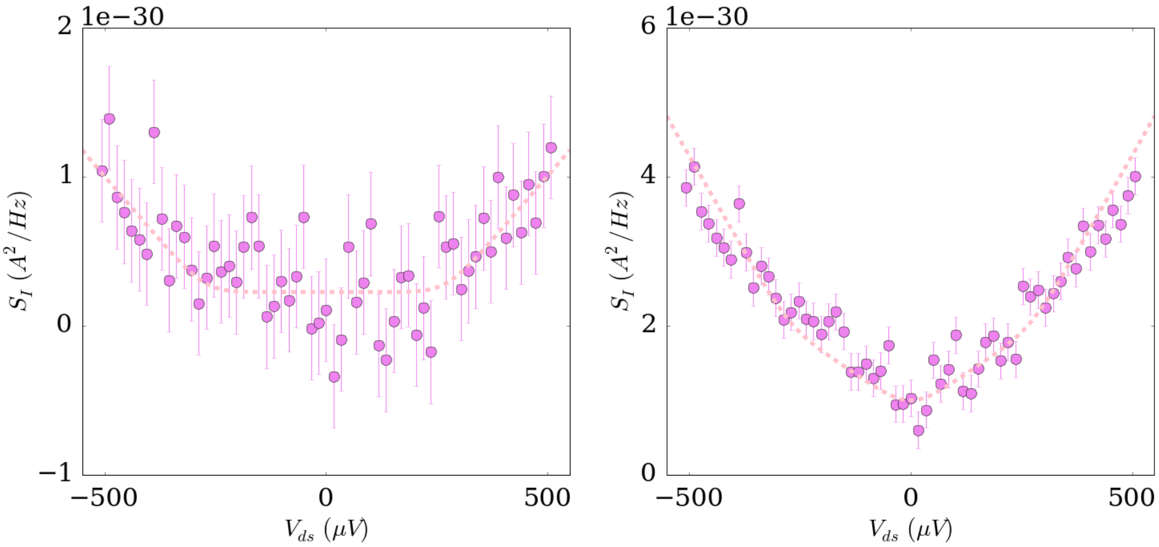

FIGURE D.16 – **PASN at ν_b = 1/3, 22 GHz and 43 dBm.** PASN at 13 T, in the WBS regime of the 1/3 FQH state. The extracted value of $|p_0|^2$ corresponds to a value $\alpha = 1.34$.

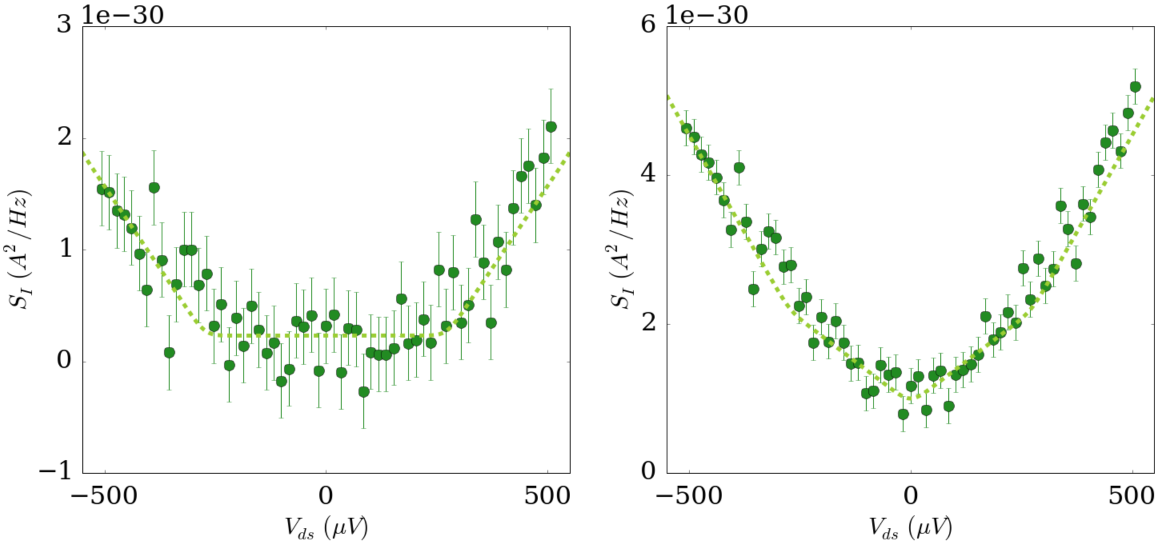

FIGURE D.17 – **PASN at ν_b = 1/3, 22 GHz and 48 dBm.** The extracted value of $|p_0|^2$ corresponds to a value $\alpha = 1.26$.

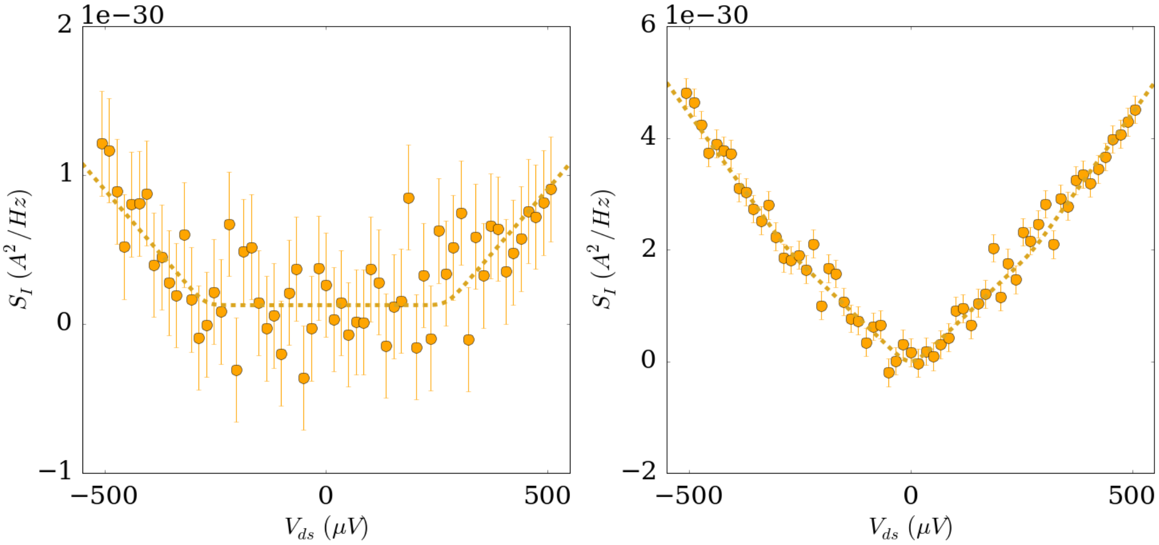

FIGURE D.18 – **PASN at ν_b = 1/3, 22 GHz and 55 dBm.** The extracted value of $|p_0|^2$ corresponds to a value $\alpha = 0.86$.

Appendix E

Current and temperature

Here we report the evolution of the I-V characteristics with the temperature. The first set of measurement is done at 11.2T corresponding to a bulk filling factor of 2/5 and V$_g$ = -0.09 V to induce a local filling factor of 1/3.

The dots are the measurements and the dotted line is the current calculated considering a constant reflection coefficient. There is a slight evolution of the mean reflection coefficient that is taken into account to fit the DCSN.

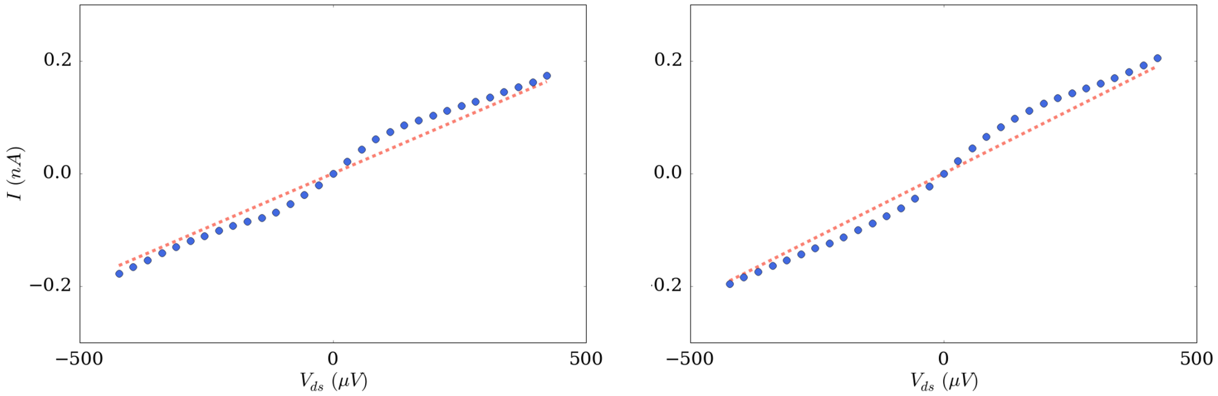

FIGURE E.1 – Backscattered current at V$_g$ = -0.09 V, 50 (left) and 70 mK (right).

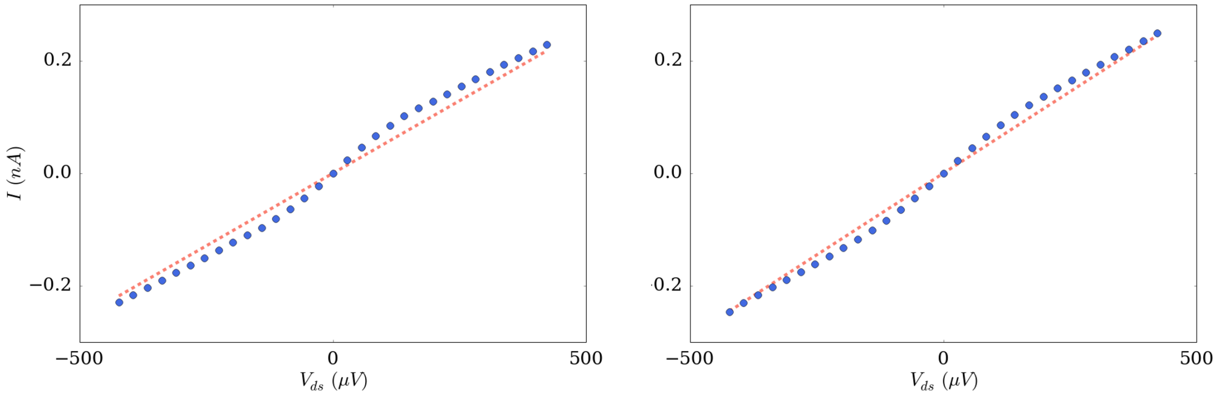

FIGURE E.2 – Backscattered current at V$_g$ = -0.09 V, 90 (left) and 100 mK (right).

This second set of measurement is done at 7 T corresponding to a bulk filling factor of $2/3$.

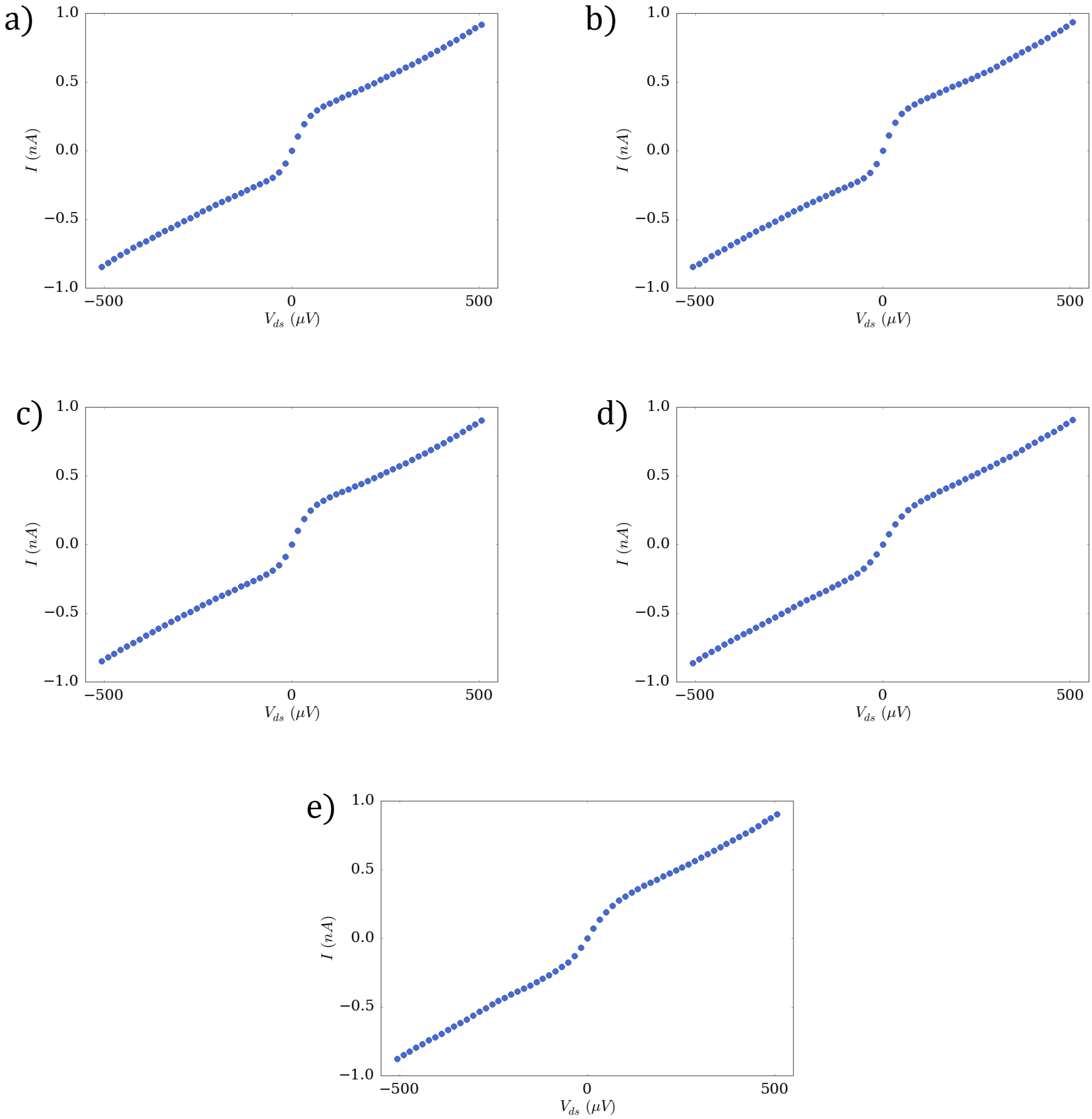

FIGURE E.3 – Backscattered current at $\nu = 2/3$. *a)* 30 mK *b)* 50 mK *c)* 70 mK *d)* 90 mK *e)* 100 mK

Appendix F

Offset in the PASN measurement

F.1 In cross-correlation

The evolution of the offset as a function of the total attenuation, at fixed gate voltage V_g (hence fixed fractional charge e^* and reflection coefficient R) and fixed frequency (so as to keep the attenuation in the wires constant) is represented for all measurements shown in section 6.2. It is fitted with an exponential evolution such that :

$$\sigma\left(x\right) = \sigma_0 exp\left(-\frac{x}{x_0}\right) \tag{F.1}$$

The datas as well as a fit using equation F.1 are shown on figures F.1 and F.2 for respectively charges e/3 and e/5. The exponential fit represents well the evolution of the offset as a function of the attenuation. However for the measurement at V_g = -0.003 V and f = 10 GHz the evolution of the offset does not seem to follow an exponential law of the attenuation, but one can note that the offset is rather small compared to other measurements hence the dispersion of the points is comparable to the other results.

	V_g = -0.09 V		V_g = -0.003 V	
f (GHz)	A (A^2/Hz)	x_0 (dB)	A (A^2/Hz)	x_0 (dB)
10	$2.5\ 10^{-27}$	7.3	$5.3\ 10^{-29}$	11
17	$1.7\ 10^{-27}$	8.7	$1.6\ 10^{-27}$	7.5
22	$7\ 10^{-29}$	15		

TABLE F.1 – Evolution of the offset in PASN measurements as a function of the attenuation at $\nu_b = 2/5$.

At fixed gate voltage, the offset varies for different excitation frequency *f*, which can be understood as the dependence of the inner attenuation of the wires on the frequency. But the offset at fixed frequency also depends on the gate voltage, which is remarkable at 10 GHz. Then the offset also depends on the transmission coefficient or the fractional charge. To discriminate the effect of those parameters, the same analysis can be done at

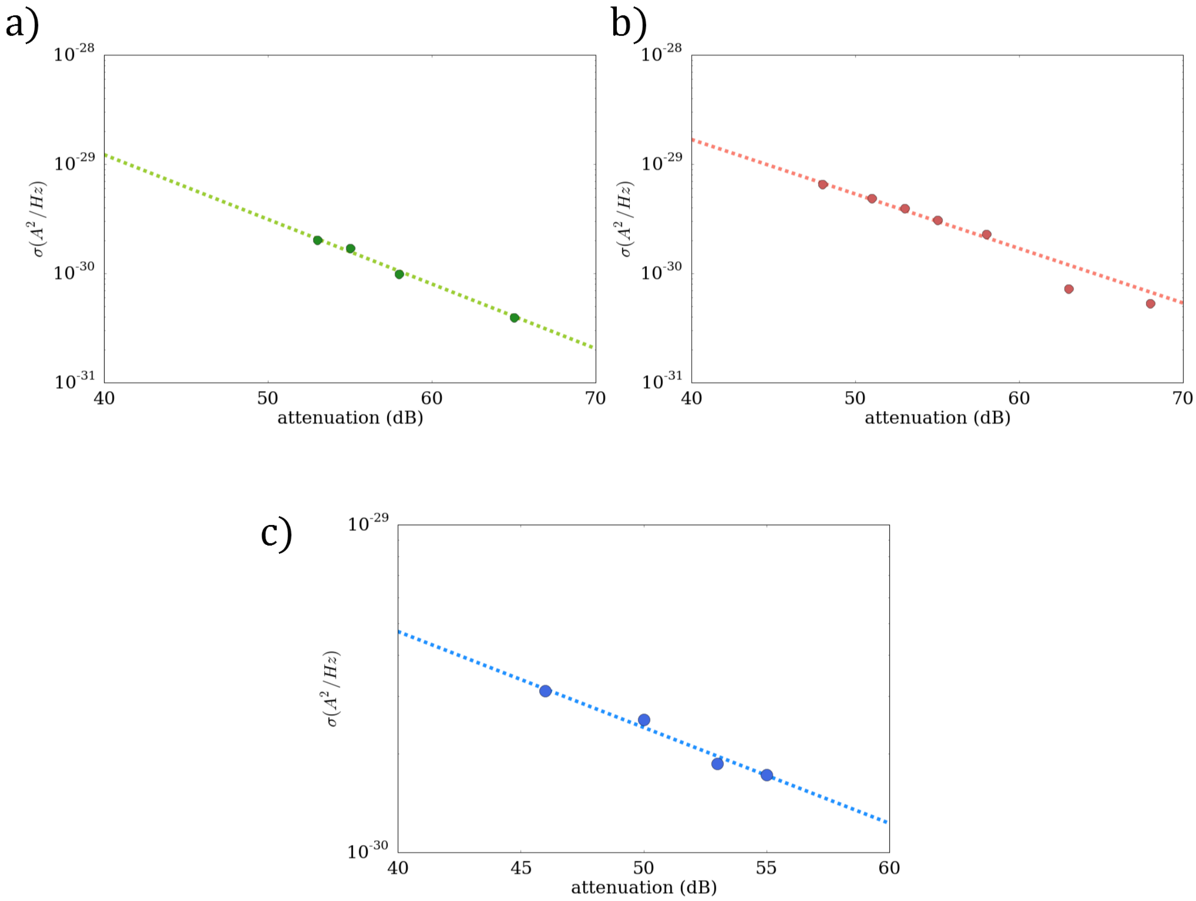

FIGURE F.1 – **Evolution of the offset for PASN measurements at $\nu_b = 2/5$ and $\nu_{QPC} = 1/3$.** All measurements are performed at V$_g$ = -0.09 V and 11 T. *a)* f = 10 GHz *b)* f = 17 GHz *c)* f = 22 GHz.

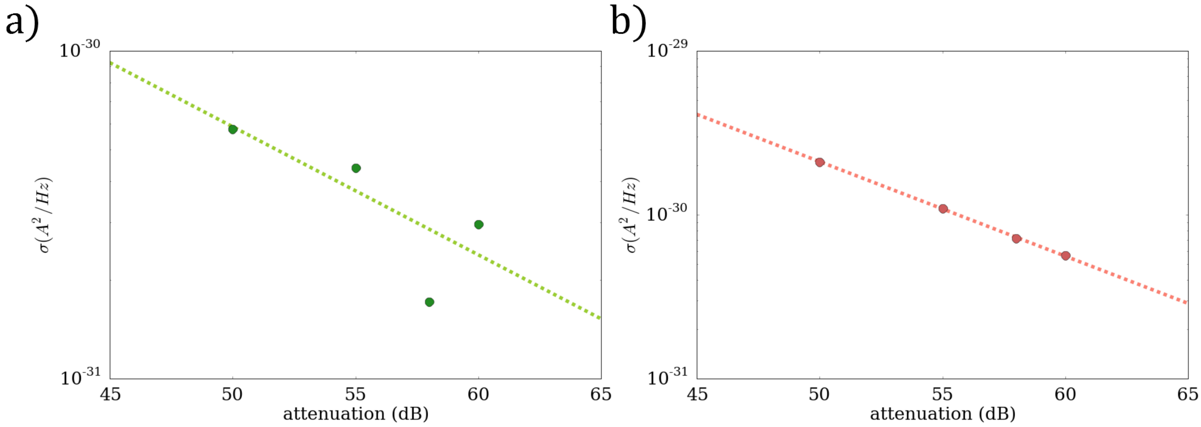

FIGURE F.2 – **Evolution of the offset for PASN measurements at $\nu_b = \nu_{QPC} = 2/5$.** All measurements are performed at V$_g$ = -0.003 V and 11 T. *a)* f = 10 GHz *b)* f = 17 GHz.

bulk filling factor $\nu_b = 1/3$ where the fractional charge have been measured to be of e/3. Surprisingly such effect, namely an offset in PASN measurement, is not observed as at most the difference between DCSN and PASN at large bias voltages is of 10^{-32} A^2/Hz for f = 22 GHz and comparable nominal RF power as for measurements at $\nu_b = 2/5$.

Another parameter that can be changed is then the transmission at fixed fractional charge, which consists in slightly changing the gate voltage so as to remain in a WBS regime. A measurement at $V_g = 0.085$ V and $f = 10$ GHz was done and the evolution of the offset at a function of the attenuation is fitted with formula F.1 with A = $6.3\ 10^{-}27$ A^2/Hz and $x_0 = 6.7$.

The exact origin of this offset remains unknown. However, one can note that for PASN measurement in the IQHE, such effect have been also observed as opposed to those without a magnetic field.

F.2 In auto-correlation

Similarly to what is found in cross-correlation, an unexpected offset appears in PASN measurement using auto-correlation. The evolution of this offset as a function of the attenuation is shown of figures F.3 and F.4 for $\nu_{QPC} = 1/3$ and figures F.5 and F.6 for $\nu_{QPC} = 2/5$.

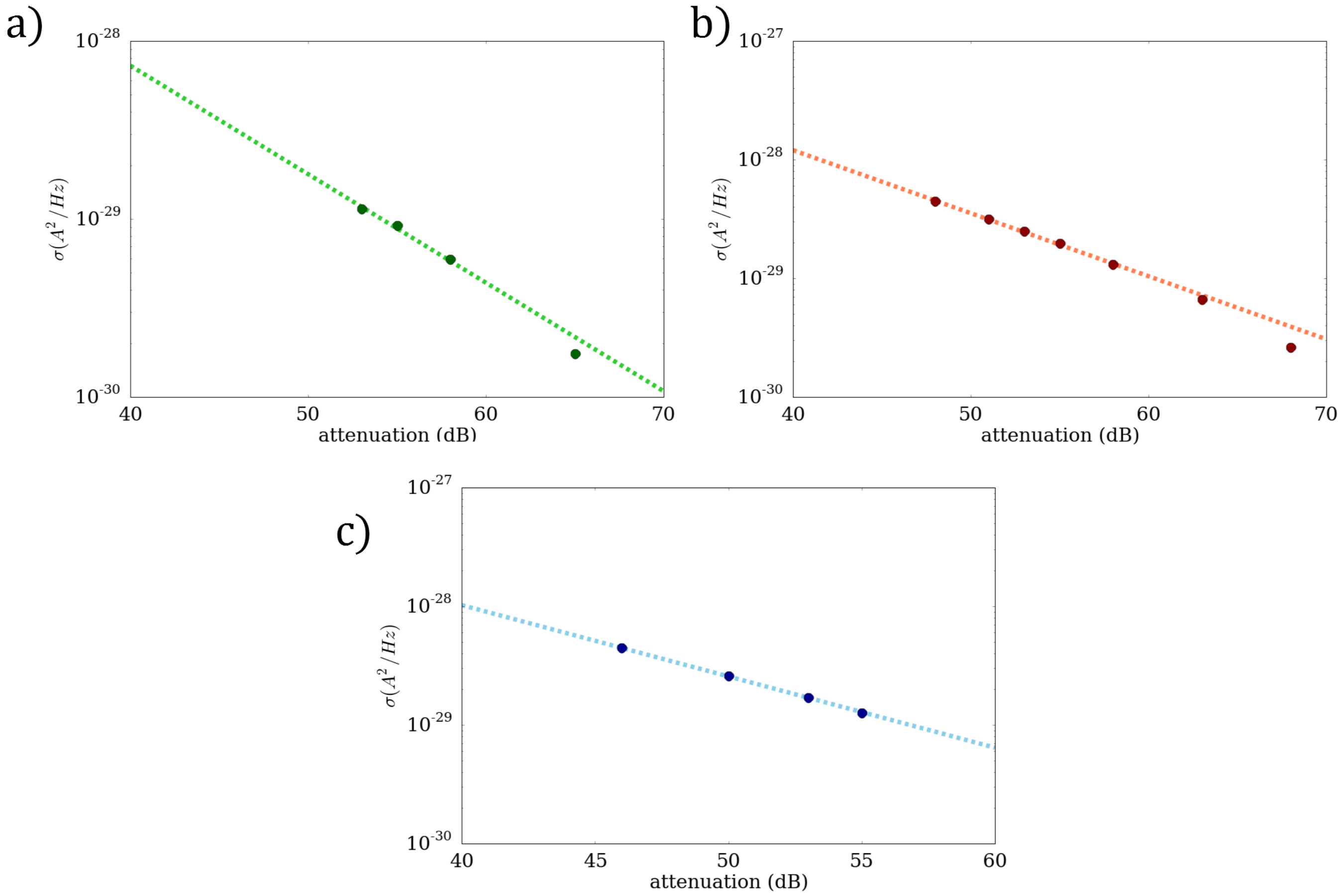

FIGURE F.3 – **Evolution of the offset at $\nu_b = 2/5$ and $\nu_{QPC} = 1/3$ using auto-correlation A.** The PASN measurement are performed at 11.2 T, V_g = -0.09 V and 30 mK using the auto-correlated shot noise A. *a)* $f = 10$ GHz, *b)* $f = 17$ GHz *c)* $f = 22$ GHz.

This evolution is fitted with equation F.1 as for the cross-correlation and the fitting parameters are reported on the tables below. We can not that the value of x_0 is of the

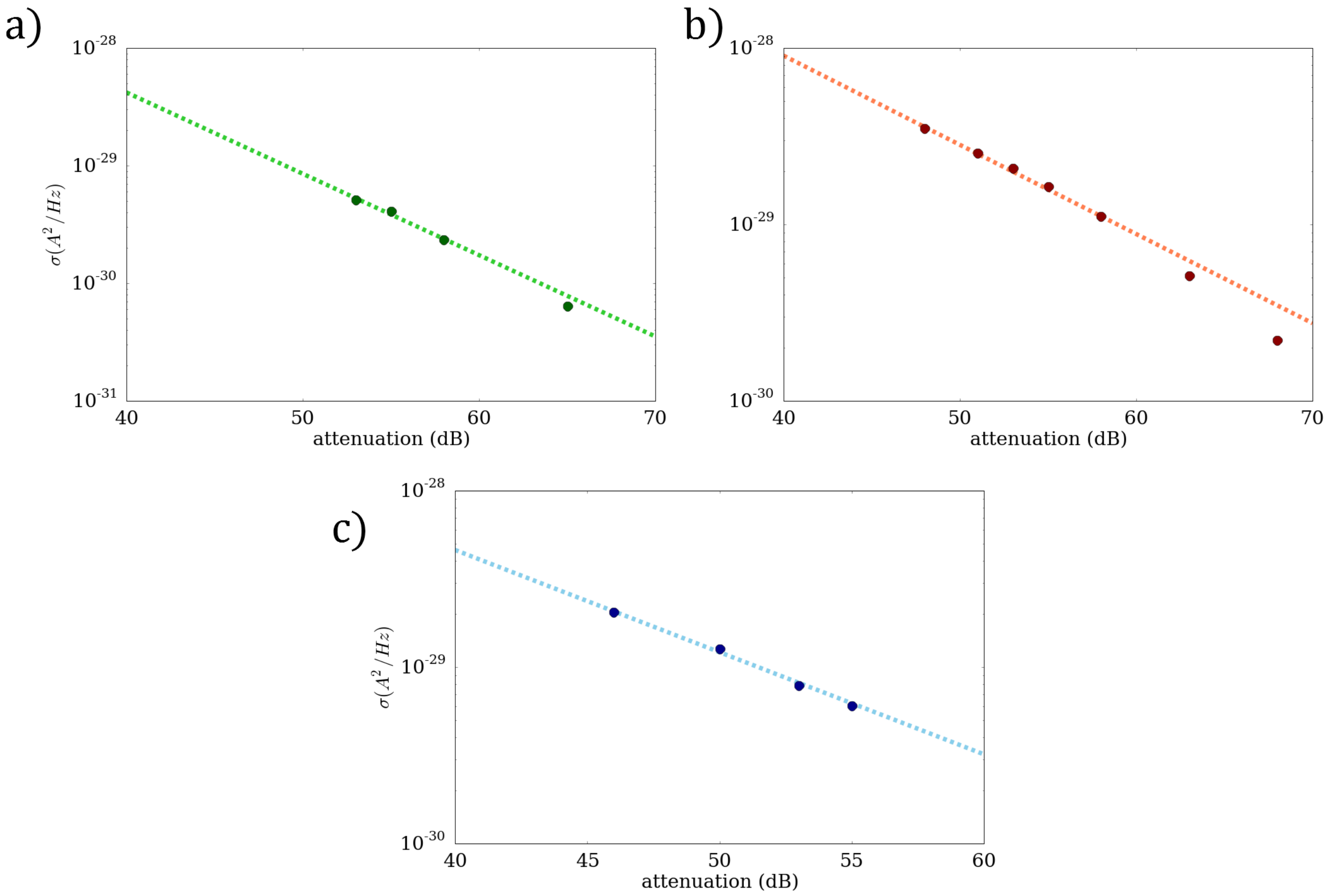

FIGURE F.4 – **Evolution of the offset at $\nu_b = 2/5$ and $\nu_{QPC} = 1/3$ using auto-correlation B.** The PASN measurement are performed at 11.2 T, V$_g$ = -0.09 V and 30 mK using the auto-correlated shot noise B. *a)* $f = 10$ GHz, *b)* $f = 17$ GHz *c)* $f = 22$ GHz.

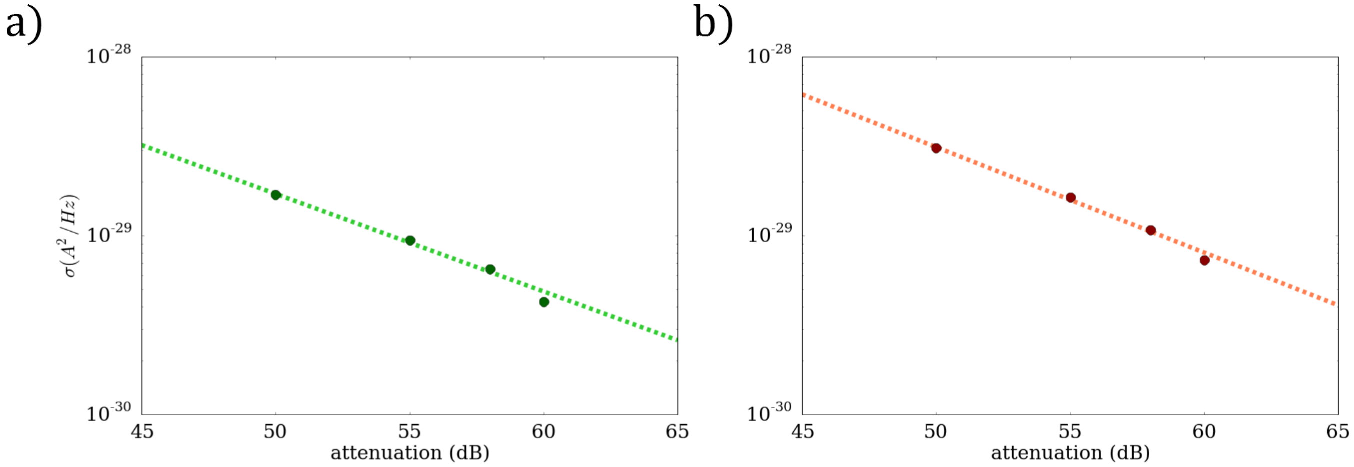

FIGURE F.5 – **Evolution of the offset at $\nu_b = \nu_{QPC} = 2/5$ using auto-correlation A.** The PASN measurement are performed at 11.2 T, V$_g$ = -0.003 V and 30 mK using the auto-correlated shot noise A. *a)* $f = 10$ GHz, *b)* $f = 17$ GHz.

same range for cross- and auto-correlation. The difference mainly exists in the parameter A.

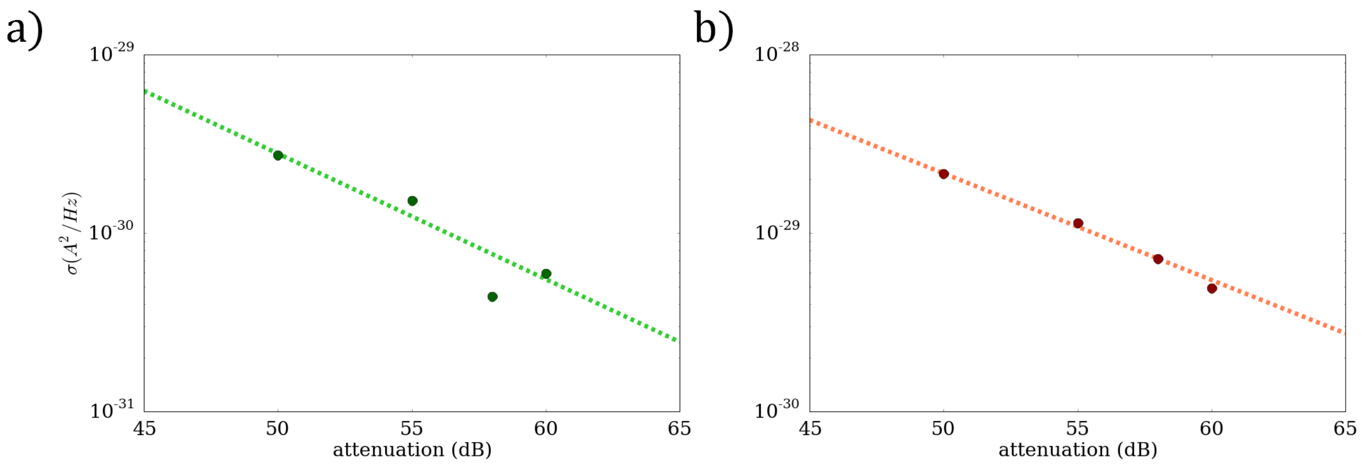

FIGURE F.6 – **Evolution of the offset at $\nu_b = \nu_{QPC} = 2/5$ using auto-correlation B.** The PASN measurement are performed at 11.2 T, V$_g$ = -0.003 V and 30 mK using the auto-correlated shot noise B. *a)* f = 10 GHz, *b)* f = 17 GHz.

	V$_g$ = -0.09 V		V$_g$ = -0.003 V	
f (GHz)	A (A$^2/Hz$)	x_0 (dB)	A (A$^2/Hz$)	x_0 (dB)
10	2 10^{-26}	7.1	9.2 10^{-27}	8
17	1.6 10^{-26}	8.2	2.8 10^{-26}	7.3
22	2.6 10^{-26}	7.2		

TABLE F.2 – Evolution of the offset as a function of the attenuation in PASN measurements using auto-correlation A at $\nu_b = 2/5$.

	V$_g$ = -0.09 V		V$_g$ = -0.003 V	
f (GHz)	A (A$^2/Hz$)	x_0 (dB)	A (A$^2/Hz$)	x_0 (dB)
10	2.4 10^{-26}	6.3	9.2 10^{-27}	6.2
17	9.5 10^{-27}	8.6	2.1 10^{-26}	7.3
22	9.6 10^{-27}	7.5		

TABLE F.3 – Evolution of the offset as a function of the attenuation in PASN measurements using auto-correlation B at $\nu_b = 2/5$.

Appendix G

Tables

2DEG	2D electron gas
CF	Composite Fermion
DCSN	DC Shot Noise
HEMT	High Electronic Mobility Transistor
HOM	Hong-Ou-Mandel
I/FQHE	Integer / Fractional Quantum Hall effect
MBE	Molecular Beam Epitaxy
PASN	Photo-assisted Shot Noise
PSD	Power Spectral Density
QPC	Quantum Point contact
RF	Radio Frequency
SBS/WBS	Strong/Weak - backscattering
SEM	Scanning electron microscope
SN	Shot Noise

Table G.1 – List of acronyms

Symbol	Definition
$h/\hbar$	Plank constant/Reduced Plank constant
k_B	Boltzman constant
T	Electron temperature
e	Elementary electron charge
e^*	Fractional charge
m_e	Elementary electron mass
m^*	Effective electron mass in AlGaAs
B	Magnetic field
ν	Filling factor
f	Frequency of the time-dependent voltage
f_J	Josephson frequency
V_{dc}	DC voltage bias
V_{ac}	Amplitude of the time-dependent voltage
α	Reduced AC amplitude
I_T, I_B, I	Transmitted / Backscattered / Total current
S_V	Voltage noise
S_I^{dc}	DC current noise
S_I^{ac}	Photo-assisted current noise
ΔS_I	Excess current noise

TABLE G.2 – List of symbols

References

[1] R. C. Ashoori, H. L. Stormer, L. N. Pfeiffer, K. W. Baldwin, and K. West. Edge magnetoplasmons in the time domain. *Physical Review B*, 45, 1992.

[2] D. Avoras, J. R. Schrieffer, and F. Wilczek. Fractional statistics and the quantum Hall effect. *Physical Review Letters*, 53, 1984.

[3] C. W. J. Beenakker. Edge channels for the fractional quantum Hall effect. *Physical Review Letters*, 64, 1990.

[4] A. Bid, N. Ofek, M. Heiblum, V. Umansky, and D. Mahalu. Shot noise and charge at the 2/3 composite fractional quantum Hall state. *Physical Review Letters*, 103, 2009.

[5] A. Bid, N. Ofek, H. Inoue, M. Heiblum, C. L. Kane, V. Umansky, and D. Mahalu. Observation of neutral modes in the fractional quantum Hall regime. *Nature*, 466, 2010.

[6] Ya. M. Blanter and M. Buttiker. Shot noise in mesoscopic conductors. *Physics Reports*, 366, 2000.

[7] N. Braslau. Ohmic contacts to GaAs. *Thin Solid Films*, 104, 1982.

[8] M. Buttiker. Absence of backscattering in the quantum Hall effect in multiprobe conductors. *Physical Review B*, 38, 1988.

[9] M. Buttiker. Scattering theory of thermal and excess noise in open conductors. *Physical Review Letters*, 65, 1990.

[10] M. Buttiker. Scattering theory of current and intensity noise correlations in conductors and wave guides. *Physical Review B*, 46, 1992.

[11] F. E. Camino, W. Zhou, and V. J. Goldman. Realization of a Laughlin quasiparticle interferometer : observation of fractional statistics. *Physical Review B*, 72, 2005.

[12] F. E. Camino, W. Zhou, and V. J. Goldman. e/3 Laughlin quasiparticle primary-filling ν=1/3 interferometer. *Physical Review Letters*, 98, 2007.

[13] A. M. Chang, L. N. Pfeiffer, and K. W. West. Observation of a chiral Luttinger behaviour in electron tunneling into fractional quantum Hall edges. *Physical Review Letters*, 77, 1996.

[14] D. B. Chklovskii, B. I. Shklovskii, and L. I. Glazman. Electrostatics of edge channels. *Physical Review B*, 46, 1992.

[15] Y. C. Chung, M. Heiblum, and V. Umansky. Scattering of bunched fractionally charged quasiparticles. *Physical Review Letters*, 91, 2003.

[16] A. Crépieux, P. Devillard, and T. Martin. Photoassisted current and shot noise in the fractional quantum Hall effect. *Physical Review B*, 69, 2004.

[17] S. Datta. *Electronic transport in mesoscopic systems.* Cambridge University Press, 1995.

[18] C. de C. Chamon, D. E. Freed, and X. G. Wen. Tunneling and quantum noise in one-dimensional Luttinger liquids. *Physical Review B*, 51, 1995.

[19] C. de C. Chamon, D. E. Freed, and X. G. Wen. Nonequilibrium quantum noise in chiral Luttinger liquids. *Physical Review B*, 53, 1996.

[20] R. de Picciotto, M. Reznikov, M. Heiblum, V. Umansky, G. Bunin, and D. Mahalu. Direct observation of a fractional charge. *Nature*, 389, 1997.

[21] L. DiCarlo, Y. Zhang, D. T. McClure, and C.M. Marcus. System for measuring auto and cross correlation of current noise at low temperatures. *Review of Scientific Instruments*, 77, 2006.

[22] M. Dolev, M. Heiblum, V. Umansky, A. Stern, and D. Mahalu. Observation of a quarter of an electron at the ν=5/2 quantum Hall state. *Nature*, 452, 2008.

[23] R. R. Du, H. L. Stormer, D. C. Tsui, A. S. Yeh, L. N. Pfeiffer, and K. W. West. The fractional quantum Hall effect with a twist. *Physical Review Letters*, 73, 1994.

[24] J. Dubois. *Vers une source mésoscopique à n-électrons basée sur des pulses de tension Lorentziens.* PhD thesis, Université Pierre et Marie Curie, 2012.

[25] J. Dubois, T. Jullien, P. Degiovanni, P. Roulleau, and D. C. Glattli. Integer and fractional charge Lorentzian voltage pulses analyzed in the framework of photon-assisted shot noise. *Physical Review B*, 88, 2013.

[26] J. Dubois, T. Jullien, P. Roche, A. Cavanna, Y. Jin, W. Wegscheider, P. Roulleau, and D. C. Glattli. Minimal-excitation states for electron quantum optics using levitons. *Nature*, 502, 2013.

[27] A. L. Efros and B. I. Shklovskii. Coulomb gap and low temperature conductivity of disordered systems. *Journal of Physics C : Solid State Physics*, 8, 1975.

[28] P. Fendley, A. W. W. Ludwig, and H. Saleur. Exact nonequilibrium dc shot noise in Luttinger liquids and fractional quantum Hall deviced. *Physical Review Letters*, 75, 1995.

[29] D. Ferraro, A. Braggio, , M. Merlo, N. Magnoli, and M. Sassetti. Relevance of multiple-quasiparticle tunneling bewteen edge states at ν=p/(2np+1). *Physical Review Letters*, 101, 2008.

[30] D. Ferraro, A. Braggio, N. Magnoli, and M. Sassetti. Charge tunneling in fraction edge channels. *Physical Review B*, 82, 2010.

[31] G. Gasse, L. Spietz, C. Lupien, and B. Reulet. Observation of quantum oscillations in the photoassisted shot noise of a tunnel junction. *Physical Review B*, 88, 2013.

[32] S. M. Girvin. Particle-hole symmetry in the anomalous quantum Hall effect. *Physical Review B*, 29, 1984.

[33] D. C. Glattli, P. Jacques, A. Kumar, P. Pari, and L. Saminadayar. A noise detection scheme with 10 mK noise temperature resolution for semiconductor single electron tunneling device. *Journal of Applied Physics*, 81, 1997.

[34] D. C. Glattli, V. Rodriguez, H. Perrin, P. Roche, Y. Jin, and B. Etienne. Shot noise and the Luttinger liquid-like properties of FQHE. *Physica E*, 6, 2000.

[35] D. C. Glattli and P. Roulleau. Levitons for electron quantum optics. *Physica status solidi B*, 254, 2017.

[36] L. I. Glazman, G. B. Lesovik, D. E. Khmel'nitskii, and R. I. Shekhter. Reflectionless quantum transport and fundamental ballistic-resistance steps in microscopic constrictions. *JETP Letters*, 48, 1988.

[37] V. J. Goldman and B. Su. Resonant tunneling in the quantum Hall regime : measurement of fractional charge. *Science*, 267, 1995.

[38] V. J. Goldman, B. Su, and J. K. Jain. Detection of composite fermions by magnetic focusing. *Physical Review Letters*, 72, 1994.

[39] T. G. Griffiths, E. Comforti, M. Heiblum, and V. Umansky. Evolution of quasiparticle charge in th fractional quantum Hall regime. *Physical Review Letters*, 85, 2000.

[40] F. D. Haldane. Fractional quantization of the Hall effect : a hierarchy of incompressible quantum fluid states. *Physical Review Letters*, 51, 1983.

[41] B. I. Halperin. Quantized Hall conductance, current-carryng edge states, and the existance of extended states in a two-dimensional disordered potential. *Physical Review B*, 25, 1982.

[42] B. I. Halperin. Statistics of quasiparticles and the hierarchy of fractional quantized Hall states. *Physical Review Letters*, 52, 1984.

[43] B. I. Halperin, P. A. Lee, and N. Read. Theory of the half-filled Landau level. *Physical Review B*, 47, 1993.

[44] M. Heiblum, M. I. Nathan, D. C. Thomas, and C. M. Knoedler. Direct observation of ballistic transort in GaAs. *Physical Review Letters*, 55, 1985.

[45] M. Henny, S. Oberholzer, C. Stunk, K. Ensslin, M. Holland, and C. Schönenberger. The fermionic Hanbury Brown and Twiss experiment. *Science*, 287, 1999.

[46] S. Hiyamizu, J. Saito, and K. Nanby. Improved electron mobility higher than 10^6 cm^2/Vs in selectively doped GaAs/N-AlGaAs heterostructures grown by MBE. *Japanese Journal of Applied Physics*, 22, 1983.

[47] C. K. Hong, Z. Y. Ou, and L. Mandel. Measurement of subpicosecond time intervals between two photons by interference. *Physical Review Letters*, 59, 1987.

[48] J. K. Jain. Composite-fermion approach for the fractional quantum Hall effect. *Physical Review Letters*, 63, 1989.

[49] X. Jehl, M. Sanquer, R. Calemczuk, and D. Mailly. Detection of doubled shot noise in short normal-metal / superconductor junctions. *Nature*, 405, 2000.

[50] J. B. Johnson. Thermal agitation of electricity in conductors. *Physical Review*, page 32, July 1928.

[51] B. D. Josephson. Possible new effects in superconductive tunneling. *Physics Letters*, 1, 1962.

[52] T. Jullien. *Mesoscopic few-electrons voltage pulse source.* PhD thesis, Université Paris-Sud, 2014.

[53] M. Kamada, T. Suzuki, F. Nakamura, Y. Mori, and M. Arai. Investigation of orientation effect on contact resistance in selectively doped AlGaAs/GaAs heterostructures. *Applied Physics Letters*, 49, 1986.

[54] C. L. Kane and M. P. A. Fisher. Transmission through barriers and resonant tunneling in an interacting one-dimensional electron gas. *Physical Review B*, 46, 1992.

[55] C. L. Kane and M. P. A. Fisher. Nonequilibrium noise and fractional charge in the quantum Hall effect. *Physical Review Letters*, 72, 1994.

[56] C. L. Kane and M. P. A. Fisher. Contacts and edge-state equilibration in the fractional quantum Hall effect. *Physical Review B*, 52, 1995.

[57] C. L. Kane and M. P. A. Fisher. Impurity scattering and transport of fractional quantum Hall edge states. *Physical Review B*, 51, 1995.

[58] C. L. Kane, M. P. A. Fisher, and J. Polchinski. Randomness at the edge : theory of quantum Hall transport at filling ν=2/3. *Physical Review Letters*, 72, 1994.

[59] J. Keeling, I. Klich, and L. S. Levitov. Minimal excitation states of electrons in one-dimensional wirres. *Physical Review Letters*, 97, 2006.

[60] L. P. Kouwenhoven, B. J. van Wees, N. C. van der Vaart, C. J. P. M. Harmans, C. E. Timmering, and C. T. Foxon. Selective population and detection of edge channels in the fractional quantum Hall regime. *Physical Review Letters*, 64, 1990.

[61] A. A. Kozhevnikov, R. J. Schoelkopf, and D. E. Prober. Observation of photon-assisted noise in a diffusive normal metal-superconductor junction. *Physical Review Letters*, 84, 2000.

[62] A. Kumar, L. Saminadayar, and D. C. Glattli. Experimental test of the quantum shot noise theory. *Physical Review Letters*, 76, 1996.

[63] R. Landauer. Spatial variation of currents and fields due to localized scatterers in metallic conduction. *IBM Journal of Research and Development*, 1, 1957.

[64] R. Landauer. Electrical resistance of disordered one-dimensional lattices. *The Philosophical Magazine*, 21, 1970.

[65] R. B. Laughlin. Quantized Hall conductivity in two dimensions. *Physical Review B*, 23, 1981.

[66] R. B. Laughlin. Anomalous quantum Hall effect : an incompressible quantum fluid with fractionally charged excitations. *Physical Review Letters*, 50, 1983.

[67] J. M. Leinaas and J. Myrheim. On the theory of identical particles. *Il nuovo cimento*, 37, 1977.

[68] G. B. Lesovik and L. S. Levitov. Noise in an ac biased junction : nonstationary Aharonov-Bohm effect. *Physical Review Letters*, 72, 1994.

[69] G. B. Lesovik, T. Martin, and J. Torrès. Josephson frequency singularity in the noise of normal-metal-superconductor. *Physical Review B*, 60, 1999.

[70] M. Levinshtein, S. Rumyantsev, and M. Shur. *Handbook series on semiconductor parameters, volume2, Ternary and Quaternary III-V compounds.* World Scientific, 1997.

[71] J. M. Luttinger. An exact soluble model for a many-fermion system. *Journal of Mathematical physics*, 4, 1963.

[72] A. H. MacDonald. Edges states in the fractional quantum Hall effect regime. *Physical Review Letters*, 64, 1990.

[73] T. Martin and S. Feng. Suppresion of scattering in electron transport in mesoscopic quantum Hall systems. *Physical Review Letters*, 64, 1990.

[74] T. Matin and R. Landauer. Wave packet approach to noise in multichannel mesoscopic systems. *Physical Review B*, 45, 1992.

[75] F. P. Milliken, C. P. Umbach, and R. A. Webb. Indications of a Luttinger liquid in the fractional quantum Hall regime. *Solid State Communications*, 97, 1996.

[76] M. Moskalets and M. Buttiker. Floquet scattering theory of quantum pumps. *Physical Review B*, 66, 2002.

[77] H. Nyquist. Thermal agitation of electric charges in conductors. *Physical Review*, page 32, July 1928.

[78] R. Ribeiro Palau, F. Lafont, J. Brun-Picard, D. Kazazis, A. Michon, F. Cheynis, O. Couturaud, C. Consejo, B. Jouault, W. Poirier, and F. Schopfer. Quantum Hall resistance standard in graphene devices under relaxed experimental conditions. *Nature Nanotechnology*, 10, 2015.

[79] F. D. Parmentier, L. N. Serkovic-Loli, P. Roulleau, and D. C. Glattli. Photon-assisted shot noise in Graphene in the THz range. *Physical Review Letters*, 66, 2016.

[80] M. H. Pedersen and M. Buttiker. Scattering theory of photon-assisted electron transport. *Physical Review B*, 58, 1998.

[81] S. Girvin R. E. Prange. *The quantum* H*all effect.* Springer-Verlag, 1987.

[82] J. Rech, D. Ferraro, T. Jonckheere, L. Vannucci, M. Sassetti, and T. Martin. Minimal excitation in the fractional quantum Hall regime. *Physical Review Letters*, 118, 2017.

[83] L.-H. Reydellet, P. Roche, D. C. Glattli, B. Etienne, and Y. Jin. Quantum partition noise of photon-created electron-hole pairs. *Physical Review Letters*, 90, 2003.

[84] M. Reznikov, R. de Picciotto, T. G. Griffiths, M. Heiblum, and V. Umansky. Observation of quasiparticles with one-fifth of an electron's charge. *Nature*, 399, 1999.

[85] M. Reznikov, M. Heiblum, H. Shtrikman, and D. Mahalu. Temporal correlation of electrons : suppression of shot noise in a ballistic quantum point contact. *Physical Review Letters*, 75, 1995.

[86] P. Roche, V. Rodriguez, and D. C. Glattli. Quantum Hall effect, chiral Luttinger liquids and fractional charges. *Comptes Rendus Physiques*, 3, 2002.

[87] P. Roulleau, F. Porier, P. Roche, A. Cavanna, G. Faini, U. Gennser, and D. Mailly. Direct measurement of the coherence length of edge states in the integer quantum Hall regime. *Physical Review Letters*, 100, 2008.

[88] I. Safi. Time-dependent transport in arbitrary extended driven tunnel junctions. *arXiv*, 1404.5950, 2014.

[89] I. Safi. Unified time-dependent perturbative relations applied to spectroscopy through photo-drag current. *arXiv*, 1809.08290, 2018.

[90] I. Safi and E. V. Sukhorukov. Determination of tunneling charge via current measurements. *Europhysics Letters*, 91, 2010.

[91] L. Saminadayar, D. C. Glattli, Y. Jin, and B. Etienne. Observation of the e/3 fractionally charged Laughlin quasiparticle. *Physical Review Letters*, 79, 1997.

[92] M. Santin. *Dynamique quantique dans des conducteurs balistiques et cohérents : interrupteur quantique et transport photo-assisté*. PhD thesis, Université Paris-Saclay, 2017.

[93] R. J. Schoelkopf, A. A. Kozhevnikov, and D. E. Prober. Observation of "photon-assisted" shot noise in a phase-coherent conductor. *Physical Review Letters*, 80, 1998.

[94] W. Schottky. Über spontane stromschwankungen in verschiedenen elektrizitätsleitern. *Annalen der Physik*, 57, 1918.

[95] S. Shapiro. Josephson currents in superconducting tunneling : the effect of microwave and other observations. *Physical Review Letters*, 11, 1963.

[96] F. Stern and S. Das Sarma. Electron energy levels in GaAs-Ga$_{1-x}$Al$_x$As heterojunction. *Physical Review B*, 30, 1984.

[97] H. L. Stormer. The fractional quantum Hall effect with a twist. *Solid State Communications*, 92, 1994.

[98] P. Streda, J.Kucera, and A. H. MacDonald. Edge states, transmission matrices and the Hall resistance. *Physical Review Letters*, 57, 1987.

[99] H. L. Störmer, R. Dingle, A. C. Gossard, W. Wiegmann, and M. C. Sturge. Two-dimensional electron gas at a semiconductor-semiconductor interface. *Solid State Communications*, 29, 1979.

[100] T. J. Thornton, M. Pepper, H. Ahmed, D. Andrews, and G. J. Davies. One-dimensional conduction in the 2D electron gas of GaAs-AlGaAs heterojunction. *Physical Review Letters*, 56, 1986.

[101] S. Tomonaga. Remarks on Bloch's method of sound waves applied to many-fermion problems. *Progress of Theoretical Physics*, 5, 1950.

[102] D. C. Tsui, H. L. Stormer, and A.C. Gossard. Two-dimensional magnetotransport in the extreme quantum limit. *Physical Review Letters*, 48, 1982.

[103] P. J. Turley, D. P. Druist, E. G. Gwinn, K. Maranowski, K. Campmann, and A. C. Gossard. Tunneling through point contacts in the quantum Hall effect. *Physica B*, 249-251, 1998.

[104] K. v. Klitzing, G. Dorda, and M. Pepper. New method for high-accuracy determination of the fine-structure constant based on quantized Hall resistance. *Physical Review Letters*, 45, 1980.

[105] B. J. van Wees, L. P. Kouwenhoven, E. M. M. Willems, C. J. P. Harmans, J. E. Mooij, H. van Houten, C. W. J. Beenakker, J. G. Williamson, and C. T. Foxon. Quantum ballistic and adiabatic electron transport studied with quantum point contacts. *Physical Review B*, 43, 1991.

[106] B. J. van Wees, H. van Houten, C. Beenakker, J. Williamson, L. Kouwenhoven, D. van der Marcel, and C. Foxon. Quantized conductance of point contacts in a two-dimensional electron gas. *Physical Review Letters*, 60, 1988.

[107] X. G. Wen. Chiral Luttinger liquid and edge excitations in the fractional quantum Hall states. *Physical Review B*, 41, 1990.

[108] X. G. Wen. Electrodynamical properties of gapless edge excitations in the fractional quantum Hall states. *Physical Review Letters*, 64, 1990.

[109] X. G. Wen. Edge transport properties of the fractional quantum Hall states and weak-impuritiy scattering of a one-dimensional charge density wave. *Physical Review B*, 44, 1991.

[110] X. G. Wen. Gapless bound excitations in the quantum Hall states and in the chiral spin states. *Physical Review B*, 43, 1991.

[111] D. A. Wharam, T. J. Thornton, R. Newbury, M. Pepper, H. Ahmed, J. E. F. Frost, D. G. Hasko, D. C. Peacock, D. A. Ritchie, and G. A. C. Jones. One dimensional transport and the quantization of the ballistic resistance. *Journal of Physics C : Solid States Physics*, 21, 1988.

[112] F. Wilczek. Quantum mechanics of fractional-spin particles. *Physical Review Letters*, 49, 1982.

[113] R. L. Willet, C. Nayak, K. Shtengel, L. N. Pfeiffer, and K. W. West. Magnetic-field-tuned Aharonov-Bohm oscillations and evidence for non-Abelian anyons at ν=5/2. *Physical Review Letters*, 111, 2013.

[114] R. L. Willet, L. N. Pfeiffer, and K. W. West. Measurement of filling factor 5/2 quasiparticle interference with observation of charge e/4 and e/2 period oscillations. *Proceedings of the National Academy of sciences of the United States of America*, 106, 2009.

[115] A. Yacoby, U. Sivan, C. P. Umbach, and J. M. Hong. Interference and dephasing by electron-electron interaction on length scales shorter than the elastic mean free path. *Physical Review Letters*, 66, 1991.

[116] D. Yoshioka. *The quantum* H*all effect.* Springer, 2002.

[117] Y. Zhang, D. T. McClure, E. M. Levenson-Falk, C. M. Marcus, L. N. Pfeiffer, and K. W. West. Distinc signature for Coulomb blockade and Aharonov-Bohm interference in electronic Fabry-Pérot interferometers. *Physical Review B*, 79, 2009.

[118] H. Z. Zheng, H. P. Wei, D. C Tsui, and G. Weimann. Gate-controlled transport in narrow GaAs/Al$_x$Ga$_{1-x}$As heterostructures. *Physical Review B*, 34, 1986.

université
PARIS-SACLAY

ÉCOLE DOCTORALE
Physique
en île-de-France
(EDPIF)

Titre: Dynamique des excitations de l'Effet Hall quantique fractionnaire: charge et fréquence Josephson fractionnaires

Mots clés: Physique mésoscopique, Effet Hall quantique fractionnaire, Bruit de grenaille, Fréquence Josephson

Résumé: Dans certains états quantique de la matière, le courant peut être transporté par des porteurs de charges ayant une fraction e^* de la charge élementaire. C'est notamment le cas de l'Effet Hall quantique fractionnaire (EHQF) qui se produit pour des systèmes électroniques bidimensionels à basse température et soumis à un fort champ magnetique perpendiculaire. Quand le nombre de quantum de flux en unité h/e est une fraction du nombre d'électrons, le courant se propage le long des bords de l'échantillon sans dissipation. Les porteurs de charges impliqués dans le transport portent une charge fractionnaire. La mise en évidence de ces charges peut être faite via les faibles fluctuations de courant dûes à la granularité de la charge. Nous présentons ici une méthode fiable de mesure de la charge fractionnaire basée sur des correlations croisées de fluctuations de courant. La dynamique de ces charges fractionnaires lorsque l'échantillon est irradié avec des photons GHz est étudiée, permettant la mesure de la fréquence Josephson des charges fractionnaires. Ces mesures valident les processus photo-assisté en régime d'EHQF et permettent une manipulation résolue en temps des charges fractionnaires, dans le but de réaliser une source d'anyon sur le principe du léviton afin de réaliser des tests de la statistique anyonique de ces charges fractionnaires.

Title: Dynamics of excitations in the Fractional Quantum Hall effect: fractional charge and fractional Josephson frequency

Keywords: Mesoscopic physics, Fractional quantum Hall effect, Shot noise, Josephson frequency

Abstract: In some quantum matter states, the current may remarkably be transported by carriers that bear a fraction e^* of the elementary electron charge. This is the case for the Fractional quantum Hall effect (FQHE) that happens in two-dimensional systems at low temperature under a high perpendicular magnetic field. When the number of magnetic flux in units of h/e is a fraction of the number of electron, a dissipationless current flows along the edges of the sample and is carried by anyons with fractional charge. The observation of the fractional charge is realized through small current fluctuations produced by the granularity of the charge. Here is presented a reliable method to measure the fractional charge by the mean of cross-correlation of current fluctuations. Moreover, the dynamical properties of those charges is probed when the sample is irradiated with photos at GHz frequency. The long predicted Josephson frequency of the fractional charge is measured. Those measurements validate Photo-assisted processes in the FQHE and enable time-domain manipulation of fractional charges in order to realize a single anyon source based on levitons to perform tests of the anyonic statistics of fractional charge.

Université Paris-Saclay
Espace Technologique / Immeuble Discovery
Route de l'Orme aux Merisiers RD 128 / 91190 Saint-Aubin, France